ATOMISTIC STUDY OF STRESS-INDUCED UNSTABLE STRUCTURAL RESPONSES OF CRYSTALS AT FINITE TEMPERATURES

by

Jing Han Wang

B.S., Department of Physics, Yunnan University, P.R.China

M.S., Department of Physics, Yunnan University, P.R.China

SUBMITTED TO THE DEPARTMENT OF NUCLEAR ENGINEERING IN PARTIAL FULFILLMENT OF THE REQUIREMENTS FOR THE DEGREE OF

DOCTOR OF PHILOSOPHY

at the

MASSACHUSETTS INSTITUTE OF TECHNOLOGY

January 1993

Signature of Author _____
Department of Nuclear Engineering
January 1993

Certified by _____
Professor Sidney Yip
Thesis Supervisor

Accepted by _____
Professor Allan F. Henry
Chairman, Department Committee on Graduate Students

ATOMISTIC STUDY OF STRESS-INDUCED UNSTABLE STRUCTURAL RESPONSES OF CRYSTALS AT FINITE TEMPERATURES

by

Jing Han Wang

Submitted to the Department of Nuclear Engineering on January 8, 1993 in partial fulfillment of the requirements for the degree of Doctor of Philosophy.

Abstract

The goal of this dissertation is to investigate the different conditions of elastic instability of an ordered crystal lattice, the corresponding mechanisms of unstable structural responses, and the final states of the transformed lattice. The study involves a combination of analytical analysis in linearized elasticity and atomistic simulation using empirical interatomic potential functions for simple f.c.c. crystals. From finite-strain continuum elasticity analysis one obtains the instability criteria, critical strains, as well as the deformation paths required for the onset of each particular instability, while simulation allows direct observation of the unstable structural responses to such prescribed deformations at finite temperatures. Together, this approach makes possible the understanding of how different modes of lattice deformation can compete with each other under conditions of finite stress and thermal activation.

Starting with the equilibrium conditions for a stressed crystal and applying the principle of virtual work to this system, we obtain an eigenvalue problem (with zero eigenvalue). The requirement of the vanishing of the determinant of the elastic constant (current) matrix C_{ij} gives three distinct instability conditions, namely, the vanishing of $C_{11} + 2C_{12}$, $C_{11} - C_{12}$, and C_{44}, corresponding to spinodal (dilatational), Born (normal distortional), and shear distortional instability, respectively. For each instability the associated eigenmode prescribes the path of strain deformation required to bring about such an instability and allows a prediction of the critical strain in terms of the finite-strain elastic constants. Of particular relevance to the present study are two results, that spinodal instability is associated with volumetric (purely dilatational) deformation, and that Born instability requires symmetry breaking and no volume change. Thus the analysis shows that the onset of a particular instability depends on how the lattice is deformed. On the other hand, such calculation cannot give the final state of deformation after the instability has set in.

Both Monte Carlo and molecular dynamics simulations are used to study directly the unstable structural response of an f.c.c. lattice and a grain-boundary superlattice (GBSL) under various stress and strain deformations at low and elevated temperatures. Two empirical interatomic potentials are used, the Lennard-Jones pair potential and a many-body potential (Embedded Atom Method) for a noble metal. By selectively

suppressing the Born instability through a constraint of maintaining lattice symmetry, we show that pure dilatation and uniaxial stretch loadings on the f.c.c. lattice and GBSL all lead to spinodal instability. At low temperatures, the transitions take the form of decohesion and cleavage fracture in the f.c.c. lattice, and grain-boundary fracture in the GBSL. At high temperatures, the unstable structural response of the f.c.c. lattice at the instability is homogeneous disordering with all the attendant features of melting. For spinodal instability, the associated structural change is a mechanical catastrophe through the mechanism of cavitation at low temperatures, while at high temperatures, homogeneous nucleation of a disordered phase with the help of enhanced vibrational amplitude. Although these transitions can take different forms depending on the temperature, their underlying cause, i.e., large stress fluctuations at the critical strain, is essentially the same. If there is no constraint on lattice symmetry, Born instability, signaled by a transient orthorhombic distortion of the simulation cell, occurs through a completely different mechanism of symmetry breaking, or bifurcation, followed by a further shear distortion. The orthorhombic distortion predicted by analytic analysis is found to play only an intermediate role in triggering the subsequent shear distortion. At the temperatures below the melting point, all the transitions of the lattice under uniaxial stress take the f.c.c. lattice to a distorted b.c.c. structure. These phase transitions are a continuous, second-order process. In contrast, in the case of pure heating to melting (P=0), the Born instability triggers a completely homogeneous structural disordering. This form of melting (mechanical) is a first-order transition.

Thesis Supervisor:	Sidney Yip
Title:	Professor of Nuclear Engineering
Thesis Reader:	Frank A. McClintock
Title:	Professor of Mechanical Engineering

Acknowledgments

I would like to take this opportunity to express my sincere gratitude to those individuals who have made this dissertation possible. For more than four years, Professor Sidney Yip has been a long standing source of guidance, support and inspiration, as a mentor and as a friend. I am grateful for his knowledge and encouragement throughout my graduate studies. I am indebted to Professor Frank A. McClintock for his helpful discussions and insightful suggestions. I would also like to thank Drs. Dieter Wolf and Simon R. Phillpot at Argonne National Laboratory. This investigation has greatly benefited from their simulating discussions and insightful suggestions. I would like to acknowledge them for their generosity in allowing me to use their simulation codes. Dr. Simon R. Phillpot helped me to calculate the zero temperature elastic constants of the grain-boundary superlattice. In addition, I would also acknowledge Drs. Paul R. Okamoto and Nghi Q. Lam for very useful discussions about solid-state amorphization.

I would like to acknowledge the financial support I have received, a Graduate Fellowship from the C. C. Wu Foundation, a Graduate Thesis Appointment at the Argonne National Laboratory, and research assistantships under grants from the National Science Foundation (CHE-8806767) and the Air Force Office of Science Research (AFOSR-91-0285). The computations performed in this work were made possible by generous allocations from the NSF San Diego Supercomputer Center. Calculations were also carried out at Argonne National Laboratory. The computing facility at MIT was also used.

I am thankful for the many true friends I have made during my graduate studies. Thanks to K. S. Cheung and T. Poon for their friendship and encouragement, thanks to X. L. Zhou, M. J. Tang, N. Sonwalkar, A. Isik, and R. Pflueger for many simulating discussions. Lastly, I am deeply grateful to my wife, Jing Yang, for her continuous support and encouragement, and to my parents for providing me with the utmost family support. I thank them for all that they have done throughout the years.

Table of Contents

List of Figures

List of Tables

Chapter 1
Introduction

1.1 Background and Motivation

A knowledge of the elastic constants of stressed crystals over a wide range of temperatures is of fundamental importance in understanding not only the inherent strength and deformability of crystals , but also a number of instability or structural transformation phenomena, such as melting, mechanical failure, martensitic transition, and homogeneous solid-state amorphization, which are associated with the vanishing of the elastic moduli.

The elastic stability of a crystalline lattice can be defined as [Grimvill 86]

$$B_T > 0,\ G(110][1\bar{1}0] > 0,\ G(100][010] > 0^* \qquad (1.1)$$

where B_T, $G(110][1\bar{1}0]$, and $G(100][010]$ are the bulk, shear moduli in (110) along $[1\bar{1}0]$ and in (100) along [010] of an f.c.c. crystal, respectively. $G(110][1\bar{1}0]$ and $G(100][010]$ are denoted as μ and sometimes μ' in the literature.

For more than half a century, many efforts have been made to interpret the observed structural phase transitions and mechanical failures based on these elastic stability criteria. The early studies were not very successful. The difficulties in direct comparison of theoretical predictions and experiments arise from several stumbling blocks: First, it has been long argued that the infinite lattice model requires a special equilibrium condition, namely that the externally applied stresses must vanish. [Venkataraman 75] This requirement is consistent with the fundamental assumption of the generalized Hooke's law, stating that in the regime of linear elasticity the elastic constants are constants. This restriction severely confines the lattice dynamics theory and leads to a long standing confusion about the reference state for which one calculates the elastic constants theoretically. [Wallace 72] It is only recently that the thermoelastic theory of stressed crystals has been formulated completely enough to clarify the differences between finite strain elastic coefficients which govern stress-strain relations and those which govern elastic wave propagation. Second, since the relation between the elastic instability and the

---

* From now on, following the literature, we will call the violation of the first inequality, i.e., $B_T = 0$, as spinodal instability or dilatatonal instability, that of the second, $G(110][1\bar{1}0] = 0$, as Born instability or normal insatbility, and of the third one, that is $G(100][010] = 0$, as shear instability. Throughout the thesis these terms will be used interchangeably.

possible structural changes has not been well understood, controversies exist in the interpretation of structural phase transformations, such as melting and solid-state amorphization. [Cahn 86a] These debates partially come from the lack of knowledge about the mechanisms of these transitions. Finally, as will be discussed in this thesis, the elastic instabilities of crystals manifest themselves only when the crystals are in the corresponding eigen-deformation states. Put in other words, the instabilities of the crystals may be suppressed by improper deformation environments.

Born [Born 39, 56] was the first in attempting to investigate the instability of crystalline lattice. According to Born, any crystal capable of homogeneous deformation may be treated as a homogeneous system with six degrees of freedom that can be chosen as the six uniform strain components, thus the Helmholtz free energy of a cubic lattice can be written as a function of temperature and of these strain components. The stability conditions of the crystal which guarantee that the quadratic term in the free energy expansion is positive and finite, are

$$\frac{1}{3}(C_{11} + C_{12}) > 0, \quad C_{11} - C_{12} > 0, \quad C_{44} > 0, \tag{1.2}$$

where the elastic constants are the second derivatives of the free energy with respect to the six strain components. He interpreted that the violation of the first inequality gives rise to sublimation, the second leads to a transition to a "gel" state, and when $C_{44} = 0$, the crystal loses its resistance to shear and melts.

More detailed studies of these three stabilities at zero temperature and careful static calculations of the bulk and shear moduli of the Morse-potential family of f.c.c., b.c.c. and simple cubic crystals under arbitrary hydrostatic pressure were carried out by Milstein et al.. [Milstein 77, 78, 79a] Their computations were extended to dilatations up to magnitudes where the lattice would in practice be unstable and studied the entire range of stability of cubic crystals. The significance of this work [Hill 77, Milstein 79a] is that they, for the first time, tried to correlate the instability conditions to the eigenstates of deformation and to explore the possible bifurcations. By applying the principles of bifurcation analysis to the deformation processes, they not only recovered all the instability criteria proposed by Born, but further revealed the eigenstates of the strain that are associated with each instability. They found that for spinodal instability the eigenstates are necessarily homogeneous and purely volumetric. They defined the dilatation imposed on the system before it fails as the fundamental path of deformation, and the eigenstates of the instability of the crystal in the unstable region are then the extension of the fundamental path. They called this extension the primary path. For the Born instability, "the

corresponding uniform eigenmodes make the lattice orthorhombic without varying the cell volume." They called this volume conserved path the secondary deformation path. For the shear instability they found "the corresponding uniform eigenmodes distort the lattice without varying the cell edges." [Milstein 79a]

The elastic instability criteria give the physical conditions under which the crystalline lattices will become unstable. In order to connect these instability conditions to any structural phase transformation, fundamental understanding of temperature and volume dependence of the elastic constants is needed. In the past few decades, measurements on inert gas solids and metals [Collard 91, Tallon 79a, 79b 80, Wallace 70] have contributed to a good body of experimental data. On the other hand, the equation of state of a large number of solids has been studied up to rather high pressures, and for some, over a wide range of temperatures [Wallace 72]. The pressure dependence provides information on the nonlinear compressibility of solids and the temperature dependence reveals the effects of anharmonicity. The volume dependence of the compressibility shows a power law [Murnaghan 44], or exponential dependence [Grover 73]. More recently, Tallon [Tallon 80] has found a more general volume dependence. Based on the assumption that the isothermal, or isobaric volume derivatives of the bulk and shear moduli are independent of temperature and volume, he showed that the volume dependence of these elastic moduli can be well described by an exponential function that, for small volume expansion, gives a linear temperature dependent relation of elastic moduli.

As is well known, thermal expansion effects can cause elastic constants to soften dramatically with increasing temperature. By means of molecular-dynamics simulations, Jaszczak and Wolf [Jaszczak 92] demonstrated the distinct thermal softening effects of atomic-level disorder and volume expansion on the elastic constants and moduli. Atomic-level structural disorder, either homogeneous or inhomogeneous, is a mechanism for elastic stiffening, while the thermal volume expansion, on the other hand, results in a softening. Whether the disorder or the volume expansion dominates the elastic response depends on the detailed nature of the disorder and the anisotropy of the volume expansion.

As mentioned above, Born tried to connect elastic instability to melting based on the observation that "the difference between a solid and a liquid is that the solid has elastic resistance against shearing stress while the liquid has not." [Born 39] He emphasized the mechanical behavior of solids when they are heated up to melting. Another well-known feature of melting is that the crystalline lattice undergoes a structural order to disorder transition. This transition is accompanied by a considerable volume expansion. Therefore, understanding the mechanism of structural disordering is relevant to understanding the mechanism of melting. In several existing theoretical models melting is treated as a

homogeneous process and associated with a lattice instability resulting from the atomic displacements exceeding a threshold value (Lindemann's criterion) [Ubbelohde 78], from the vanishing of the shear modulus (Born criterion) [Born 39, 56], or from the spontaneous generation of a critical concentration of vacancies [Ubbelohde 78]. On the other hand, clear experimental evidence, gathered from attempts to probe mechanism of melting in various materials, points to the dominant effects of interfaces in the actual melting processes [Cahn 86b]. Obviously by regarding melting as a homogeneous phenomenon, the above models are unable to address the issue of melting at an interface, clearly an intrinsically heterogeneous process.

Significant progress in this topic was made by means of MD simulations. It has been clearly demonstrated [Wolf 90b] that one can distinguish two kinds of melting transitions, thermodynamic melting and mechanical melting. Thermodynamic melting [Lutsko 89b] basically is determined by the free energies of both the crystalline and liquid states. In this case, the solid melts through the nucleation and growth of a liquid phase at extended defects, such as interface, voids, or dislocations, and thus is a slow, heterogeneous process. In contrast, mechanical melting is triggered by an elastic instability causing the sudden collapse of the entire crystalline lattice, a fast, homogeneous process. The mechanical melting temperature T_s gives the highest temperature that one can superheat a solid. Since all realistic materials contain a large number of extended defects, it is not surprising that nature prefers thermodynamic melting.

Very interesting piece of experimental evidence that shows the possibility of mechanical melting was noted by Tallon. [Tallon 79a] He examined the existing elastic moduli data measured for metals, inert gases, silver bromide and benzene as functions of isobaric volume expansion from absolute zero to the melting point and in the melt. He noted that in extrapolating the measured data to large volume expansion, except for the inert gases, one finds the isothermal bulk modulus varies continuously with volume through the melting expansion, and in every case either $(C_{11} - C_{12})/2$ or C_{44} falls continuously to essentially zero at the volume of the melt at the freezing point. This indicates that by suppressing thermodynamic melting one can directly correlate mechanical instability with melting.

Based on his study Tallon emphasized the importance of an expansion-induced mechanical instability (either one of the two shear moduli vanishes) as the fundamental cause of melting, and he concluded that the transition is purely first-order. Boyer [Boyer 85] has also concluded that melting is the onset of a mechanical instability, but, on the contrary, arrived at a quite different conclusion regarding the nature of the transition. He has compared his purely continuous view of mechanical melting with the somewhat similar

picture often used to describe low temperature, displacive or martensitic-type, solid-state transformations. He pointed out that in general, a crystal structure is defined by two sets of parameters, one which defines the lattice and another defines the positions of atoms within the unit cell of the lattice. To make the analogy between melting and displacive transition he proposes that a solid-liquid transition at the melting temperature takes place when the structural parameter defining the lattice, changes from a static to a fluctuating dynamic variable, whereas displacive transitions involve a similar change except in the parameter describing the atom positions in the unit cell of the lattice. In both cases the crystal goes from high to low symmetry. Clearly, since both of these conclusions are closely related to elastic instability, a direct study of mechanical melting and instability may help to resolve the controversy.

That solid-state amorphization is analogous to melting in certain respects has been recognized by a number of authors. [Johnson 86, Cahn 86a, Richet 88, Okamoto 88, Fecht 89, Wolf 90] Cahn and Johnson have pointed out that these two phenomena are closely related in the sense of both involving the destruction of crystalline order. Okamoto et al. [Okamoto 90] have discussed the similarity in the volume dependence of the shear modulus during irradiation and heating-induced melting. In particular, Wolf et al [Wolf 90] proposed that considerations of thermodynamic parallels between conventional melting by heating and solid-state amorphization suggest a unified picture of how crystals undergo structural disordering. In this view, a crystalline lattice undergoes structural disordering in two different forms, a high-temperature crystal-to-liquid transition that manifests as conventional melting, and a low-temperature crystal-to-glass transition in the form of solid-state-amorphization. The basis of this generalized view of melting is that volume expansion plays a central role in all disordering processes, whether it is induced by temperature or by external means. A fundamental question in this context is thus whether the lattice can disorder under homogeneous expansion at a constant temperature.

More recently, Sciortino et al. [Sciortino 92] studied ice I_h and SiO_2 under compression and tension by simulations. They found that for both systems a rapid collapse of the crystalline lattices occurs at the onset of diverging compressibility under both compression and tension. Li and Johnson [Li 92] simulated a Lennard-Jones potential model of two species at constant stress. The system amorphizes when the atomic size difference exceeds a critical value. They observed a shape change of the simulation cell from cubic to orthorhombic before the system loses its long-range order. They suggested that this mechanical instability indicates that the crystal to glass transition is caused by frustrations of local shear deformations.

Another category of "mechanical-failure" phenomena closely related to the elastic instability is the stress- or strain- induced mechanical failures and phase transitions of materials. In the past decade several attempts have been made primarily to study the processes of fracture. It was assumed in these studies that the solid remains in thermal equilibrium, i.e., responds reversibly to applied stress, all the way up to the breakdown point. Soules and Busbey [Soules 83] have considered plastic deformation through cavity formation in "pristine" glasses. Kieffer and Angell [Kieffer 88] have focused on the isotropic expansion of silica network in an effort to explore the fracture structures and dynamics induced by increasing negative pressure.

More recently several MD and MC studies of fracture of crystals have been carried out by a group of investigators [Blumgerg Selinger 90, 91, Wang 91]. They showed that when a crystal is subjected to an uniaxial or hydrostatic stress, it remains in metastable equilibrium all the way up to a critical value of the applied stress, at which point the crystal fails irreversibly via the nucleation of microcracks. The critical load (or failure strength) is found to decrease strongly with temperature. In a statistical-thermodynamic approach to fracture, they treated the solid under stress as a metastable state of equilibrium, then showed that the system fractures at a failure threshold corresponding to a metastability limit, or spinodal, and fails in the form of homogeneous nucleation of fracture.

Martensitic transition is a type of structural phase transformation that does not involve long range diffusion of atoms. The transition is accomplished through a collective motion of all the atoms. Consequently, the parent and daughter phases show certain orientational relations. Since historically martensite was obtained during the quenching of steels, martensitic transition has been referred to as concentration modulation induced by temperature variation. However, studies by various groups [Bolling 69, 70a, 70b, 71, Delaey 74] have shown that the enthalpies of the parent and daughter phases have strong dependence on the variations in stress as well as in temperature. In particular, Najafabadi and Yip [Najafabadi 83] have carried out a Monte Carlo study of stress induced reversible b.c.c. to f.c.c. transition. Cheung and Yip [Cheung 92] have studied the f.c.c. to h.c.p. structural transition in α-iron under uniaxial loading. In the present study we are not interested in the martensitic transition itself, but rather in making the connection between the Born instability and martensitic transition.

Milstein and Farber [Milstein 80] were the first to systematically study the possible athermal structural phase transformation of crystals following exactly the elastic instability criterion and its eigenstates. Guided by their theoretical results on elastic instability, they studied model systems of an f.c.c. crystal using Morse type potential functions, with the parameters adjusted to reproduce the experimental values of cohesive energy, lattice

parameter, and bulk modulus for b.c.c. Fe [Girifalco 59], and lattice parameter and elastic constants C_{11} and C_{12} for f.c.c. Ni [Milstein 73]. They showed for f.c.c. Fe and Ni, by static calculation, that when the crystal is subjected to an initial uniaxial [100] tensile load, the crystal follows the primary path, i.e., as the load is increased the crystal stretches in the direction of the load and contracts in the lateral directions. At the "invariant eigenstate" at which the elastic moduli satisfy $C_{11} = C_{12}$, there exists a special bifurcation enabling the crystal to depart upon a secondary path along which the tetragonal symmetry is broken. Along this new path, with decreasing load, the crystal starts to expand in one of the two lateral directions and eventually its extension in that lateral direction "catches up" with the [100] extension. The system ends up for Fe, at zero load, in an b.c.c. structure, while for Ni again in a tetragonal face-centered structure. On the compression side along the primary path, both Fe and Ni crystals undergo an f.c.c. to b.c.c. transition.

Parrinello and Rahman [Parrinello 81] extended the MD method beyond the constant-volume scheme. They were primarily interested in the possibility of stress-induced polymorphism in solids involving crystal lattice with different symmetries. To study the behavior of solids at finite temperatures and high level of external stress, in particular at high values of the stress at which spontaneous defect generation and crystal structure transformation become possible, the constant pressure MD approach of Andersen [Andersen 80] was generalized to allow arbitrary shape (in addition to volume) for the periodic simulation cell. Their new Lagrangian, then, involves the full anisotropic stress tensor (rather than a scalar, hydrostatic pressure) and each cell edge (rather than the volume) can fluctuate independently.

Using their MD method and the same Morse potential as used by Milstein [Milstein 80], Parrinello and Rahman [Parrinello 81] studied how a single crystal of Ni behaves under uniform uniaxial compressive and tensile loads. Their work confirmed some of the results of Milstein and Farber. But they also showed that at finite temperature the bifurcation predicted by the static calculation does not occur. Instead very close to the bifurcation point the system fails. Moreover, they found a new result that, for this model of Ni, upon uniform uniaxial compression, the f.c.c. structure transforms into an h.c.p. arrangement. They concluded that since their results of the stress-strain relation before the bifurcation point is in good agreement with the results of static calculation, the departure of their results away the static results is itself in the right direction because the system will be "softer" in the presence of thermal agitation.

In the context of the above review, one can see that all these mechanical failures and structural phase transformations are closely related to elastic instabilities. Although the elastic instability criteria themselves have been known for more than half a century, the

connection between the criteria and the elastic deformations, the validity of these criteria at finite temperature, and the mechanisms of the possible mechanical failures or structural phase transitions are still not well understood.

1.2 Problem Statement and Approach of Study

Considering an infinite crystal lattice under stress or strain deformation, there is no doubt that the lattice will fail when the deformation becomes large enough to destablize the lattice. But fundamental questions one can ask are what is the underlying physics, what are the mechanisms responsible for the failure, and what is the final state into which the system will evolve. In principle, one can define the instability of crystal lattice at zero temperature, solve the instability criterion and all the possible unstable modes of deformation either through energetic argument [Milstein 77] or finite-strain continuum elasticity analysis (see Chapter 2 for detail). But at finite temperatures, the thermal activated micro-stress and strain fluctuation add new degrees of freedom. It is not clear how these microscopic movements will initiate the macroscopic state changes of the crystals.

The goal of this dissertation is to investigate the different conditions of elastic instability of an ordered crystal lattice, the corresponding mechanisms of unstable structural responses, and the final states of the transformed lattice at finite temperatures. The study involves a combination of analytical analysis of finite-stain elasticity and atomistic simulations using empirical interatomic potential functions for simple f.c.c. crystals. From the finite-strain elasticity analysis we obtain the instability criteria, critical strains, as well as the deformation paths required for the onset of each particular instability, while simulation allows direct observation of the unstable structural responses to such prescribed deformations at finite temperatures. Together this approach makes possible the understanding of how different modes of lattice deformation can compete with each other under conditions of finite stress and thermal activation.

The first question of the study concerns the underlying physics of a mechanical deformation process - the instability of a crystal lattice. Given a thermodynamic system at equilibrium, if the thermodynamic variables are changed in a virtual process so as to bring the system out of equilibrium, then there will be a restoring force which tends to drive the system back to equilibrium. The presence of this restoring force means that the system is stable. The original equilibrium configuration could be unstable if force develops which tends to move the system further away from equilibrium. Consider a thermodynamic function, such as the internal energy U, the general statement of thermodynamic stability

requires the internal energy to be a minimum, with respect to all virtual variations of the thermodynamic variables. At equilibrium:

$$d^2U > 0. \tag{1.3}$$

It can be shown [Wallace 70] that this condition is equivalent to the requirement that all the second derivatives of the internal energy with respect to thermodynamic variables are positive finite. The equation

$$d^2U = 0 \tag{1.4}$$

therefore determines the inflection point of the internal energy.

One can define crystal thermodynamic instability through the solutions of Eq. (1.4). The stability requires that the internal energy function to have positive curvature. The system is unstable when the curvature of the internal energy becomes negative. The inflection point thus define the thermodynamic instability criteria. It is known [Wallace 70] that thermodynamic stability can be described in terms of the standard solution of an eigenvalue problem involving a matrix composed of second derivatives of the internal energy. In the present case, to approach the first question above one needs to develop a similar equation of instability as (1.4). The thermodynamic function should be generalized to include the strain variables. Following this idea one can recover the three instability criteria, Eq. (1.2) that are well known in literature. [Born 39, 56, Milstein 79]

Given these instability criteria the question naturally arises as to what are the corresponding unstable states. In the same context it can be asked how does a crystal fail in any of these unstable states. By intuition it seems that the crystal will fail at the onset of whichever instability that gives the minimum critical strain. As one will see in this thesis, this is only true under certain conditions. In fact the crystal does fail when it is deformed beyond the inflection point since some of the elastic moduli will become negative, but it does not necessarily fail at the minimum critical strain.

Starting with the equilibrium conditions for a stressed crystal and applying the principle of virtual work to this system we obtain an eigenvalue problem (with zero eigenvalue). As usual, to obtain a nontrivial solution requires the determinant of the elastic constant (current) matrix C_{ij} to vanish. Taking the lattice with cubic symmetry as an example, we find three distinct instability conditions already given in Eq. (1.2), namely, the vanishing of $C_{11} + 2C_{12}$, $C_{11} - C_{12}$, and C_{44}, which we will refer to as spinodal (dilatational), Born (normal distcrtional), and shear distortional instability, respectively.

The first condition corresponds to the vanishing of the bulk modulus, and the other two to the vanishing of the shear modulus in specific directions. It should be emphasized that these instability criteria are only valid for an infinite system under stress boundary condition.

Although these different instability conditions have been known for a long time, there still exists some conceptual confusion about the instability criteria and the failure modes of a lattice. Among these three criteria the failure modes associated with the first and the third are quite simple to understand. Since it is a consequence of the vanishing of the bulk modulus, the spinodal instability corresponds to a decohesive failure mode. On the other hand, the shear distortional instability corresponds to a pure shear distortion mode. The Born instability is more subtle. It is given by a combination of the elastic constants, C_{11} and C_{12}, yet it triggers a complicated shear failure mode.

In the present study we will not only focus on the instability but also follow through with the solution of eigenvalue problem to obtain the eigenstates (strain) corresponding to the different modes. These eigenstates naturally define the specific deformation paths and reveal the particular failure modes associated with each instability. They also allow a prediction of the critical strain for each instability in terms of the finite-strain elastic constants. Of particular relevance to our work are two results: first spinodal instability is associated with volumetric (purely dilatational) deformation, and secondly, Born instability requires symmetry breaking without changing volume and brings about a bifurcation on the primary path of deformation. Thus the analysis shows that the onset of a particular instability depends on how the lattice is deformed.

As pointed out earlier, although the theoretical study gives insight into the nature of the instabilities and the eigenmodes of the deformation, it does not give the final states of deformation after the instability has set in. A complete study of the problem entails also taking into account the effects of different interatomic interactions, temperature, and inhomogeneity of the crystal. Furthermore, relatively little theoretical work has been done on the determination of the critical strains for each of the crystal instabilities. These present opportunities for atomistic simulation which is a unique technique to explore all these aspects of the instability problem.

For our simulation study, we choose two potential models, the Lennard-Jones (L-J) potential and an Embedded-Atom Method (EAM) potential. The L-J potential is a softer interaction relative to the EAM potential, the former is usually used for inert gas elements while the latter is constructed more specifically for metals. Both Monte Carlo (MC) and molecular dynamics (MD) simulations are performed on an f.c.c. crystal using one or the other of these two potentials. We calculate the elastic constants as a function of strain for

these two potential models. Assuming linear elasticity and combining with the instability criteria, we obtain estimates of the critical strains for the spinodal and Born instabilities in the case of cubic and tetragonal symmetry. Along the simulation path, we also calculate all the mechanical, structural and dynamic properties such as potential energy, pressure, lattice parameter, structure factor and mean-squared displacement. By the analysis of simulation data which include the direct observation of unstable structural responses to the successively increasing external stress or strain loading along the deformation paths, we are able to verify the three instabilities predicted by theory. We explicitly demonstrate that while different potentials give different values of the critical strain, the same instabilities occur in both potential models. The scope and main results of the study of this dissertation are summarized in Fig. 1.1. The theoretic results, namely, the instability criteria and the eigen-deformation paths, are valid above the arrows marked with T (finite temperature), while the simulations follow the eigen-deformation paths and determine the final states of transformed at finite temperatures (except the pure shear distortion indicated by the dashed arrow).

To our knowledge, the present simulation study of deformed crystals constitutes the first systematic investigation of crystal instability and stress-induced unstable structural responses of crystals at finite temperatures using both pairwise and many-body potentials. Along the dilatation path, it is found that at low temperatures both the L-J and EAM f.c.c. crystals fail in the form of nucleation of cavitation. This transition occurs at smaller strain than that predicted by the bulk modulus for spinodal instability. Detailed analysis shows that this is caused by the thermal activation of inhomogeneous nucleation of cavitation. At high temperatures a homogeneous structural disordering is observed in both models.

In order to study the effects of crystalline inhomogeneity on the transition we use a so-called grain-boundary superlattice (GBSL) model. This model consists of thin slabs of f.c.c. crystal of the same material. These slabs are rotated with respect to each other about the (001) plane normal to form a periodic array of high-angle twist grain boundaries. The elastic constant matrix of this model has tetragonal symmetry. The simulations are carried out at temperatures T = 300K and 500K along the primary path of deformation. We observe gain boundary fracture under hydrostatic stress and uniaxial strain. This suggests that crystalline inhomogeneity does not affect the course of the spinodal instability.

The thesis is organized in the following manner. In chapter 2 we present our theoretical results of finite-elasticity analysis of a deformed crystal. By applying the principle of virtual work, we solve the instability conditions which determine the inflection point of the strain energy and the corresponding eigenstates. These analyses bring out the three instabilities of the crystal and enable us to assign certain distinct characteristic aspects

of the instability. In chapter 3 we begin with an introductory discussion about the L-J and EAM potentials we will use and the basic simulation procedures. The elastic, mechanical, dynamic and structural properties we will calculate and analyze are defined in this chapter. Chapter 4 is devoted to temperature effects on elastic instabilities and mechanical melting. In this chapter we will show that mechanical melting is a first-order phase transformation, demonstrate that both the spinodal instability and Born instability are efficient in triggering mechanical melting. In chapters 5 and 6 we present our MC and MD simulation results on a single crystal with L-J and EAM potentials, where we explicitly demonstrate the spinodal and Born instabilities and discuss the detailed characterization of the transition mechanisms. The effects of potential and temperature are also examined in these chapters. In chapter 7 we present the MD simulation results on the unstable structural responses of GBSL with EAM potential, where we focus our attention on the effects of crystalline inhomogeneity. In the last chapter we summarize all our results and give recommendations for further studies.

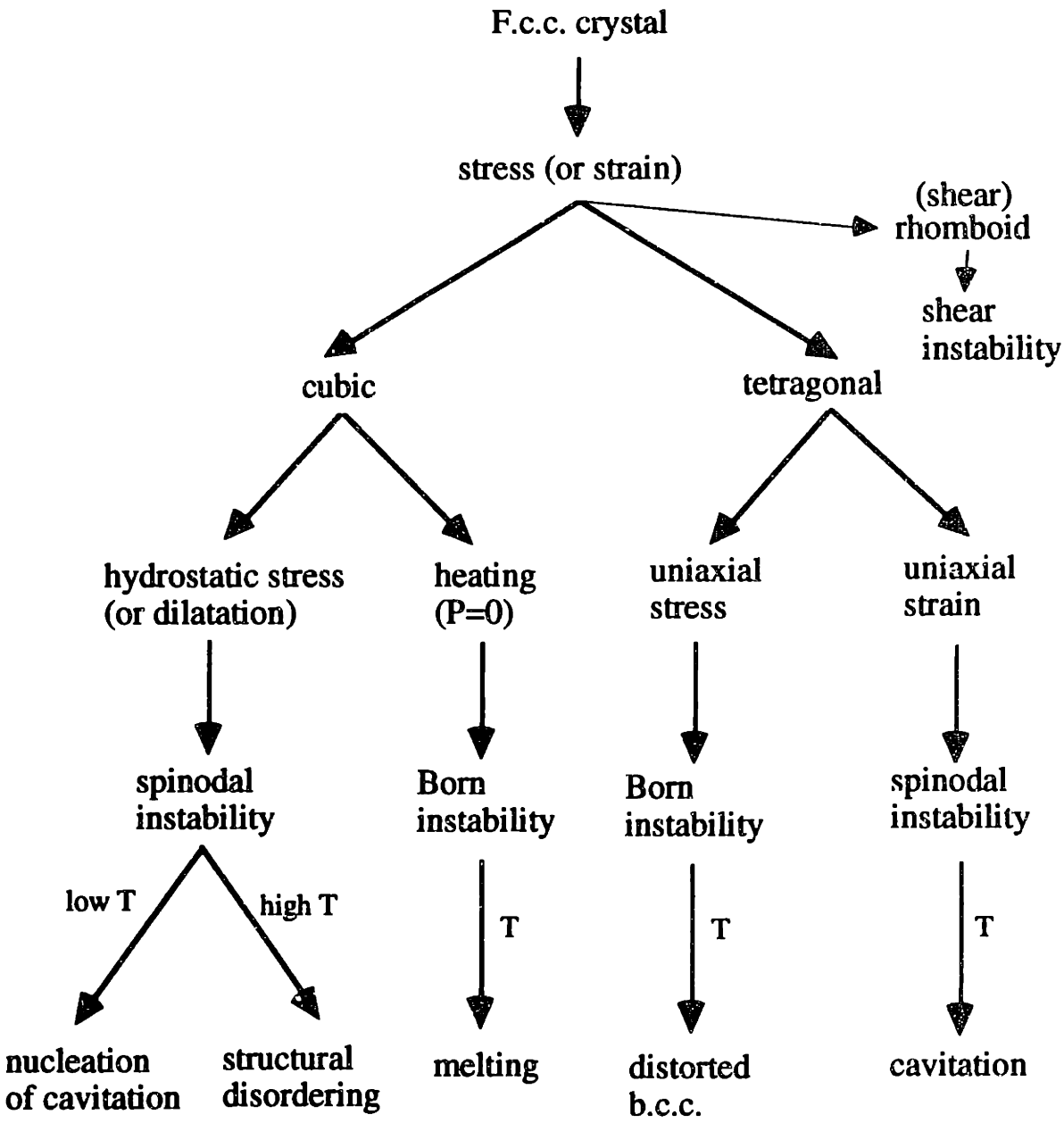

Fig. 1.1 Scope of investigation

Chapter 2

Continuum Analysis of Elastic Instability

2.1 Elastic Constant Matrices and Elastic Moduli

The theoretical description of the mechanical behavior of a body is largely based on elasticity theory. we shall briefly review some fundamental thermodynamic definitions of stress and strain, and the basic formulas of linear elasticity theory.

Consider a homogeneously deformed elastic object, having an arbitrary initial configuration **X** corresponding to an arbitrary applied stress Σ and a finite strain ε. Suppose that a further small deformation $\delta\varepsilon$ is imposed on this system, then its free energy change can be expressed [Landau 70, Wallace 72], in the differential form, as

$$dF = - SdT + \Omega\, \sigma_{\alpha\beta} d\varepsilon_{\alpha\beta}, \quad (\alpha, \beta = x, y, z \in \mathbf{x}). \tag{2.1}$$

Here, the summation is implied over repeated subscript indices *. Ω is the volume of the system at its initial configuration, σ and ε are the internal stress and strain tensor. The elastic part of the free energy change can be defined as

$$dW = \sigma_{\alpha\beta} d\varepsilon_{\alpha\beta} \tag{2.2}$$

where W is called the strain energy density. The internal stress is then defined by

$$\sigma_{\alpha\beta} = \left(\frac{\partial W}{\partial \varepsilon_{\alpha\beta}}\right)_{\varepsilon'} = \left(\frac{\partial F}{\partial \varepsilon_{\alpha\beta}}\right)_{\varepsilon',T} \tag{2.3}$$

where the prime indicate all the other components of strain except $\varepsilon_{\alpha\beta}$. And the isothermal elastic constants are defined as

$$C_{\alpha\beta\chi\eta} = \left(\frac{\partial^2 W}{\partial \varepsilon_{\alpha\beta} \partial \varepsilon_{\chi\eta}}\right)_{\varepsilon'} = \left(\frac{\partial \sigma_{\alpha\beta}}{\partial \varepsilon_{\chi\eta}}\right)_{\varepsilon'} \tag{2.4}$$

which is a fourth rank tensor. In equations (2.3) and (2.4) the subscript of the bracket means that the derivatives are evaluated at the initially stressed reference state.

---

* For convenience, we shall use repeated indices to indicate summation, boldface to be tensors of any order, Greek to indicate the component of Cartesian coordinate and Latin indices the atom number throughout of this thesis, except where they are otherwise specified.

For a large number of solids at low applied stresses, the internal stresses are proportional to the strains. The elastic constant tensor relates the stress and strain by the generalized Hooke's law [Saada 74, Grimvall 86]

$$\sigma_{\alpha\beta} = C_{\alpha\beta\chi\eta}\varepsilon_{\chi\eta}. \tag{2.5}$$

The inverse relation of (2.5)

$$\varepsilon_{\chi\eta} = \left[\mathbf{C}^{-1}\right]_{\alpha\beta\chi\eta}\sigma_{\alpha\beta} \tag{2.6}$$

defines the compliance tensor $\mathbf{S} = \mathbf{C}^{-1}$, which expresses strain in terms of stress.

Hooke's law (2.5) holds for both polycrystalline and single-crystal specimens. The number of independent elastic constants $C_{\alpha\beta\chi\eta}$ or compliances $S_{\alpha\beta\chi\eta}$ depends on the symmetry of the system. Within the principal coordinate system [Saada 74], by using the shorthand Voigt notation

$$\begin{array}{lll} xx \rightarrow 1 & yy \rightarrow 2 & zz \rightarrow 3 \\ yz \rightarrow 4 & xz \rightarrow 5 & xy \rightarrow 6 \\ zy \rightarrow 4 & zx \rightarrow 5 & yx \rightarrow 6 \end{array} \tag{2.7}$$

the elastic constant tensor of a cubic crystal, which is characterized by three independent elastic constants C_{11}, C_{12} and C_{44}, is

$$\mathbf{C} = \begin{pmatrix} C_{11} & C_{12} & C_{12} & & & \\ C_{12} & C_{11} & C_{12} & & 0 & \\ C_{12} & C_{12} & C_{11} & & & \\ & & & C_{44} & & \\ & 0 & & & C_{44} & \\ & & & & & C_{44} \end{pmatrix} \tag{2.8}$$

and the compliance tensor is

$$\mathbf{S} = \begin{pmatrix} S_{11} & S_{12} & S_{12} & & & \\ S_{12} & S_{11} & S_{12} & & 0 & \\ S_{12} & S_{12} & S_{11} & & & \\ & & & S_{44} & & \\ & 0 & & & S_{44} & \\ & & & & & S_{44} \end{pmatrix}. \tag{2.9}$$

For a tetragonal system, six independent elastic constants C_{11}, C_{12},C_{13},C_{33},C_{44} and C_{66} are needed to specify the symmetry, then the elastic constant tensor becomes

$$\mathbf{C} = \begin{pmatrix} C_{11} & C_{12} & C_{13} & & & \\ C_{12} & C_{11} & C_{13} & & 0 & \\ C_{13} & C_{13} & C_{33} & & & \\ & & & C_{44} & & \\ & 0 & & & C_{44} & \\ & & & & & C_{66} \end{pmatrix} \tag{2.10}$$

and the compliance tensor

$$\mathbf{S} = \begin{pmatrix} S_{11} & S_{12} & S_{13} & & & \\ S_{12} & S_{11} & S_{13} & & 0 & \\ S_{13} & S_{13} & S_{33} & & & \\ & & & S_{44} & & \\ & 0 & & & S_{44} & \\ & & & & & S_{66} \end{pmatrix}. \tag{2.11}$$

The elastic moduli are obtained from the inverse of the diagonal elements of the compliance tensor [Grimvall 86, Wolf 92]:

Young's moduli

$$Y_x = S_{11}^{-1}, \quad Y_y = S_{22}^{-1}, \quad Y_z = S_{33}^{-1} \tag{2.12}$$

Bulk modulus

$$B = [S_{11}+S_{22}+S_{33}+2\,(S_{12}+S_{13}+S_{23})]^{-1} \tag{2.13}$$

Shear moduli

$$G_{yz}=S_{44}^{-1}=C_{44}, \quad G_{xz}=S_{55}^{-1}=C_{55}, \quad G_{xy}=S_{66}^{-1}=C_{66}. \tag{2.14}$$

For cubic crystal Eqs. (2.12), (2.13), and (2.14) give

$$Y_x \equiv Y_y \equiv Y_z = S_{11}^{-1} = \frac{(C_{11}-C_{12})^2(C_{11}+2C_{12})}{C_{11}+C_{12}} \tag{2.15}$$

$$B = \frac{C_{11}+2C_{12}}{3} \tag{2.16}$$

and

$$G_{yz} \equiv G_{xz} \equiv G_{xy} = C_{44} \tag{2.17}$$

For tetragonal symmetry one has

$$Y_x \equiv Y_y = S_{11}^{-1} = (C_{11}-C_{12})\left[1 + \frac{C_{12}C_{33}-C_{13}^2}{C_{11}C_{33}-C_{13}^2}\right] \tag{2.18a}$$

$$Y_z = S_{33}^{-1} = C_{33} - \frac{2C_{13}^2}{C_{11}+C_{12}} \tag{2.18b}$$

$$B = \frac{(C_{11}+C_{12})C_{33}-2C_{13}^2}{C_{11}+C_{12}+2C_{33}-4C_{13}} \tag{2.19}$$

$$G_{yz} \equiv G_{xz} = C_{44}, \quad G_{xy} = C_{66} \ . \tag{2.20}$$

In the regime of the linear elasticity theory, the behavior of any isotropic elastic body can be completely described by a set of so called field equations. In material coordinate system, one has fifteen differential equations for uniquely determining the state of the body [Malvern 69]. These equations are:

Three equations of motion

$$\frac{\partial \sigma_{\alpha\beta}}{\partial x_\beta} + \rho F_\alpha = \rho \frac{d^2 u_\alpha}{dt^2} \tag{2.21}$$

where ρ is the density of the system, F_α is the αth component of the body force and u_α is the αth component of displacement **u**, six equations of Hooke's law

$$\sigma_{\alpha\beta} = \lambda \varepsilon_{\chi\chi} \delta_{\alpha\beta} + 2G\varepsilon_{\alpha\beta} \tag{2.22}$$

where λ is the Lame coefficient, and six geometric equations

$$\varepsilon_{\alpha\beta} = \frac{1}{2}\left(\frac{\partial u_\alpha}{\partial x_\beta} + \frac{\partial u_\beta}{\partial x_\alpha}\right). \tag{2.23}$$

Among these fifteen equations, the first three determine the three components of displacement **u**, the last six define the six strains and the six equations of Hooke's law relate corresponding stresses and strains. Once the displacement **u** is determined for given boundary conditions, it uniquely defines the corresponding stress and strain state of the body.

2.2 General Definition of Instability

In this section we will introduce the basic concept of elastic instability of a crystal by examining a very simple example of a stress-strain curve, and define the elastic instability more precisely on the basis of linear elasticity theory. A brief discussion about the principle of virtual work will be presented, which we shall use to derive the equations that determine the inflection point of strain energy density and instability conditions.

2.2.1 Concepts of Elastic Instability of Crystal

Let us consider an elastic body under applied stress Σ and zero body force, as sketched in Fig. 2.1 (a). The deformation induced by this applied stress is described by a strain tensor ε. Then the work done by this applied stress is

$$W = \int_S \Sigma_{\alpha\beta} d\varepsilon_{\alpha\beta} \tag{2.24}$$

where S is the surface of elastic body. When the system is in equilibrium, the internal stress is equal to the applied stress

$$\sigma(\varepsilon) = \Sigma\,, \tag{2.25}$$

thus

$$W = \int_S \sigma_{\alpha\beta} d\varepsilon_{\alpha\beta}. \tag{2.26}$$

For simplicity, let us consider an applied hydrostatic stress, so the deformation is pure dilatation and can be described by a single variable ε with $\varepsilon_{\alpha\alpha} = \varepsilon\delta_{\alpha\beta}$. Eq. (2.26) is then simplified as

$$W = 3\int_S \sigma d\varepsilon. \tag{2.27}$$

Fig. 2.1 (b) shows schematically the strain energy density as a function of strain ε. Using Eqs. (2.3) and (2.27) one can get a stress-strain relation as shown in Fig. 2.1 (c).

From Fig. 2.1 (c) one can see that for an equilibrium crystal lattice when a surface traction Σ is applied on the system, there is at least one solution of Eq. (2.25) which gives the corresponding deformation state of strain. But when the magnitude of the applied stress is increased beyond the level of Σ_i, Eq. (2.25) has no solution any more. Physically this means that the system will become unstable. The point ε_i is called the inflection point of the strain energy density which gives the stability limit of the lattice. We will define the conditions that determine the inflection point as the instability criteria of the crystal lattice. In general, there could be several deformation modes at the inflection point. The system must become unstable against at least one of these modes. The inflection point of the strain energy density thus also define a bifurcation point of the primary deformation path.

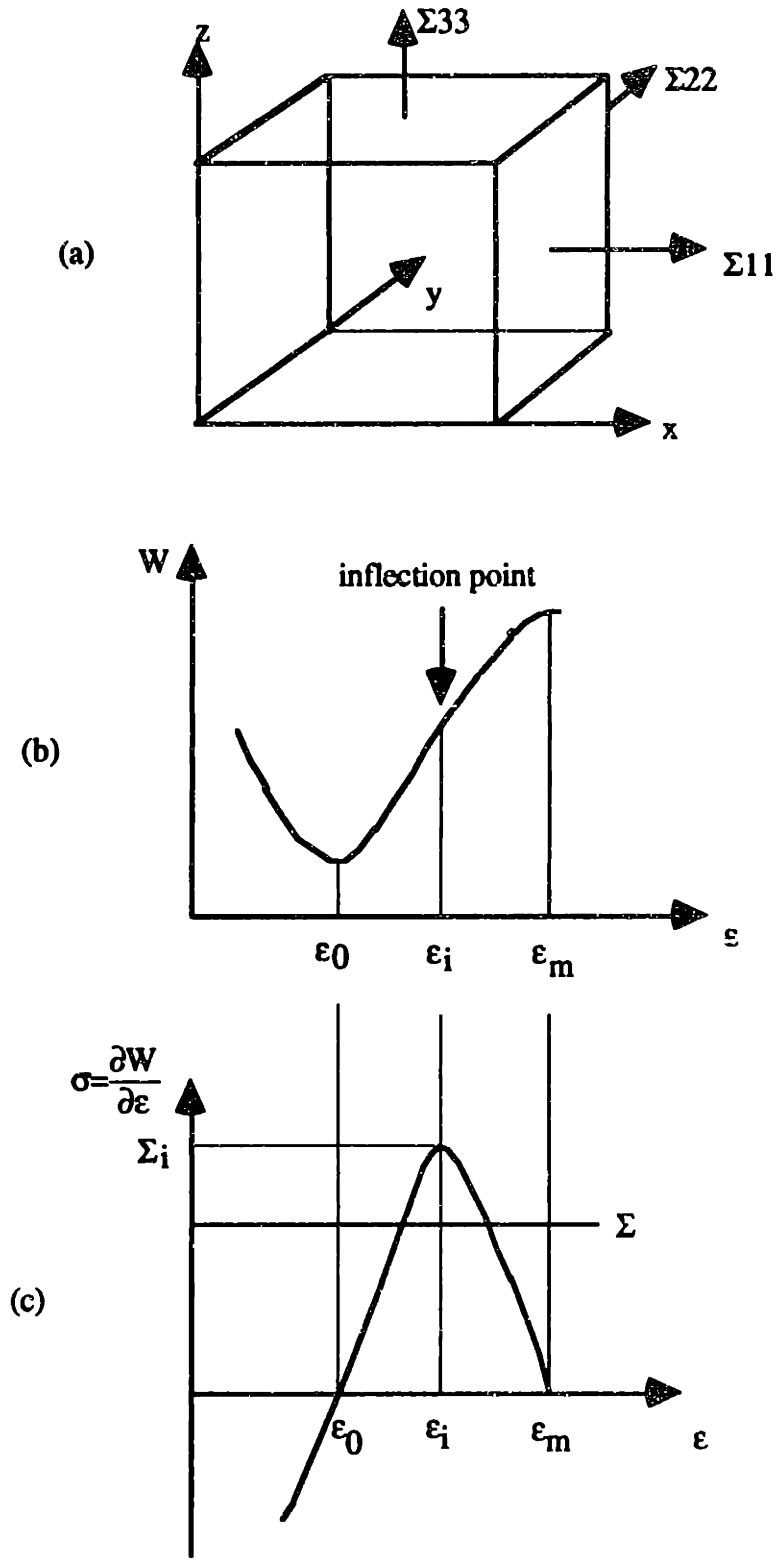

Fig. 2.1 Schematic diagram illustrating the definition of inflection point and elastic instability.

2.2.2 Principle of Virtual Work and Instability

In this section we will begin with a brief discussion of the principle of virtual work, then apply it to a deformed crystal with different elastic symmetries. For detail discussion about this principle one can refer to [Malvern 69, Reismann 80].

Let us consider an elastic body which is in equilibrium under the action of a prescribed body force F_α in volume Ω, surface traction T_α^* on surface S of the volume. The equilibrium conditions for this body are summarized as follows:

$$\frac{\partial \sigma_{\alpha\beta}}{\partial x_\beta} + F_\alpha = 0 \tag{2.28}$$

$$\sigma_{\alpha\beta} n_\beta - T_\alpha^* = 0 \tag{2.29}$$

where $\sigma_{\alpha\beta}$ is the internal stress and n_β is the unit normal vector to the surface.

Now imagine that the body is displaced slightly from its equilibrium configuration by the amount δu_α. This "virtual displacement" is arbitrary. The principle of virtual work relates the work done by the external forces during a virtual displacement to the corresponding change in strain energy. It can be derived as follows. As a consequence of Eqs. (2.28) and (2.29) we can write

$$-\int_\Omega \delta u_\alpha \left(\frac{\partial \sigma_{\alpha\beta}}{\partial x_\beta} + F_\alpha \right) d\Omega + \int_S \left(\sigma_{\alpha\beta} n_\beta - T_\alpha^* \right) \delta u_\alpha \, dS = 0 \tag{2.30}$$

However, with the aid of the divergence theorem one can easily show that

$$\int_S \sigma_{\alpha\beta} n_\beta \delta u_\alpha dS = \int_\Omega \sigma_{\alpha\beta} \frac{\partial \delta u_\alpha}{\partial x_\beta} d\Omega + \int_\Omega \delta u_\alpha \frac{\partial \sigma_{\alpha\beta}}{\partial x_\beta} d\Omega. \tag{2.31}$$

Furthermore,

$$\sigma_{\alpha\beta} \frac{\partial \delta u_\alpha}{\partial x_\beta} = \sigma_{\alpha\beta} \delta \varepsilon_{\alpha\beta} = \frac{\partial W}{\partial \varepsilon_{\alpha\beta}} \delta \varepsilon_{\alpha\beta} = \delta W \tag{2.32}$$

and the change in the strain energy

$$\delta U = \int_\Omega \delta W \, d\Omega. \tag{2.33}$$

Therefore Eq. (2.30) can also be written as

$$\delta U = \int_{\Omega} F_\alpha \delta u_\alpha d\Omega + \int_S T_\alpha^* \delta u_\alpha dS. \tag{2.34}$$

Thus during a virtual displacement, the work done by the external forces is equal to the change in strain energy of the body.

Substituting Eqs. (2.31) and (2.32) into equation (2.30) yields the variational principle

$$\delta \Pi = 0 \tag{2.35}$$

where

$$\Pi = \int_{\Omega} (W - F_\alpha u_\alpha) d\Omega - \int_S T_\alpha^* u_\alpha dS. \tag{2.36}$$

Since Π represents the total strain energy of the system in its equilibrium configuration, Eq. (2.36) states that the change in strain energy which occurs during a virtual displacement from an equilibrium configuration is zero.

We have shown that the strain energy of an elastic body is stationary in an equilibrium configuration. Since we are interested in the intrinsic instability of a deformed crystal rather than its equilibrium state, we will go a step further, by using this principle again, to investigate the stability of the equilibrium state.

Let us assume that u_α is the displacement field corresponding to an equilibrium configuration of the body. The corresponding strain energy is then given by equation (2.36). If the body is given a virtual displacement δu_α, then, for the new configuration, the strain energy is

$$\Pi(u_\alpha+\delta u_\alpha) = \int_{\Omega} \left(W(\varepsilon_{\alpha\beta}+\delta\varepsilon_{\alpha\beta}) - F_\alpha(u_\alpha+\delta u_\alpha)\right) d\Omega - \int_S T_\alpha^*(u_\alpha+\delta u_\alpha) dS. \tag{2.37}$$

The difference in potential energy between these two states is then

$$\Pi(u_\alpha+\delta u_\alpha) - \Pi(u_\alpha) = \int_{\Omega} \left[\left(W(\varepsilon_{\alpha\beta}+\delta\varepsilon_{\alpha\beta}) - W(\varepsilon_{\alpha\beta})\right)\right] d\Omega - \int_{\Omega} F_\alpha \delta u_\alpha d\Omega - \int_S T_\alpha^* \delta u_\alpha dS. \tag{2.38}$$

However, $W(\varepsilon_{\alpha\beta}+\delta\varepsilon_{\alpha\beta}) - W(\varepsilon_{\alpha\beta})$ can be expanded into a Taylor series

$$\left(W(\varepsilon_{\alpha\beta}+\delta\varepsilon_{\alpha\beta}) - W(\varepsilon_{\alpha\beta})\right) = \frac{\partial W}{\partial \varepsilon_{\alpha\beta}}\delta\varepsilon_{\alpha\beta} + \frac{1}{2}\frac{\partial^2 W}{\partial\varepsilon_{\alpha\beta}\partial\varepsilon_{\chi\eta}}\delta\varepsilon_{\alpha\beta}\delta\varepsilon_{\chi\eta} + \cdots$$

$$= \delta W + \delta^2 W + \cdots.$$

Therefore

$$\Pi(u_\alpha+\delta u_\alpha) - \Pi(u_\alpha) = \delta\Pi + \delta^2\Pi + \cdots \tag{2.39}$$

where

$$\delta\Pi = \int_\Omega \delta W\, d\Omega - \int_\Omega F_\alpha \delta u_\alpha d\Omega - \int_S T^*_\alpha \delta u_\alpha dS \tag{2.40}$$

and

$$\delta^2\Pi = \int_\Omega \delta^2 W\, d\Omega = \frac{1}{2}\int_\Omega d\Omega \frac{\partial^2 W}{\partial\varepsilon_{\alpha\beta}\partial\varepsilon_{\chi\eta}}\delta\varepsilon_{\alpha\beta}\delta\varepsilon_{\chi\eta}. \tag{2.41}$$

Since we assumed that the system is in equilibrium, we have $\delta\Pi = 0$. Therefore, for an infinitesimal virtual displacement, we can approximate equation (2.38) by

$$\Pi(u_\alpha+\delta u_\alpha) - \Pi(u_\alpha) = \delta^2\Pi. \tag{2.42}$$

The physical meaning of this equation is clear. When a sufficiently small virtual displacement is applied on an equilibrium elastic body, the corresponding increase in the elastic potential energy is given by equation (2.42). If $\delta^2\Pi$ is positive definite, any further deformation tends to increase the potential energy of the system. Then, the equilibrium state determined by equation (2.35) has a local minimum of potential energy, and thus is a stable equilibrium state. While when (2.42) is negative, it indicates that the state determined by equation (2.35) has a maximum of potential energy. This state is an unstable equilibrium state because any more deformation will decrease its potential energy. When (2.42) is equal to zero, it determines the inflection point at which the potential energy of the system changes its curvature. When the deformation brings the system across this point, the system becomes unstable. Thus the inflection point of the potential energy could be used to define the elastic instability of any elastic system.

Recalling the definition of the elastic constants and thermodynamic stress we can write equation (2.41) as follows

$$\delta^2\Pi = \frac{1}{2}\int_\Omega d\Omega \frac{\partial^2 W}{\partial\varepsilon_{\alpha\beta}\partial\varepsilon_{\chi\eta}} \delta\varepsilon_{\alpha\beta}\delta\varepsilon_{\chi\eta} = \frac{1}{2}\int_\Omega d\Omega\, C_{\alpha\beta\chi\eta}\, \delta\varepsilon_{\alpha\beta}\delta\varepsilon_{\chi\eta} \qquad (2.43)$$

or equivalently

$$\delta^2\Pi = \frac{1}{2}\int_\Omega d\Omega \frac{\partial^2 W}{\partial\varepsilon_{\alpha\beta}\partial\varepsilon_{\chi\eta}} \delta\varepsilon_{\alpha\beta}\delta\varepsilon_{\chi\eta} = \frac{1}{2}\int_\Omega d\Omega\, \delta\sigma_{\alpha\beta}\, \delta\varepsilon_{\alpha\beta}. \qquad (2.44)$$

Now we consider the instability criterion for the general case where the virtual work of the external forces involves the quadratic terms of strain. The physical meaning of Eq. (2.44) is that if a virtual deformation were imposed on a system the virtual work required for the deformation would be equal to the elastic energy stored in the system. If this work is zero there is no resistance to this distortion. In other words the system is unstable with regard to this deformation. Therefore, the instability of the system requires

$$\int_\Omega d\Omega\, \delta\sigma_{\alpha\beta}\, \delta\varepsilon_{\alpha\beta} = 0.$$

Since $\delta\sigma_{\alpha\beta}\,\delta\varepsilon_{\alpha\beta}$ should be positive definite the integral can only be zero if $\delta\sigma_{\alpha\beta}\,\delta\varepsilon_{\alpha\beta} = 0$. But $\varepsilon_{\alpha\beta}$ are independent variables so for any deformation $\delta\varepsilon$ $\delta\sigma_{\alpha\beta}\,\delta\varepsilon_{\alpha\beta}$ equals to zero only if

$$\delta\sigma_{\alpha\beta} = 0 \qquad (2.45a)$$

or equivalently

$$C_{\alpha\beta\chi\eta}\delta\varepsilon_{\chi\eta} = 0, \qquad \alpha\,\beta = 1, 2, 3. \qquad (2.45b)$$

These equations state that when the system is unstable the internal stress responded to the further deformation becomes stationary. This situation occurs at the inflection point of the elastic energy density that, in general, is determined by Eqs. (2.45). Eqs. (2.45a) and (2.45b) are the basic equations we will use in investigating the intrinsic instability of deformed crystals.

2.3 Elastic Instability Criteria for Cubic and Tetragonal Symmetry

In the preceding discussions we have been concerned with the instability of a deformed crystal. The equation of instability concerns virtual variations, i.e., variations of the system away from equilibrium stable state. The elastic instability criteria thus give the up bounds that one can maintain the crystal in an equilibrium state. It has been shown that the inflection point is such an important point at which the restoring force against further deformation becomes stationary. Analytically this point can be determined by the solution of Eq. (2.45a) or (2.45b). By solving these equations one can get not only the elastic instability criteria but also the corresponding eigenstates of deformation. These eigenstates give all the possible unstable modes that the system may get into when the instability criteria are satisfied. In this and following sections we will investigate in detail the conditions and eigenmodes of instability for the crystal with different elastic symmetries. Besides, we will also estimate the critical strain and stress corresponding to each of the instabilities.

2.3.1 Instability Conditions with Zero Eigenvalue of Elastic Constant Matrix

Eqs. (2.45b) are general in determining instability conditions. We rewrite it in the form of a matrix using Voigt notation

$$\mathbf{C}\,\delta\varepsilon = 0 \tag{2.46}$$

One immediately see that solving this equation for the instability conditions is equivalent to solving an eigenvalue problem of elastic constant matrix with a zero eigenvalue. The conditions determined by these equations give the up-limit of the stability of a crystal.

In the following we will consider crystals with cubic and tetragonal symmetry. We will solve the equations for the crystal with tetragonal symmetry first. Then the cubic case can be easily found by setting $C_{11} = C_{33}$, $C_{12} = C_{13}$, and $C_{44} = C_{66}$.

For a crystal of tetragonal symmetry, since $C_{11} = C_{22}$ and $C_{44} = C_{55}$ Eq. (2.46) gives

$$C_{11}\delta\varepsilon_{xx} + C_{12}\delta\varepsilon_{yy} + C_{13}\delta\varepsilon_{zz} = 0$$

$$C_{12}\delta\varepsilon_{xx} + C_{11}\delta\varepsilon_{yy} + C_{13}\delta\varepsilon_{zz} = 0$$

$$C_{13}\delta\varepsilon_{xx} + C_{13}\delta\varepsilon_{yy} + C_{33}\delta\varepsilon_{zz} = 0 \qquad (2.47)$$

$$C_{44}\delta\varepsilon_{yz} = 0$$

$$C_{44}\delta\varepsilon_{xz} = 0$$

$$C_{66}\delta\varepsilon_{xy} = 0$$

These homogeneous equations would have at least one eigensolution which leads to the vanishing of the quadratic terms of the potential energy. In order that equations (2.47) have nontrivial solution the necessary and sufficient condition is that the determinant of the coefficient matrix is zero,

$$\det \mathbf{C} = 0$$

or

$$\begin{vmatrix} C_{11} & C_{12} & C_{13} & & & \\ C_{12} & C_{11} & C_{13} & & 0 & \\ C_{13} & C_{13} & C_{33} & & & \\ & & & C_{44} & & \\ & 0 & & & C_{44} & \\ & & & & & C_{66} \end{vmatrix} = 0. \qquad (2.48)$$

This gives

$$(C_{11} - C_{12})\left[(C_{11} + C_{12})C_{33} - 2C_{13}^2\right]C_{44}^2 C_{66} = 0.$$

The solutions are

$$\left[(C_{11} + C_{12})C_{33} - 2C_{13}^2\right] = 0 \qquad (2.49)$$

$$(C_{11} - C_{12}) = 0 \qquad (2.50)$$

$$C_{44} = C_{66} = 0. \qquad (2.51)$$

Each of these conditions defines an intrinsic instability of the crystal.

For cubic symmetry, where $C_{12} = C_{13}$, $C_{11} = C_{33}$, and $C_{44} = C_{66}$, the corresponding instability conditions are:

$$(C_{11} + 2C_{12}) = 0 \tag{2.52}$$

$$(C_{11} - C_{12}) = 0 \tag{2.53}$$

$$C_{44} = 0. \tag{2.54}$$

The zero eigenvalue of the elastic constant matrix brings out three kinds of instabilities, spinodal (dilatational) instability, Born (normal distortional) instability and shear distortional instability. Each of them may cause different structural responses of the crystal. In the following subsections we will discuss the physical meaning and consequences of these instability conditions.

2.3.2 Spinodal Instability and Born Instability

Spinodal instability originates from a singularity of compressibility and is defined by the condition $\left(\frac{\partial P}{\partial V}\right)_T = 0$ from the equation of state [Speedy 82, Zheng 90]. Born instability is defined by $C_{11} - C_{12} = 0$ which gives the limit of the stability of $C_{11} - C_{12} > 0$ which was first discussed by Born [Born 56]. Although both of these instabilities result in the vanishing of elastic moduli, each is of a different nature.

1. Spinodal Instability

In the case of tetragonal and cubic symmetry, the spinodal instability criteria are

$$[(C_{11} + C_{12})C_{33} - 2C_{13}^2] = 0 \tag{2.55}$$

and

$$(C_{11} + 2C_{12}) = 0 \tag{2.56}$$

If we substitute these conditions into the expressions of the bulk modulus and Young's moduli (2.15), (2.16), (2.18) and (2.19) for each symmetry case, one can see that for both cases the instability conditions bring the bulk and Young's moduli to zero. This means that when the crystal becomes unstable, any small increase in the stress will cause a huge amount of strain. In the case of the vanishing of bulk modulus, any more tension

will cause the system to fall apart. So the failure associated with this instability must have the characteristic of decohesion.

2. Born instability

For this instability we have

$$(C_{11} - C_{12}) = 0 \tag{2.57}$$

for both tetragonal and cubic symmetry. In both symmetries, the instability conditions only cause the vanishing of some of the elastic moduli. In the case of cubic symmetry, it leads to the vanishing of the Young's modulus (2.15), but the bulk modulus (2.16) is left in finite. This implies that in this state the system still can withstand further uniform expansion, but it will yield to any stress increase along any one of the cubic axes. In the case of tetragonal symmetry, the instability condition leaves both the bulk modulus (2.19) and one Young's modulus Y_z (2.18b) finite, while bringing the Young's moduli, Y_x and Y_y, (2.18a), in the degenerate x-y plane, to zero. In this case the finite bulk modulus indicates that even when C_{11} is equal to C_{12}, the crystal is still stable against hydrostatic tension or pure dilatation. The finite Young's modulus suggest that under uniaxial loading the system can remain stable along this direction, but it is unstable in the two transverse directions. There must be some in-plane structural change responding to the instability in the transverse directions. By viewing these results one may expect that so long as the symmetry is conserved along the deformation path, the system will be stable against Born instability. Put in other words, the occurrence of Born instability requires a breaking of symmetry.

3. Shear distortional instability

Shear instability is a consequence of the vanishing of the shear modulus. For a shear distortion in the (100) plane the instability occurs when $C_{44} = 0$. On the other hand, if the crystal is sheared in the (110) plane along the $[1\bar{1}0]$ direction, the system becomes unstable against further shear when $C_{11} - C_{12} = 0$ [Kittel 56].

2.3.3 Critical Strain and Critical Stress

We must emphasize that all the elastic constants in the equation of instability refer to an initially stressed reference state. This means that the instability criteria discussed above are the instabilities of the stressed state. In the regime of linear elasticity theory, the elastic constants are taken as those of the system under zero applied stress. In practice when one deals with the elastic problem, in most cases the strains are small, the zero stress elastic constants are enough to treat the problem. However, in the discussion of instability, we are interested not only in the state of zero applied stress but in any arbitrary stressed state. In this case the elastic constants will be a function of strain which is measured with respect to the stress-free state. But the further strain is evaluated from the current stressed state.

In previous discussions of instability the elastic constants are treated as a function of the strain ε. The reference state from which we measure a further deformation $\delta\varepsilon$ is the current state under arbitrary applied stress, so the all instability criteria refer to the current external stress state. This current linearized elasticity theory enables us to treat the finite strain problem using the formulas of the linear elasticity theory, even in the non-linear region. This treatment is valid as far as $\delta\varepsilon << \varepsilon$.

This treatment also allows us to estimate the critical strain in terms of the finite-strain elastic constants. Tallon [Tallon 80] has shown that the volume dependence of elastic moduli can be well described by an exponential function, which, for small volume expansion, gives a linear temperature dependent relation of elastic moduli. For simplicity we assume that the elastic constants in the stressed state are linear functions of the strain, i.e., $C_{ij} = C_{ij}^0 + \alpha_{ij}\varepsilon_{ij}$, where C_{ij}^0's are the elastic constants of the zero applied stress state and α_{ij}'s are constants, and i, j = 1, 2, 3 or x, y, z*. We will examine several simple examples, (i) dilatation, (ii) uniaxial strain, and (iii) uniaxial stress. In all cases we take a stress-free cubic crystal as the reference state. All the estimates are made to the first order in the strain.

---

* In this section, for convenience, we shall use Voigt notation for elastic constants, and α_{ij}, β_{ij}, and γ_{ij} to denote the linear coefficients.

(i) Dilatation

The deformation is sketched in Fig. 2.2 (a), where a cubic crystal is uniformly expanded about the zero stress state. The expansion is characterized by a strain ε. The elastic constants after expansion are given by

$$C_{11} = C_{11}^0 + \alpha_{11}\varepsilon \tag{2.58}$$

$$C_{12} = C_{12}^0 + \alpha_{12}\varepsilon. \tag{2.59}$$

Then the Young's moduli and the bulk modulus of the strained crystal are, from (2.15) and (2.16),

$$Y = \frac{(C_{11} - C_{12})^2(C_{11} + 2C_{12})}{C_{11} + C_{12}}$$

$$= \frac{\left[\left(C_{11}^0 + \alpha_{11}\varepsilon\right) - \left(C_{12}^0 + \alpha_{12}\varepsilon\right)\right]^2\left[\left(C_{11}^0 + \alpha_{11}\varepsilon\right) + 2\left(C_{12}^0 + \alpha_{12}\varepsilon\right)\right]}{\left(C_{11}^0 + \alpha_{11}\varepsilon\right) + \left(C_{12}^0 + \alpha_{12}\varepsilon\right)} \tag{2.60}$$

and

$$B = \frac{1}{3}(C_{11} + 2C_{12}) = \frac{1}{3}\left[\left(C_{11}^0 + \alpha_{11}\varepsilon\right) + 2\left(C_{12}^0 + \alpha_{12}\varepsilon\right)\right]. \tag{2.61}$$

By setting these moduli to zero we have either

$$\left(C_{11}^0 + \alpha_{11}\varepsilon\right) + 2\left(C_{12}^0 + \alpha_{12}\varepsilon\right) = 0 \tag{2.62}$$

or

$$\left(C_{11}^0 + \alpha_{11}\varepsilon\right) - \left(C_{12}^0 + \alpha_{12}\varepsilon\right) = 0. \tag{2.63}$$

Here (2.62) corresponds to the spinodal instability and (2.63) to the Born instability.

Solving these two equations gives the critical strains ε_c^s and ε_c^B,

$$\varepsilon_c^s = -\frac{C_{11}^0 + 2C_{12}^0}{\alpha_{11} + 2\alpha_{12}} \tag{2.64}$$

and

$$\varepsilon_c^B = -\frac{C_{11}^0 - C_{12}^0}{\alpha_{11} - \alpha_{12}}. \tag{2.65}$$

Here superscripts s and B refer to spinodal and Born instability respectively. Using Hooke's law (2.5) we can calculate the corresponding critical stresses σ_c^s and σ_c^B. They are

$$\sigma_c^s = \left(C_{11}^0 + 2C_{12}^0\right)\varepsilon_c^s = -\frac{\left(C_{11}^0 + 2C_{12}^0\right)^2}{\alpha_{11} - \alpha_{12}} \tag{2.66}$$

and

$$\sigma_c^B = \left(C_{11}^0 + 2C_{12}^0\right)\varepsilon_c^B = -\frac{\left(C_{11}^0 + 2C_{12}^0\right)\left(C_{11}^0 - C_{12}^0\right)}{\alpha_{11} - \alpha_{12}}. \tag{2.67}$$

These two equations can be used to approximate the strengths of the crystal. It should be pointed out that in the literature extensive simulation studies have been carried out to investigate the strength of crystals [Ashurst 76; Milstein 77, 78, 79; Dodson 84; Blumberg 90, 91; Wang 91]. Different boundary conditions have been used and different values of critical stresses have been obtained. Actually these different values, as we will show in the following sections, correspond to the different deformation paths and result from different instabilities.

(ii) Uniaxial strain

As shown in Fig. 2.2 (b), by uniaxial strain we mean that the cubic crystal is stretched in the z direction with strain ε while its sizes in the transverse directions are held fixed. In this case the elastic constant matrix has tetragonal symmetry. The elastic constants can be expressed as

$$\begin{aligned} &C_{11} = C_{22} = C_{11}^0,\ C_{33} = C_{33}^0 + \beta_{33}\varepsilon = C_{11}^0 + \beta_{33}\varepsilon, \\ &C_{12} = C_{12}^0,\ C_{13} = C_{13}^0 + \beta_{13}\varepsilon = C_{12}^0 + \beta_{13}\varepsilon \end{aligned} \tag{2.68}$$

where the β_{ij}'s are constants. The elastic moduli are

$$\begin{aligned} Y_z &= \frac{\left(C_{11} + C_{12}\right)C_{33} - 2C_{13}^2}{C_{11} + C_{12}} \\ &= \frac{\left(C_{11}^0 + C_{12}^0\right)\left(C_{11}^0 + \beta_{33}\varepsilon\right) - 2\left(C_{12}^0 + \beta_{13}\varepsilon\right)^2}{C_{11}^0 + C_{12}^0} \end{aligned} \tag{2.69}$$

$$Y_x = Y_y = \frac{(C_{11} - C_{12})\left[(C_{11} + C_{12})C_{33} - 2C_{13}^2\right]}{C_{11}^0 + C_{12}^0}$$

$$= \frac{\left(C_{11}^0 - C_{12}^0\right)\left[\left(C_{11}^0 + C_{12}^0\right)\left(C_{11}^0 + \beta_{33}\varepsilon\right) - 2\left(C_{12}^0 + \beta_{13}\varepsilon\right)^2\right]}{C_{11}^0 + C_{12}^0} \tag{2.70}$$

and

$$B = \frac{(C_{11} + C_{12})C_{33} - 2C_{13}^2}{C_{11} + C_{12} + 2C_{33} - 4C_{13}}$$

$$= \frac{\left(C_{11}^0 + C_{12}^0\right)\left(C_{11}^0 + \beta_{33}\varepsilon\right) - 2\left(C_{12}^0 + \beta_{13}\varepsilon\right)^2}{C_{11}^0 + C_{12}^0 + 2\left(C_{11}^0 + \beta_{33}\varepsilon\right) - 4\left(C_{13}^0 + \beta_{13}\varepsilon\right)}. \tag{2.71}$$

Again by setting (2.69), (2.70) and (2.71) to zero we only have

$$\left(C_{11}^0 + C_{12}^0\right)\left(C_{11}^0 + \beta_{33}\varepsilon\right) - 2\left(C_{12}^0 + \beta_{13}\varepsilon\right)^2 = 0 \tag{2.72}$$

for spinodal instability. Keeping ε to the first order and solving (2.72) gives the critical strain

$$\varepsilon_c^s = -\frac{\left(C_{11}^0 + C_{12}^0\right)C_{11}^0 - 2\left(C_{12}^0\right)^2}{\left(C_{11}^0 + C_{12}^0\right)\beta_{33} - 4C_{13}^0\,\beta_{13}}. \tag{2.73}$$

Using Hooke's law the critical stresses are obtained as

$$\sigma_{11c}^s = \sigma_{22c}^s = C_{12}^0\varepsilon_c^s = -\frac{C_{12}^0\left[\left(C_{11}^0 + C_{12}^0\right)C_{11}^0 - 2\left(C_{12}^0\right)^2\right]}{\left(C_{11}^0 + C_{12}^0\right)\beta_{33} - 4C_{13}^0\,\beta_{13}} \tag{2.74}$$

and

$$\sigma_{33c}^s = C_{11}^0\varepsilon_c^s = -\frac{C_{11}^0\left[\left(C_{11}^0 + C_{12}^0\right)C_{11}^0 - 2\left(C_{12}^0\right)^2\right]}{\left(C_{11}^0 + C_{12}^0\right)\beta_{33} - 4C_{13}^0\,\beta_{13}}. \tag{2.75}$$

(iii) Uniaxial Stress

Uniaxial stress is a more physically realizable deformation. In this case the stretch is still along z direction with the strain ε_{zz}, but now Poisson's effect is allowed in the response along the lateral directions, as shown in Fig. 2.2 (c). The strains in x and y

directions are the same under tetragonal or cubic symmetry, $\varepsilon_{yy} = \varepsilon_{xx}$. After stretch the system has tetragonal symmetry and the elastic constants have the form

$$C_{11} = C_{11}^0 + \gamma_{11}\varepsilon_{xx},\ C_{12} = C_{12}^0 + \gamma_{12}\varepsilon_{xx} \text{ and}$$
$$C_{13} = C_{12}^0 + \gamma_{13}\varepsilon_{zz},\ C_{33} = C_{11}^0 + \gamma_{33}\varepsilon_{zz} \tag{2.76}$$

where γ_{ij}'s are constants. We write the elastic moduli

$$Y_z = \frac{(C_{11}+C_{12})C_{33} - 2C_{13}^2}{C_{11}+C_{12}}$$
$$= \frac{\left[\left(C_{11}^0+\gamma_{11}\varepsilon_{xx}\right)+\left(C_{12}^0+\gamma_{12}\varepsilon_{xx}\right)\right]\left(C_{11}^0+\beta_{33}\varepsilon\right) - 2\left(C_{12}^0+\beta_{13}\varepsilon\right)^2}{\left(C_{11}^0+\gamma_{11}\varepsilon_{xx}\right)+\left(C_{12}^0+\gamma_{12}\varepsilon_{xx}\right)} \tag{2.77}$$

$$Y_x = Y_y = \frac{(C_{11}-C_{12})\left[(C_{11}+C_{12})C_{33} - 2C_{13}^2\right]}{C_{11}^0+C_{12}^0}$$
$$= \left[\left(C_{11}^0+\gamma_{11}\varepsilon_{xx}\right)-\left(C_{12}^0+\gamma_{12}\varepsilon_{xx}\right)\right]\times \tag{2.78}$$
$$\frac{\left[\left(C_{11}^0+\gamma_{11}\varepsilon_{xx}\right)+\left(C_{12}^0+\gamma_{12}\varepsilon_{xx}\right)\right]\left(C_{11}^0+\gamma_{33}\varepsilon_{zz}\right) - 2\left(C_{12}^0+\gamma_{13}\varepsilon_{zz}\right)^2}{\left(C_{11}^0+\gamma_{11}\varepsilon_{xx}\right)+\left(C_{12}^0+\gamma_{12}\varepsilon_{xx}\right)}$$

and bulk modulus

$$B = \frac{(C_{11}+C_{12})C_{33} - 2C_{13}^2}{C_{11}+C_{12}+2C_{33}-4C_{13}}$$
$$= \frac{\left[\left(C_{11}^0+\gamma_{11}\varepsilon_{xx}\right)+\left(C_{12}^0+\gamma_{12}\varepsilon_{xx}\right)\right]\left(C_{11}^0+\gamma_{33}\varepsilon_{zz}\right) - 2\left(C_{12}^0+\gamma_{13}\varepsilon_{zz}\right)^2}{\left(C_{11}^0+\gamma_{11}\varepsilon_{xx}\right)+\left(C_{12}^0+\gamma_{12}\varepsilon_{xx}\right)+2\left(C_{33}^0+\gamma_{33}\varepsilon_{zz}\right)-4\left(C_{13}^0+\gamma_{13}\varepsilon_{zz}\right)}. \tag{2.79}$$

Setting (2.77)-(2.79) to zero we have equations

$$\left[\left(C_{11}^0+\gamma_{11}\varepsilon_{xx}\right)+\left(C_{12}^0+\gamma_{12}\varepsilon_{xx}\right)\right]\left(C_{11}^0+\gamma_{33}\varepsilon_{zz}\right) - 2\left(C_{12}^0+\gamma_{13}\varepsilon_{zz}\right)^2 = 0 \tag{2.80}$$

and

$$\left(C_{11}^0+\gamma_{11}\varepsilon_{xx}\right)-\left(C_{12}^0+\gamma_{12}\varepsilon_{xx}\right) = 0 \tag{2.81}$$

which correspond to spinodal and Born instability respectively.

Solving (2.81) directly we get the critical strain for Born instability

$$\varepsilon^{B}_{xxc} = \frac{C^0_{11} - C^0_{11}}{\gamma_{11} - \gamma_{12}}. \tag{2.82}$$

In order to solve equation (2.81) we need one more equation. Recalling the definition of the Poisson's ratio

$$\nu_{xz} \equiv - \frac{\varepsilon_{xx}}{\varepsilon_{zz}} = \frac{C_{13}}{C_{11} + C_{13}} = \frac{\left(C^0_{12} + \gamma_{13}\varepsilon_{zz}\right)}{\left(C^0_{12} + \gamma_{13}\varepsilon_{xx}\right) + \left(C^0_{12} + \gamma_{13}\varepsilon_{zz}\right)}. \tag{2.83}$$

In first order approximation we have for (2.83)

$$\varepsilon_{xx} = - \frac{C_{13}}{C_{11} + C_{13}} \varepsilon_{zz}.$$

Substituting this result into (2.80) and keeping the first order of strain we get

$$\varepsilon^{s}_{zzc} = - \frac{\left(C^0_{11} + C^0_{12}\right) C^0_{11} - 2C^{0\,2}_{12}}{\frac{C^0_{11} C^0_{12}(\gamma_{11} + \gamma_{12})}{C^0_{11} + C^0_{12}} + \left(C^0_{12} + C^0_{12}\right)\gamma_{33} - 4C^0_{12}\gamma_{13}} \tag{2.84}$$

and

$$\varepsilon^{\varepsilon}_{xxc} = - \frac{\frac{C^0_{12}}{C^0_{11} + C^0_{12}}\left[\left(C^0_{11} + C^0_{12}\right) C^0_{11} - 2C^{0\,2}_{12}\right]}{\frac{C^0_{11} C^0_{12}(\gamma_{11} + \gamma_{12})}{C^0_{11} + C^0_{12}} + \left(C^0_{12} + C^0_{12}\right)\gamma_{33} - 4C^0_{12}\gamma_{13}}. \tag{2.85}$$

The corresponding critical stress can be obtained from Hooke's law.

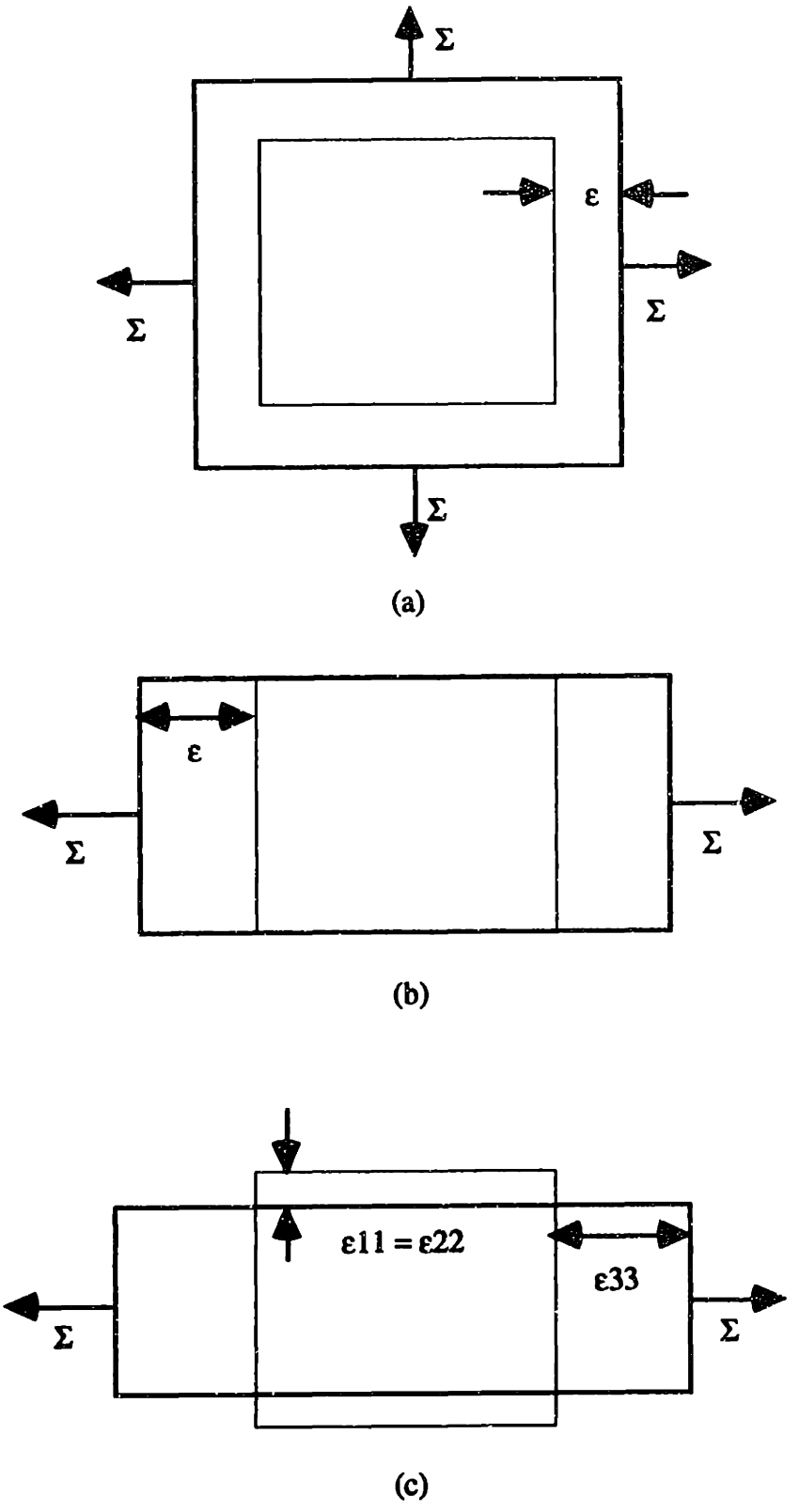

Fig. 2.2 Schematic diagram illustrating elastic deformation: (a) Dilatation, (b) Uniaxial strain, and (c) Uniaxial stress. The thin-line square is the initial configuration of the elastic body.

2.4 Deformation Modes of Instability

We have developed the instability criteria which determine the inflection point of the strain energy density of the deformed system. At this point the strain energy changes its curvature. We have shown that at the inflection point the elastic system becomes unstable against appropriate deformations which cause one or more of the elastic moduli to vanish. The question one can ask further is that given the instability conditions and the strain states of these instability conditions, will the system break down always, or is there a particular mode of deformation such that the system fails in a spectacular way only when it exists in this mode? Since these instability conditions lead to a zero eigenvalue of the elastic constant matrix, one expects that the answer to these questions will become clear once the eigenstates of the zero eigenvalue of the current elastic constant matrix are determined and inspected.

2.4.1 Eigenstates of Zero Eigenvalue of Elastic Constant matrix

We will continue to consider the tetragonal and cubic symmetries in the following. In this subsection all elastic constants are the current elastic constants.

(1) Tetragonal Symmetry

For tetragonal symmetry the eigenvalue equations are

$$C_{11}\delta\epsilon_{xx}+ C_{12}\delta\epsilon_{yy} + C_{13}\delta\epsilon_{zz}= 0 \tag{2.86}$$

$$C_{12}\delta\epsilon_{xx}+ C_{11}\delta\epsilon_{yy} + C_{13}\delta\epsilon_{zz}= 0 \tag{2.87}$$

$$2C_{13}\left(\delta\epsilon_{xx}+ \delta\epsilon_{yy}\right) + C_{33}\delta\epsilon_{zz}= 0 \tag{2.88}$$

$$C_{44}\delta\epsilon_{yz} = 0, C_{44}\delta\epsilon_{xz} = 0, C_{66}\delta\epsilon_{xy} = 0. \tag{2.89}$$

We will solve the eigenstates for the spinodal instability first and discuss the Born and shear distortional instabilities later.

(i) Spinodal Instability

We have shown that the spinodal instability conditions are given by

$$\left[(C_{11} + C_{12})C_{33} - 2C_{13}^2\right] = 0 \tag{2.90}$$

$$(C_{11} - C_{12}) \neq 0 \tag{2.91}$$

$$C_{44} \neq 0, \text{ and } C_{66} \neq 0 . \tag{2.92}$$

From (2.89) and (2.92) we immediately get

$$\delta\epsilon_{yz} = \delta\epsilon_{xz} = \delta\epsilon_{xy} = 0. \tag{2.93}$$

Subtracting (2.87) from (2.86) gives

$$(C_{11} - C_{12})(\delta\epsilon_{xx} - \delta\epsilon_{yy}) = 0.$$

Since $(C_{11} - C_{12}) \neq 0$, then

$$\delta\epsilon_{xx} = \delta\epsilon_{yy}. \tag{2.94}$$

Substituting this result into (2.89) we have

$$2C_{13}\,\delta\epsilon_{xx} + C_{33}\,\delta\epsilon_{zz} = 0 .$$

This gives

$$\delta\epsilon_{xx} = -\frac{C_{33}}{2C_{13}}\delta\epsilon_{zz} \tag{2.95}$$

and no further constraint on $\delta\epsilon_{zz}$. Hence the eigenstate of spinodal instability is

$$\delta\epsilon = \left(-\frac{C_{33}}{2C_{13}}, -\frac{C_{33}}{2C_{13}}, 1, 0, 0, 0\right)\delta\epsilon_{zz}. \tag{2.96}$$

(ii) Born Instability

For Born instability we have conditions

$$\left[(C_{11} + C_{12})C_{33} - 2C_{13}^2\right] \neq 0 \tag{2.97}$$

$$(C_{11} - C_{12}) = 0 \tag{2.98}$$

$$C_{44} \neq 0, \text{ and } C_{66} \neq 0 . \tag{2.99}$$

Again, combining (2.89) and (2.99) we have

$$\delta\varepsilon_{yz} = \delta\varepsilon_{xz} = \delta\varepsilon_{xy} = 0. \tag{2.100}$$

Since $(C_{11} - C_{12}) = 0$, (2.86) becomes

$$C_{11}\left(\delta\varepsilon_{xx} + \delta\varepsilon_{yy}\right) + C_{13}\delta\varepsilon_{zz} = 0 \tag{2.101}$$

Multiplying (2.101) by $2C_{13}$ and (2.88) by C_{11}, then subtracting one from the other, we have

$$\left(C_{11}C_{33} - C_{13}^2\right)\delta\varepsilon_{zz} = 0.$$

Since $C_{11}C_{33} - C_{13}^2 \neq 0$,

$$\delta\varepsilon_{zz} = 0. \tag{2.102}$$

Substituting (2.102) into (2.101) we get

$$\delta\varepsilon_{xx} + \delta\varepsilon_{yy} = 0 . \tag{2.103}$$

This gives

$$\delta\varepsilon_{yy} = -\delta\varepsilon_{xx}. \tag{2.104}$$

Combining (2.100), (2.102) and (2.104) the eigenstate of Born instability is

$$\delta\varepsilon = (\,1, -1, 0, 0, 0, 0\,)\,\delta\varepsilon_{xx} \tag{2.105}$$

with the constraint of conserving area (2.103) in x-y plane. Since $\delta\varepsilon_{zz} = 0$, this constraint is equal to requirement of volume conservation.

(iii) Shear distortional instability

The shear instability conditions are

$$(C_{11} + C_{12})\,C_{33} - 2C_{13}^2 \neq 0 \tag{2.106}$$

$$C_{11} - C_{12} \neq 0 \tag{2.107}$$

and

$$C_{44} = 0 \text{ or } C_{66} = 0. \tag{2.108}$$

Multiplying (2.106) with (2.107) we have

$$(C_{11} - C_{12})\left[(C_{11} + C_{12})C_{33} - 2C_{13}^2\right] \neq 0.$$

The left hand side of this equation is just the determinant of the coefficients of (2.86), (2.87) and (2.88). That it does not equal to zero indicates the only solutions for these equations are

$$\delta\varepsilon_{xx} = \delta\varepsilon_{yy} = \delta\varepsilon_{zz} = 0. \tag{2.109}$$

This means that the shear deformation considered here requires no changes in lengths.

For the shear instability, i.e., either $C_{44} = 0$ or $C_{66} = 0$, from (2.89) we have

$$\delta\varepsilon_{yz} = \delta\varepsilon_{xz} = 0$$

and

$$\delta\varepsilon_{xy} = 0 .$$

These give the eigenstates

$$\left.\begin{aligned} \delta\varepsilon &= (0, 0, 0, 1, 0, 0)\,\delta\varepsilon_{yz} \\ \delta\varepsilon &= (0, 0, 0, 0, 1, 0)\,\delta\varepsilon_{xz} \end{aligned}\right\} \text{ for } C_{44} = 0 \tag{2.110}$$

and

$$\delta\varepsilon = (0, 0, 0, 0, 0, 1)\,\delta\varepsilon_{xy} \text{ for } C_{66} = 0. \tag{2.111}$$

These give no restrictions on the values of $\delta\varepsilon_{yz}$, $\delta\varepsilon_{xz}$ or $\delta\varepsilon_{xy}$.

(2) Cubic symmetry

For cubic symmetry we have $C_{11} = C_{33}$, $C_{12} = C_{13}$ and $C_{44} = C_{66}$.. Then the eigenstate equations are simplified as

$$C_{11}\delta\varepsilon_{xx} + C_{12}\left(\delta\varepsilon_{yy} + \delta\varepsilon_{zz}\right) = 0 \tag{2.112}$$

$$C_{12}\left(\delta\varepsilon_{xx} + \delta\varepsilon_{zz}\right) + C_{11}\delta\varepsilon_{yy} = 0 \tag{2.113}$$

$$C_{12}\left(\delta\varepsilon_{xx}+\delta\varepsilon_{yy}\right)+C_{11}\delta\varepsilon_{zz}=0 \tag{2.114}$$

$$C_{44}\delta\varepsilon_{yz}=0,\ C_{44}\delta\varepsilon_{xz}=0 \text{ and } C_{44}\delta\varepsilon_{xy}=0. \tag{2.115}$$

Again, we will consider the spinodal instability first and then Born instability and shear instability.

(i) Spinodal Instability

In this case the instability conditions are

$$C_{11}+2C_{12}=0 \tag{2.116}$$

$$C_{11}-C_{12}\neq 0 \tag{2.117}$$

and

$$C_{44}\neq 0. \tag{2.118}$$

Combining (2.117) and (2.118) we have

$$\delta\varepsilon_{yz}=\delta\varepsilon_{xz}=\delta\varepsilon_{xy}=0. \tag{2.119}$$

Subtracting (2.110) from (2.109) gives

$$\left(C_{11}-C_{12}\right)\left(\delta\varepsilon_{xx}-\delta\varepsilon_{yy}\right)=0.$$

Since $C_{11}-C_{12}\neq 0$, there must be

$$\delta\varepsilon_{xx}-\delta\varepsilon_{yy}=0$$

or

$$\delta\varepsilon_{xx}=\delta\varepsilon_{yy}. \tag{2.120}$$

Substituting (2.120) into (2.114) and using $C_{11}=-2C_{12}$ we get

$$\delta\varepsilon_{zz}=\delta\varepsilon_{xx}.$$

or

$$\delta\varepsilon_{xx}=\delta\varepsilon_{yy}=\delta\varepsilon_{zz}=\delta\varepsilon \tag{2.121}$$

where $\delta\epsilon$ is an arbitrary strain. Then (2.119) and (2.121) give the eigenstates of the spinodal instability

$$\delta\epsilon = (1, 1, 1, 0, 0, 0) \delta\epsilon \tag{2.122}$$

with no constraint on magnitude of $\delta\epsilon$.

(ii) Born instability

For Born instability we have the conditions

$$C_{11} + 2C_{12} \neq 0 \tag{2.123}$$

$$C_{11} - C_{12} = 0 \tag{2.124}$$

and

$$C_{44} \neq 0. \tag{2.125}$$

With (2.115) and (2.125), the shear strains are

$$\delta\epsilon_{yz} = \delta\epsilon_{xz} = \delta\epsilon_{xy} = 0. \tag{2.126}$$

Under the condition $C_{11} = C_{12}$, the three equations (2.112), (2.113) and (2.114) are identical. This gives

$$\delta\epsilon_{xx} + \delta\epsilon_{yy} + \delta\epsilon_{zz} = 0. \tag{2.127}$$

This equation says that $\delta\epsilon_{xx}$, $\delta\epsilon_{yy}$ and $\delta\epsilon_{zz}$ can take any arbitrary values so long as their sum is zero. Physically this requires volume conservation all along the deformation path. Thus the eigenstates of Born instability in cubic symmetry is

$$\delta\epsilon = \left(\delta\epsilon_{xx}, \delta\epsilon_{yy}, \delta\epsilon_{zz}, 0, 0, 0 \right) \tag{2.128}$$

with the constraint of volume conservation.

(iii) Shear distortional instability

Following the same argument in the case of tetragonal symmetry, we can get the eigenstates for shear instability

$$\left.\begin{array}{l} \delta\varepsilon = (\,0,0,0,1,0,0\,)\,\delta\varepsilon_{yz} \\ \delta\varepsilon = (\,0,0,0,0,1,0\,)\,\delta\varepsilon_{xz} \\ \delta\varepsilon = (\,0,0,0,0,0,1\,)\,\delta\varepsilon_{xy} \end{array}\right\}, \quad \text{for } C_{44} = 0 \tag{2.129}$$

with no any restrictions on the values of $\delta\varepsilon_{yz}$, $\delta\varepsilon_{xz}$ or $\delta\varepsilon_{xy}$.

In Table 2.1 we summarize all the results we have obtained for cubic and tetragonal symmetry. Concerning the "zero" eigenvalue, one argument one may make is that in the standard eigenvalue problem, the zero eigenvalue is trivial, because any vector of strain could be the eigenstate of the zero eigenvalue. This is true, of course, in general. But since we are looking at some particular conditions that cause the zero eigenvalue of elastic constant matrix, these physical conditions will narrow down the eigenstate to several special branches. Even if we cannot determine the exact state, which is actually not needed for our purpose, this analysis gives insight into the nature of each instability.

Table 2.1 Summary of instability criteria and corresponding eigenstates for cubic and tetragonal elastic symmetries.

Cubic symmetry		Tetragonal symmetry	
Instability criterion	Eigenstates	Instability criterion	Eigenstates
$C_{11} + 2C_{12} = 0$	$(1,1,1,0,0,0)\delta\varepsilon$	$(C_{11}+C_{12})C_{33}-2C_{13}^2=0$	$\left(\frac{C_{33}}{2C_{13}},\frac{C_{33}}{2C_{13}},1,0,0,0\right)\delta\varepsilon_{zz}$
$C_{11} - C_{12} = 0$	$(\delta\varepsilon_{xx},\delta\varepsilon_{yy},\delta\varepsilon_{zz},0,0,0)$ *	$C_{11} - C_{12} = 0$	$(1,-1,0,0,0,0)\delta\varepsilon_{xx}$*
$C_{44} = 0$	$(0,0,0,1,0,0)\delta\varepsilon_{yz}$	$C_{44} = 0$	$(0,0,0,1,0,0)\delta\varepsilon_{yz}$
$C_{44} = 0$	$(0,0,0,0,1,0)\delta\varepsilon_{xz}$	$C_{44} = 0$	$(0,0,0,0,1,0)\delta\varepsilon_{xz}$
$C_{44} = 0$	$(0,0,0,0,0,1)\delta\varepsilon_{xy}$	$C_{66} = 0$	$(0,0,0,0,0,1)\delta\varepsilon_{xy}$

* with restriction $\delta\varepsilon_{xx} + \delta\varepsilon_{yy} + \delta\varepsilon_{zz} = 0$.

2.4.2 Volumetric Deformation

In previous sections we have seen that when, and only when, at least one of the three instability criteria is violated, the determinant of the equation of instability vanishes. Each instability criterion is thus associated with a particular branch of eigenstates. We have proved that these are the only possible eigensolutions. These eigenstates characterize particular failure modes of the deformed crystal. Each mode terminates a stable region of deformation and defines an eigen-deformation path which takes the crystal to an unstable region. If the system deformation is not allowed to follow the eigen-deformation path, then the system can be considered to maintained in a metastable region.

By looking at Table 2.1, one can immediately recognize that a significant feature of the spinodal instability is that its eigenstates still keep the same symmetry as that of the original reference state. This means that in order for the crystal to get into these eigenstates the load must be imposed in such a way that it keeps the original symmetry of the elastic constant matrix. This kind of load brings the system to failure with the approach of the spinodal. We will define, following Milstein [Milstein 77, 80], this path as the primary deformation path. This path conserves the original symmetry of the reference states along the entire deformation path. This is the only path that allows the spinodal instability to show up. This statement is easy to be verified. For convenience, let us consider a cubic crystal with the reference state of zero applied stress. Suppose that the system is now unstable against the Born instability, i.e., $C_{11} - C_{12} = 0$, while the load is imposed along the primary path $(\delta\epsilon, \delta\epsilon, \delta\epsilon, 0, 0, 0)$. The stress arisen from this small distortion is given by Hooke's law

$$\sigma = C_{11}\delta\epsilon + C_{12}\delta\epsilon + C_{12}\delta\epsilon = (C_{11} + 2C_{12})\delta\epsilon = 3C_{11}\delta\epsilon, \qquad (2.130)$$

which is not zero. This tells us that even the system is unstable regarding Born instability, there is still a finite restoring force that tends to bring the system back to original stable equilibrium state. This simple example points an important fact that it is not complete if one wants to study elastic instability of a crystal without considering the loading environment.

2.4.3 Symmetry Breaking and Bifurcation

It was shown by Milstein and his collaborators [Hill 77, Milstein 80] that when an f.c.c. crystal is uniaxially stressed, it follows a primary path of deformation. At a point where $C_{22} - C_{23} = 0$, a secondary path branches the system out of the primary path of extension. Along the secondary path, with decreasing load, the tetragonal symmetry is broken; i.e., $a_2 \neq a_3$, where a_2 and a_3 are the lattice parameters in the lateral directions. This point, characterized by Born instability $C_{22} - C_{23} = 0$, defines a bifurcation point. Along the secondary path two structures can be identified when the crystal is unloaded. For Ni, based on their static calculation, they found that at the first zero load point, the system is identified in a b.c.c. state, and at the second zero load point the system is in a tetragonal state. The b.c.c. state is at a local energy maximum and the tetragonal one at a local minimum. The existence of this secondary path was proposed as a possible mechanism of an f.c.c. to a b.c.c. transition under conditions of a strictly [100] tensile load. Parrinello and Rahman [Parrinello 81] studied the same bifurcation problem for Ni at finite temperature by MD simulation. They found that bifurcation does not occur. Instead, a failure was observed. The "bifurcation failure" was observed only under extreme conditions of shock. The final state that the shocked crystal transforms into is an h.c.p. rather than a b.c.c. as predicted by the static calculation.

From our calculation, table 2.1, we find that Born instability has two significant characteristics: First, the loss of the stability of the crystal is the consequence of symmetry breaking and associated with a possible bifurcation on the primary path of deformation. Secondly, the eigenstates of Born instability require a volume, in the case of cubic symmetry, or area, for tetragonal symmetry, conservation along the entire bifurcation path. This requirement implies that Born instability may trigger a further shear distortion. These features may allow the crystal to undergo a continuous allotropic phase transformation [Milstein 80, Cheung 92] or structural disordering [Sabochik 91, Li 92].

Returning to instability, we argue that for a stress-free cubic crystal under pure heating Born instability should occur earlier than spinodal instability. This is clear by comparing the criterion of these two instabilities. Born instability can be satisfied even both C_{11} and C_{12} are still positive finite, while the spinodal instability only occurs when either both C_{11} and C_{12} become zero or at least one of them becomes negative. In the

case of uniaxial tensile load, the situation is complicated. No evidence one can argue just by comparison of these two criteria.

In summary of our discussion in previous sections, a complete study of instability of a crystal must concern not only the instability conditions but also the eigendeformation modes associated with each of the instabilities. The latter is necessary to define the specific deformation path that allows the corresponding instability to occur. Spinodal instability is a singularity of compressibility. Its eigendeformation path has the characteristics of symmetry conservation and pure volumetric deformation. The possible unstable structural responses of a crystal to this instability may be a decohesive failure. Born instability, on the other hand, requires a breaking of the original symmetry and only results in the vanishing of some of the elastic moduli. The eigendeformation mode of this instability requires a volume conservation and then may be associated with a shear distortion. These features may allow a crystal to undergo allotropic phase transformation or structural disordering.

Chapter 3
Simulation Models and Procedures

As mentioned earlier the objective of the research is to gain insight on the nature of the instability of stressed crystalline materials under various border conditions, e. g. stress or strain border conditions. Although in Chapter 2 theoretical approach of elastic analysis of a stressed f.c.c. crystal with different elastic symmetries has given the three well-known instability criteria in a crystalline material and the generic features of elastic deformation modes associated with each instability, there are still some open questions needed to be further studied. First, the theoretical results obtained in Chapter 2 are needed to be verified. Second, since the theory does not give the final state of the transformed lattice, one may naturally hope that direct observations from the dynamic evolution of a system well defined by dynamic equations may make it possible to study all the possible final state of the transition associated with each of the instabilities. Finally, since the eigenstates of each instability condition do not put any constraint on the driving force that takes the crystal to the instability region, the change of temperature, inhomogeneity of crystals and defects must have some effects on the structural response when the crystal becomes unstable. All theses give a large room for atomistic simulation to study the possible transitions and mechanisms of the transitions related to each instability. In following sections we will briefly discuss the potential models and simulation procedures that will be used in present study.

3.1 Interatomic Potentials (Lennard-Jones and Embedded Atom Method)

The interatomic potential is essential to simulating the behavior of a model system. In general, the potential energy of a system containing N atoms can be expressed as a function of the coordinates of individual atoms, pairs, triplets etc.:

$$V = \sum_{i}^{N} v_1(\mathbf{r}_i) + \sum_{j>i}^{N} v_2(\mathbf{r}_i,\mathbf{r}_j) + \sum_{k>j>i}^{N} v_3(\mathbf{r}_i,\mathbf{r}_j,\mathbf{r}_k) + \cdots. \qquad (3.1)$$

Where the first term $v_1(\mathbf{r}_i)$ represents the body force (for example, the electromagnetic field, gravity and so on) on the system. All the other terms represent atomic interactions. The second term is the pair potential, it is very important because even only including this term in the potential energy simulation starts to show interesting properties and behavior of the

model system. The pair potential only depends on the magnitude of the pair separation $r_{ij} = |\mathbf{r}_i - \mathbf{r}_j|$. The remaining terms $v_3(\mathbf{r}_i, \mathbf{r}_j, \mathbf{r}_k)$, $v_4(\mathbf{r}_i, \mathbf{r}_j, \mathbf{r}_k, \mathbf{r}_l)\cdots$, all together are so-called many body interactions. These terms take into account the cluster effects of interactions on the atom where there are more than one atom around it. Obviously, the many-body interaction is extremely important for the covalent bonding materials, and even so in the metallic bonding.

In our simulation studies we adopt two kinds of potentials commonly used in computer simulations. These are the simpler, more idealized Lennard-Jones (L-J) pair potential, and the embedded atom method (EAM) many-body potential.

The L-J potential we used has the form of so called force-shifted potential [Allen 87]:

$$v(r_{ij}) = 4\varepsilon\left[\left(\frac{\sigma}{r_{ij}}\right)^{12} - \left(\frac{\sigma}{r_{ij}}\right)^{6}\right] + c_1(r_c - r_{ij}) + c_2 \qquad \text{for } r_{ij} \le r_c \qquad (3.2)$$

$$v(r_{ij}) = 0 \qquad \text{for } r_{ij} \le r_c,$$

where $c_1 = 0.1\varepsilon$, $c_2 = 0.025\varepsilon$ and r_c is the cutoff distance. This potential has two adjustable parameters, σ and ε (not stress and strain), defining the length and energy scales. The potential has a long-range attractive tail of the form $\left(-\frac{1}{r_{ij}}\right)^6$ until the cutoff r_c; a negative well of depth ε , and a steeply rising repulsive wall at distance less than $r \sim \sigma$. Although this potential provides a reasonable description of the properties of argon, it may be viewed as a generic potential for an f.c.c. material if all energies and distances are scaled with ε and σ respectively. In present study the L-J potential used was fitted to the lattice parameter and melting point of Cu with $\varepsilon = 0.167$ eV, $\sigma = 2.315$A [Lutsko 88].

The EAM potential takes into account the role of many-body effects. It combines density functional concepts with traditional pairwise potentials. In addition to the two-body interaction in EAM, the potential energy for each atom is also determined by the energy required to embed the atom in the local electronic environment provided by the other atoms in the system. Thus EAM potential expresses the total potential energy, U, of a system of N interacting metal atoms as a summation of a bonding term and a repulsive term. According to [Daw 83, 84; Finnis 84]

$$U = \sum_i F(\rho_{hi}) + \sum_{i,j>i} \phi(r_{ij}), \qquad (3.3)$$

where ρ_{hi} is the host electron density at atom i due to the surrounding atoms in the system, $F(\rho_{hi})$ is the many-body energy needed to embed atom i into the background electron density

$$\rho_{hi} = \sum_{j} \rho_{ij}(r_{ij}), \tag{3.4}$$

and $\phi(r_{ij})$ is the core-core pairwise repulsive energy between atoms i and j separated by distance $r_{ij} = |r_i - r_j|$. The EAM potential we used in our simulation was fitted empirically to five properties of Au [Daw 84].

In order to avoid discontinuities in the energy and forces (and, the charge density in the case of EAM potential), both potentials were shifted smoothly to zero at the cutoff distances [$r_c/a_0 = 1.49$ (1.32) for the L-J (EAM) potential] [Wolf 92]. The zero temperature lattice parameters, a_0, were determined to be 3.6160A (L-J) and 4.8028A (EAM). In the principal cubic coordinate system (with x, y, z || <100>), the Young's moduli, Y_0, were found to be 1.08×10^{12} dyn/cm^2 (L-J) and 0.346×10^{12} dyn/cm^2 (EAM), whereas the shear moduli, G_0, are 1.01×10^{12} dyn/cm^2 (L-J) and 0.440×10^{12} dyn/cm^2 (EAM). The Poisson's ratios for these potentials are 0.360 and 0.465 respectively.

A very important difference between the pairwise and many-body potentials is that the pair potential automatically satisfies the Cauchy relation with the elastic constants $C_{12} = C_{44}$, while the many-body potential still leaves all three elastic constants of a cubic metal to be determined. Although the L-J and EAM potentials are parameterized to describe Cu and Au respectively, it is not the primary focus of this study to investigate the elastic behaviors of these particular metals. Rather, it is intended that by employing these two very different potentials, the generic features of the intrinsic instability of f.c.c. metals can be separated from effects depending on the description of particular interatomic forces.

Another significant difference between these two potentials is that the L-J potential has a relatively small curvature of the cohesive energy curve comparing to the EAM potential [Wolf 89]. Thus the L-J potential gives rise to considerable lower values of the elastic constants. It will be seen later that this weak volume dependence of the internal stress makes it difficult to distinguish between the criteria even if it does not change the course of the instability of the crystals.

3.2 Models with and without Interfaces

Consistent with the theoretical study we wish to choose models containing cubic and tetragonal symmetry in their elastic constant matrices. The first choice we can make is the simple f.c.c. crystal. The elastic properties of this crystal and its instability at zero temperature have been extensively studied [Hill 77, Milstein 77, 78, 79a, 79b, 80]. F.c.c. crystal has cubic elastic symmetry. It can also have tetragonal elastic symmetry under some proper loading environment, such as uniaxial stress or strain.

Another well-defined model we will study is the so-called grain-boundary superlattice (GBSL) [Yip 89] consisting of a periodic arrangement, $\cdots|A|B|A|B|\cdots$, of thin slabs A and B of equal thickness (see Fig. 3.1). This gives tetragonal symmetry. The slabs A and B consist of the same material (in the present case: Au) and are merely rotated with respect to each other about the z axis by a angle of 43.60° (between A|B) or - 43.60° (between B|A), respectively. The interfaces between A and B are called high-angle twist boundaries. In present case of twist rotation of 43.60°, the grain boundary is commonly referred as the $\Sigma 29$ twist grain boundary. The periodicity of these twist grain boundaries is given by the supermodulation wavelength Λ. The GBSL we will use has the supermodulation wavelength $\Lambda = 8a_0$.

The advantage of this model lies in the factor that it possesses not only the tetragonal symmetry we need but also the inherent inhomogeneity that is the cause of anomalous elastic behavior (the so-called supermodulus effect). These elastic anomalies include anisotropic thermal expansion where the thermal expansion of a_z is larger than that of a_x in the GBSL's, while a_x itself shows a larger thermal expansion in the GBSL than in the perfect crystal [Jaszczak 92]. The existence of grain boundaries causes a stiffening of Young's modulus Y_z (parallel to the interface-plane normal) and a softening in shear modulus G_{xz} (for shear parallel to the interface-plane) [Wolf 89]. It was also noted [Wolf 89] that even the inherent inhomogeneity of the interface leads to the supermodulus effect while there seems not to be a "super elastic-constant effect". It was also found [Jaszczak 92] that the softening of elastic moduli (or elastic constants) with change of temperature or volume remains normal. That is, They decrease with increase of temperature or volume expansion. This well-characterized grain boundary superlattice system offers a very good model for our present study of instability.

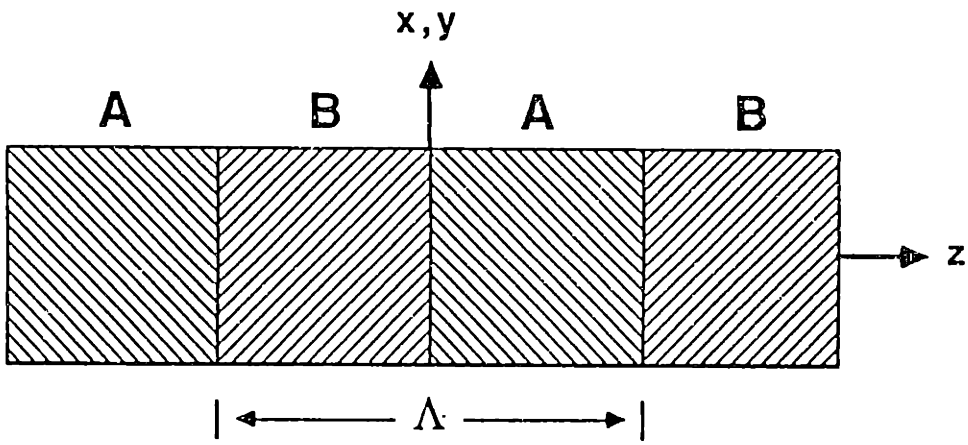

Fig. 3.1 periodic arrangement of thin slabs, A and B, to form a "grain-boundary superlattice" (GBSL). A and B are thin slabs of the same material, each of thickness Λ/2, rotated about the GB-plane normal (||z) to form a periodic array of twist boundaries in the x-y plane. The overall arrangement of atoms is thus periodic in all three dimenstions.

3.3 Simulation Methods

With very rapid development of computer systems, computer simulation provides a new bridge between the analytical theory and experiment. The use of atomistic-simulation models consisting of several hundred to a few thousand particles has a vast success in studying structural, thermodynamic, mechanical and kinetic properties of simple physical systems in several areas of condensed matter physics and theoretical chemistry. We are concerned here with the use of molecular dynamics (MD) method [Allen 87, Parrinello 81, Ray 84] and Monte Carlo (MC) method of Metropolis [Metropolis 53, Allen 87, Binder 85] to determine the behavior of an atomic system with and without interfaces in the stressed and thermal environment.

3.3.1 Molecular dynamics (MD)

In the MD method, the motion of the atoms is determined by Lagrangian dynamics. MD simulation generates the atomic trajectories by numerically solving the Lagrangian equations of motion for N atoms in the simulated system

$$\frac{d}{dt}\left(\frac{\partial L}{\partial \dot{q}_i}\right) - \left(\frac{\partial L}{\partial q_i}\right) = 0 \qquad \text{for } i=1, \cdots, N \tag{3.5}$$

where the Lagrangian function $L(\mathbf{q},\dot{\mathbf{q}})$ is defined in terms of kinetic energy and potential energy

$$L = K - V \tag{3.6}$$

and is considered to be a function of the generalized coordinates q_i and their time derivatives $\dot{q}_i$. For an atomic system if we choose the Cartesian coordinates and the usual definitions of K and V, then equation (3.5) gives Newton's equation of motion

$$m_i \ddot{\mathbf{r}}_i = \mathbf{f}_i \tag{3.7}$$

where m_i is the mass of the ith atom and

$$\mathbf{f}_i = \nabla_{\mathbf{r}_i} L = - \nabla_{\mathbf{r}_i} V \tag{3.8}$$

is the force exerted on the atom i by the remaining atoms in the system. Thus the model system evolves according to the atomic forces and to the prescribed border conditions.

In order to study the structural responses of a crystal to any external stress we will employ the generalized molecular dynamics method that first developed by Parrinello and Rahman [Parrinello 81] and latter modified by Ray and Rahman [Ray 84]. This method allows changes in both the size and shape of the simulation cell to respond to any imbalance between the internal stress tensor and an external applied stress. The simulation cell is completely described by three vectors **a**, **b** and **c** that span the edges of the cell. The vectors can have different lengths and arbitrary mutual orientations. This specification can be conveniently expressed in terms of a 3×3 matrix $\mathbf{h} = \{\mathbf{a},\mathbf{b},\mathbf{c}\}$, the columns of which gives the components of each vector.

In this modified Parrinello-Rahman method, in addition to the equations of motion for N atoms in the simulation cell, there are six equations of motion for **h** matrix which contains the imposed tensor Γ

$$W\ddot{\mathbf{h}} = \hat{\sigma}\mathbf{h}^{-1}\Omega - \mathbf{h}\Gamma, \qquad \Gamma = \Omega_0\mathbf{h}_0^{-1}\mathbf{t}\mathbf{h}_0^{t^{-1}} \tag{3.9}$$

where superscripts t and -1 donate the transpose and inverse of a matrix respectively; Ω and Ω_0 are the volumes of the simulation cell with and without external applied stress; $\mathbf{h}_0$ is the **h** matrix at zero applied stress, $\hat{\sigma}$ is the instantaneous internal stress tensor, and **t** is defined as the tensor of thermodynamic tension which is related to the external applied stress Σ (which is equal to the internal stress $\langle\hat{\sigma}\rangle$when in equilibrium) by

$$\mathbf{t} = \frac{\Omega\mathbf{h}_0\mathbf{h}^{-1}\Sigma\mathbf{h}^{t^{-1}}\mathbf{h}_0^{t^{-1}}}{\Omega_0}. \tag{3.10}$$

As pointed out by Ray and Rahman [Ray 84], Eq. (3.7) and (3.10) will generate a thermodynamically consistent (HtN) ensemble. In present study we are interested in the behavior of the model system in a thermal and stressed environment. In order to generate a (TtN) ensemble [or (TΣN) ensemble], we rescale the atomic velocities at every time step so that the mean kinetic energy corresponding to the given temperature T. Thus by specifying the temperature T, external stress Σ and interatomic potential V, we may simulate the equilibrium properties of N atoms consistent with the chosen border conditions imposed at the faces of the simulation cell.

The proper border conditions to be specified depend on the system properties to be studied. For bulk properties in a homogeneous system it is usually appropriate and also

convenient to impose periodic traction border conditions which have the effect of embedding the simulation model in an infinite system composed of replicates of the finite size model in all directions. This border condition is suitable for the models of both f.c.c. crystal and GBSL we will study.

3.3.2 Monte Carlo Method (MC)

The MC method does not generate a true dynamic history of an atomic system, but rather a Markovian chain of spatial configurations according to stochastic dynamics. In classical statistical mechanics, the canonical ensemble average of potential energy is given by

$$\langle U \rangle = \int_{\Omega} U(\mathbf{R})\, f(\mathbf{R})\, d\mathbf{R} \tag{3.11}$$

where the potential function of the system depends on the configuration $\mathbf{R} = (\mathbf{r}_1, \mathbf{r}_2, \cdots, \mathbf{r}_N)$ of the N atoms, and the probability distribution function for the configuration is given by

$$f(\mathbf{R}) = \frac{\exp[-U(\mathbf{R})/k_B T]}{\int_{\Omega} \exp[-U(\mathbf{R})/k_B T]\, d\mathbf{R}}. \tag{3.12}$$

From equations (3.11) and (3.12) one sees that <U> may be calculated by randomly selecting a huge number of spatial configurations and averaging the energy over these configurations, weighting with the appropriate Boltzmann factor. This method obviously is not practical because the number of configurations required to get a reasonable average is enormous. However, in the MC method which is widely used in present simulation study, the procedure is to select configurations with a frequency proportional to the Boltzmann factor $\exp[-U(\mathbf{R})/k_B T]$ and average over the selected configurations with equal weight. This ideal was first proposed by Metropolis et al [Metropolis 53]. We will outline the Metropolis algorithm for an atomic system with potential energy $U(\mathbf{R}) = \sum_{i,j>i}^{N} v(r_{ij})$ in three dimensions.

Suppose that a system of N atoms is placed in an arbitrary initial configuration in a volume Ω at a fixed temperature T, the configurations in this (TΩN) ensemble are

generated according to the following rules: (1) select an atom at random; (2) select random displacements Δx, Δy, Δz , each of them can be either positive or negative such that $(\Delta x)^2+(\Delta y)^2+(\Delta z)^2 \le (\Delta r_{max})^2$; (3) calculate the change in potential energy δU on displacing the chosen atom by (Δx, Δy, Δz); (4) if δU is negative accept the new configuration; (5) otherwise, generate a random number ξ which is uniformly distributed in the interval (0,1); (6) if $\exp(\delta U/k_B T) < \xi$, accept the old configuration; (7) otherwise, the new configuration and the new potential energy become the "present" properties of the system; (8) repeat the steps (1) to (7) again. Usually the early configurations generated in this way are dropped in the calculations of system properties since they may be not in equilibrium and will slow down the convergence of the averages. The maximum displacement Δr_{max} is chosen to optimize convergence. Typically, Δr_{max} is chosen such that approximately half of trials are actually accepted. For given potential function, the choice of Δr_{max} is usually governed by the density N/V and the temperature T of the system.

An advantage of the MC method is that it can be readily used in the calculation of averages in any ensemble. Wood [Wood 68a, 68b; 70] first showed that the MC method could be extended to the isothermal-isobaric ensemble. In the constant pressure MC simulation, a configuration of N atoms at temperature T and pressure P is represented by 3N coordinates confined within a simulation cell of variable volume. A new configuration is generated by selecting an atom randomly and giving it a random displacement and by changing the volume of the cell randomly within a prescribed range. The change of volume requires the scaling of all atomic coordinates by a appropriate factor. If we donate the potential energy of the old and new configurations by U and U', and the corresponding volumes of the cell by Ω and Ω', respectively, the total energy change can be expressed as

$$\delta W = (U - U') + P(\Omega - \Omega') - N k_B T \ln(\Omega'/\Omega). \qquad (3.13)$$

If the change of the total energy is negative, the new configuration is accepted, If it is positive, the new configuration is accepted only with the probability is equal to or greater than $\exp(\delta W/k_B T)$. Repeating this procedure gives rise to a chain of configurations distributed in phase space with a probability proportional to the classical Boltzmann factor.

3.4 Property Calculation

In order to study the stress-induced structural response of crystals in elastic unstable region, it is important to know the properties of the model system in equilibrium.

In this section we will introduce some basic formula for property calculation. The system properties we are interested in include thermodynamic properties such as internal energy or enthalpy, mechanical and dynamic properties like internal stress tensor, pressure and mean square displacement; structural properties such as pair correlation function and structure factor (or diffraction patterns); and finite strain elastic constants. Since most of these properties were well defined in the literature [Allen 87, Haile 92], discuss some of them which are important in our study.

3.4.1 Pair Correlation Function and Structure Factor

The structural properties we will keep tracking along with simulation are the pair correlation function and the structure factor.

The pair correlation function is simply defined as

$$g(r) = \frac{1}{N} \sum_{i,j>i} \delta(r_{ij} - r) \tag{3.14}$$

which gives the probability of finding another atom at a distance r away from the given atom. For crystalline materials their structural difference can be well characterized and easily distinguished from the peaks of g(r) and their positions. For example, for a perfect f.c.c. crystal at zero temperature, g(r) would have a δ-function peak of height 12 at the nearest-neighbor distance $r/a_0 = \sqrt{2}/2$, and a peak of height 6 at the second nearest-neighbor separation of $r/a_0 = 1$, and so on.

Another way of people usually getting structure information is from the diffraction patterns of waves that interacts with atoms and has a wavelength comparable with the interatomic spacing. From the classic scattering theory [Kittel 56] we have known that the diffraction amplitude is

$$A = \int_{\Omega} d\mathbf{r}\, n(\mathbf{r}) \exp(i\mathbf{k}\cdot\mathbf{r}) \tag{3.15}$$

where n(r) is the electron density function and k is the wave vector difference of the income and scattered wave, or equivalently the reciprocal lattice vector. To simplify the calculation we assume that the electron density function has the form

$$n(\mathbf{r}) = \sum_{i=1}^{N} \delta(\mathbf{r} - \mathbf{r}_i) \tag{3.16}$$

where $\mathbf{r}_i$ is the position of the ith atom. Substituting (3.16) into (3.15) we have

$$\begin{aligned} A &= \int_{\Omega} d\mathbf{r} \sum_{i=1}^{N} \delta(\mathbf{r} - \mathbf{r}_i) \exp(i\mathbf{k}\cdot\mathbf{r}) \\ &= \sum_{i=1}^{N} \exp(i\mathbf{k}\cdot\mathbf{r}). \end{aligned} \tag{3.17}$$

Then the diffraction intensity per atom is proportional to AA^*, that is

$$\begin{aligned} I \approx \frac{AA^*}{N} &= \frac{1}{N}\left|\sum_{i=1}^{N} \exp(i\mathbf{k}\cdot\mathbf{r})\right|^2 \\ &= 1 + \frac{2}{N} < \sum_{i,j>i}^{N} \cos\left[\mathbf{k}\cdot(\mathbf{r}_i - \mathbf{r}_j)\right] >. \end{aligned} \tag{3.18}$$

Which is also defined as the static structure factor S(**k**) [Wolf 90a].Where < > donates a configuration average. For a bulk crystal, by varying wave vector **k** one can calculate the diffraction patterns of the crystal. Sometimes for convenience we only calculate the structure factor for several wave vectors which we know will give maximum diffraction density. By keeping track of the values of the structure factor, we can monitor the structural change of the model system. One can also calculate the planar structure factor, $S_p(\mathbf{k})$. In this case only atoms in a given lattice plane are considered. In the case of a GBSL, the slabs A and B are rotate relative to one another. A reciprocal lattice vector lying in a (001) plane in slab A will not be a reciprocal-lattice vector in slab B. Thus two different wave vectors, $\mathbf{k}_1$ and $\mathbf{k}_2$, are required to monitor planar order in the A and B region. They are related by the relative rotation of the two kinds of slabs. For a well-defined lattice plane, for example in slab A, $S_p(\mathbf{k}_1)$ then fluctuates about a finite value, somewhat less than unity, while $S_p(\mathbf{k}_2)$ fluctuates about a value that is essentially zero. In the interface region, due to local disorder, one expect somewhat lower values of the structure factor. By monitoring $S_p(\mathbf{k}_1)$ and $S_p(\mathbf{k}_2)$, every plane may be characterized as (a) belonging to slab A [if $S_p(\mathbf{k}_1)$ is near unity and $S_p(\mathbf{k}_2)$ is near zero], (b) belonging to slab B [if $S_p(\mathbf{k}_1)$ is near zero and $S_p(\mathbf{k}_2)$ is near unity], or (c) disordered or changed to another crystal structure [if both $S_p(\mathbf{k}_1)$ and $S_p(\mathbf{k}_2)$ are near zero].

3.4.2 Internal Stress Tensor and Strain

The most fundamental mechanical properties in this research are the internal stress tensor and elastic constants. For a homogeneous system (where, by definition, the stress or the strain is the same throughout the system) the internal stress is arisen when a strain deformation is imposed on the system. There are several definitions of strain in the literature of elasticity theory [Landau 70, Hill 77, Lutsko 91], for convenience of the simulation, we will choose the definition of Lagrangian strain

$$\varepsilon = \frac{1}{2}\left(\mathbf{h}_0^{t^{-1}}\mathbf{h}^t\mathbf{h}\mathbf{h}_0^{-1} - \mathbf{I}\right) \tag{3.19}$$

which is appropriate when all quantities are referred to a fixed set of axes. Here these exes are well-defined by the **h** matrix of the simulation cell as interpreted in section 3.3.1.

From the virial theorem of Clausius an expression for the tensor σ which describes the state of stress of the entire system can be derived and is widely used in atomistic simulation to calculate the system pressure [Allen 87]. The stress tensor of an atomistic system can also be derived from thermodynamic quantities as the derivatives of the free energy F with respect to strain

$$\begin{aligned}\Omega_0 t_{\alpha\beta} &= -\frac{\partial F}{\partial \varepsilon_{\alpha\beta}} \\ &= -\left[\mathbf{h}_0\mathbf{h}^{-1}\right]_{\alpha\alpha'} < D_{\alpha'\beta'}\widehat{\mathbf{H}} > \left[\left(\mathbf{h}_0\mathbf{h}^{-1}\right)^t\right]_{\beta'\beta}\end{aligned} \tag{3.20}$$

where $\widehat{\mathbf{H}}$ is the Hamiltonian of the system, < > donates an ensemble average, and operator D is defined as

$$D_{\alpha\beta} \equiv \left(r_{i\alpha}\frac{\partial}{\partial r_{i\beta}} + r_{i\beta}\frac{\partial}{\partial r_{i\alpha}} - P_{i\alpha}\frac{\partial}{\partial P_{i\beta}} - P_{i\beta}\frac{\partial}{\partial P_{i\alpha}}\right) \tag{3.21}$$

where $r_{i\alpha}$ and $r_{i\beta}$ are the α and β components of the position vector $\mathbf{r}_i$ of atom i, $P_{i\alpha}$ and $P_{i\beta}$ are respectively the α and β components of atom i's momentum. For detailed derivation of expression (3.20) we refer the reader to [Lutsko 89a,91]. It turns out that the "stress tensor" of this definition is actually the thermodynamic tension tensor [Ray 84] that we discussed in section 3.3.1, which is artificially introduced in Ray and Rahman's work [Ray 84] in order to bring the formula and the simulation results of MD into consistent with

the theory of finite elastic deformation developed by Thurston [Thurston 64], Murnaghan [Murnaghan 51] and Wallace [Wallace 70]. The thermodynamic tension tensor **t** is related to the physical stress of virial theorem

$$\sigma_{\alpha\beta} = \frac{1}{\Omega} < \sum_{i=1}^{N} \frac{P_{i\alpha}P_{i\beta}}{m} - \sum_{i,j>i}^{N} \frac{1}{r_{ij}} \frac{\partial V}{\partial r_{ij}} r_{ij\alpha} r_{ij\beta} > \tag{3.22}$$

by equation (3.10). Here Ω is the volume of the system, $\sigma_{\alpha\beta}$ is the $\alpha\beta$ component of the stress tensor, $r_{ij\alpha}$ and $r_{ij\beta}$ are respectively the α and β components of r_{ij}, the relative position vector between atom i and j, and V is the total potential of the system given by Eq. (3.1).

For a system of N atoms that interacts via a pairwise potential $\phi(r_{ij})$ the physical stress tensor can be computed from the following expression

$$\sigma_{\alpha\beta} = \frac{1}{\Omega} < \sum_{i=1}^{N} \frac{P_{i\alpha}P_{i\beta}}{m} - \sum_{i,j>i}^{n} \frac{1}{r_{ij}} \frac{\partial \phi(r_{ij})}{\partial r_{ij}} r_{ij\alpha} r_{ij\beta} >. \tag{3.23}$$

In the case of EAM potentials, the stress tensor can extended to include the contributions from the embedding function

$$\sigma_{\alpha\beta} = \frac{1}{\Omega} < \sum_{i=1}^{N} \frac{P_{i\alpha}P_{i\beta}}{m} - \sum_{i,j>i}^{N} \frac{1}{r_{ij}} \frac{\partial \phi(r_{ij})}{\partial r_{ij}} r_{ij\alpha} r_{ij\beta} - \sum_{i,j>i}^{N} \frac{\partial F}{\partial \rho_{hi}} \frac{\partial \rho_{ij}}{\partial r_{ij}} \frac{r_{ij\alpha} r_{ij\beta}}{r_{ij}} > \tag{3.24}$$

where all the terms involving the EAM functions have the same meanings as in Eq. (3.3). These two expressions will be used in our simulation study of L-J potential and EAM potential model systems.

3.4.3 Finite Strain Elastic Constants

There are several ways to calculate elastic constants. The zero temperature elastic constants can be evaluated directly using the Born approach [Born 56], where the elastic constants are expressed in terms of the curvature of the potential energy. At finite temperature the elastic constants can be calculated either using fluctuation formulas or from a numerical simulation of stress-strain curve experiment. In what follows we will discuss these last two methods in more detail.

Before we start our discussion on the methodology of elastic constant calculation, one thing which is worth emphasizing is that we are really interested in the elastic constant at finite strain. There was a confusion about the reference state which is characterized by $\mathbf{h}_0$. Purely from the point of view of the definition of the strain

$$\boldsymbol{\varepsilon} = \frac{1}{2}\left(\mathbf{h}_0^{t^{-1}}\mathbf{h}^t\mathbf{h}\mathbf{h}_0^{-1} - \mathbf{I}\right)$$

the choice of $\mathbf{h}_0$ is obviously arbitrary. However, in the expression for the elastic energy and elastic constants the choice does make a difference. When take $\mathbf{h}_0 = \langle \mathbf{h} \rangle$ as originally done by Parrinello and Rahman [Parrinello 81] the elastic energy W generated in a deformation around a state of the system which is not a state of zero stress but the state under that stress σ. Thus the reference value from which W is measured is not zero but the elastic energy in a deformed state. And the strain value is also measured with respect to this deformed state. When the elastic energy W is defined as $W = \Omega_0 \, \mathrm{Tr}\, \mathbf{t}\boldsymbol{\varepsilon}$ using the thermodynamic tension tensor $\mathbf{t}$, the value of $\mathbf{h}_0$ should be chosen as the average value of $\mathbf{h}$ when the stress is zero, i.e., the stored elastic energy is zero if the system is not acted on by any external stress. Although these two choices make difference in the expression of stored elastic energy and the expression of elastic constant they do not affect the final results of the quantities. The only care must be taken that they are evaluated with respect to the different reference states.

In following we will follow Lutsko [Lutsko 89a, 91] to get the fluctuation formula. In general the elastic constant tensor is defined as the derivative of thermodynamic tension with respect to strain

$$C_{\alpha\beta\chi\sigma} = -\frac{\partial t_{\alpha\beta}}{\partial \varepsilon_{\chi\sigma}}. \tag{3.25}$$

Consider a elastic homogeneous system of N atoms with Hamiltonian

$$\hat{H} = \frac{1}{2m}\sum_{i=1}^{N} \mathbf{P}_i^2 + V(\{\mathbf{r}_i\}) \tag{3.26}$$

where $\mathbf{P}_i$ and $\mathbf{r}_i$ are the momentum and the position vector of the ith atom respectively. Following Ray and Rahman [Ray 84], we introduce a canonical transformation to a new coordinate system $\mathbf{s}_i$ and $\mathbf{p}_i$, defined by the following equations

$$\mathbf{r}_i = \mathbf{h} \cdot \mathbf{s}_i$$
$$\mathbf{P}_i = \mathbf{h}^{t-1} \cdot \mathbf{p}_i \qquad (3.27)$$

where **h** matrix is the same as defined in section 3.3.1. It can be shown [Lutsko 89a] that on a (ThN) ensemble the thermodynamic tension tensor can be expressed as

$$\Omega_0 \mathbf{t} = \mathbf{h}_0 \mathbf{h}^{-1} < D\widehat{\mathbf{H}} > (\mathbf{h}_0 \mathbf{h}^{-1})^t = \Omega \mathbf{h}_0 \mathbf{h}^{-1} < \widehat{\sigma} > (\mathbf{h}_0 \mathbf{h}^{-1})^t \qquad (3.28)$$

where Ω_0 and Ω are the volumes of the system at zero and finite applied stress respectively, the superscript t donate the transpose of the matrix, and the physical stress tensor

$$\sigma = < \widehat{\sigma} > = - \frac{1}{\Omega} < D\widehat{\mathbf{H}} > \qquad (3.29)$$

which is the same as Eq.(3.22). We also can define the instantaneous thermodynamic tension tensor as

$$\Omega_0 \hat{\mathbf{t}} = \mathbf{h}_0 \mathbf{h}^{-1} D\widehat{\mathbf{H}} (\mathbf{h}_0 \mathbf{h}^{-1})^t = \Omega \mathbf{h}_0 \mathbf{h}^{-1} \widehat{\sigma} (\mathbf{h}_0 \mathbf{h}^{-1})^t. \qquad (3.30)$$

Taking into account the periodic border condition [Lutsko 91] the operator D defined in Eq. (3.21) can be expressed as

$$D_{\alpha\beta} \equiv \frac{1}{2} \left[\sum_{i,j>i}^{N} \left(r_{ij\alpha} \frac{\partial}{\partial r_{ij\beta}} + r_{ij\beta} \frac{\partial}{\partial r_{ij\alpha}} \right) - \left(P_{i\alpha} \frac{\partial}{\partial P_{i\beta}} + P_{i\beta} \frac{\partial}{\partial P_{i\alpha}} \right) \right]. \qquad (3.31)$$

Therefore, the instantaneous stress tensor

$$\widehat{\sigma}_{\alpha\beta} = - \frac{1}{\Omega} D_{\alpha\beta} \widehat{H} = \frac{1}{\Omega} \sum_{i=1}^{N} \frac{P_{i\alpha} P_{i\beta}}{m} - \frac{1}{\Omega} \sum_{i,j>i}^{N} \frac{\partial V}{\partial r_{ij}} \frac{r_{ij\alpha} r_{ij\beta}}{r_{ij}}. \qquad (3.32)$$

It should not be confused here that in Eq.(3.32) although the derivative of potential V is taken with respect to the separation of i and j atoms, it is not the same as saying that the potential is pairwise potential. Actually all potentials can be written in terms of differences in atom the coordinates of pairs of atoms [Daw 83]. Lutsko [Lutsko 89a] has showed that,

in general, the derivative of a general function of the atom coordinates $\hat{A}(\{\mathbf{r}_i\}) = \hat{A}(\{\mathbf{h}\cdot\mathbf{s}_i\})$ with respect to strain can be expressed as

$$\begin{aligned}\frac{\partial<\hat{A}>}{\partial\varepsilon} &= \mathbf{h}_0\mathbf{h}^{-1}\left\{<D\hat{A}> - \frac{1}{k_BT}\left(<\hat{A}D\hat{H}> - <\hat{A}><D\hat{H}>\right)\right\}(\mathbf{h}_0\mathbf{h}^{-1})^t \\ &= \mathbf{h}_0\mathbf{h}^{-1}\left\{<D\hat{A}> + \frac{\Omega}{k_BT}\left(<\hat{A}\hat{\sigma}> - <\hat{A}><\hat{\sigma}>\right)\right\}(\mathbf{h}_0\mathbf{h}^{-1})^t \\ &= <\left[\mathbf{h}_0\mathbf{h}^{-1}D(\mathbf{h}_0\mathbf{h}^{-1})^t\right]\hat{A}> + \frac{\Omega_0}{k_BT}\left(<\hat{A}\hat{t}> - <\hat{A}><\hat{t}>\right). \end{aligned} \tag{3.33}$$

To make it more clear we write (3.33) in more obvious form

$$\begin{aligned}\frac{\partial<\hat{A}>}{\partial\varepsilon_{\chi\eta}} &= \left[\mathbf{h}_0\mathbf{h}^{-1}\right]_{\chi\chi'}\left\{<D_{\chi'\eta'}\hat{A}> + \frac{\Omega}{k_BT}\left(<\hat{A}\hat{\sigma}_{\chi'\eta'}> - <\hat{A}><\hat{\sigma}_{\chi'\eta'}>\right)\right\}\left[(\mathbf{h}_0\mathbf{h}^{-1})^t\right]_{\eta'\eta} \\ &= <\left[\mathbf{h}_0\mathbf{h}^{-1}\right]_{\chi\chi'}D_{\chi'\eta}\left[(\mathbf{h}_0\mathbf{h}^{-1})^t\right]_{\eta'\eta}\hat{A}> + \frac{\Omega_0}{k_BT}\left(<\hat{A}\hat{t}_{\chi\eta}> - <\hat{A}><\hat{t}_{\chi\eta}>\right). \end{aligned} \tag{3.34}$$

Using Eq.(3.33) and the definition (3.25) elastic constants can be found as

$$\begin{aligned}C_{\alpha\beta\chi\eta} &= -\frac{\partial t_{\alpha\beta}}{\partial\varepsilon_{\chi\eta}} \\ &= -<\left[\mathbf{h}_0\mathbf{h}^{-1}\right]_{\chi\chi'}D_{\chi'\eta}\left[(\mathbf{h}_0\mathbf{h}^{-1})^t\right]_{\eta'\eta}\hat{t}_{\alpha\beta}> - \frac{\Omega_0}{k_BT}\left(<\hat{t}_{\alpha\beta}\hat{t}_{\chi\eta}> - <\hat{t}_{\alpha\beta}><\hat{t}_{\chi\eta}>\right) + \\ &\quad \frac{1}{2}\left\{\left[\mathbf{h}_0\mathbf{h}^{-1}\right]_{\beta\beta'}\delta_{\beta'\eta}\left[(\mathbf{h}_0\mathbf{h}^{-1})^t\right]_{\eta'\eta}<\hat{t}_{\alpha\chi}> + \left[\mathbf{h}_0\mathbf{h}^{-1}\right]_{\alpha\alpha'}\delta_{\alpha'\eta}\left[(\mathbf{h}_0\mathbf{h}^{-1})^t\right]_{\eta'\eta}<\hat{t}_{\beta\chi}>\right\} + \\ &\quad \frac{1}{2}\left\{\left[\mathbf{h}_0\mathbf{h}^{-1}\right]_{\beta\beta'}\delta_{\beta'\chi}\left[(\mathbf{h}_0\mathbf{h}^{-1})^t\right]_{\chi'\chi}<\hat{t}_{\alpha\eta}> + \left[\mathbf{h}_0\mathbf{h}^{-1}\right]_{\alpha\alpha'}\delta_{\alpha'\chi}\left[(\mathbf{h}_0\mathbf{h}^{-1})^t\right]_{\chi'\chi}<\hat{t}_{\beta\eta}>\right\} \\ &= \frac{\Omega}{\Omega_0}\left[\mathbf{h}_0\mathbf{h}^{-1}\right]_{\chi\chi}\left[(\mathbf{h}_0\mathbf{h}^{-1})^t\right]_{\eta'\eta}\left[\mathbf{h}_0\mathbf{h}^{-1}\right]_{\alpha\alpha}\left[(\mathbf{h}_0\mathbf{h}^{-1})^t\right]_{\beta'\beta}\times \\ &\quad \left\{ - <D_{\chi'\eta'}\hat{\sigma}_{\alpha'\beta'}> - \frac{\Omega_0}{k_BT}\left(<\hat{\sigma}_{\alpha'\beta'}\hat{\sigma}_{\chi'\eta'}> - <\hat{\sigma}_{\alpha'\beta'}><\hat{\sigma}_{\chi'\eta'}>\right) + \right. \\ &\quad \left. \frac{1}{2}\left(\delta_{\beta'\chi'}<\hat{\sigma}_{\alpha'\eta'}> + \delta_{\alpha'\eta'}<\hat{\sigma}_{\beta'\chi'}> + \delta_{\beta'\chi'}<\hat{\sigma}_{\alpha'\eta'}> + \delta_{\alpha'\chi'}<\hat{\sigma}_{\beta'\eta'}>\right)\right\}. \end{aligned} \tag{3.35}$$

The explicit stress terms appearing in Eq.(3.35) arise from the action of the strain derivative on the explicit h dependence of the thermodynamic tension tensor [see Eq.(3.28)]. We will prove that the first term and last term in the bracket of the last line of Eq.(3.35) will give the so-called Born term and the kinetic term of the elastic constant. Let us write

$$- \langle D_{\chi'\eta'} \hat{\sigma}_{\alpha'\beta'} \rangle = \left\langle \frac{1}{2} \left(P_{i\chi} \frac{\partial}{\partial P_{i\eta'}} + P_{i\eta} \frac{\partial}{\partial P_{i\chi'}} \right) \left(\frac{1}{\Omega} \sum_{j=1}^{N} \frac{P_{j\alpha'} P_{j\beta'}}{m} \right) \right\rangle +$$
$$\left\langle \frac{1}{2} \sum_{i,j>i}^{N} \left(r_{ij\chi} \frac{\partial}{\partial r_{ij\eta'}} + r_{ij\eta} \frac{\partial}{\partial r_{ij\chi'}} \right) \left(\frac{1}{\Omega} \sum_{k,l>k}^{n} r_{kl\alpha'} r_{kl\beta} \frac{\partial V}{\partial r_{kl}} \right) \right\rangle. \quad (3.36)$$

It is easy to show that the first term in Eq.(3.36) gives rise to the kinetic term of the elastic constants

$$\left\langle \frac{1}{2} \left(P_{i\chi} \frac{\partial}{\partial P_{i\eta'}} + P_{i\eta} \frac{\partial}{\partial P_{i\chi'}} \right) \left(\frac{1}{\Omega} \sum_{j=1}^{N} \frac{P_{j\alpha'} P_{j\beta'}}{m} \right) \right\rangle = 2nk_B T \left(\delta_{\chi'\beta'} \delta_{\alpha'\eta'} + \delta_{\eta'\beta'} \delta_{\alpha'\chi'} \right) \quad (3.37)$$

where $n = N/\Omega$ is the number density of the system. And the second term of Eq.(3.36) combing with the last term of Eq.(3.35) gives the Born term

$$C^{B}_{\alpha'\beta'\chi'\eta'} = \left\langle \frac{1}{2} \sum_{i,j>i}^{N} \left(r_{ij\chi} \frac{\partial}{\partial r_{ij\eta'}} + r_{ij\eta} \frac{\partial}{\partial r_{ij\chi'}} \right) \left(\frac{1}{\Omega} \sum_{k,l>k}^{N} \frac{\partial V}{\partial r_{kl}} \frac{r_{kl\alpha'} r_{kl\beta'}}{r_{kl}} \right) \right\rangle +$$
$$\frac{1}{2} \left(\delta_{\beta'\chi'} \langle \hat{\sigma}'_{\alpha'\eta'} \rangle + \delta_{\alpha'\eta'} \langle \hat{\sigma}'_{\beta'\chi'} \rangle + \delta_{\beta'\chi'} \langle \hat{\sigma}'_{\alpha'\eta'} \rangle + \delta_{\alpha'\chi'} \langle \hat{\sigma}'_{\beta'\eta'} \rangle \right)$$
$$= S\hat{E}_{\alpha'\beta'\chi'\eta'}, \quad (3.38)$$

where

$$\hat{\sigma}'_{\alpha'\chi'} = \frac{1}{\Omega} \sum_{i,j>i}^{N} \frac{\partial V}{\partial r_{ij}} \frac{r_{ij\chi'} r_{ij\alpha'}}{r_{ij}} \quad (3.39)$$

is only the potential contribution to the microscopic stress, and

$$\hat{E}_{\alpha'\beta'\chi'\eta'} = \frac{1}{\Omega} \left\langle \sum_{i,j>i}^{N} \left(\frac{r_{ij\chi'} \delta_{\beta'\eta'} r_{ij\alpha'}}{r_{ij}} \frac{\partial V}{\partial r_{ij}} + r_{ij\beta'} r_{kl\eta'} V_{ij\chi',kl\alpha'} \right) \right\rangle + 2\delta_{\beta'\eta'} \langle \hat{\sigma}'_{\alpha'\chi'} \rangle \quad (3.40)$$

here we have introduced the matrix of second derivatives, or force constant matrix, defined as

$$V_{ij\eta',kl\beta'} = \frac{\partial^2 V}{\partial r_{ij\eta'} \partial r_{kl\beta'}} \quad (3.41)$$

and the symmetrizing operator S defined by its action on Cartesian coordinates

$$S\hat{E}_{\alpha'\beta'\chi'\eta'} = \frac{1}{4}\left(\hat{E}_{\alpha'\beta'\chi'\eta'} + \hat{E}_{\beta'\alpha'\chi'\eta'} + \hat{E}_{\alpha'\beta'\eta'\chi'} + \hat{E}_{\beta'\alpha'\eta'\chi'}\right). \tag{3.42}$$

For the purpose of our following calculations, we give here the explicit forms of the general potential functions relating to the evaluation of elastic constants for pairwise interactions and EAM potential. We will start with the pairwise potential. Consider a potential of the form

$$V = \sum_{i,j>i}^{N} \phi(r_{ij}) \tag{3.43}$$

where $r_{ij} = |\mathbf{r}_i - \mathbf{r}_j|$. Since

$$\frac{\partial V}{\partial r_{ij}} = \sum_{l,n>l}^{N} \frac{\partial \phi(r_{ln})}{\partial r_{ln}} \frac{\partial r_{ln}}{\partial r_{ij}} = \sum_{l,n>l}^{N} \frac{\partial \phi(r_{ln})}{\partial r_{ln}} \delta_{il}\delta_{jn} = \sum_{i,j>i}^{N} \frac{\partial \phi(r_{ij})}{\partial r_{ij}}$$

and

$$\frac{\partial^2 V}{\partial r_{ij\eta'}\partial r_{ij\beta'}} = \frac{\partial}{\partial r_{ij\eta'}} \sum_{l,n>l}^{N} \frac{\partial \phi(r_{ln})}{\partial r_{ln}} \frac{r_{ln\beta'}}{r_{ln}} \delta_{il}\delta_{jn}$$

$$= \sum_{i,j>i}^{N} \left(\frac{\delta_{\beta'\eta'}}{r_{ij}} \frac{\partial \phi(r_{ij})}{\partial r_{ij}} + \frac{r_{ij\beta'} r_{ij\eta'}}{r_{ij}} \frac{\partial^2 \phi(r_{ij})}{\partial r_{ij}^2} - \frac{r_{ij\beta'} r_{ij\eta'} \partial \phi(r_{ij})}{r_{ij}^3 \quad \partial r_{ij}} \right).$$

Combining these results and noticing Eq.(3.39), we come up with

$$\hat{E}_{\alpha'\beta'\chi'\eta'} = -2\delta_{\beta'\eta'}\langle \hat{\sigma}'_{\alpha'\chi'} \rangle + \frac{1}{\Omega} \left\langle \sum_{i,j>i}^{N} X_{ij}^{p} \frac{r_{ij\alpha'} r_{ij\beta'} r_{ij\chi'} r_{ij\eta'}}{r_{ij}^2} \right\rangle + 2\delta_{\beta'\eta'}\langle \hat{\sigma}'_{\alpha'\chi'} \rangle$$

$$= \frac{1}{\Omega} \left\langle \sum_{i,j>i}^{N} X_{ij}^{p} \frac{r_{ij\alpha'} r_{ij\beta'} r_{ij\chi'} r_{ij\eta'}}{r_{ij}^2} \right\rangle \tag{3.44}$$

where

$$X_{ij}^{p} = \left(\frac{\partial^2 V(r_{ij})}{\partial r_{ij}^2} - \frac{1}{r_{ij}} \frac{\partial V(r_{ij})}{\partial r_{ij}} \right). \tag{3.45}$$

The superscript p of X_{ij}^{p} refers to the pairwise potential. Thus the final form of Born term is

$$C^{B}_{\alpha'\beta'\chi'\eta'} = \frac{1}{\Omega} < \sum_{i,j>i}^{N} X^{p}_{ij} \frac{r_{ij\alpha'} r_{ij\beta'} r_{ij\chi'} r_{ij\eta'}}{r_{ij}^{2}} > \tag{3.46}$$

and the elastic constants of the pairwise potential are given by

$$C_{\alpha\beta\chi\eta} = \frac{\Omega}{\Omega_0} [h_0 h^{-1}]_{\chi\chi} [(h_0 h^{-1})^{t}]_{\eta'\eta} [h_0 h^{-1}]_{\alpha\alpha} [(h_0 h^{-1})^{t}]_{\beta'\beta} \times \Big\{ C^{B}_{\alpha'\beta'\chi'\eta'} + - \frac{\Omega_0}{k_B T} \left(<\hat{\sigma}_{\alpha'\beta'} \hat{\sigma}_{\chi'\eta'}> - <\hat{\sigma}_{\alpha'\beta'}><\hat{\sigma}_{\chi'\eta'}> \right) + 2nk_B T \left(\delta_{\chi'\beta'} \delta_{\alpha'\eta'} + \delta_{\eta'\beta'} \delta_{\alpha'\chi'} \right) \Big\} \tag{3.47}$$

which is the same as that got by Ray et al [Ray 85a, 85b].

We new consider the EAM potential. For EAM potential which has the form

$$V = \sum_{i} F(\rho_{hi}) + \sum_{i,j>i} \phi(r_{ij}) \tag{3.48}$$

where the host charge density on atom i, ρ_{hi}, is the sum of the charge density due to all other atoms

$$\rho_{hi} = \sum_{j} \rho_{ij}(r_{ij}), \text{ and again } \quad r_{ij} = |\mathbf{r}_i - \mathbf{r}_j|. \tag{3.49}$$

The first term in the right-hand side of Eq.(3.48) is a purely repulsive central-force pair potential and its contributions to the Born term are given by Eq.(3.39). We shall therefore only consider the contributions to the Born term.

From Eq.(3.24) we have found that the embedding-term contribution to the microscopic stress is given by

$$\hat{\sigma}^{e}_{\alpha'\beta'} = -\frac{1}{\Omega} \sum_{i,j\neq i}^{N} \left(\frac{\partial F(\rho_{hi})}{\partial \rho_{hi}} \right) \left(\frac{\partial \rho_{hi}}{\partial r_{ij}} \right) \frac{r_{ij\alpha'} r_{ij\beta'}}{r_{ij}}. \tag{3.50}$$

Here the superscript e donates embedding-term contribution. Substituting this results into Eq.(3.40) and evaluating the derivatives yields the Born contribution to the elastic constants, which are found to be

$$C^{eB}_{\alpha'\beta'\chi'\eta'} = \frac{1}{\Omega} S\left[\sum_{i,j\neq i}^{N}\left(\frac{\partial F(\rho_{hi})}{\partial \rho_{hi}}\right) X^{e}_{ij} \frac{r_{ij\alpha'} r_{ij\beta'} r_{ij\chi'} r_{ij\eta'}}{r_{ij}^{2}} + \sum_{i}^{N}\left(\frac{\partial F(\rho_{hi})}{\partial \rho_{hi}}\right) f_{i\alpha'\beta'} f_{i\chi'\eta'}\right] \quad (3.51)$$

where

$$X^{e}_{ij} = \frac{\partial^2 \rho_{hi}(r_{ij})}{\partial r_{ij}^2} - \frac{1}{r_{ij}} \frac{\partial \rho_{hi}(r_{ij})}{\partial r_{ij}} \quad (3.52)$$

and

$$f_{i\alpha'\beta'} = \sum_{i,j\neq i}^{N} \frac{\partial \rho_{hi}(r_{ij})}{\partial r_{ij}} \frac{r_{ij\alpha'} r_{ij\beta'}}{r_{ij}}. \quad (3.53)$$

By adding Eq.(3.51) to Eq.(3.46) and using Eq.(3.24) for the stress we can calculate the elastic constants of the EAM potential from Eq.(3.47) for finite temperatures and finite applied external stress. These formula will be used to compute the elastic constants through out our MD and MC simulation study.

Another method we will use to calculate elastic constants, as mentioned above, is the computer experiment of stress-strain curve method. Based on Eq. (3.22), the strain tensor to be imposed on a system can be fixed by adjusting the appropriate components in the system's h matrix. If the simulation is performed under a constant volume ensemble, or more generally a (ThN) ensemble, the imposed strain will stay constant throughout the entire simulation. By successively change one component of the strain tensor while hold the remains constant one can produce stress-strain curves. Then the slope of the stress-strain curve will give the corresponding elastic constant. As example, we will take the f.c.c. crystal to show how this naive calculation can be done. For cubic crystal there are only three independent elastic constants, C_{11}, C_{12}, and C_{44}, the normal stress and strain of the system is related by the generalized Hook's law (note we now take the pre-strained state as the reference state)

$$\sigma_{11} = C_{11}\varepsilon_{11} + C_{12}\varepsilon_{22} + C_{12}\varepsilon_{33} \quad (3.31)$$

$$\sigma_{22} = C_{12}\varepsilon_{11} + C_{11}\varepsilon_{22} + C_{12}\varepsilon_{33} \quad (3.32)$$

$$\sigma_{33} = C_{12}\varepsilon_{11} + C_{12}\varepsilon_{22} + C_{11}\varepsilon_{33}. \quad (3.33)$$

By examining these stress-strain relations, it is obvious that MD or MC simulation with constant strain tensor will be appropriate for the direct evaluation of the elastic constants. This can be achieved by imposing a strain tensor with only one changeable component such that only one term will vary with the corresponding strain on the right hand side of these equations. For example, by leaving ε_{11} to be the only variable strain component while hold the others constant, one can evaluate C_{11} as $C_{11} = \left(\frac{\partial \sigma_{11}}{\partial \varepsilon_{11}}\right)_{\varepsilon'}$ and C_{12} as $C_{12} = \left(\frac{\partial \sigma_{22}}{\partial \varepsilon_{11}}\right)_{\varepsilon'}$ from Eqs.(3.31) and (3.32). This type of stress-strain experiments, or the (ThN) simulations, are being used to calculate the two elastic constants of C_{11} and C_{12} of the f.c.c. crystal at various temperatures.

Chapter 4

Thermoelastic Behavior and Mechanical Melting of F.c.c. Crystal

Intrinsic instability of crystals is closely related to elastic deformation. The effects of homogeneous deformations can be induced either by the change of temperature in the case of thermal expansion, or by the external applied stresses or strain load in the case of hydrostatic tension or compression. This chapter will donate to the pure temperature effect on the thermoelastic behavior of the model systems with different potentials under thermal expansion. Our attention will be focused on the mechanical melting.

The ultimate process of thermal disordering in the solid manifests itself in melting. It has been clearly demonstrated [Wolf 90b]that one can classifies two kinds of melting: Thermodynamic melting and mechanical melting. Thermodynamic melting [Lutsko 89b] basically is determined by the free energies of both the crystalline and liquid states. In this case, the solids melt through the nucleation and growth mechanism of liquid phase at extended defects, such as interface, voids, or dislocations; and thus is a slow, heterogeneous process. In contrast, the mechanical melting is triggered by an elastic instability causing the sudden collapse of the entire crystalline lattice, and is therefore a fast, homogeneous process. The mechanical melting temperature T_s gives the highest temperature that one can superheating a solid.

Although the mechanism of the thermodynamic melting is quite clear, the underlying cause of the mechanical melting is still not well understood. In literature several theoretical models have been proposed to probe the mechanism of the mechanic melting (note although these models were originated from attempts to consider the melting in general, since they regarded melting as a homogeneous phenomenon and did not take into account the effect of the extended defects, they are actually relevant to the mechanical melting). In these theories melting is treated as a lattice instability associated with the vanishing of the shear modulus (Born's criterion) [Born 39, 56, Wolf 90b], with the atomic displacement exceeding a threshold value (Lindemann's criterion), or with the spontaneous generation of a critical concentration of vacancies. [Ubbelohde 78] The theories all pointed out some aspects of the mechanical melting, while there must be some unified model which can explain this phenomenon in relevance to the existing theories. In section 3 of this chapter we will analyze our simulation results of the mechanical melting based on the elastic instability we have developed in Chapter 2.

4.1 Thermal Expansion

The thermal expansion data at zero pressure is very important for the study of elastic behavior of the system at finite temperature. It carries information that characterizes the reference state, i.e., the state with respect to which we measure the strain for each temperature. For cubic crystal the thermal expansion coefficient β_T is defined as

$$\beta_T = \frac{1}{V}\left(\frac{\partial V}{\partial T}\right)_P \qquad (4.1)$$
$$= 3\,\alpha_T$$

for isotropic materials. Where α_T is the linear thermal expansion coefficient. In general, β is a tensor [Wallace 72] that relates the thermal strain tensor to temperature increment ΔT. The symmetric thermal strain tensor is defined as

$$\beta_{ij} = \left(\frac{\partial \eta_{ij}}{\partial T}\right)_\sigma . \qquad (4.2)$$

Considering a reference state **X** and a strained state **x**, the thermal expansion coefficient

$$\beta_T = \frac{1}{V(X)}\left(\frac{\partial V(x)}{\partial T}\right)_\sigma$$
$$= \left[\frac{\partial}{\partial T}\left(\frac{V(x)}{V(X)}\right)\right]_\sigma$$

since

$$\frac{V(x)}{V(X)} = 1 + \frac{\Delta V(x)}{V(X)} = 1 + \sum_i \eta_{ii} \qquad (4.3)$$

therefore, in the anisotropic case

$$\beta_T = \sum_i \left(\frac{\partial \eta_{ii}}{\partial T}\right)_\sigma = \sum_i \beta_{ii}. \qquad (4.4)$$

The simulation data of L-J and EAM potentials are generated by a series constant zero pressure simulations of an f.c.c. crystal containing 108 atoms. The relations of the

normalized lattice parameter a/a_0 (where a_0 is the zero-temperature lattice parameter) and temperature for each case are obtained by successively step increment of temperature in simulations. Typical runs of MD and MC include the first 10000 time steps or moves per atom of equilibration and another 30000 time steps or moves per atom for property calculation. Fig. 4.1 (a) shows the internal energy as a function of temperature and Fig. 4.1 (b) the thermal expansion curves of an f.c.c. crystal with L-J. Fig. 4.2 (a) and (b) give the corresponding curves of EAM potential. From these figures one see that although both curves of thermal expansion for these two potentials show the similar, pretty much linear, feature, the magnitudes of them are very different. The EAM potential has much smaller thermal expansion coefficient, and correspondingly, because of its relatively deeper potential well, a large amount of energy is needed for the same expansion.

In each case a second order polynomial is fitted to the data points to get analytic expression of the thermal expansion curve, and the thermal expansion coefficients at various temperatures are calculated from Eq. (4.2). These data will be used as references late in the study of stress-induced structural response for individual temperatures. We got thermal expansion, for L-J potential

$$a/a_0 = 1.0000 + 2.7850\times10^{-5}T + 7.8941\times10^{-9}T^2 \qquad (4.5)$$

and for EAM Au

$$a/a_0 = 1.0001 + 1.0389\times10^{-5}T + 4.4858\times10^{-9}T^2. \qquad (4.6)$$

These two expressions give the room temperature thermal expansion coefficients $\beta_T^{LJ} = 9.6271\times10^{-5}\ K^{-1}$ and $\beta_T^{EAM} = 3.9220\times10^{-5}\ K^{-1}$, which are reasonably in agreement with the experimental values $5.04\times10^{-5}K^{-1}$ and $4.23\times10^{-5}K^{-1}$ for Cu and Au [Dalliace 72, Kirby 63].

4.2 Thermal Softening of Elastic Constants and Moduli*

As is well known, when allowing thermal expansion the elastic constants dramatic softening with increasing temperature. In fact this softening results from a combining effects of temperature induced structural disordering and the volume expansion enhanced anharmonicity [Jaszczak 92]. Experiments have also found

* In this and following chapters our model systems are all treated as classical system, no any quantum mechanical effect is taken into account even at vary low temperatures.

similar results in the metals of Cu [Overton 62] and Au [Neighbours 58]. This feature has very important relevance to the instability of the crystals. Our results also show the same softening behavior in the elastic constants. Since the aim of our investigation concentrates on the intrinsic instability of crystals, we are not only interested in the softness of the individual elastic constant, but rather the elastic moduli which are the combinations of elastic constants.

Fig. 4.3 show the thermal softening of an f.c.c. crystal under thermal expansion with its atoms interacting with L-J potential. It can be seen that the all three elastic constants decrease linearly with the increasing temperature [Fig. 4.3 (a)]. When temperature is increased to T = 1000K, the elastic constants are softened by over 60% compared to their values at T = 0K. The elastic moduli show the similar softening behavior. As can be seen in Fig. 4.3 (b) and (c), in a wide range of temperature the bulk modulus and shear moduli also decrease linearly with temperature. Again, for T =1000K a softening of over 60% in both bulk modulus and shear moduli are observed.

The thermal softening of elastic constants in EAM potential is quite different comparing to that in L-J potential, as is shown in Fig. 4.4. First of all, for same increment of temperature the thermal softening for EAM potential is smaller than in L-J potential. Secondly, in stead of linear decrease in all elastic constants in L-J potential, the elastic constants in EAM model show a quadratic softening behavior. Although in EAM potential all elastic constants show qualitatively the similar softening behavior (quadratic decrease), their softening rate (the slopes) are different.

The similarity in thermal softening behavior between these two potential models is clear by comparison of Fig. 4.3 and 4.4. When one compare Fig. 4.4 (b) and (c) to Fig. 4.3 (b) and (c) one can find that both the bulk modulus and shear moduli of EAM potential system, the same as in L-J potential, can be well fitted to a linear decreasing function of temperature in a wide range of temperature. At still higher temperature, the data points of elastic constants of EAM potential model start to level off and deviate from the fitting curves, indicating a largely increased softening in this temperature region. In our belief this must also be true in the case of L-J potential model (actually this is seen in Chapter 5 when we study the stress induced structural responses of L-J potential model. See, for example, Fig. 5.1). This anomalous softening feature is the key to understand the spinodal transition.

The underlying physics of elastic softening will become clear once one recall the different contributions to the elastic constants. Let us rewrite the fluctuation formula we have developed in Chapter 3 as

$$C_{ij} = \langle B_{ij} \rangle + \langle F_{ij} \rangle + \langle K_{ij} \rangle. \qquad (4.7)$$

There are three contributions which account for the behavior of elastic constants: The so called Born term contribution $\langle B_{ij} \rangle$, which is the leading term and given by Eq. (3.38), comes from the lattice energy (or potential energy). This term is relatively weakly volume and temperature dependent until the system is expanded close to the inflection point of the potential energy, and thus should not change much in a wide range of temperature. The second term is so called fluctuation term which is calculated from $\langle F_{ij} \rangle = \frac{\Omega}{k_B T}\left(\langle \hat{t} \rangle \langle \hat{t} \rangle - \langle \hat{t}\hat{t} \rangle\right)$ and is a direct measure of the stress fluctuation. This term is, except strongly dependent on the temperature and volume, very sensitive to the structural change, for instance the structural disordering or creation of point defects. It always gives a negative contribution to the elastic constants. The third term is the kinetic term $\langle K_{ij} \rangle$ [see Eq. (3.37)] which gives rise to a linear temperature dependence of the elastic constants.

Fig. 4.5 (a) shows, take the EAM potential as an example, the separate contributions of these individual terms to the elastic constants as a function of temperature. As clearly seen, all the Born terms show a weak temperature dependence at $T \leq 1200K$ (linear decrease as T increases). When temperature is greater than 1200K, $\langle B_{11} \rangle$ and $\langle B_{12} \rangle$ show an enhanced softening, while $\langle B_{44} \rangle$ keeps its linear decreasing behavior till the highest temperature (T = 1380K) for which we calculated the elastic constants. The change in fluctuation terms are more interesting. At low temperatures $\langle F_{11} \rangle$ shows a quadratic softening, $\langle F_{12} \rangle$ softens in a similar way as $\langle F_{11} \rangle$ but with a smaller magnitude. The softening of $\langle F_{44} \rangle$ is only a weakly linearly decreasing function of temperature. When the system is heated to high temperatures the magnitudes of the fluctuation terms start to increase more rapidly. This increase is more significant in $\langle F_{11} \rangle$ and $\langle F_{12} \rangle$. When the temperature gets closer and closer to the melting point the increase in the magnitude of $\langle F_{11} \rangle$ and $\langle F_{12} \rangle$ become so dramatic that they can eventually make the elastic constants negative. At critical temperature, or equivalently critical volume, the magnitude of fluctuation terms $\langle F_{11} \rangle$ and $\langle F_{12} \rangle$ can be as large as, or even several times larger than the corresponding Born terms $\langle B_{11} \rangle$ and $\langle B_{12} \rangle$. [see Fig. 4.5 (c)]

In order to calculate the internal stress correctly, we have checked the correlation of the instantaneous stress tensor by calculating the autocorrelation function of the stress. We found a correlation time of 100 time steps for both L-J potential and EAM potential at T = 500K. For 20 time steps the autocorrelation function gives the value about 0.1. In our present stress calculation, to keep the computation efficiency, we take the configurations after every 20 time steps to calculate the stress and correct the possible correlations in

estimation of the error bars. The increase in the magnitude of fluctuation terms thus may imply increasing correlations of the stresses. At very temperature close to the melting point, a stress distribution may have been established. From this point of view, the large fluctuations in normal stresses indicate that, at high temperatures, some large normal stress-gradient regions may be spontaneously formed in the system. These large normal stress-gradient regions may be highly localized since the still large fluctuation in $\langle F_{12} \rangle$ suggests that the large stress gradient of one component of the normal stress will affect the other components in lateral directions through the Poisson's effect. At very high temperatures these stress-condensed regions may destablize the lattice and allow the nucleation of new phases. On the other hand, the smaller fluctuations in shear stresses suggest that the shear stresses are more uniform throughout the lattice.

These arguments based on the stress fluctuations can be seen more promisingly in the combinations of the elastic constants, i.e., the elastic moduli, in Fig. 4.5 (b). There the contributions of stress fluctuations are more significant in the bulk modulus but largely weakened in the shear modulus. These effects result from the fact that since the bulk modulus is calculated using the formula of $B_T = (C_{11} + 2C_{12})/3$, thus the effect of the stress fluctuations is largely enhanced. However, in the case of shear modulus, $G(110)[1\bar{1}0]$ is calculated from the relation $(C_{11} - C_{12})/2$, the stress-fluctuation contributions in C_{11} and C_{12} actually cancel each other, at least partially, and give rise to a overall weak effect of the fluctuation on shear modulus. These features caused by the stress fluctuations imply that the transitions triggered by spinodal instability must be characterized by the catastrophic changes in the system properties and therefore are discontinuous transition (first order).

Fig. 4.5 (c) shows the time evolution of the Born term and fluctuation term of EAM potential at the mechanical melting temperature $T_s = 1380K$. Within the first 500 time steps the magnitude of the fluctuation terms $\langle F_{11} \rangle$ and $\langle F_{12} \rangle$ become so large that make the elastic constants C_{11}, C_{12}, and the bulk modulus negative. These large fluctuations in normal stresses bring about the spinodal instability. This process is finished within a short time period.

In summary of our observations of thermal softening in both L-J potential and EAM potential models, we have noted two significant features:

(1) In a wide range of temperature all elastic moduli we calculated show a linear dependence of temperature. From our calculations one can see that below the melting temperature, the Born term is dominant and several times larger in magnitude than that of the fluctuation term. Since Born term shows a linear temperature dependent behavior, bulk modulus also show the similar temperature dependence. For shear moduli, although the Born term contributions is reduced by subtraction, the fluctuation terms also cancel each

each other and do not change the linear temperature dependent behavior of shear moduli. These behaviors are in agreement with the thermalelastic theory of elastic modulus developed by various authors [Murnaghan 44, Grover 73, Swenson 68, Tallon 79a, 79b, 80].

(2) When the systems are heated to the temperature near to the mechanical melting point T_s, an anomalous normal-stress fluctuation is observed. This stress fluctuation results in a drastic softening in bulk modulus but does not show much significant effect on the shear moduli. This feature is very important in understanding the mechanism of the mechanical melting which we will discuss in next section.

4.3 Mechanical Melting of An F.c.c. Crystal

It is well known that when a crystal is heated to high temperature it will melt into a state in which the crystal completely loses its long-range crystalline order. One can distinguish two kinds of melting transitions: the thermodynamic melting and mechanical melting. These two transitions refer to the same physical process, but are governed by completely different mechanisms. Although the mechanism of thermodynamic melting has been clearly evidenced [Wolf 90b] as a heterogeneous nucleation and growth of the liquid phase at extended lattice defects, the underlying cause of the mechanical melting is still not well understood.

In terms of impact on mechanical properties, it is clear that melting is probably the most significant of all phase changes which show the total loss of shear resistance. Based on this fact, Born, in his early work [Born 39], defined melting as the complete loss of shear resistance of the crystal, i.e., $G(100)[010] = C_{44} = 0$. He interpreted the vanishing of bulk modulus as a criterion for sublimation because the lattice has no cohesion at all. In the same work he suggested that when $C_{11} = C_{12}$ is satisfied (this criterion, later on, is named as Born criterion), the solid will transform into a state in which the stress is hydrostatic pressure (as in a liquid) but nevertheless an elastic resistance against shearing survives. He called this state a "gel". In later work on melting [Wolf 90b, Phillpot 90], Born criterion was also used to define the mechanical melting simply because of the relation of Born criterion to the shear modulus $G(110)[1\bar{1}0] = (C_{11} - C_{12})/2$.

As discussed in Chapter 1 and at the beginning of this chapter, although several theoretical models have been proposed in attempt to interpret mechanical melting, the underlying cause of this transition is still very much under debate. In this section we will show that the mechanical melting is a discontinuous, first-order process, and can be

It is well known that the experimental difficulties in observing superheating due to the inevitable presence of free surfaces and, in most materials, a sufficient atomic concentration of lattice dislocations [Daeges 86]. In computer simulations, in contrast, extrinsic defects can be eliminated simply by using a perfect-crystal simulation cell with periodic border conditions in all three dimensions. Thermodynamic melting can thus be suppressed, allowing an investigation of how melting can occurs in a homogeneous system.

We have carried out simulation studies of the mechanical melting on f.c.c. crystals with their atoms interacting through L-J potential and EAM potential under zero pressure. Fig. 4.6 show the results of L-J potential. When the system was heated through a step-up increment of temperature, the internal energy of the system increases gradually [Fig. 4.6 (a)]. This response continues until a high temperature T = 1365K, at which a sudden jump of internal energy occurs. Correspondingly, a very rapid volume expansion is observed which is clearly seen in Fig. 4.6 (b), the variation of lattice parameter a as a function of temperature. Since the system is under constant pressure (P = 0), these sudden jump behaviors indicate that a latent heat and a latent volume are involved in this transition. Consequently, the mean-squared displacement of the system shows a rapid jump and persistent increase, indicating the system has melting into a state of liquid. As clearly evidenced by the static structure factor shown in Fig. 4.6 (d) the system has completely lost its crystalline order due to this transition. The changes in S(**k**) also show clearly the rapid and homogeneous feature of this transition.

Fig. 4.7 shows the simulation results of mechanical melting with EAM potential interaction between the atoms. In stead of making runs on a (TΣN) ensemble in the case of L-J potential, we simulated a (ThN) ensemble. In each run for certain temperature, the volume of the system was fixed at the value given by the thermal expansion curve [Fig. 4.2 (b)], which, if no any phase changes, should give zero average pressure. As can be seen in the figures, all the system properties show the same characteristics of sudden jumps that one has seen in the case of L-J potential. Note that in Fig. 4.7 (b), instead of plotting the changes of lattice parameter with temperature, we plot the pressure changes as a function of temperature.

In above simulations a constraint of cubic symmetry conservation is imposed. This constraint prevents the Born instability. To investigate if the mechanical melting can be induced by Born instability, we carried out constant pressure (P = 0) and temperature MD simulations of a large f.c.c. lattice of 1372 Au atoms interacting through the EAM potential. Fig. 4.8 (a) shows the internal energy as a function of temperature. When the system is heated up the internal energy increases gradually until the mechanical melting point, at

which a sudden jump occurs. Comparing to the previous case of constant strain simulation [cf. Fig. 4.7 (a)] the magnitude of the internal energy in present case is smaller. This is understandable since in present simulation both the internal stress and strain can fluctuate, thus more strain energy is stored in the system. Fig. 4.8 (b) show the variation of lattice parameters with the temperature. At low temperatures the thermal expansion of in both simulations [cf. Fig. 4.7 (c)] are similar. But at the melting point the behavior of the lattice parameters are quite different. Although a overall volume expansion is observed in both cases, the lattice parameters in the constant strain simulation are all increased, by contrast, an tetragonal distortion of the simulation cell in the constant pressure simulation, signaled the occurrence of Born instability, leads to a bifurcation of lattice parameters. The persistent increase in mean-squared displacement [see Fig. 4.8 (c)] and the sudden drop of structure factor S(k) to zero [Fig. 4.8 (d)] clearly show that the system has been in a liquid phase.

In summary of our simulation results, several features of the mechanical melting are interesting: First of all, the requirement of the latent heat (or the latent volume) for this transition shows that the mechanical melting is a first-order phase transformation. Secondly, both spinodal and Born instability can trigger mechanical melting depending on what geometric constraint is imposed. If there is no any constraint the Born instability will win the competition, as one may expect. Finally, the volume is obviously not conserved in the mechanical melting transition. According to the theoretical analysis in Chapter 2, the eigenmode of the Born instability conserve the volume, is any contradiction between the theory and simulation results? The answer is "No." Fig. 4.9 (a) and (b) show the time evolution of the lattice parameters, system volume, and S(k)'s of the melting run. The bifurcation starts after 2500 time steps and a second symmetry breaking occurs at 6000 time steps. During this period the system volume is conserved and the system is still in crystalline order. The volume expansion occurs after the second symmetry breaking that completely destroys the crystalline order.

All these evidences lead us to conclude that the mechanical melting is a discontinuous, first-order process. It happens through the sudden collapse of the entire crystalline lattice, and is therefore a fast, homogeneous process. This transition can be induced by either spinodal instability or Born instability. Although the transition takes the transformed lattice to the same final state, the driving forces of this transition are quite different. In the case caused by the spinodal instability, the triggering force of the transition is the large normal stress fluctuation, while in the case caused by the Born instability, the complete loss of crystalline order is the consequence of the symmetry breaking and a shear distortion.

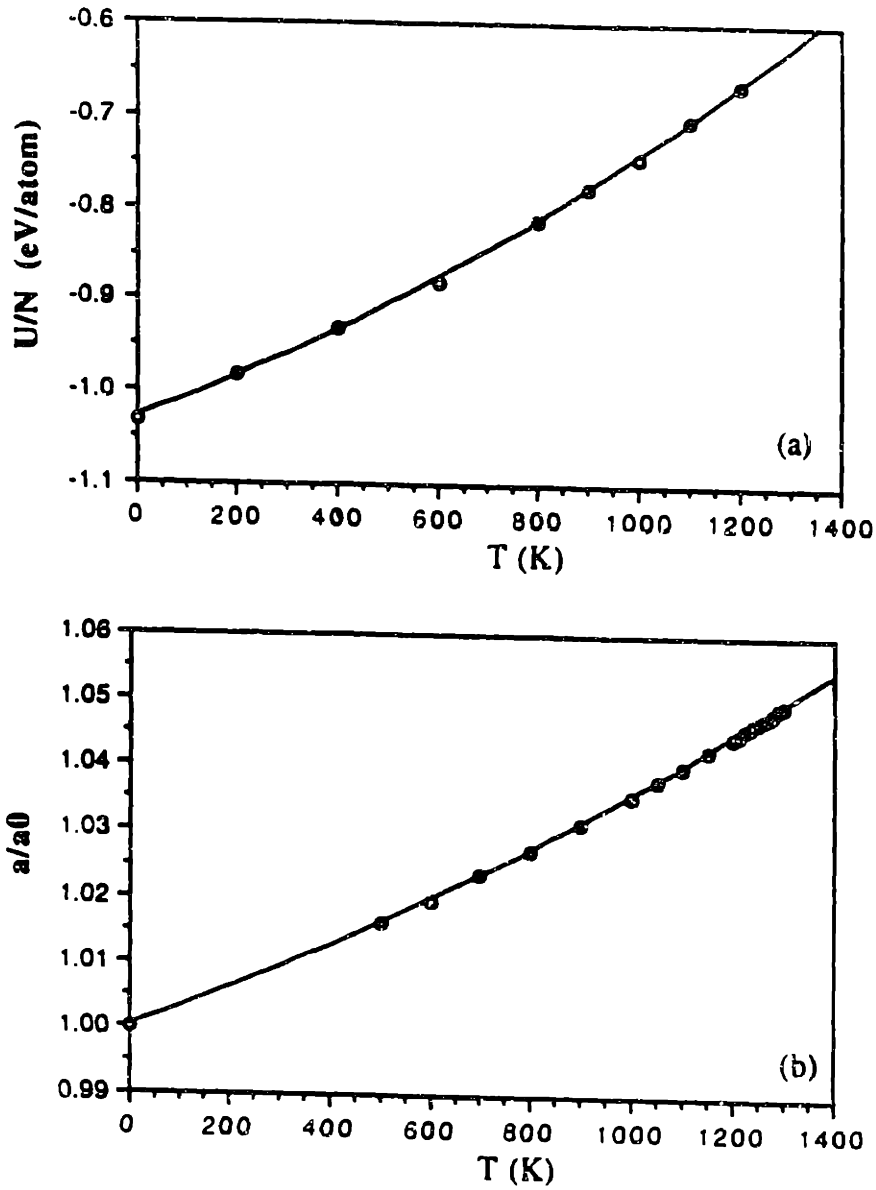

Fig. 4.1 Thermal expansion of an f.c.c. lattice with L-J potential. Thermal expansions, shown by the changes in the internal energy (a), and the average lattice parameter a(T) (b), which is normalized by the zero temperature value of a0.

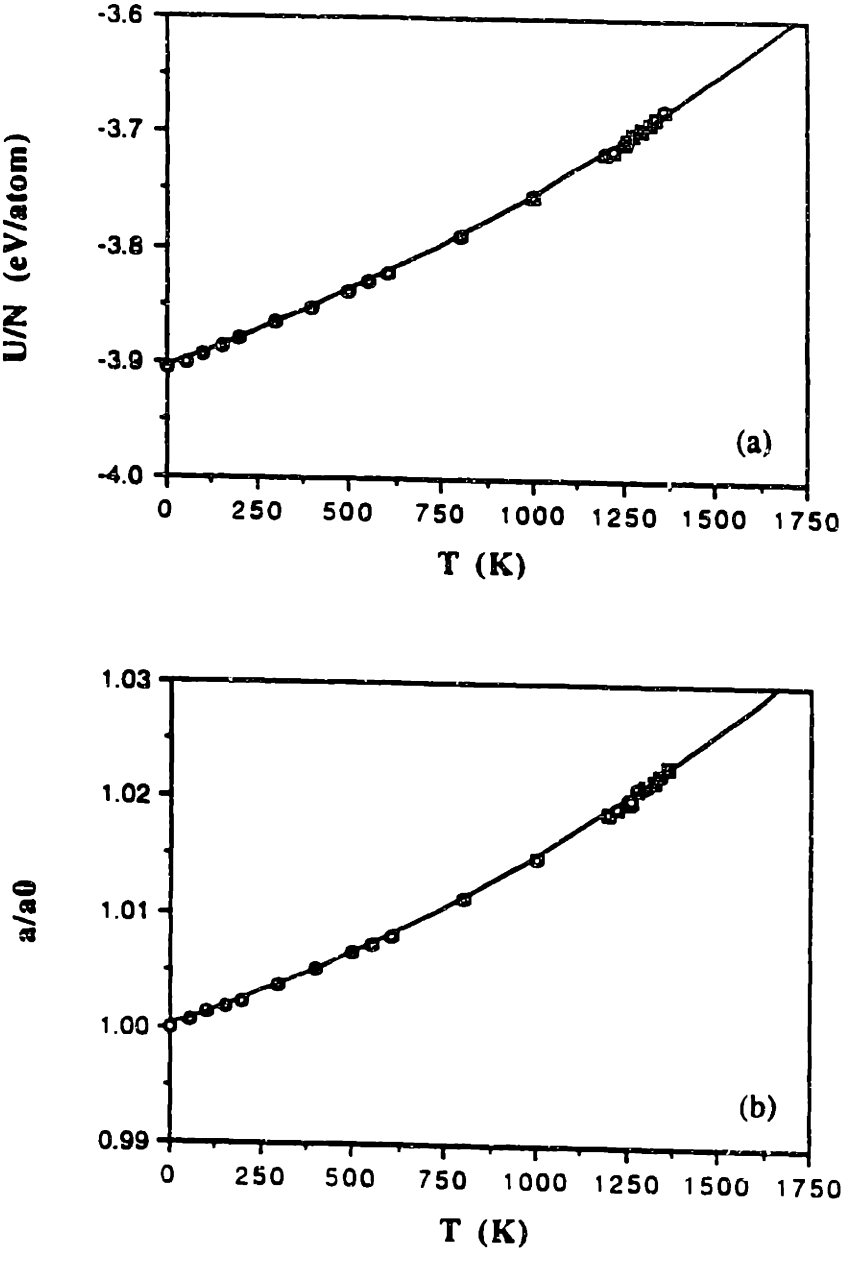

Fig. 4.2 Thermal expansion of an f.c.c. lattice with EAM potential. The same as Fig. 4.1 except now the quantities are calculated for EAM potential.

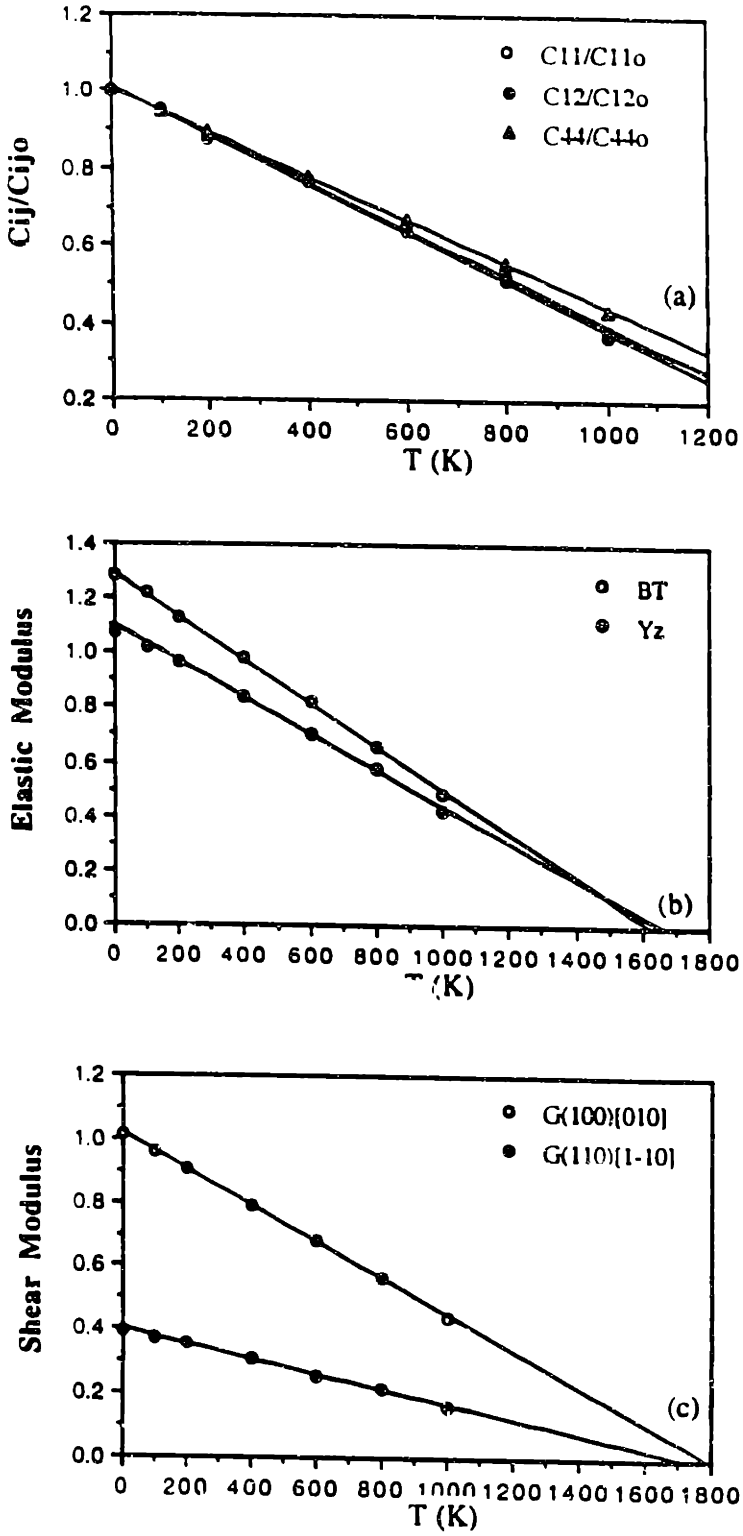

Fig. 4.3 Thermal softening of elastic properties of L-J potential.
(a) Isothermal elastic constants of a perfect f.c.c. crystal as a function of temperature under zero applied stress. Their values, for explicity, are normalized to the zero-temperature elastic constants. (b) Variations of bulk and Young's modulus with temperature. It is seen that in a wide range of temperature they can be well fitted to a linear function of temperature. (c) Changes of shear moduli with temperature. Similar to bulk modulus they decrease linearly with temperature up to the region near to melting.

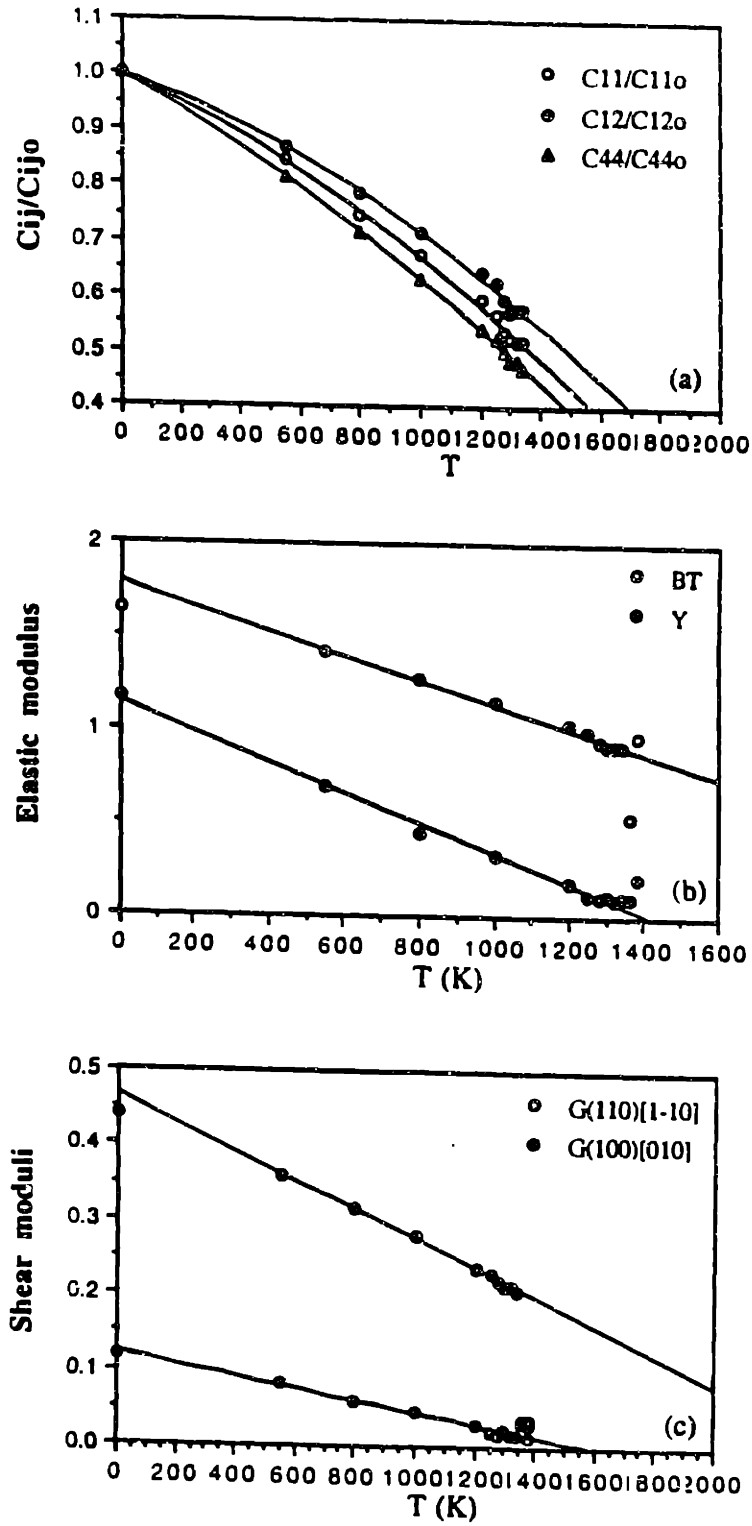

Fig. 4.4 Thermal softening of elastic properties of EAM potential. The same as Fig. 4.3 except for the EAM potential.

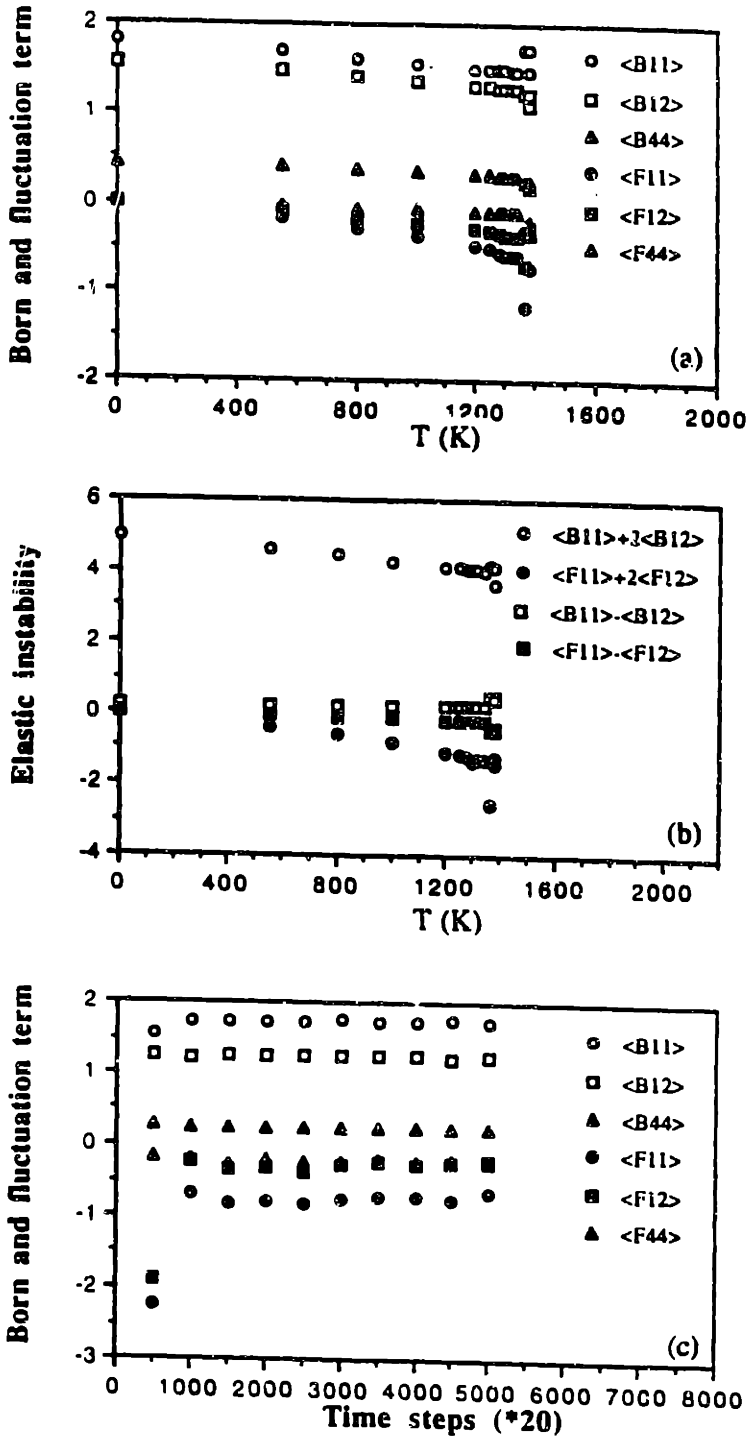

Fig. 4.5 Thermal softening of elastic properties.
(a) Born and fluctuation term contributions to elastic constants, (b) Born and fluctuation contributions to spinodal and Born instability criteria, and (c) Time evolutions of the Born and fluctuation terms at T = 1380K.

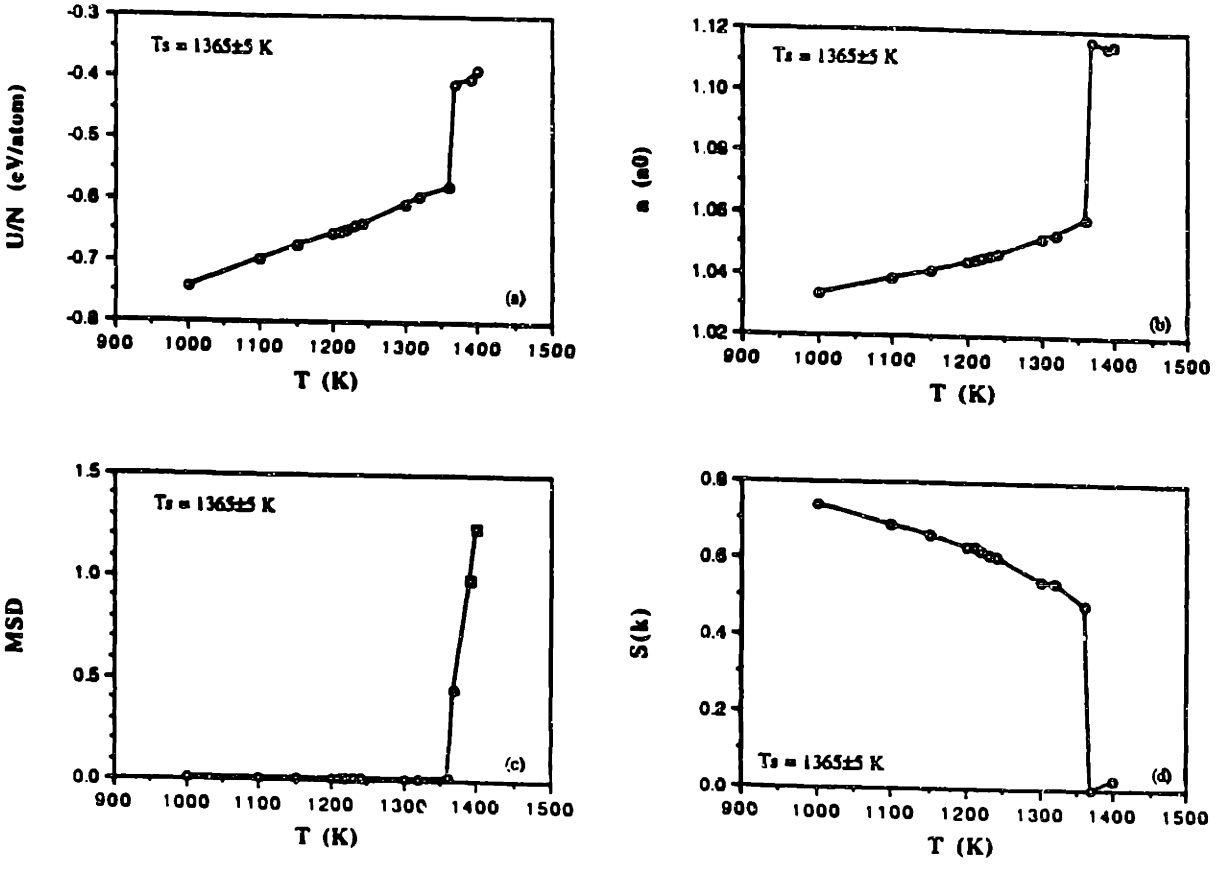

Fig. 4.6 Mechanical melting of an fcc crystal with L-J potential. Shown in this figure are variations of the internal energy (a), lattice parameter (b), mean-squared displacement (c), and static structure factors (d), with temperature. The sudden changes in these quantities point to the onset of mechanical melting. The anomalous increases in internal energy and lattice parameter indicate that latent heat and volume are required in this transition in order to keep the system on the isobar. This transition is therefore a first-order phase transformation.

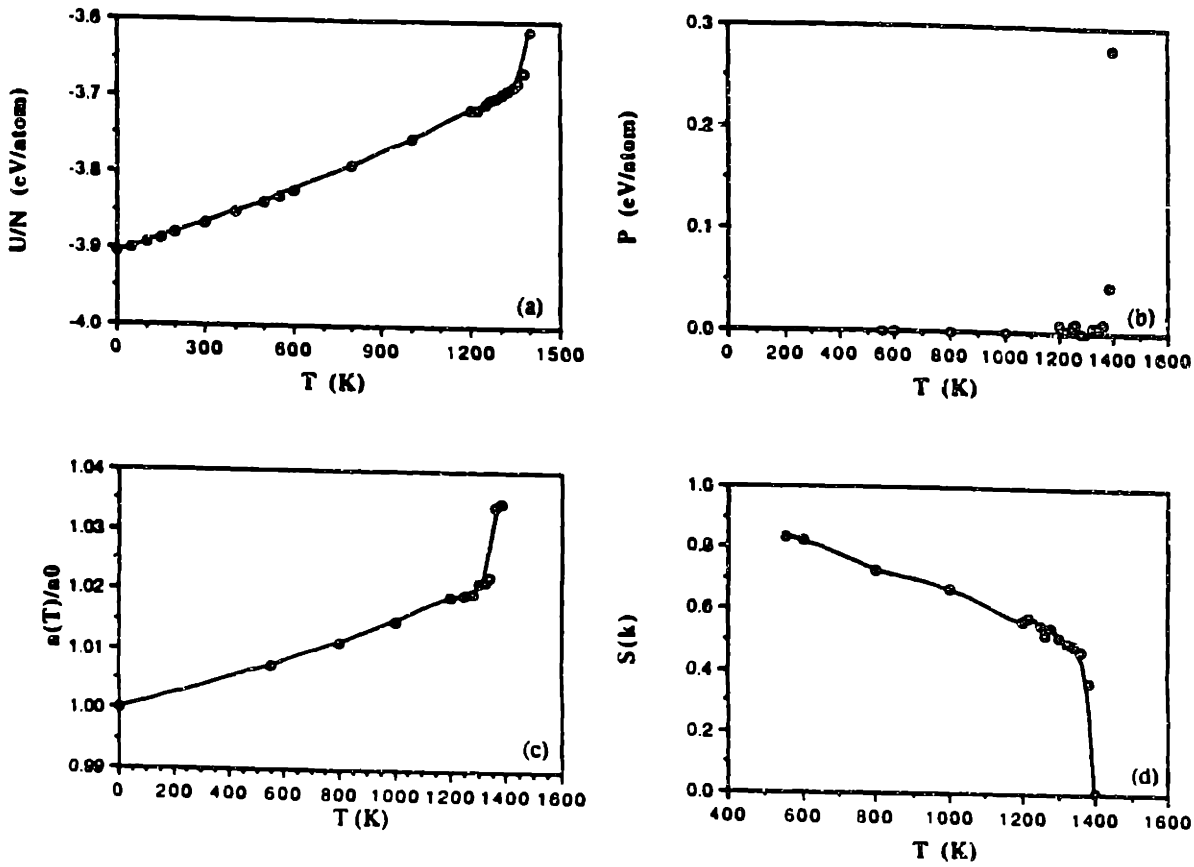

Fig. 4.7 Mechanical melting of an f.c.c. crystal with EAM potential. Shown in this figure are variations of the internal energy (a), pressure (b), lattice paramter (c), and strucutre factors (d) with temperature. These figures show the same qualitative features of the transition as in the case of L-J potential. This suggests that the instability criterion is general for different materials.

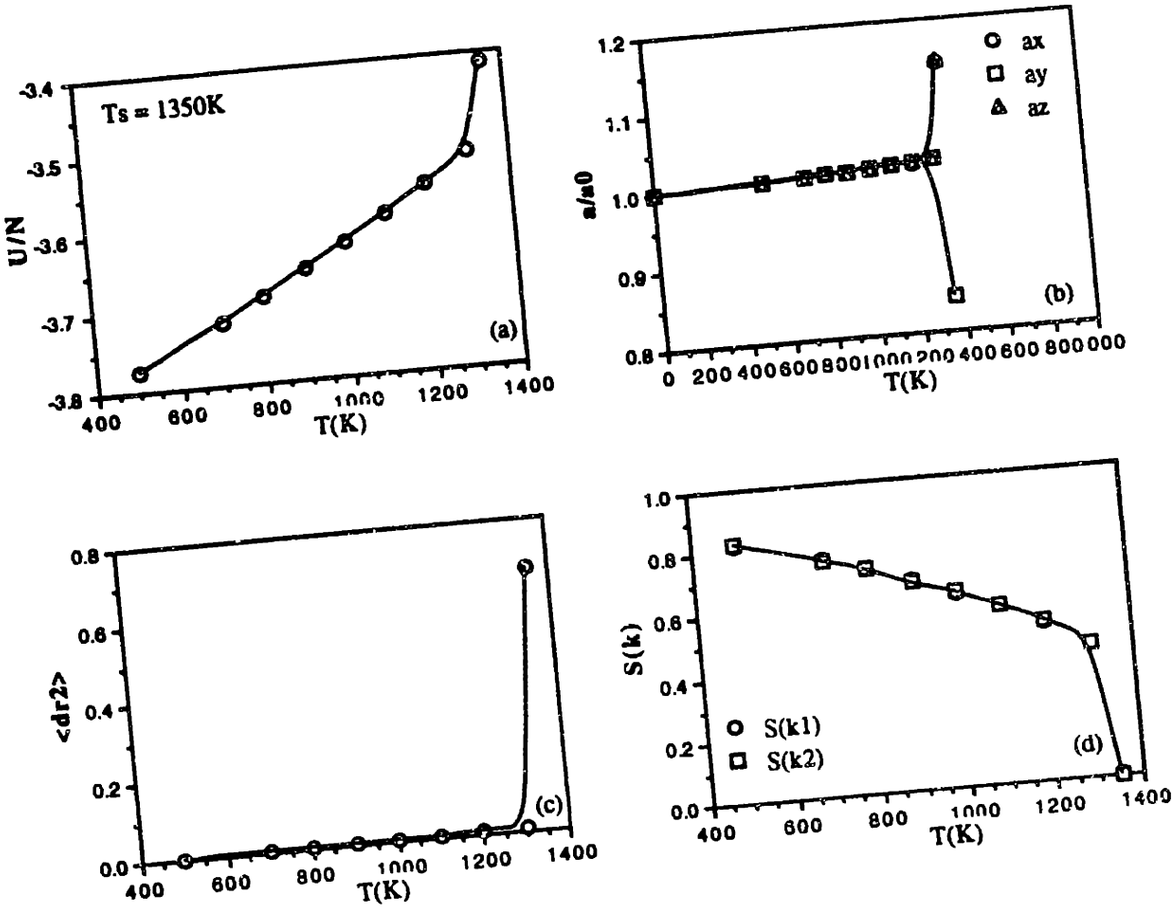

Fig. 4.8 Mechanical melting of an f.c.c. lattice induced by Born instability. Shown in this figure are the internal energy (a), lattice parameters (b), mean-squared displacement (c), and structure factors (d) as a function of temperature. These figures show that the mechanical melting can also be induced by the Born instability but with different mechanism of symmetry breaking and further shear distortion.

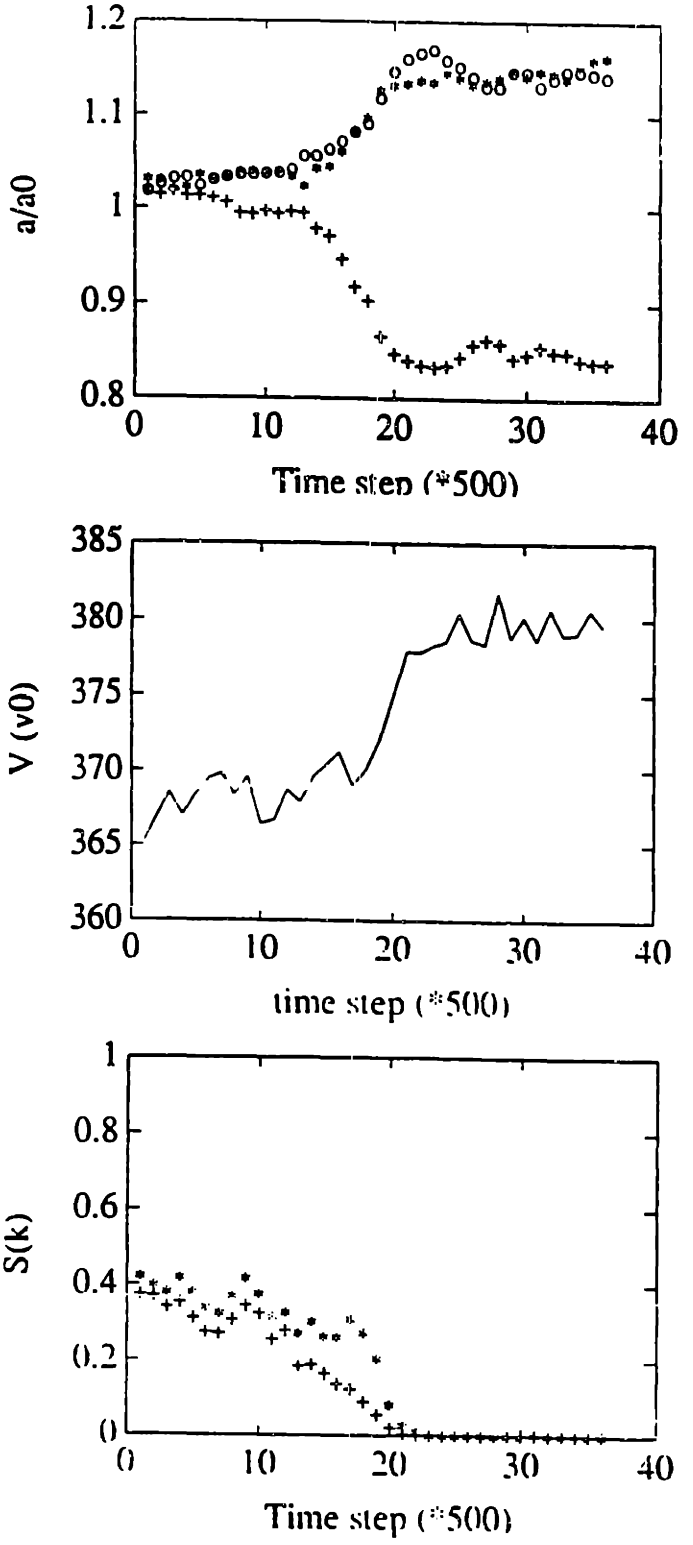

Fig. 4.9 Time evolutions of system properties during the mechanical melting transition.
(a) lattice parameters, (b) system volume, and (c) the structure factors as a function of simualtion time step. The Born instability, signaled by the first split of lattice parameter, triggers a further shear distortion which eventually brings the system to a complete disordered structure.

Chapter 5
Unstable Structural Response to Spinodal Instability of An F.c.c. Lattice with L-J Potential

In this Chapter we will study the unstable structural responses of an f.c.c. crystal to pure dilatation imposed at constant temperatures by Monte Carlo simulation. The purpose of the study is to test the prediction of lattice instability based on elastic-constant criterion and to investigate the nature of spinodal transitions at finite temperatures by direct observation from simulations. Using the Lennard-Jones potential to model the interatomic interaction of Cu atoms, we find that the critical strain at which structural change occurs is well predicted by the spinodal instability. At low temperatures (T = 242.3K and 581.4K), anisotropic lattice decohesion occurs at the critical strain and overall the system remains crystalline (T = 242.3K), and cavitation-like local deformation occurs with indications of anisotropic disordering (T = 581.4K). At higher temperatures (T = 969.1K, and 1550.5K) the lattice disorders uniformly with all the characteristics of melting. For reference the thermodynamic melting temperature of this L-J f.c.c. lattice is about 1200K.

5.1 Elastic Properties and Critical Strains

The simulation system is a cubic cell of N particles arranged on an f.c.c. lattice. The particles interact with each other through the L-J potential which is truncated at a distance r_c and shifted to zero at the cutoff. The cell is periodic in all three directions. In each simulation run at a certain temperature, the lattice parameter a is held fixed while the particles are allowed to move by Monte Carlo [Metropolis 53]. The process is then repeated at an incrementally larger a. Typically the first 10,000 moves per particle are discarded as equilibration, and another 30,000 moves per particle are made to accumulate the configurations for property calculations.

Simulation of strain-induced response has been carried out at the temperatures T = 242.3K, 581.4K, 969.1K, and 1550.5K. Most of the runs were made with a cell of 500 particles, but runs using N = 108 and 864 were also performed to give some indications of system size effects. In all the runs the value of r_c is taken to be $1.4900a_0$, the distance between the 4th and the 5th nearest neighbors. a_0 is the lattice parameter at T = 0K.

The isothermal elastic constants of the cubic lattice were determined using the fluctuation formula. (For details see Chapter 3) Fig. 5.1 shows the elastic constants C_{11} and C_{12} at T = 0K, and Fig. 5.2 is the elastic constants C_{11}, C_{12}, and C_{44} at finite

temperatures T = 242.3K (a), 581.4K (b), 969.1K (c), and 1550.5K (d). All the elastic constants have the unit of 10^{12} dyn/cm^2. One may notice that at T = 0K, and low temperatures T = 242.3K and 581.4K, the Cauchy relation $C_{12} = C_{44}$ holds. But at high temperatures the obvious deviation of this relation is seen. This indicates that the thermal fluctuation is coming into play and has a large effect on the elastic behavior of the crystal.

Isothermal bulk modulus B_T and shear moduli, $G(110)[010]$ and $G(110)[1\bar{1}0]$, were also calculated using the relations $B_T = (C_{11} + 2C_{12})/3$, $G(100)[010] = C_{44}$, and $G(110)[1\bar{1}0] = (C_{11} - C_{12})/2$, respectively. (For these formulae see Chapter 2) Fig. 5.3 and 5.4 show the results. Following the crystal instability criteria of the vanishing of the bulk modulus for spinodal instability and shear modulus $G(110)[1\bar{1}0]$ for Born instability, we computed the critical strains from above results. The values of the critical strains are given in Table 5.1.

It can be seen in Fig. 5.2, 5.3, and 5.4 that when the imposed strain increases all the elastic constants and moduli decrease. For each temperature the variations of the elastic constants and moduli with imposed strain follow well-fitted curves until some value of imposed strain, at which the data points start to run away from the curves. This indicates the onset of the instability. Since our predication of the critical strains are based on the fitting curves, one can expect a difference between the predicated and observed values of the critical strains.

Since we are interested in the unstable structural responses of the system under pure dilatation in the region near the critical strain where the thermal and stress fluctuation may become anomalously large, we must make sure that our results are not affected by the size of the model system. In order to check the model size effect on the elastic behavior and understand the difference in critical strains between the prediction and observation, we simulated three models containing 108, 500, and 864 atoms at temperature T = 581.4K, respectively. We calculated all the elastic constants along the entire pure dilatation path (primary deformation path), before, during, and after the transition. Although during and after the transition the elastic constants may not have the exact physical meaning as they are defined (since during and after the transition the system is not homogeneous any more), they are useful to give some indications of system size effects and fluctuation effects.

Fig. 5.5 shows the three elastic constants with the imposed strain for the three systems of different sizes. It can be seen that all three elastic constants have decreased to quite small values in the region of the critical strain. The elastic constants behave normally while they are still positive, but once the system has reached the critical strain of the spinodal instability, subsequent behavior of the elastic constants at still larger strain shows unphysical oscillations. We have known that in the fluctuation formula [Eq. (3.36)] the

second term in the braces represents the effects of stress tensor fluctuations. In the critical-strain region it is large and fluctuates strongly, thus giving rise to appreciable uncertainties in the calculated elastic constants. As a result we can only say that as C_{11} approaches C_{12}, both appear to be approaching zero. At the same time, the data suggest that C_{44} also approaches zero at the critical strain. Within the estimated statistical error the mechanical stability limit seems to be consistent with ε_c.

The size effect is seen in both elastic constants and elastic moduli Fig. 5.6 shows the variation of elastic moduli, B_T and $G(110)[1\bar{1}0]$, with imposed strain. A small system shows a delayed behavior in response to the uniform expansion. This can be understood since the elastic behavior of the system is closely related to the long wave length of the elastic waves, for the small system the periodic border condition constrains the lattice vibration of the system in the regime of the short wavelength modes. This limitation stabilizes the system until even larger deformation. For the large system of N = 500 and 864, the elastic constants and moduli show the anomalous behavior at almost the same critical strain. The similarity of system behavior is also seen late in the structural responses of the system (see sec. 5.2). Thus the 500 atom system is a reasonable system which can give reliable results. We will use 500 atom system in our simulation study in this Chapter except where it is noticed.

5.2 Cavitation and Cleavage Fracture at Low Temperatures

Fig. 5.7 (a) shows the variation at T = 242.3K and 581.4k of the normal stresses, calculated using the virial expression [Eq.(3.22)], as the imposed strain is increased incrementally. Starting at a value of the imposed strain which gives zero normal stress, the system is seen to go into positive stresses (or negative pressure) as isotropic strain is increased. The normal stresses increase monotonically and appear to level off at a maximum value. With further lattice dilatation the stresses first decrease somewhat and then drop abruptly to a considerably reduced though still finite value.

Fig. 5.7 (b) shows the potential energies of the system in response to isotropic imposed strain. As the lattice goes into negative pressure, more and more strain energy is stored in the system. This continues until the normal stresses change suddenly [cf. Fig. 5.7 (a)], at which point the potential energies drop correspondingly.

As has been seen in Fig. 5.7, at certain value of imposed strain the system undergoes large and swift changes in normal stress and potential energy which cannot possibly be described as elastic deformations. The critical strain is well defined by sudden change in normal stress or potential energy. The observed critical strain for T = 242.3K is

$\varepsilon_c^o = 0.0867$, and $\varepsilon_c^o = 0.0746$ for T = 581.4K, where the superscript o of ε is referred to observation value of the critical strain.

The existence of a critical value of imposed strain, as indicated in Figs. 5.7 (a) and (b), suggests the onset of a structural transition which we will investigate in the following by examining directly the atomic configurations produced at each incremental strain. As for the nature of the transition, one can ask what is the connection between the behavior observed in Fig. 5.7 and the instabilities which we have derived for a uniform lattice in Chapter 2. We have known that along the primary deformation path pure dilatation will lead to the spinodal instability, at which the isothermal bulk modulus vanishes. The normal stress-strain relation (or equivalently the pressure-volume relation in present case of uniform expansion) shows this feature very clearly. The sudden drop of the stress shows that the transition associated with spinodal instability has the nature of a first order phase transformation.

We have already noted that at both temperatures the normal stress appears to reach a maximum value of σ_m at a lattice parameter which we will denote as a_m and that a_m is distinctly smaller than the critical value at which the normal stress drops suddenly which we will denote by a_c. Since we have results for three system sizes at T = 581.4K, we can perform a 1/N extrapolation on the value of a_c as directly observed in the simulation data. This gives a critical strain of $\varepsilon_c^o = 0.0710$. To determine a_m, we fit for each N the several data points for the normal stress in the vicinity of σ_m to a polynomial, and calculate $d\sigma/da = 0$ from the fit. After a similar 1/N extrapolation we obtain $\varepsilon_m = 0.0648$. The apparent discrepancy between ε_m and ε_c^o is believed not to be significant given the large fluctuations in the system stress in the region of the critical behavior, and the fact that system size effects may not have been fully eliminated in our 1/n-extrapolation based on limited data.

The onset of a sudden change in normal stress and potential energy is an indication that an accompanying structural change must have also occurred. The above consideration of crystalline instability, while useful for determining the critical strain at which the change takes place, tells us nothing about the state into which the system evolves. For this information it is necessary to examine the atomic configurations at various stages of imposed strain.

We will characterize the atomic configurations in terms of the radial distribution function g(r) which provides a measure of local spatial correlation regardless of direction, and the corresponding quantity, the static structure factor S(**k**), with **k** being a wave vector. By computing S(**k**) for a large number of suitably chosen **k**, one can generate a diffraction pattern which provides a measure of direction-dependent structural order in the system.

Fig. 5.8 shows the g(r) and S(**k**) results for the T = 581.4K runs with N = 500 at three values of the imposed strain ε, $\varepsilon = \varepsilon_1 = 0.0746$ specifies the system strain just before the normal stress drop (cf. Fig. 5.7), $\varepsilon = \varepsilon_2 = 0.0854$ is the value after two strain increments, and $\varepsilon = \varepsilon 3 = 0.1015$ is the last dilatation imposed in this series. First we notice that in all three cases the g(r) results are quite similar, in particular a distinct peak can be seen at r ~ 1.7, the characteristic second-neighbor shell of the f.c.c. lattice. However, whereas the diffraction pattern at ε_1 is quite symmetric, an asymmetry along k_x and k_y about the Bragg position $k_x = k_y = 1$ can be noticed at ε_2 and ε_3.

More detailed information on the structural change in going from ε_1 to ε_2 and ε_3 is provided by the density profiles given in Figs. 5.9 - 5.11. One sees that at ε_1 (Fig. 5.9) the atomic planes along each direction of cubic symmetry are well ordered as in a perfect (undeformed) lattice. At ε_2 (Fig. 5.10), after the normal stress drop, symmetry is clearly broken in the y-direction; there appears to be an extra atomic plane along this direction, and the system is no longer uniform along this direction. Another feature that can be seen in Fig. 5.10 is the distinctly nonzero value of the minima in the density profiles which implies significant atomic displacements from the original lattice positions. In going from ε_2 to ε_3 (Fig. 5.11) the density profile along the y-direction shows two extra planes relative to the x- and z-directions. We interpret this as a tendency to change from cubic to tetragonal structure. Also the nonuniform density profiles along the x- and y- directions suggest the nucleation of cavitation, first seen in Fig. 5.10 along the y-direction.

One may ask whether further structural changes will take place if the dilatation were increased further. In the series of simulations at T = 581.4K using the N = 864 system, we have taken the system out to larger values of imposed strain as shown in Fig. 5.12. Up to approximately the same value of $\varepsilon = \varepsilon_3$, the observed behavior is similar to the N = 500 data shown in Figs. 5.8 - 5.11. When the imposed strain is increased to $\varepsilon_4 = 0.1041$ and $\varepsilon_5 = 0.1090$, the density profiles, given in Figs. 5.13 and 5.14, show (i) pronounced cavitation along the direction of broken symmetry (x-direction in this N = 864 series in contrast to y-direction in N = 500 series), and (ii) increasing loss of well-ordered planar structure along the cubic directions of the original lattice.

It is interesting that the structural deformations which are clearly indicated by the density profiles seem not to give rise to any characteristic features in the g(r) and S(**k**) results in Fig. 5.12, aside from an indication of asymmetry in the latter. In fact the well-defined peaks of the g(r)'s in Fig. 5.12 indicate that the system is still in ordered structure. The shift of the position of the diffraction spot suggests that the lattice has been largely distorted. In going from ε_4 to ε_5 the system continues to relax and lose its planar order, at still large strain ε_5 the system is divided into a order region and a cavitation region. The

cavitation void is located at the corner of the cross of the (001) and (010) planes. The disordering around the void (see Fig. 5.14) is responsible for the smearing out of the diffraction spot in Fig. 5.12.

The potential energies drops shown in Fig. 5.7 corresponds to the release of the system strain energy. The amount of released strain energy is converted into the surface energy of the cavitation void. This energy conversion mechanism makes an important distinction between the low temperature spinodal transition and, as will be seen later, the high temperature spinodal transition.

The structural responses at T = 242.3K generally are similar to those just presented at T = 581.4K. The onset of cavitation is quite clearly seen, and at the same time, the system becomes nonuniform by formation of a local region of relatively low density. As the system is further dilated, spinodal decohesion of lattice planes occurs along one of the three high symmetric directions and leads to cleavage fracture. Throughout all the process of dilatation the system maintains well-defined planar order in other two high symmetry directions, and ends up in a state in which the system completely breaks down into two pieces with each a perfect f.c.c. crystal. Two surfaces are created.

The mechanism of the spinodal transition at low temperatures is the nucleation of cavitation, and the underlying cause of this transition is the large stress fluctuation at the critical strain. To see these let us examine the evolution of the density profiles and the stress fluctuation at the onset of the transition. Since the nature of the transition in the case T = 242.3K is the same as that at T = 581.4K, we only analyze the data of T = 242.3K. Fig 5.15 shows evolution of the density profile along the broken-symmetry direction (z-direction in this case) for the observed critical strain of $\varepsilon = 0.0746$. A low density region is being developed during the first 1000 MC sweeps. Then the density is fluctuating until 5000 MC sweeps. The low density region is well localized about the 20th plane. The density profile at 6000, 8000, and 10000 MC sweeps show that a stable cavity is created at the 20th plane within two planes. A question one may ask immediately is that how a uniform expansion can induce an anisotropic structural response. Actually this resulted from the large fluctuation of the normal components of the internal stress. As shown in Fig. 5.16 during the first 1000 MC sweeps the magnitudes of the fluctuation terms are so large (as we have seen in Chapter 4) that the elastic constants and bulk modulus become negative. From Fig. 5.16 one can see that the contribution of the stress fluctuation to C_{11} and C_{12} is significant while not much fluctuation is seen in the shear stress. This situation is similar to the case of pure heating to melting.

5.3 Homogeneous Disordering at High Temperatures

The structural responses at T = 969.1K and 1550.5K, on the other hand, are quite different from that at T = 242.3K and 581.4K. Fig. 5.16 (a) shows the normal stresses drop at the critical strains, but now the corresponding potential energy changes are an increase instead of a decrease as in Fig. 5.7. This shows the form of the energy conversion in the present phase transformation is completely different from that in the low temperature situations. A latent heat is required to accomplish the transition. Even the phase transformation is still first order, that a latent heat is involved indicates a different transition mechanism in the present case. One may notice that for the L-J potential system the temperature T= 1550.5K is above the melting temperature. The similarity of the system behavior at these two temperatures suggests that the transitions at high temperature fall into another category of phase transformation, i.e., the melting transition.

Examination of g(r)'s, S(**k**)'s and density profiles at the strain after the normal stress drops confirms this conclusion. Fig. 5.17 shows the density profiles, g(r), and the diffraction pattern of the system just before the transition ($\varepsilon = 0.0445$) at T = 969.1K. The well-defined planar order in all high symmetry directions and the diffraction spot leave no doubt that the system is still a perfect f.c.c. crystal. After the stress drops the system shows dramatic differences in its properties and dynamic behavior. The overall constant density profiles [see Fig. 5.17 (a), (b), and (c)] indicate that the system has lost its planar order structures, and the ring-like diffraction pattern shows clearly the system has become completely disordered. It is also noteworthy that the mean-squared-displacement function evaluated at the strain before and after the stress drop, given in Fig. 5.19 (a) and (b), shows dramatically different mobility behavior over the same number of Monte Carlo sweeps. The essentially linear variation of the mean-squared-displacement and the increased magnitude of this quantity observed after the drop are strong indications of a liquid-like environment.

5.4 Finite Temperature Spinodal Instability of the L-J Crystal

In this work we have determined by Monte Carlo simulation and elastic constant calculations the spinodal instability of an f.c.c. Lennard-Jones lattice under symmetric isothermal extension along the three directions of initial cubic symmetry. We have shown that at several temperatures the critical strains determined by the spinodal instability criterion involving the elastic constants agree with the direct observations from the MC simulations. It is seen in Fig. 5.20 that at low temperatures the observed critical strains are

quite close to that predicted by bulk modulus. At high temperatures the observed critical strains are smaller than the theoretical values. The reason for this behavior can be traced to the presence of the large thermal fluctuations at high temperature (see discussion in sec. 6.4). The significance of our simulation results is that although the melting at high temperature and the fracture at low temperature have very different final structural states of the transitions, the underlying cause of them is essentially the same.

The behavior of the crystal in the region of critical strain is well predicted by spinodal instability. The values of these critical strains define an instability curve in the temperature-density phase diagram as shown in Fig. 5.21. It has been suggested that the freezing curve which, like the melting curve, is defined only for temperatures above the triple point T_t, is effectively also the mechanical instability curve in the sense of heating a crystal rapidly up to the limit of superheating. [Wolf 90b] It can be seen in Fig. 5.21 that the critical strains observed in the present work delineate the extension of the mechanical instability curve to temperatures below T_t. It has been conjectured that in crossing this instability curve the lattice will become disordered, thus providing a simple thermodynamic connection between melting and solid-state amorphization. [Wolf 90b] (For more detailed discussion about this topic see Chapter 8) What we have found is that in crossing such a curve the lattice does become mechanically unstable as manifested by sudden jumps in the hydrostatic pressure and the potential energy; however, the atomic configuration into which it evolves depends on the temperature. At low temperatures, the spinodal instability is accompanied by symmetry breaking as shown by the density profiles along the three cubic directions. At the same time, the system becomes nonuniform by the formation of a local region of relatively low density. We interpret this crystal response as cavitation which at T = 242.3K (about 0.20 T_t) leads to cleavage fracture upon further lattice dilatation. At T = 581.4K (about 0.48 T_t), in addition to cavitation-like behavior, significant local disordering occurs as the system is strained beyond the instability. At high temperature T = 969.1K (0.81 T_t) the system response at the instability is homogeneous and complete disordering as in a melting transition. At a still higher temperature T =1550.5K (1.29 T_t) the system, of course, melts even under compression.

The different final states of spinodal transition at low and high temperatures suggest that the mechanisms of the transitions are somewhat different. While a homogeneous volume expansion is imposed on the f.c.c. lattice, the crystal responds anisotropically in the form of inhomogeneous nucleation of cavitation in the low temperatures, and at high temperatures, a homogeneous nucleation of disordered phase destroys the crystalline order completely. It is also interesting to check the causes of the transitions at different temperatures. In Table 5.2 we summarize the Born and fluctuation term contributions to

the elastic constants at the onset of the transitions for different temperatures. We note that although the spinodal transitions take different forms depending on the temperature, their underlying cause, i.e., the large fluctuations in the normal components of the stress, is essentially the same.

Along with the critical strain curves of spinodal instability in Fig. 5.20 we also plot the critical strains of Born instability predicted by the vanishing of the shear modulus $G(11)[1\bar{1}0]$. It can be seen that at low temperatures the Born instability curve lies underneath the spinodal curve, as the temperature is increased they cross each other, and at high temperatures the critical strains of Born instability are larger than that of spinodal instability. According to our theoretical analysis pure dilatation will depress the Born instability. This seems to be true in our observation. But since the values of the critical strains of both the Born and spinodal instabilities are close to each other there is some ambiguity. Part of the ambiguity stems from the relatively shallow well-depth of the potential as compared to an EAM-type potential [Daw 84, Wolf 89a] for metals. Thus the Lennard-Jones potential gives considerably lower values for the elastic constants which makes it difficult to distinguish between critical strains of the spinodal and Born instabilities. To study these two instabilities distinguishably we have also performed MD simulations using an EAM potential for f.c.c. metal. The results of the study will be presented in the next Chapter.

Table 5.1 Critical strains of spinodal (ε_c^S) and Born (ε_c^B) instabilities at different temperatures. Values calculated from the conditions: $B_T = 0$, and $G(100)[1\bar{1}0]$.

T (K)	ε_c^S	ε_c^B
0	0.1000	0.0741
242.3	0.0804	0.0726
581.4	0.0724	0.0713
969.1	0.0444	0.0545
1365*	0.0085	0.0179
1550.5	-0.0256	-0.0202

* T_s = 1365K is the mechanical melting temperature of this L-J crystal. (See Chapter 4)

Table 5.2 The Born and fluctuation term contributions to the elastic constants [$\langle C_{ij} \rangle = \langle B_{ij} \rangle + \langle F_{ij} \rangle + \langle K_{ij} \rangle$, see Eq. (4.7)] at the onset of the spinodal instability at different temperatures. The elastic constants are in the unit of 10^{12} dyn/cm^2.

T (K)	ε_c	C_{ij}	$\langle C_{ij} \rangle$	$\langle F_{ij} \rangle$	$\langle B_{ij} \rangle$
232.4	0.0834	C_{11}	-25.4027	-26.3500	0.9430
		C_{22}	-26.0149	-26.9756	0.9564
		C_{33}	-38.3406	-39.2138	0.8689
		C_{12}	-25.8818	-26.2018	0.3199
		C_{13}	-31.4191	-31.8873	0.4685
		C_{23}	-31.5836	-32.0441	0.4605
		C_{44}	-0.2305	-0.5525	0.3199
		C_{55}	-2.0688	-2.5392	0.4685
		C_{66}	-0.3837	-0.8563	0.4605
581.4	0.0746	C_{11}	-1.4443	-2.3585	0.9037
		C_{22}	-0.9836	-1.9982	1.0044
		C_{33}	-1.4008	-2.3986	0.9874
		C_{12}	-0.9700	-1.4600	0.4900
		C_{13}	-1.1600	-1.6538	0.4938
		C_{23}	-1.4503	-1.8016	0.3514
		C_{44}	0.1047	-0.3904	0.4900
		C_{55}	-0.5649	-1.0639	0.4938
		C_{66}	-0.2520	-0.6085	0.3514
696.1	0.0445	C_{11}	-0.1040	-0.8796	0.7578
		C_{22}	-0.0869	-0.8632	0.7584
		C_{33}	-0.0752	-0.8509	0.7578
		C_{12}	-0.1220	-0.5143	0.3911
		C_{13}	-0.1234	-0.5166	0.3932
		C_{23}	-0.1031	-0.4971	0.3940
		C_{44}	0.1118	-0.2894	0.3911
		C_{55}	0.1190	-0.2831	0.3932
		C_{66}	0.1192	-0.2837	0.3940

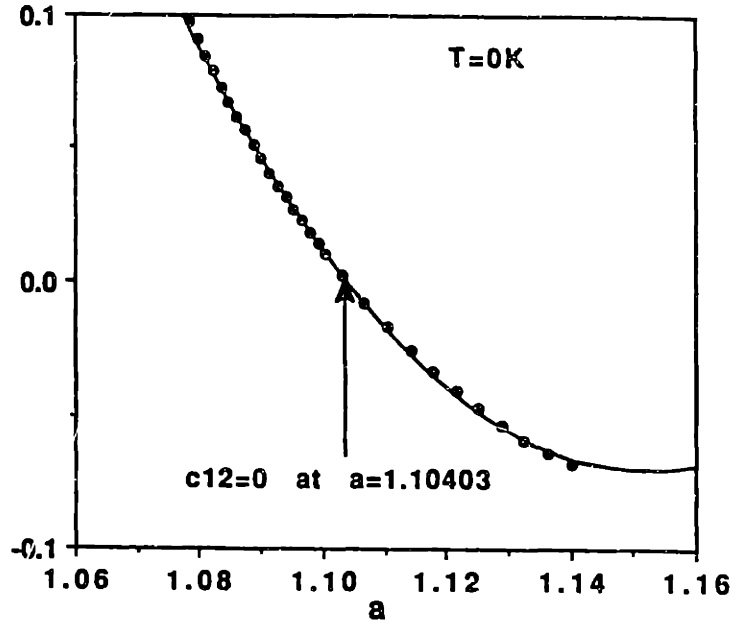

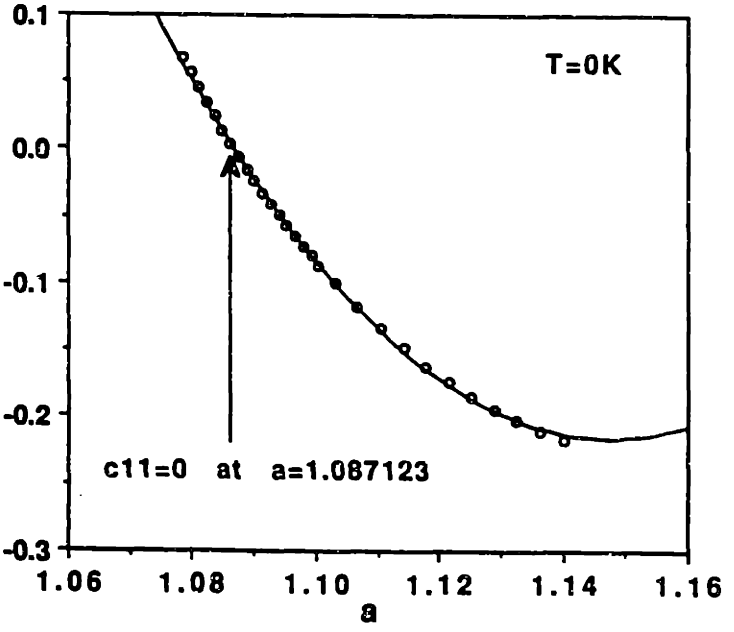

Fig. 5.1 Variations of the elastic constants, C11 and C12, with imposed strain at T = 0K.

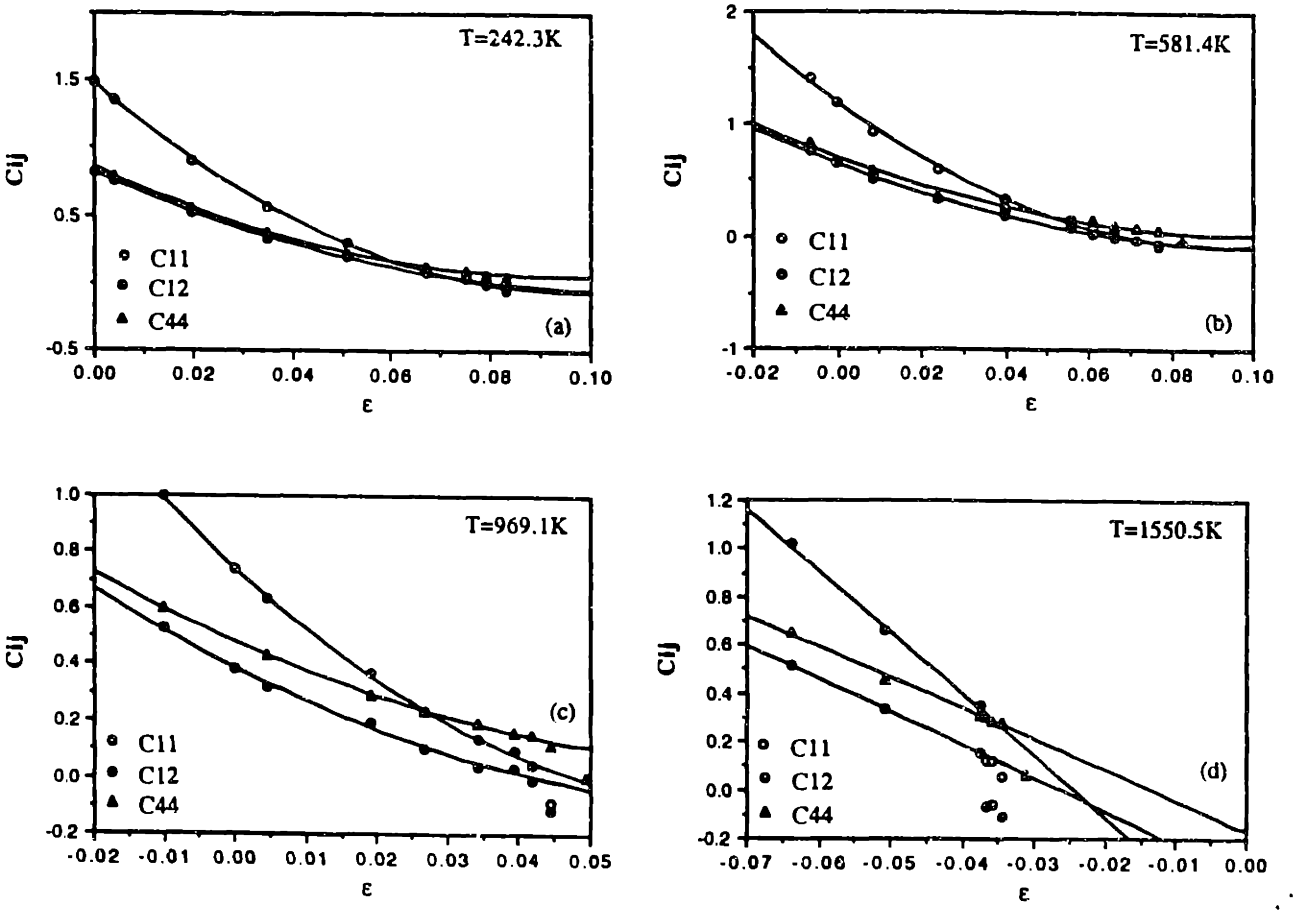

Fig. 5.2 Variations of the elastic constants, C11, C12, and C44, with imposed strain at finite temperatures.
Strain dependence of the elastic constants at different temperatures T = 242.3K (a), 581.4K (b), 969.1K (c), and 1550K (d) (the triple point temperature is approximately Tm = 1200K for this potential).

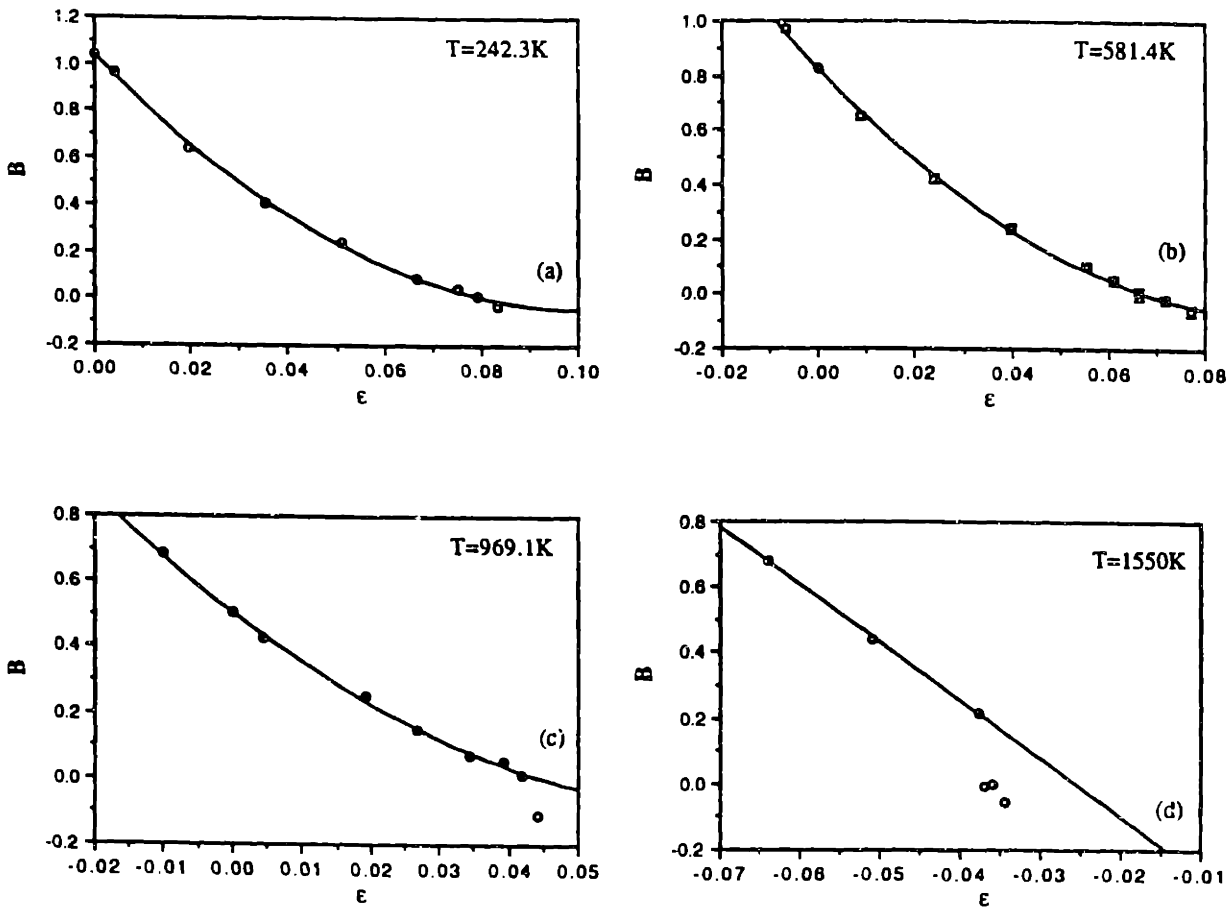

Fig. 5.3 Bulk modulus BT as a function of imposed strain at finite temperatures.
As the imposed strain increases the bulk modulus decreases. For each temperature there is a strain at which the data points starts to run away from the curve, this indicates the onset of the instability.

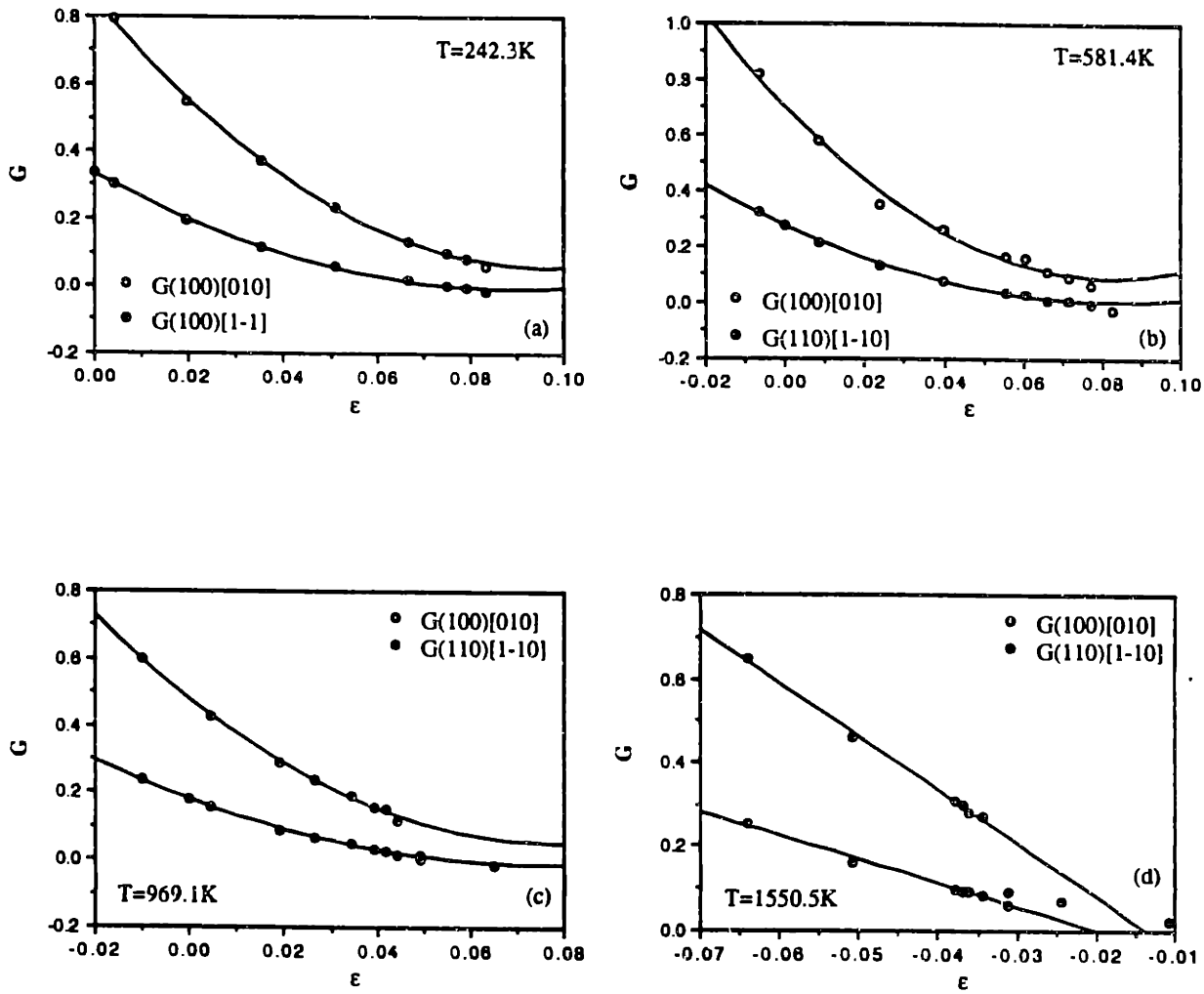

Fig. 5.4 Shear modulus G as a function of imposed strain at finite temperatures.
Same as in Fig. 5.3 but for shear modulus. G(100)[010] is the shear modulus in (100) plane along [010] direction, G(110)[1$\bar{1}$0] is in (110) along [1$\bar{1}$0] direction.

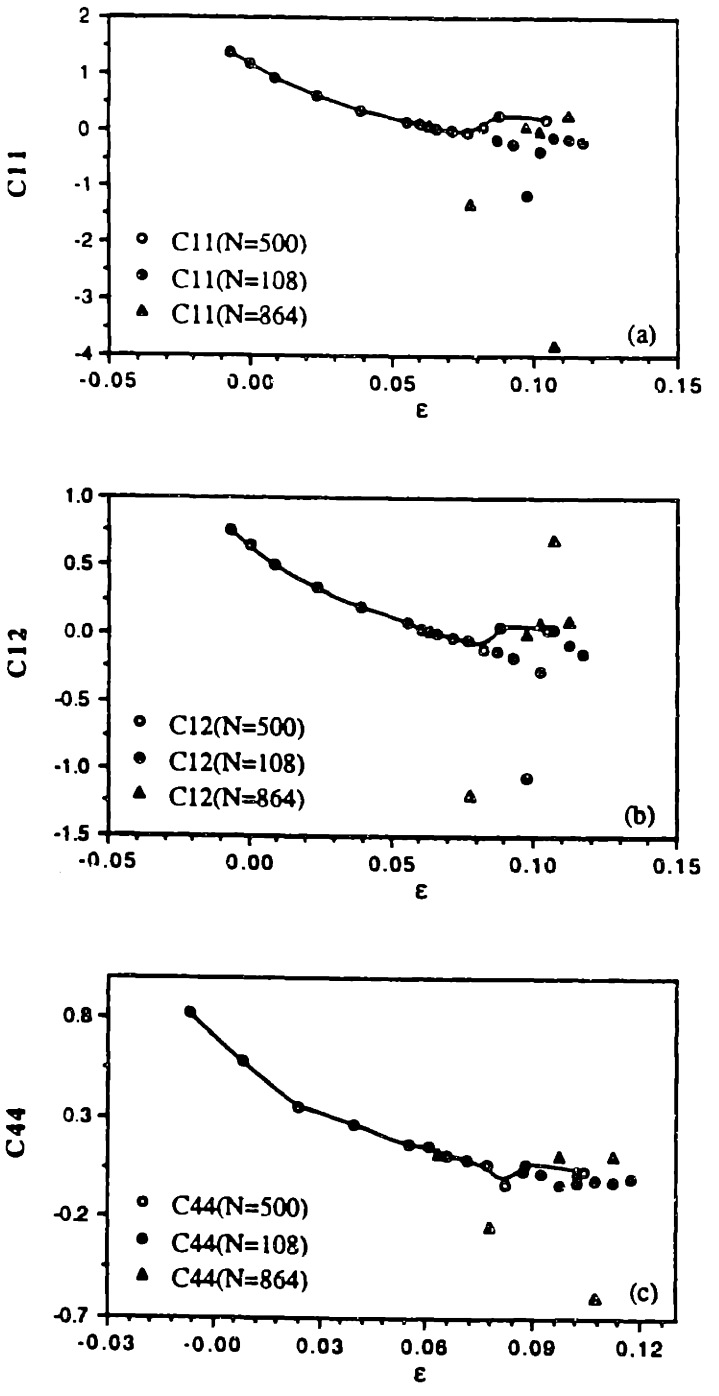

Fig. 5.5 Size effect on elastic constants at T = 581.4K. Presented are the variations of the elastic constants, C11 (a), C12 (b), C44 (c), with the imposed strain at T = 581.4K. To check the size effect three system sizes N = 108, 500, 864 were simulated. There is a size dependence of elastic constants. Since the elastic constants is closely related to the long wavelength of the elastic waves, small system size cuts off the wave length and postpones the transition. The systems of N = 500 and 864 give very close values of elastic constants. We used 500 atom system in our simulation since this system is good enough for the purpose of this study and the computation convenience.

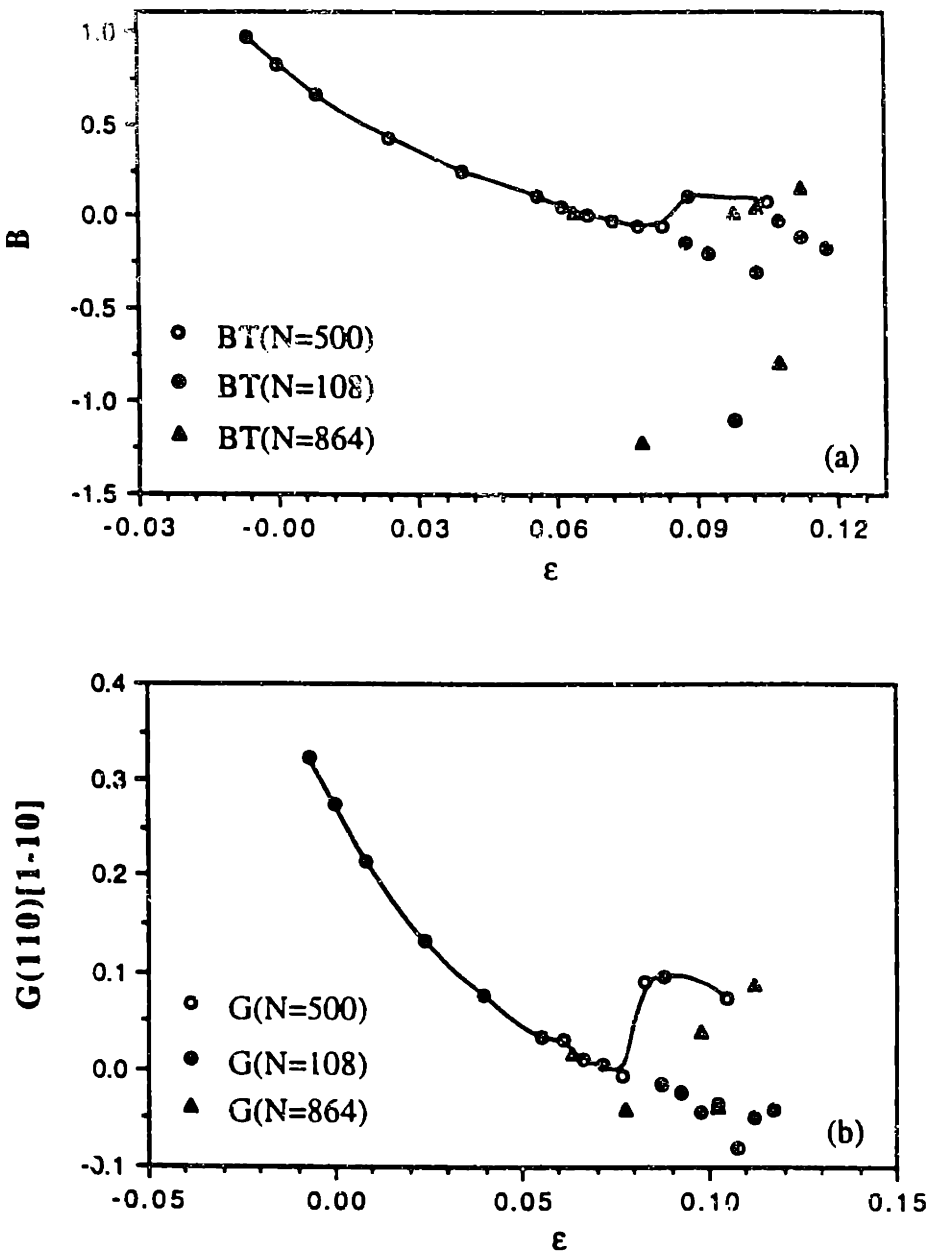

Fig. 5.6 Size effect on bulk modulus and shear moduli at T = 581.4K.
Same as in Fig. 5.5 except shown here are bulk modulus and shear modulus. The same size effect is seen.

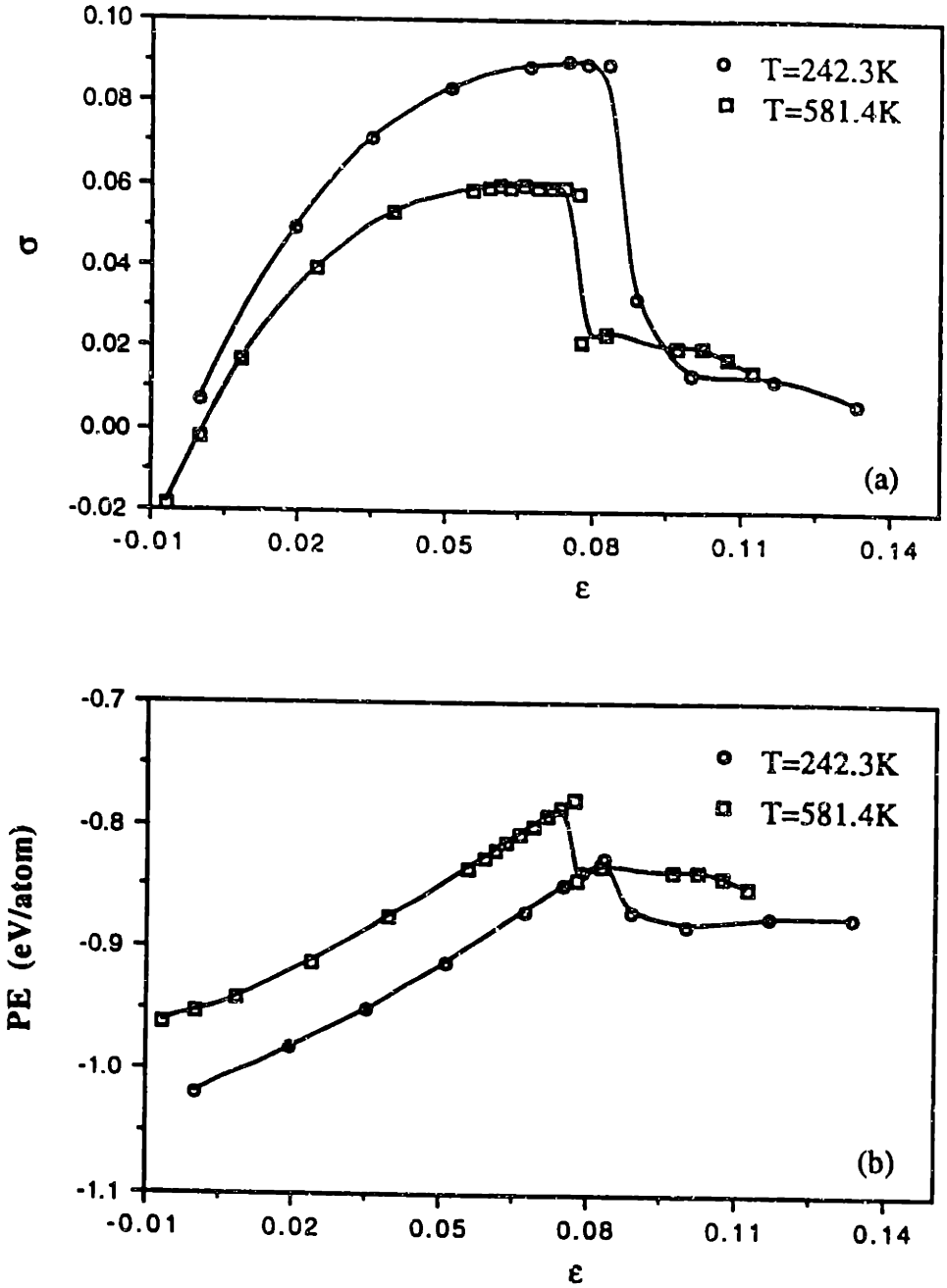

Fig. 5.7 Variations of normal stresses and potential energies with strain at T = 242.3K and 581.4K.
System responses, normal stresses s in unit of 10^{12} dyn/cm^2 (a), and potential energies PE in unit of eV/atom (b). The suddenly drops in normal stresses and potential energies point to the onset of the spinodal instability. Sharp changes in stresses indicate that the transition is first order phase transformation. System releases its strain by creating new surfaces in the form of cleavage fraction or cavitation.

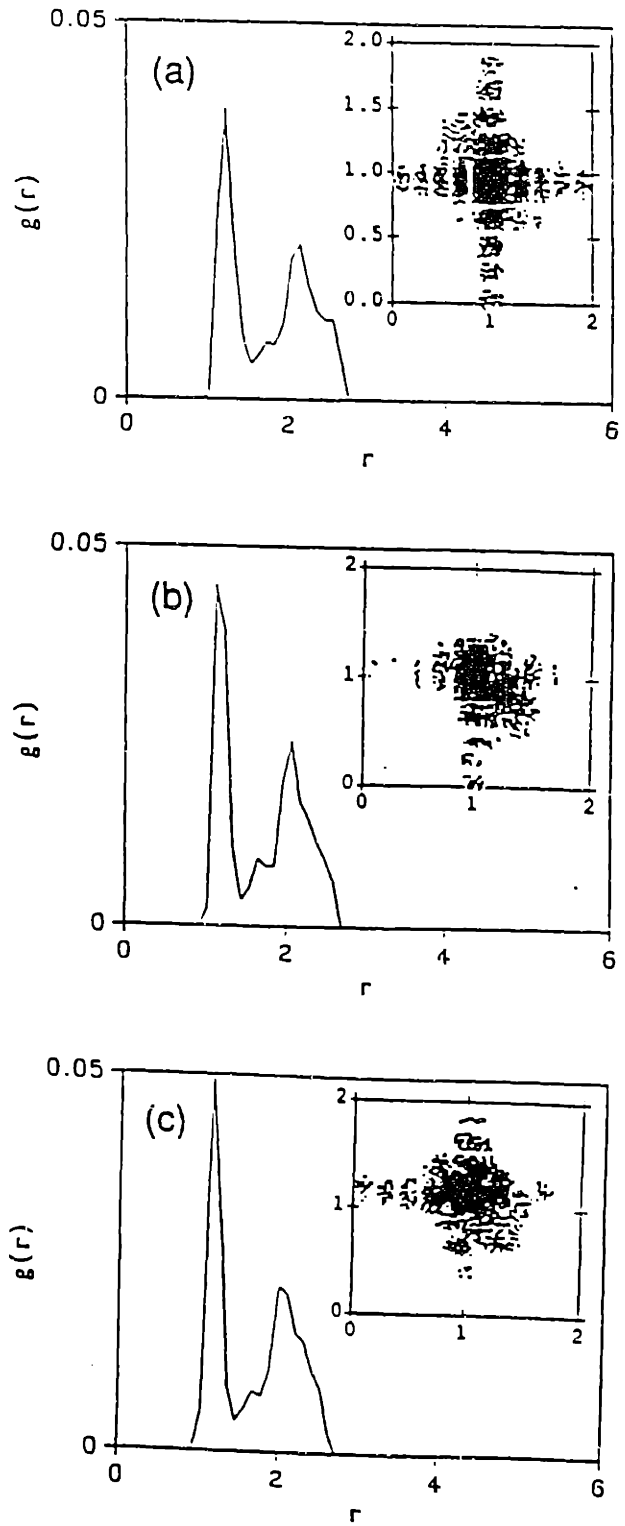

Fig. 5.8 System responses, g(r) and diffraction pattern S(k) at T = 581.4K, N=500, and three values of strains, $\varepsilon_1 = 0.0746$ (a), $\varepsilon_2 = 0.0854$ (b), and $\varepsilon_3 = 0.1015$ (c). S(k) is shown in the inset as projection on kx (horizontal axis) and ky (vertical axis). In case (a) system is in the static just before the transition. The peaks of g(r) are low and broad, the spot of the diffraction pattern indicates that the system is in crystalline. Case (b) and (c) show the behavior of the system after the transition. As seen that the peaks of g(r) become sharper while there is no changes in S(k).

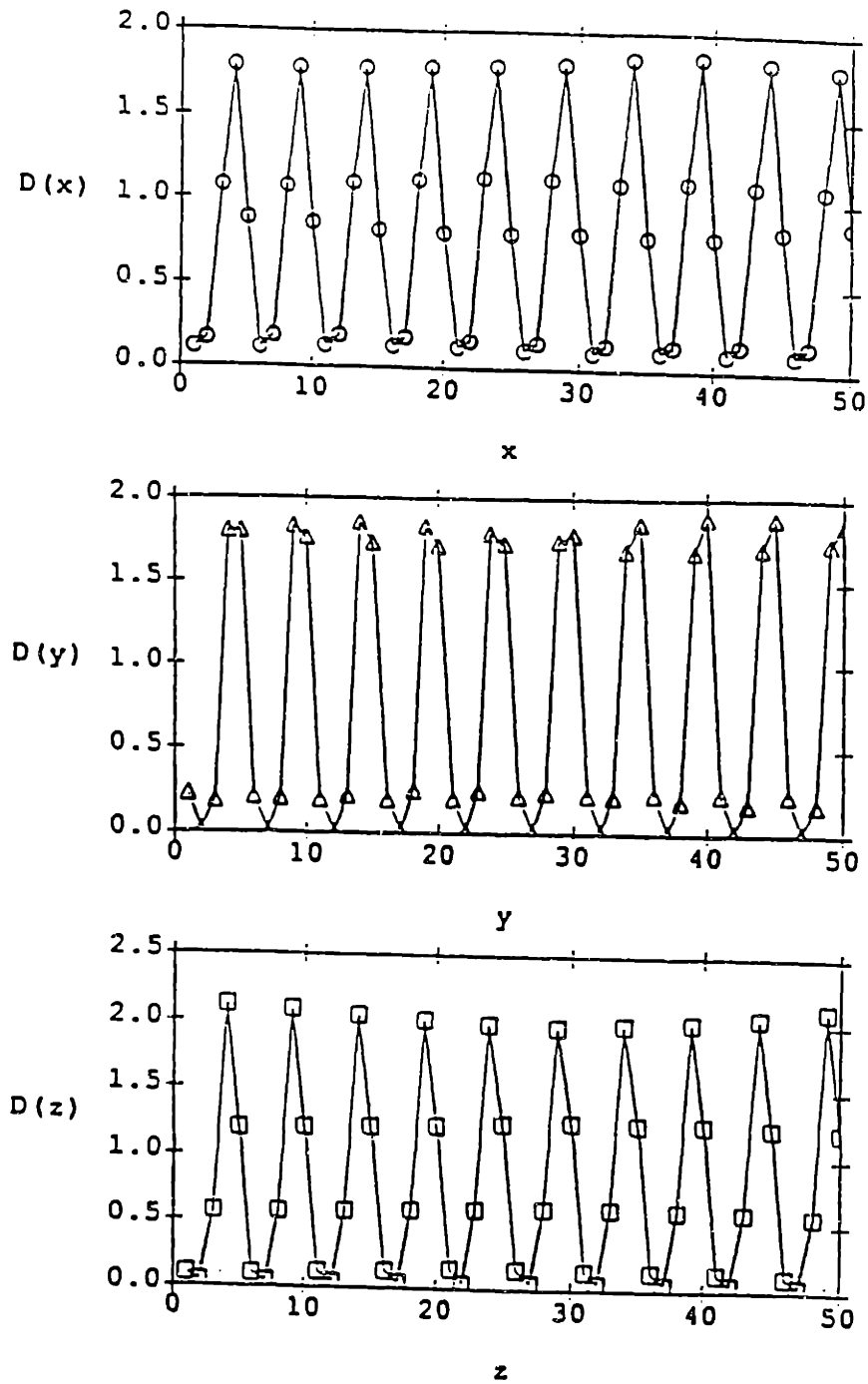

Fig. 5.9 Density profiles corresponding to Fig. 5.8 (a). The density profiles show that the atomic planes along each directions of cubic symmetry are well ordered as in the perfect (undeformed) f.c.c. lattice.

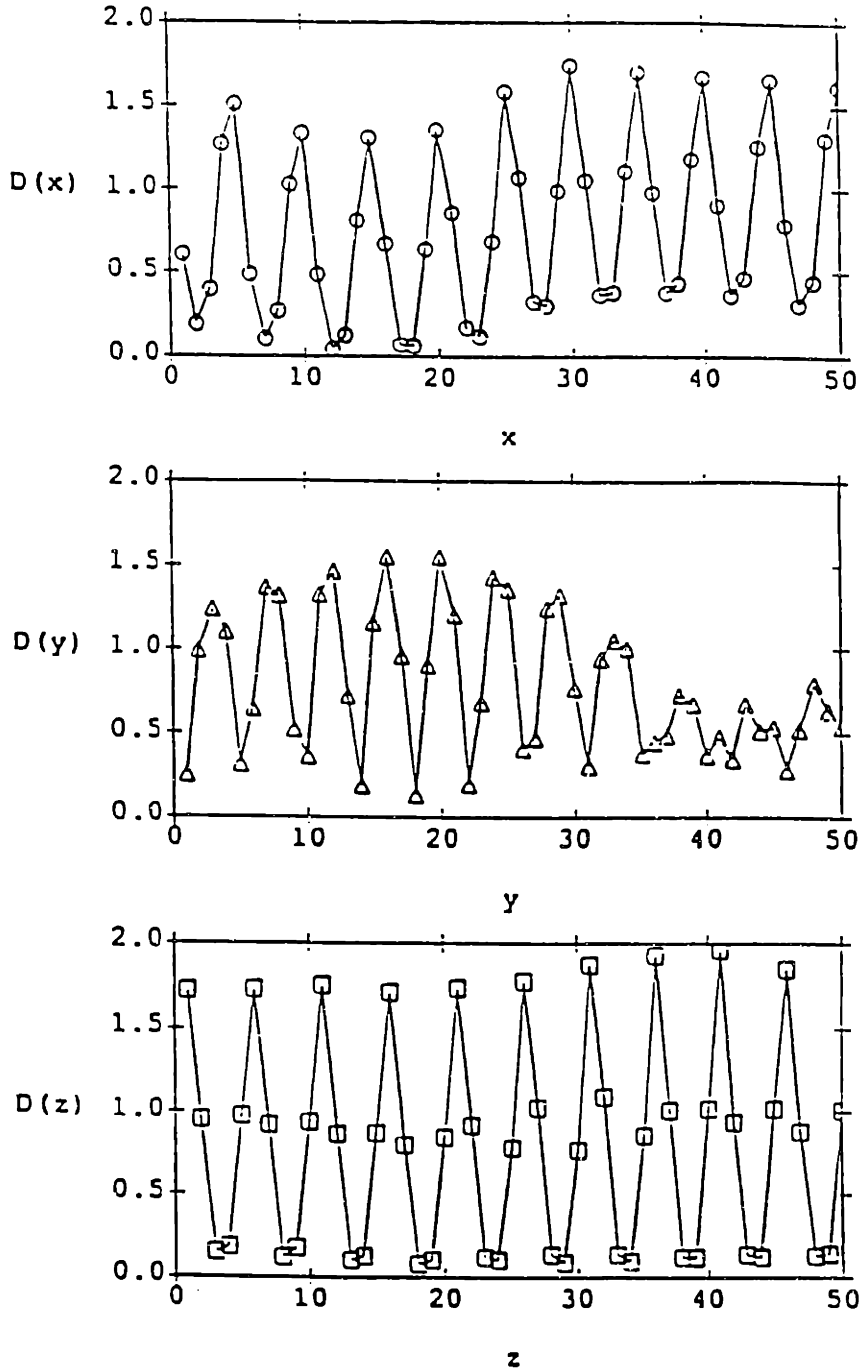

Fig. 5.10 Density profiles corresponding to Fig. 5.8 (b).
As shown in the density profile along y direction, after the pressure jump, the symmetry of the system is clearly broken in the y-direction. There appears an extra atomic plane along this direction. The system is no longer uniform along this direction. The distinctly nonzero value of the minima in the density profile implies significant atomic displacements from the original lattice positions.

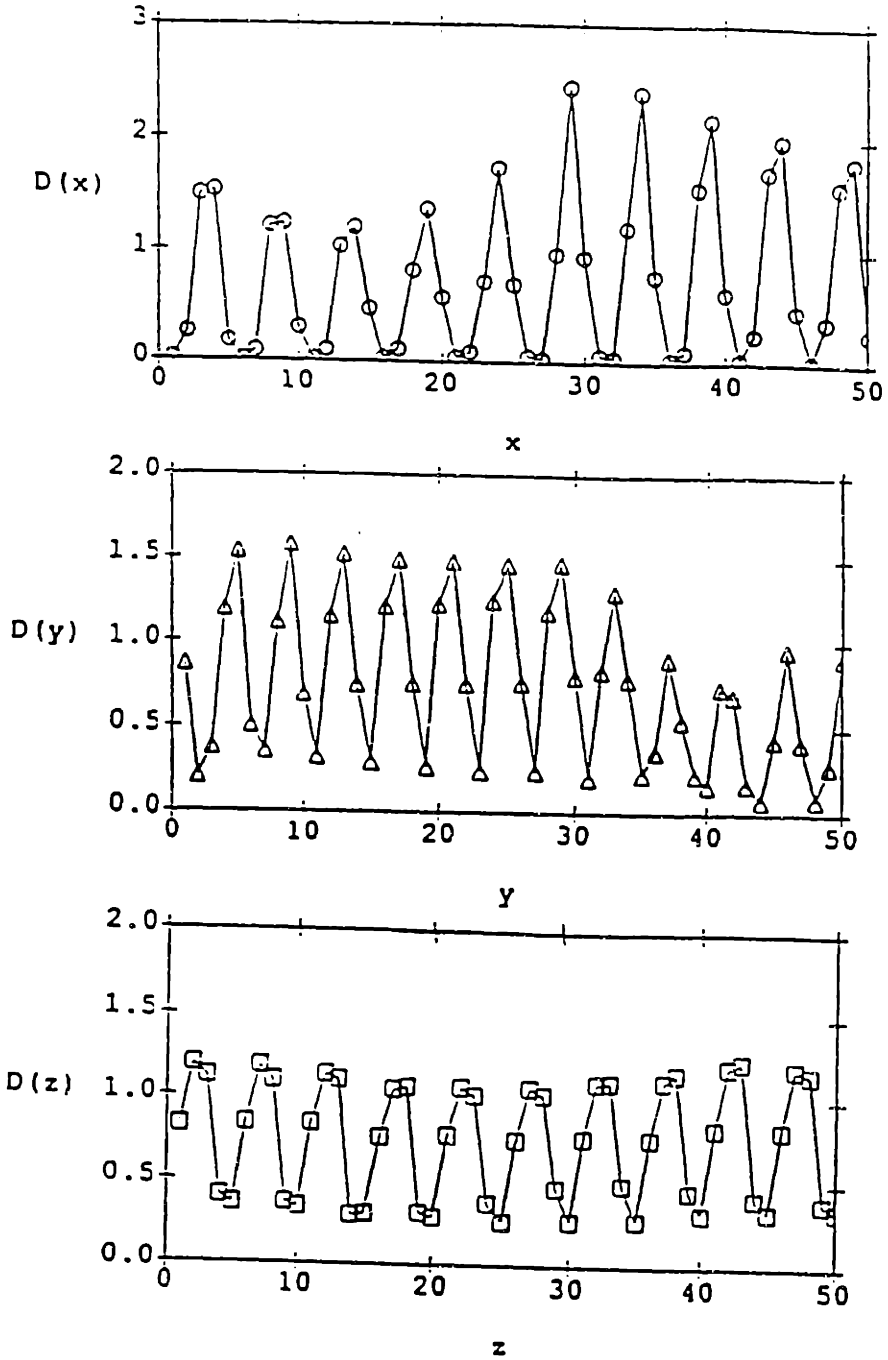

Fig. 5.11 Density profiles corresponding to Fig. 5.8 (c). In going from ε_2 to ε_3 the density profile along y-direction shows two extra planes relative to x- and z-directions. The nonuniform density profiles in x- and y-directions suggest the nucleation of cavitation, first seen in Fig. 5.10 along y-direction.

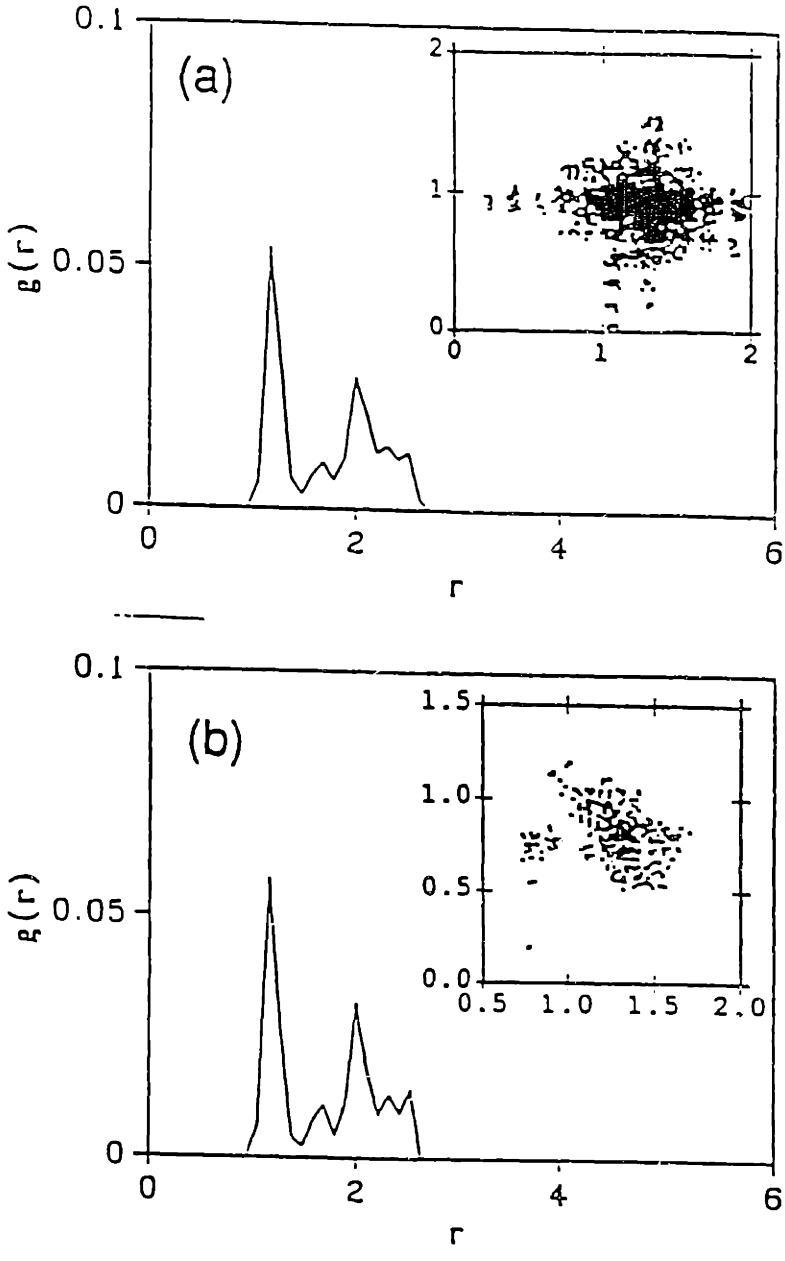

Fig. 5.12 Same as Fig. 5.8 except N = 864 and the two strain values $\varepsilon_4 = 0.1041$ (a), and $\varepsilon_5 = 0.1090$ (b).
Shown here are the g(r)'s of the system after the pressure drops down and at even larger strain than that in the case of N=500 (Fig. 5.8). The well-defined peaks of the g(r)'s indicate system still in order, but the shift of the position of the diffraction spot suggests that the lattice has been largely distorted.

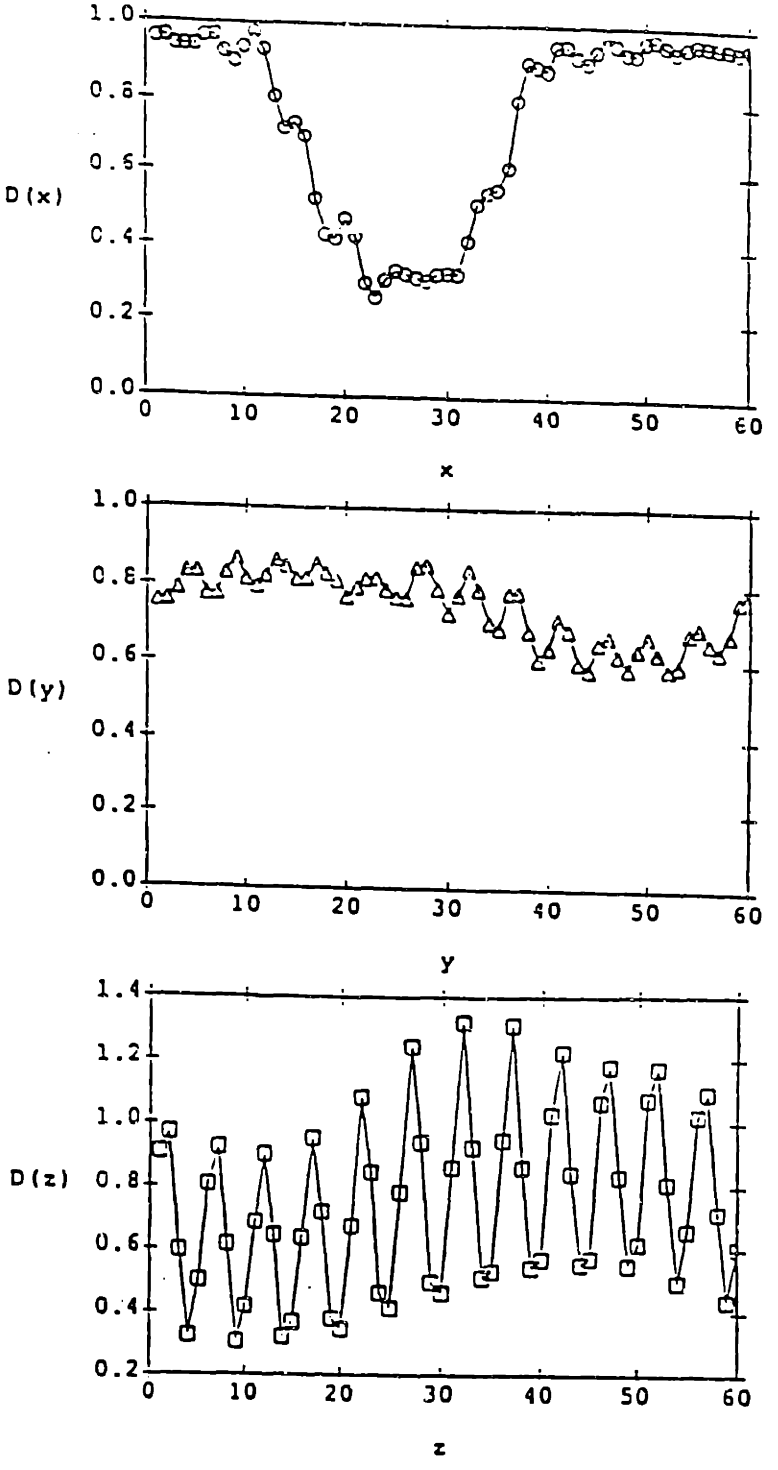

Fig. 5.13 Density profiles corresponding to Fig. 5.12 (a). The density profiles show the pronounced cavitation along the direction of broken symmetry (x-direction instead of y-direction in N = 500 series).

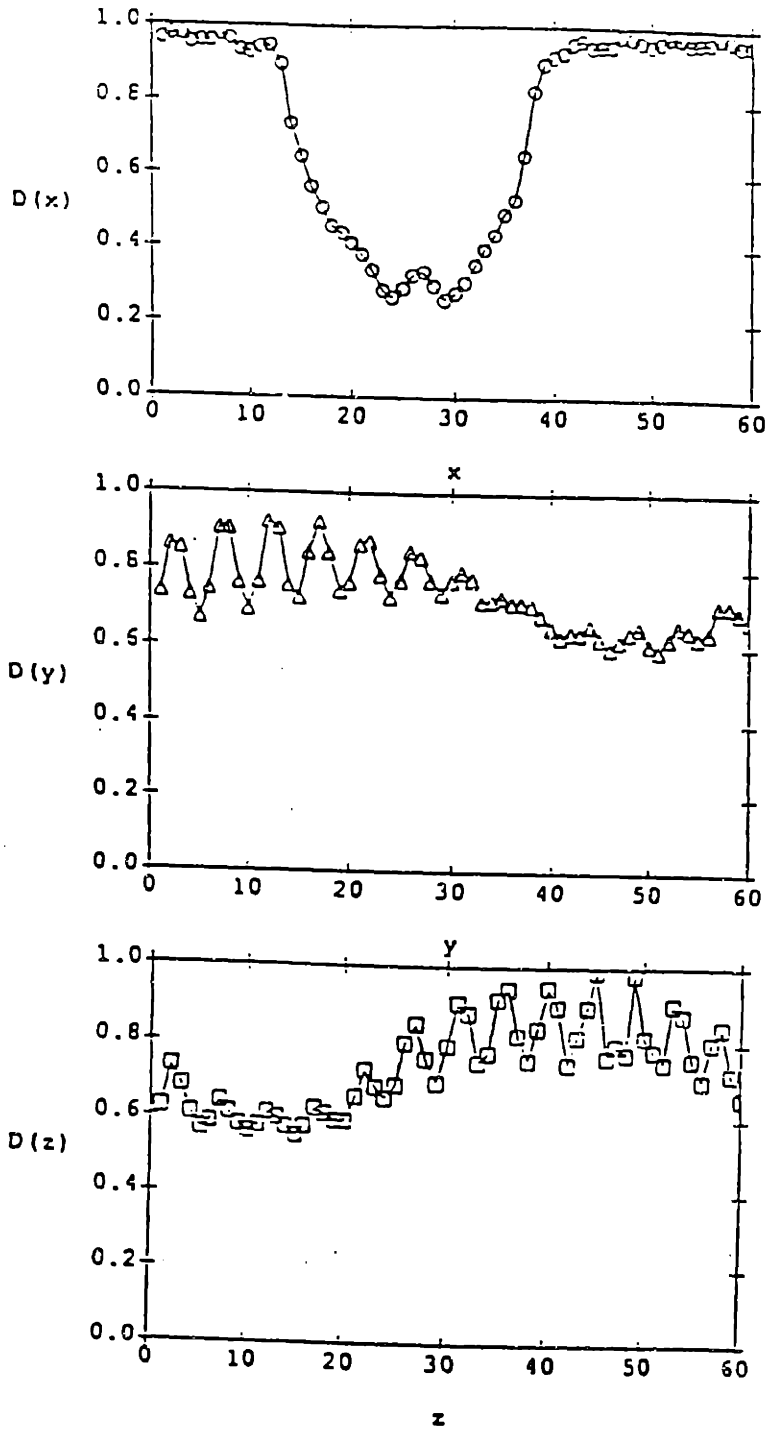

Fig. 5.14 Density profiles corresponding to Fig. 5.12 (b). At still larger strain the system has been divided into a order region and a cavitation region (a completely disordered region around the cavitation void).

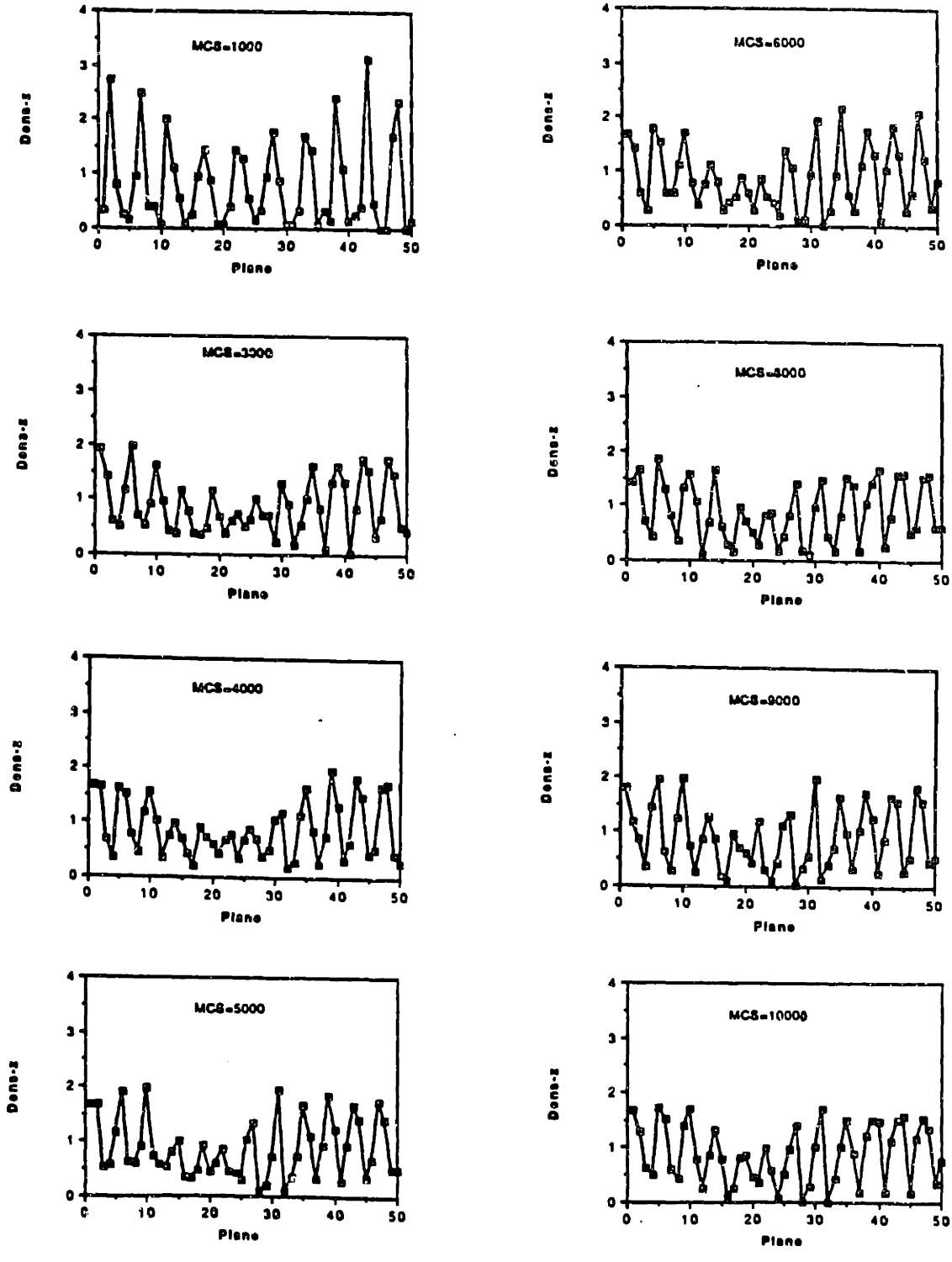

Fig. 5.15 Evolution of density profile along the symmetry-breaking direction at T = 242.3K. Shown here are only the density profile of the system along the symmetry-broken direction. They show clearly the processes of the nucleation of cavitation.

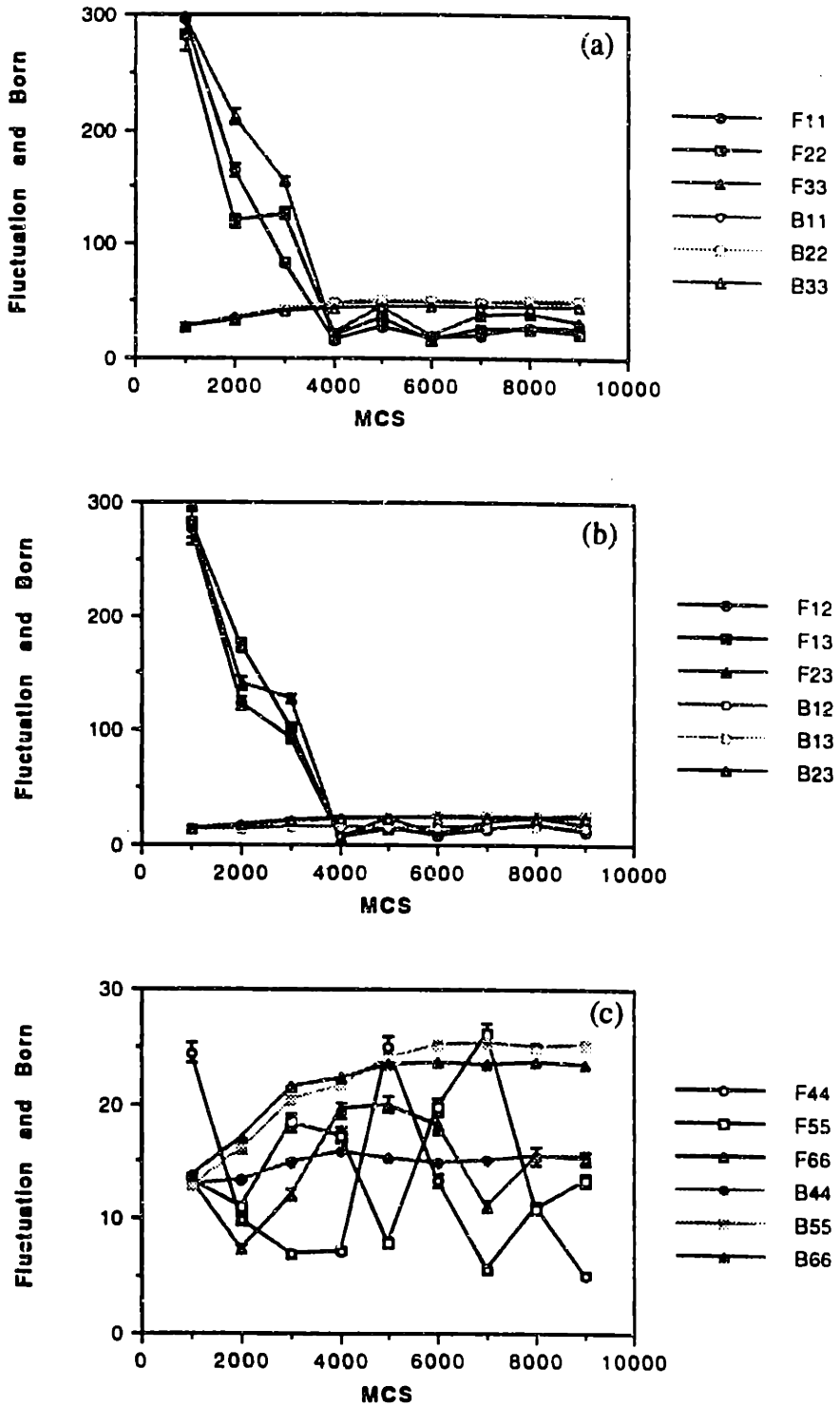

Fig. 5.16 Born and fluctuation terms contribute to the elsatic constants. Shown are the contibutions of Born and fluctuation terms to C11 (a), C12 (b), and C44 (c) at the critical strain of 0.0746 and T = 242.3K.

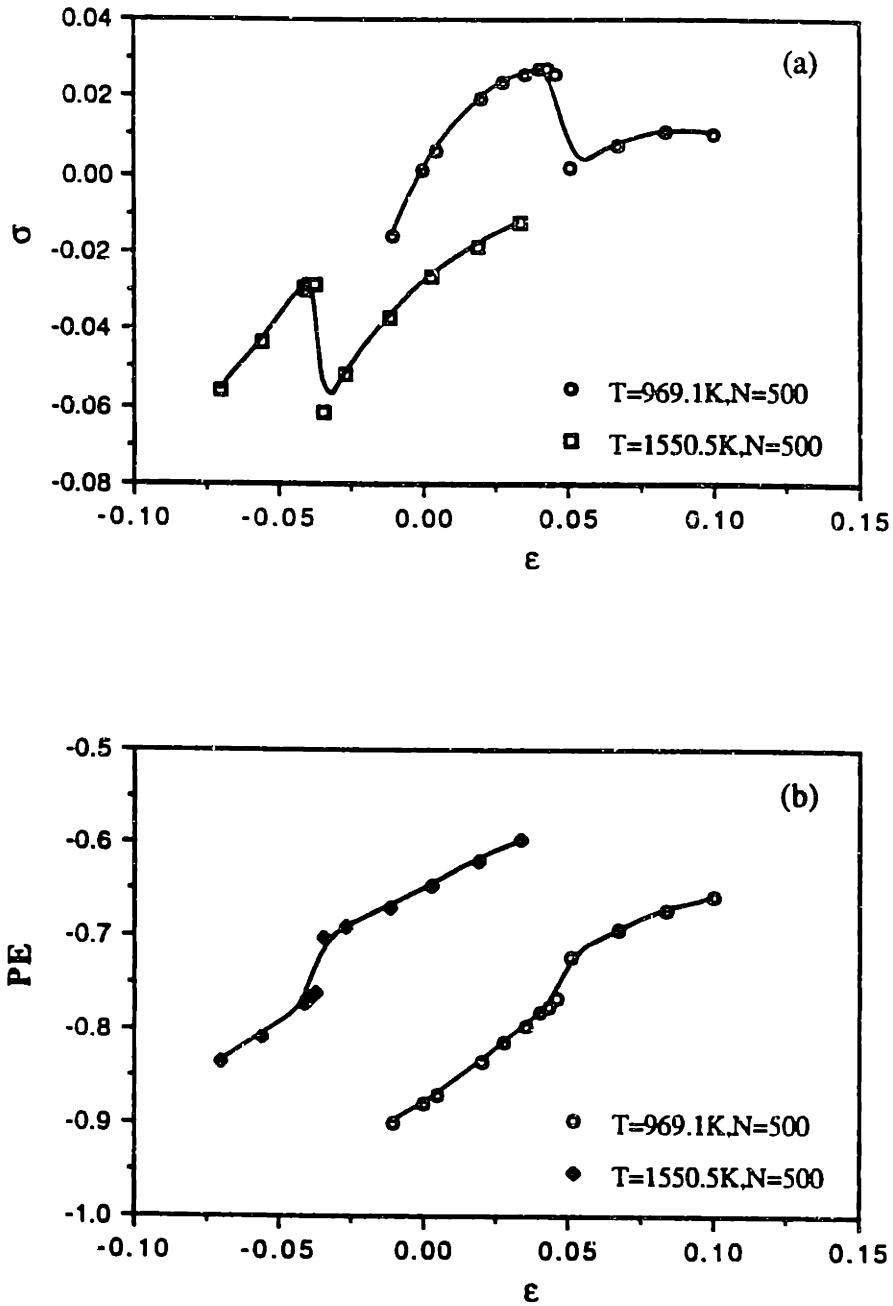

Fig. 5.17 Variation of the normal stresses and potential energies with imposed strain at T = 969.1K and 1550.5K (above melting temperature).
The drop down of normal stresses (a) at the critical strains shows that the transitions are still the first order, but now, in contrast to low temperature cases, the potential energies jump up. This shows that there is a latent heat involved in this transition (instead of the release of strain energy by creating new surfaces at low temperature cases). The similar behavior of the system at these two temperatures suggest that the transitions at high temperatures fall into another category of phase transformation, i.e., the melting transition.

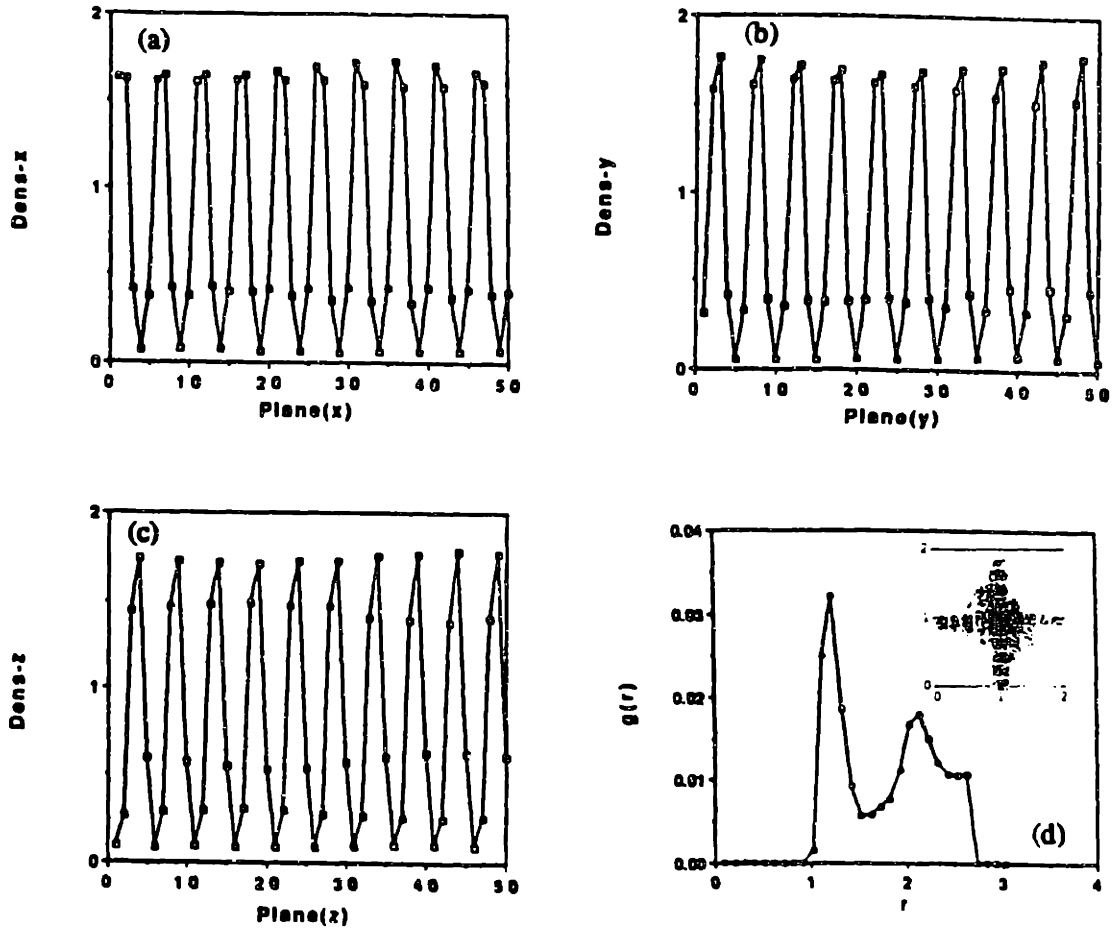

Fig. 5.18 Structural responses, density profiles (a), (b), and (c), g(r) and S(k) (d), of the system before the stress drop. Presented are the density profiles, g(r), and S(k) at ε = 0.0443, one MC run just before the transition. It is clear that the system is in well-defined f.c.c. order.

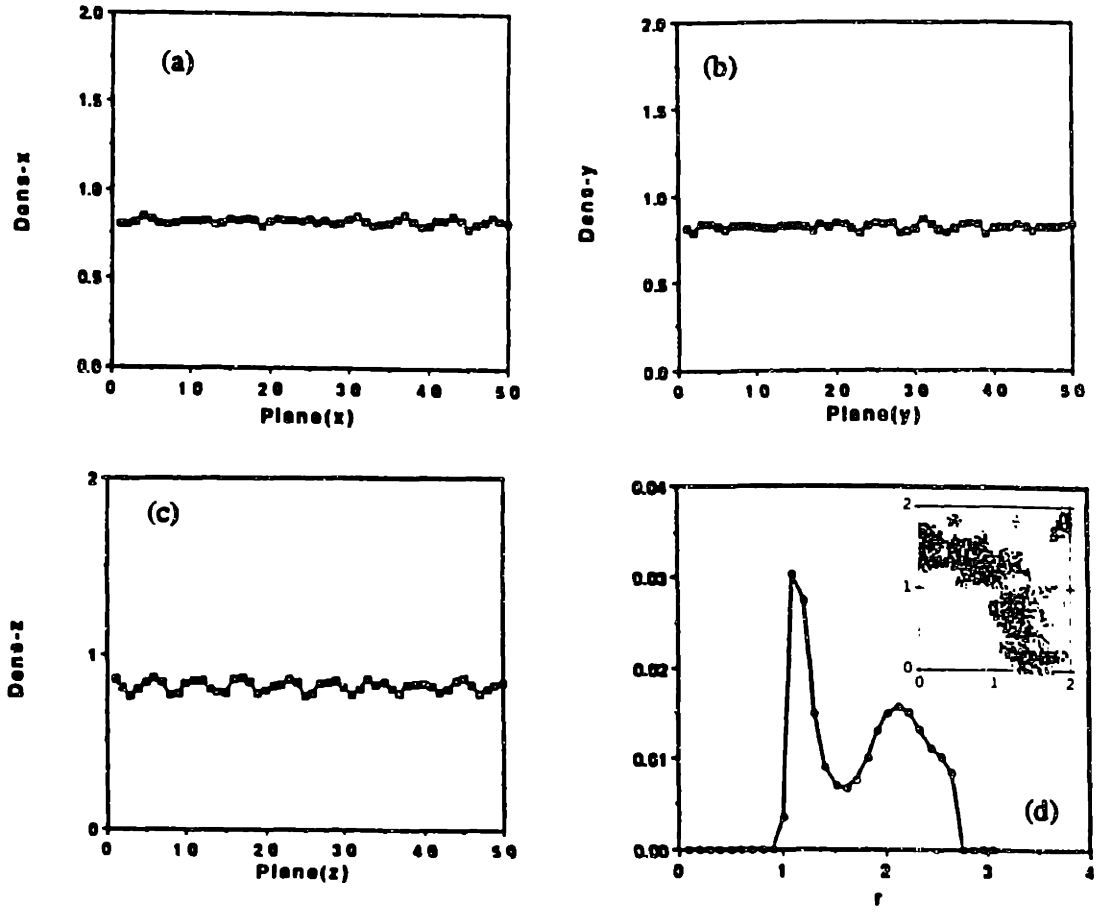

Fig. 5.19 Structural disordering at still larger imposed strain ε = 0.0494.
The density profiles (a), (b), and (c), g(r), and S(k) show dramatically different behavior in response to the normal stress drop. The ring of the diffraction pattern (d) indicates that the system has been completely disordered. The uniform density profiles about the mean-density show that, instead of breaking symmetry, the transition now takes the system to a homogeneous disordered state.

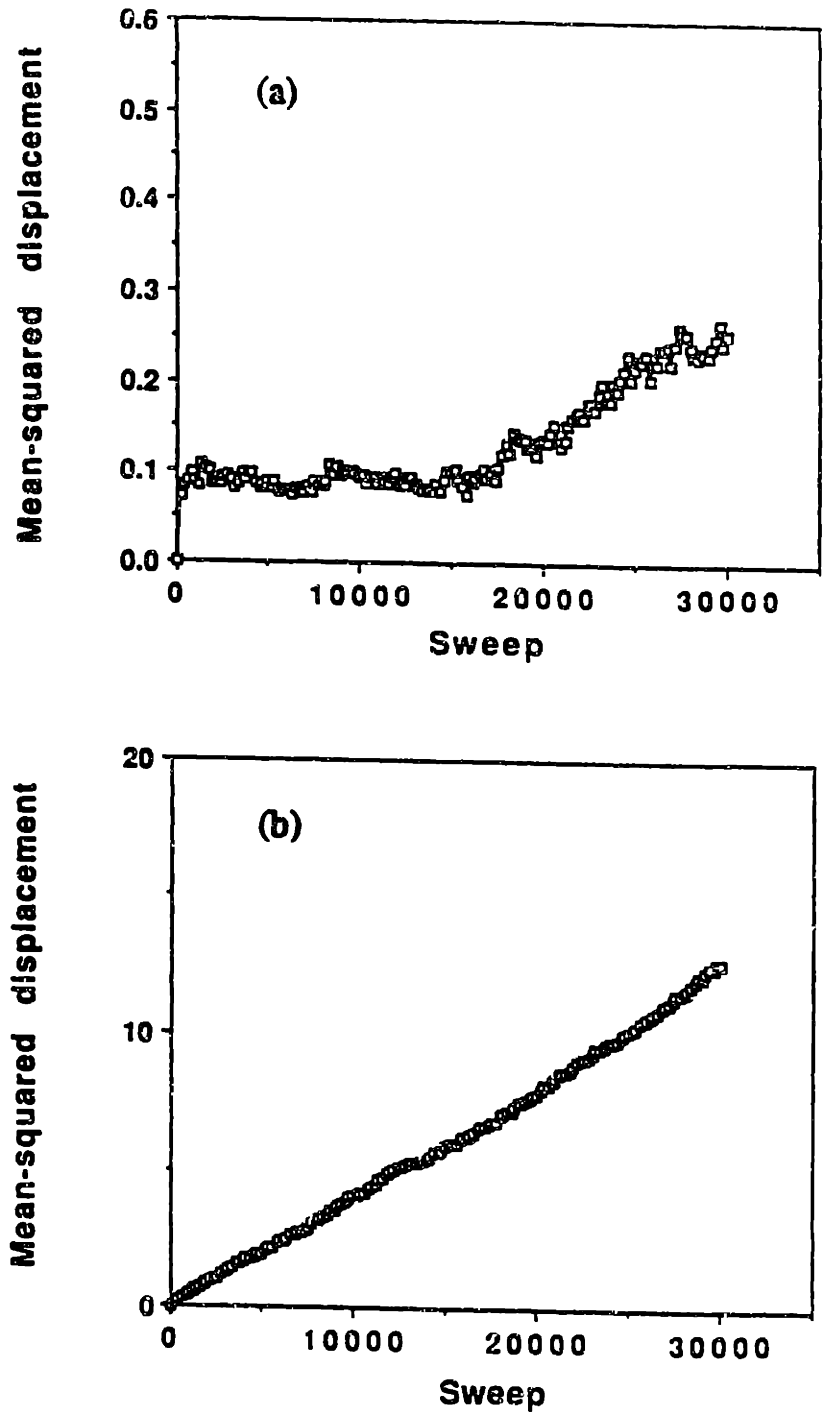

Fig. 5.20 Variation of mean-squared displacement function with MC sweeps at two system strain states. The huge difference in the magnitude of MSD shows dramatically mobility behavior of the system just before (a) and just after (b) the normal stress drop. The persistent increasing of the MSD are strongly indications of a liquid-like environment.

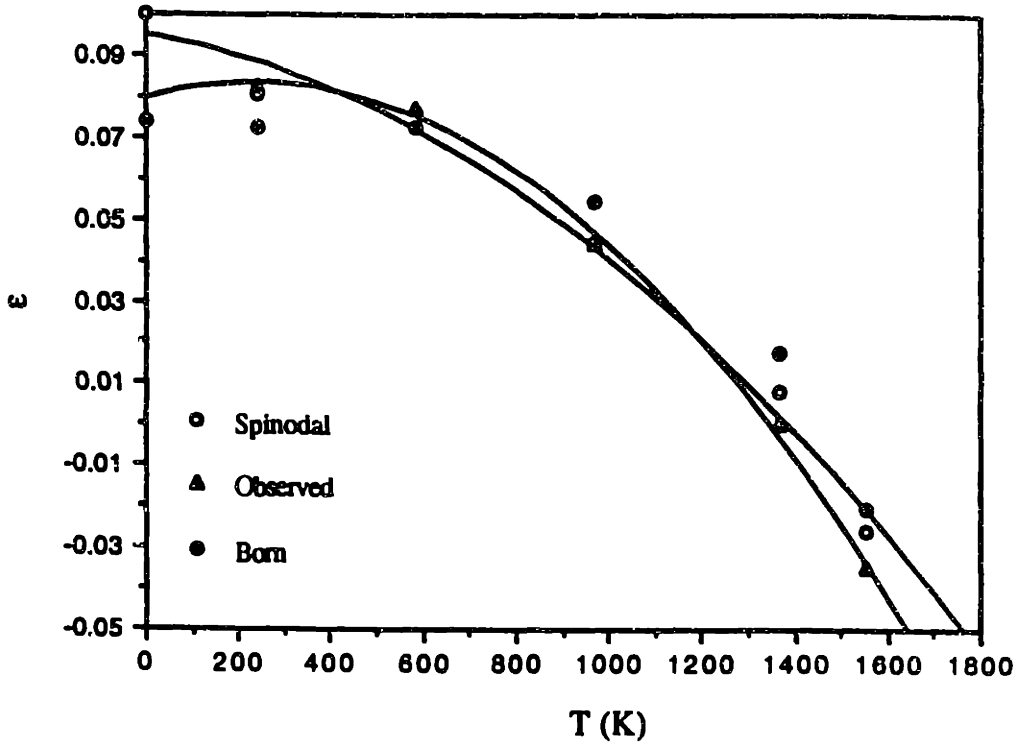

Fig. 5.21 Comparison of the critical strains at different temperatures.
Shown are the critical strain predicted by spinodal instability and Born instability, and by direct observations. It is seen that at low temperatures the observed critical strains are quite close to that predicted by buik modulus, but at high temperatures they are smaller the theoretical values.

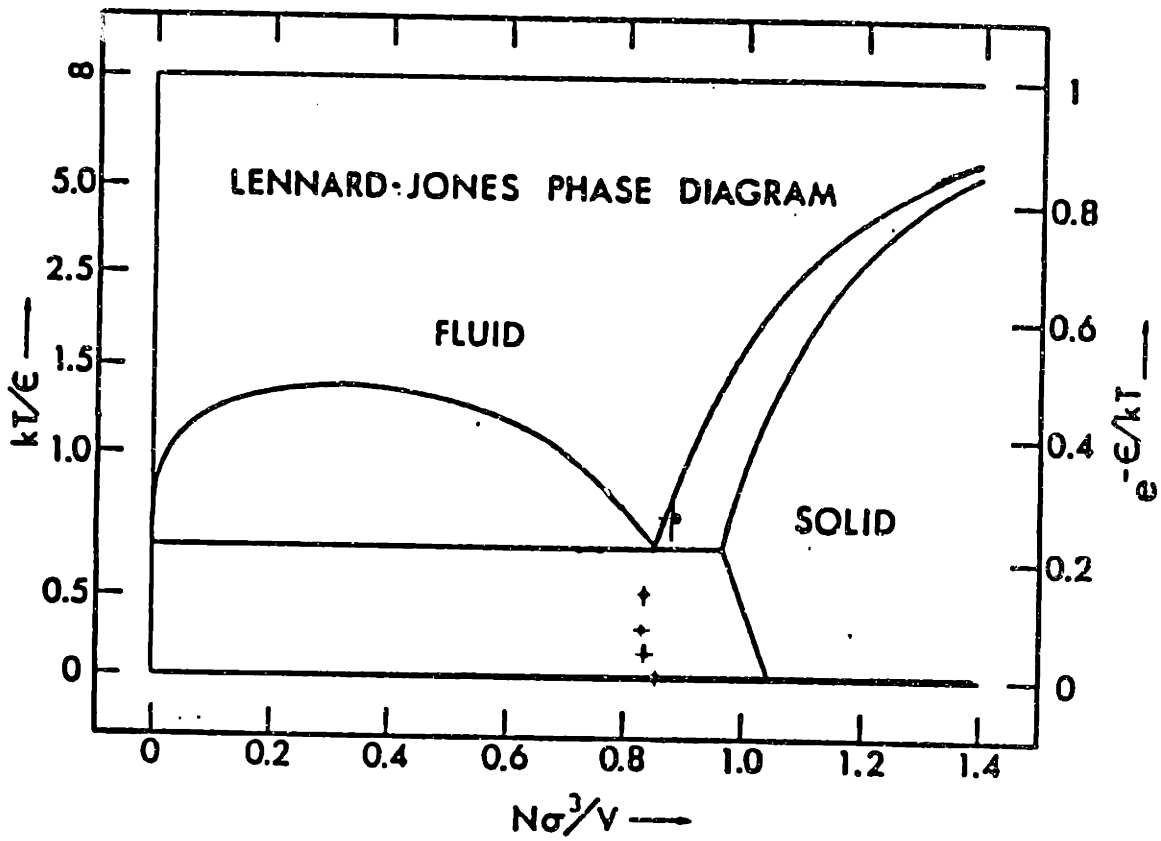

Fig. 5.22 Temperature-volume phase diagram of an atomic system in which the particles interact via the Lennard-Jones potential function [Hoover 75].
Critical strains, converted to densities, observed in the present simulation are added as solid circles at the various temperatures.

Chapter 6

Unstable Responses to Spinodal and Born Instability of An F.c.c. Lattice with EAM Potential

In chapter 2 we have established an elastic-mechanics-based description of the instability of a crystal. We have shown that the elastic instability of the crystal is closely related to the inflection point of the strain energy of a crystal lattice. We have also showed that only the instability criteria themselves are not enough to characterize all the elastic instabilities because they do not carry any information about how the system can become unstable. The eigenstates of the elastic constant matrix suggest that each of the instability is associated with a specific set of deformation states. These eigenstates define the particular failure mode of the instability. Each mode terminates a stable region of deformation and then defines a deformation path which takes the crystal to an unstable region. Each instability is able to show up when and only when the system is in its eigenstates.

The eigenstates of spinodal instability have the characteristics of symmetry conservation and pure volumetric deformation. Born instability requires a breaking of the original symmetry and then is associated with a shear distortion. Therefore, one can define the eigen-deformation path which belongs to a certain instability. Following Milstein [Milstein 77] and making it clearer we define the primary deformation path (primary path) as a series of deformations which conserve the original elastic symmetry of the deformed crystal; bifurcation point as a point on the primary path at which system breaks its symmetry (Born instability criterion is satisfied); and a secondary deformation path (secondary path) as a path along which the system maintains the broken symmetry.

In Chapter 4 we have seen that temperature plays an important role in softening elastic constants and driving the system to elastic instability. In Chapter 5 we have studied the spinodal instability of an L-J f.c.c. lattice under pure dilatation. It seems clear that the strain deformation is able to bring about the spinodal instability, while the constant stress environment allows the Born instability to compete with the spinodal instability. Thus computer simulation is a suitable method to study these elastic instabilities separately. In Chapter 4 we have studied the pure temperature effect at zero applied stress. In Chapter 5 we have focused on the instability under finite applied stress environment. But since the property of softness in L-J potential, this potential gives considerably lower values of elastic constants when the lattice is deformed. This makes it difficult to distinguish one instability from another. As far as the final state of the structural phase transformation is concerned, this difficulty also causes uncertainty in specifying the correspondence between

the instability and the structure phase transformation. The EAM potential is a desirable potential for the study of the elastic instabilities under both finite strain and stress deformation.

The objective of this chapter is to confirm the theoretical prediction about the instabilities. The focuses will be, first, the eigenmode of the deformation which can expose certain instability and hide the others and, second, the final structural states into which the system will evolve under both finite strain and stress deformations.

6.1 Elastic Constants and Critical Strains

The isothermal elastic constants are determined for f.c.c. crystal as a function of the strain in pure dilatation using both fluctuation formula (FF) and stress-strain curve (SSC) method (see 3.4.3) at temperature T = 500K. In the calculation using fluctuation formula, a (ThN) ensemble MD simulation was used, where **h** is the matrix we introduced in Chapter 3. A model system of 108 atoms at a fixed volume was first equilibrated for 20000 to 30000 time steps, then the elastic constants were calculated and averaged over 100000 time steps. With a successive increment of the volume a series such MD simulations were performed and the elastic constants were calculated for each increment of strain. Fig. 6.1 gives the results of fluctuation formula.

In stress-strain curve method, the stress-strain curves were computed via MD simulations by applying a series of fixed uniaxial strains, with $\Delta\varepsilon$ range from -0.006 to 0.006 for each fixed strain, to the simulation cell, then the resulting stresses were evaluated. The stresses were averaged over 100000 time steps after an equilibration of 20000 to 30000 time steps under the applied strain. Then the negative slopes [Ray 88] of the stress-strain curve give the corresponding elastic constants. In present calculations only the normal strains were imposed so the elastic constants we could get were C_{11} and C_{12}. The elastic constants of the model system were calculated for three different temperatures of T = 500K, 800K and 1000K using this method. For each temperature three stress-strain curves were generated and three values of each elastic constant were obtained for three imposed strains. These data were fitted to a straight line or quadratic curve of the strain to get the critical strains of the spinodal and Born instabilities. Fig. 6.2 shows a typical stress-strain curve at T = 500K. Table 6.1 gives the fitting results of elastic constants as a function of the strain at T = 500K, 800K and 1000K.

The critical strains of the instabilities for each temperature are shown in Table 6.2. The critical strains were calculated from the simulation data using the instability conditions: $C_{11}(\varepsilon_c^B) = C_{12}(\varepsilon_c^B)$ for Born instability, and $C_{11}(\varepsilon_c^S) + 2C_{12}(\varepsilon_c^S) = 0$ for spinodal instability

respectively, where the superscripts B and S indicate the Born and spinodal instability respectively. We have noticed that the critical strains of Born instability are always smaller than that of spinodal instability. One may think, by intuition, that this fact suggests that Born instability should always show up at lower strain, because spinodal instability requires at least one of elastic constants being negative or both of them being zero, but Born instability could be satisfied even both elastic constants are positive finite. In literature, both instabilities were reported [Macmillan 72, Milstein 71, 73, 80, Scitortino 92]. We will demonstrate in the following sections that the temperature-induced thermal effect and the stress-induced mechanical effect both contribute to the driving force for the instability. The key for the Born instability to occur is a stress-free condition.

6.2 Dilatational Decohesion under Hydrostatic Stress and Volume Expansion

For a pure dilatation the strain of the cubic crystal only has one independent component. So the strain state of the system can be well defined by one parameter ε. From Table 6.2 one sees that at different temperatures the critical strains of Born instability are always smaller than that of the spinodal instability. At first glance one might expect that along the primary deformation path (in this case the pure dilatation) when the strain is greater than ε_c^B the system would become unstable against Born instability. In chapter 4 we already saw that this is true. Our explanation there was that by constraining the external stress to be zero the stress does not contribute to driving the system to instability. The temperature-induced thermal fluctuation plays a dominant role in triggering the spontaneous breaking of the symmetry and enabling the system to depart on the secondary path of deformation. The temperature induced structural disordering, at large, determines the final structure state of the transition.

In what follows we will demonstrate by MD simulations that one can purposefully see the spinodal instabilities by simply confining the strain fluctuation. In simulation this is easy to achieve by constant strain (or constant volume) simulation, or in the case of hydrostatic pressure simulation, by constraining all the diagonal elements of the strain tensor fluctuating in the same manner. Since the volume expansion is along the primary path of deformation the dilatation only leads the system to spinodal instability at which a violation of bulk modulus ($B_T < 0$) occurs.

6.2.1 Spinodal Failure on the Primary Deformation Path

The isothermal volume expansion at fixed temperature T = 500K was simulated by a series of MD simulations performed on (ThN) and (TΣN) ensembles with successive change in the lengths of the simulation cell and the imposed hydrostatic stress respectively. The model system consists of 504 atoms which contains three unit cells in both x and y directions and fourteen unit cells in z direction. This geometric arrangement was made to include as many long wavelength phonons as possible since the elastic constants of a crystal is closely related to the elastic waves of long wavelength in lattice vibration. In each individual run the system was first equilibrated several thousand to ten thousand time steps, then another fifty thousand time steps were used to generate the trajectories for property calculation. Throughout the simulation the internal energy U/N or enthalpy H/N, internal stresses σ, mean-squared displacement and the static structural factor S(k) were monitored

In the hydrostatic stress ($\Sigma = \Sigma_{11} = \Sigma_{22} = \Sigma_{33}$) simulation at T = 500K, when the value of the imposed hydrostatic stress increases all the three components of the normal internal stress respond properly in the same way and are eventually equal to the value of the external stress after equilibrium (Fig. 6.3). Meanwhile, the internal strain and the enthalpy of the system increase monotonically with the increment of external stress, as shown in Fig. 6.4 (a) and (b). This equilibrium is maintained even the internal strain passes the critical value of Born instability [indicated by the arrow in Fig. 6.4(a)]. A sudden drop of the internal stress occurs at an even higher value $\Sigma = 0.1162\ 10^{12}$ dyn/cm^2 of the hydrostatic load. The corresponding strain is 0.0513. The sharp decrease in the enthalpy and increase in strain point to the onset of spinodal instability. The rapid change in system properties characterizes the transition associated with this instability. One notes that the observed critical strain $\varepsilon_c = 0.0513$ is smaller than that predicted by elastic constants.

As seen in Fig. 6.5, contemporaneously with the rapid changes in σ, ε and H/N, the static structure factor S(k) decreases from ~ 0.7 to ~ 0, shows that the crystalline order of the system was completely destroyed after 50000 time steps. Since the system has lost its resistance to further volume expansion the hydrostatic stress causes a persistent expansion in the volume. The system eventually falls apart into pieces. Fig. 6.6 shows projections of an intermediate atomic configuration after t = 5000 Δt. A very similar behavior of an Lennard-Jones fluid in fragmentation near its spinodal line was reported by Holian et al. [Holian 88].

Since we have known that in the (TΣN) ensemble MD simulation both the internal stress and strain can fluctuate, it is difficult to reach the maximum value of strain with a small size (N = 500) system. In order to fix the gap of the difference in critical strain

between the observed and predicted value, we performed an MD simulation on a (ThN) ensemble. In this case one can prevent the shape fluctuation of the simulation cell. A similar behavior of the system at the critical strain similar to (TΣN) ensemble simulation was observed. The internal stress and energy in response to the imposed strain [see Fig. 6.7 (a) and (b)] show all features of spinodal transition. The transition occurs at the critical stain $\varepsilon_c = 0.0493$ which is still 17% smaller than the value of 0.0595 predicted by elastic constants. This result strongly suggests that there must be some physics underlying the difference. We will discuss this in more detail in sec. 6.4.

The static structure factor at the end of the $\varepsilon = 0.0493$ run is shown in Fig. 6.8. In spite of the large drop in stress, the S(k)'s still stay finite and do not show clear evidence of a new structure. However, the decrease in internal energy indicates that the system has transformed into a lower energy state. And the drop in internal stress is also a manifestation of a release of elastic energy during the transition. Fig. 6.9 shows the projections of an instantaneous atomic configuration after the transition. This figure displays clearly that a cleavage fracture occurs parallel to the two small dimensions of the simulation cell. Two new surfaces are created. The creation of new surfaces converts the strain energy of the system into the surface energy, and thus is responsible for the decrease of the internal energy and the relaxation of the internal stress of the system.

We have demonstrated that in both (TΣN) and (ThN) ensemble simulation, pure dilatation, along the primary path, takes the system all the way down to spinodal instability. At the critical strain all three normal components of the internal stress drop down. In the (TΣN) ensemble simulation, before failure, the internal stress of the system always balances with the external stress. Thus the system equilibrates at certain volume. When the expansion of the system approaches the critical strain, the internal stress decreases very rapidly. The imbalance between the imposed and internal stress suddenly results in a huge expansion strain rate and acceleration. This feature is very much like the method for the generation of shock waves. This sudden shock produces a large velocity gradient among the atoms in the system even when we keep rescaling the atomic velocities. This rapid volume expansion leads the system to a fragmentation [Holian 88]. In the case of (ThN) ensemble simulation, when the imposed strain is beyond the critical strain the system cannot stand for this expansion any more. Since the elastic instability is closely related to the elastic wave of long wavelength one can expect that the failure will start along the long dimensions of the simulation cell. This failure ends up as a decohesive cleavage fracture and lowers the energy of the system by creating new surfaces.

6.2.2 Reversibility along the Primary Deformation Path

In previous simulation studies we have seen that the system seemed to be stable against volume expansion in the Born instability region where $C_{11} - C_{12} < 0$. One question one may ask is, since the critical strain observed by simulation experiment is still smaller than that predicted by spinodal instability condition, if it is possible that the transition we have observed is the consequence of a "delayed" Born instability. Obviously if this is so something must have happened before the system fails. Otherwise the system must be stable with respect to volume expansion.

A series of inverse simulations, that is compression, were performed on a (ThN) ensemble along the same path as in the previous expansion simulation in an attempt to check the stability in the "Born instability region". We started from the configuration with its strain just below the value of the observed critical strain, then reduced the imposed strain from 0.0470 to 0.0251 by several intermediate stages. In each stage the volume of the simulation cell was fixed at the strain we wanted, the system was equilibrated for 500 time steps and the properties such as the internal energy, stress, mean-squared displacement and the static structure factor were computed. We found that in every intermediate stage the properties of the system show the same values as that in the previous expansion simulations. Fig. 6.10 shows the results of the internal stress and energy for both expansion and compression simulations. Where the open circles denote the property for expansion and the solid circles for compression. As is clearly seen from Fig. 6.10 all the properties of the system are completely reversible. The reversibility of the system along the primary path shows that the system is very stable even in the strain region where Born instability is satisfied.

This conclusion can also be seen from the generalized Hooke's law. For pure dilatation the stress-strain relation can be expressed as

$$\delta\sigma = (C_{11} + 2C_{12})\,\delta\varepsilon. \qquad (6.1)$$

Even for $C_{11} - C_{12} \leq 0$, there is a storing force $\delta\sigma$ arisen which tends to move the system back to previous equilibrium state and thus prevents Born instability.

We conclude that along the primary path of deformation, in this case pure dilatation, the system is stable against Born instability. As will be shown in the next subsection this is so even under a small shear perturbation.

6.2.3 Shear Perturbation on the Primary Deformation Path

It has been shown that in elastic wave propagation the Born instability gives rise to a growing transverse wave propagating along [110] direction. [Kettle 56] This is a transverse wave in which a local shear distortion in (110) plane of a cubic crystal is required. When Born instability is satisfied, that is $C_{11} - C_{12} = 0$, the velocity of the propagating wave becomes zero. When $C_{11} - C_{12} < 0$ this velocity becomes complex and the amplitude of the shear vibration will grow exponentially with time t. Therefore, the shear distortion in $[1\bar{1}0]$ direction will become larger and larger, and eventually causes the failure of the system. In this subsection we will study that given the constraint of equal diagonal elements of the strain tensor and a hydrostatic stress which tends to hold the cubic symmetry (so called compliant boundary condition), can an impulsive shear perturbation in (100) along $[1\bar{1}0]$ still bring the system to Born instability. This will be a crucial check to the theoretic prediction that the deformation along the primary path will forbid the occurrence of Born instability.

The MD simulation was carried out on a (TΣN) ensemble. The model system contains 108 atoms with interatomic interaction described by EAM potential. A hydrostatic stress was imposed on the cubic simulation cell to expand the system to a prescribed strain of $\varepsilon_0 = 0.0356$. The system is now in the Born instability region. A small shear distortion in (110) along $[1\bar{1}0]$ direction was imposed on the system. The system was first equilibrated for 5000 Δt at this fixed strain, then the shear perturbation was released. The simulation was switched on the (TΣN) ensemble and the evolution of the system was monitored for another 30000 time steps. Fig. 6.11 shows three projections of a time averaged atomic configuration after 30000 Δt, where the x-y plane is the (001) and (110) is along the diagonal of the x-y plane. As is seen clearly in Fig. 6.11 the system completely recovers from the shear distortion to the original f.c.c. crystal. The full coverage of the system from the small shear distortion demonstrates that keeping the system in cubic symmetry (here by imposed hydrostatic stress) prevents Born instability.

In summary of all our results in this section we come to the following conclusions: (1) As long as the deformation forces the system to go along the primary path the only instability that can occur is the spinodal instability. The underlying physics of this instability is that when the bulk modulus vanishes, all the three normal components of the internal stress become zero. The system has no more resistance to further volume expansion. (2) Although the instability conditions themselves reveal the underlying physics that make the system unstable, they do not carry information about how the system becomes unstable. A complete description of instability must include the instability

criterion as well as the eigen-deformation mode. (3) For an f.c.c. crystal Born instability is forbidden by the pure stress-induced dilatation because along the entire deformation path the uniform expansion conserve the original cubic symmetry of the crystal. (4) Spinodal instability leads to a structural phase transformation, but the final structural state of the transition depends on the physical condition which drives the system to instability. In the case of imposed stress the transition takes the form of fragmentation, while in the case of imposed strain the system ends up either as cavitation or decohesive cleavage fracture.

6.3 Martensitic Transition under Anisotropic Stress

Martensitic transition is a type of structural phase transformation which does not involve long range diffusion of atoms. The transition is accomplished th gh a collective motion of all the atoms. Consequently, the parent and daughter phases show certain orientational relations. Since historically the martensite was obtained during the quenching of steels, martensitic transition referred to the concentration modulation induced by temperature variation. However, studies by various group [Bolling 69, 70a, 70b, 71, Delaey 74] have shown that the enthalpies of the parent and daughter phases have strong dependence on the variations in stress as well as in temperature. In particular, Najafabadi and Yip [Najafabadi 83] carried out Monte Carlo study of stress induced reversible b.c.c. to f.c.c. transition. Chueng and Yip [Chueng 92] have studied the f.c.c. to h.c.p. structural transition in α-iron under uniaxial loading. In present study we are not only interested in martensitic transition but rather in making connection between the Born instability and martensitic transition.

We have already known that Born instability requires a breaking of elastic symmetry. This means that the transition associated with Born instability will bring the system to lower elastic symmetry and increase the number of independent elastic constants. In Chapter 2 we have showed that for a crystal with tetragonal symmetry there exists a strain state at which all components of the internal stress become stationary. An extension and contraction along the two low symmetry directions can spontaneously occur, a new path in stress-strain relation becomes possible along which the tetragonal symmetry is broken. Milstein and Farber [Milstein 80] considered an f.c.c. crystal of Ni under tensile load in [100] direction. They have showed that along this new path, with decreasing load, the system starts to expand in one of the two lateral directions and eventually its extension in that lateral direction catches up with the [100] extension. The system ends up, at zero load, again in an f.c.t. structure. Parrinello and Rahman [Parrinello 81] also studied the same system. They concluded that at finite temperature the bifurcation predicted by static

calculations [Milstein 80] does not occur. Instead very close to the bifurcation point the system actually fails. In this section we will simulate an f.c.c. crystal of Au under uniaxial tensile stress load and demonstrate that at Born instability bifurcation does occur, but the nature of the transition on the secondary path depends on the extension rate or the symmetry constraints.

6.3.1 Strain Bifurcation and Martensitic Transition

The model system in this simulation study was a 108-particle system of Au atoms on a perfect f.c.c. lattice. Atoms of the model system are interacting within a (TΣN) ensemble under periodic border condition. To simulate uniaxial loading, an anisotropic external stress was being applied through the symmetry tensor Σ which controls the trajectories of the simulation cell border. When an external stress is applied to the system in the [100] direction through the symmetric tensor Σ, one would expect the system to elongate in the loading direction and contract in the transverse direction due to the Poisson's effect.

Two series of simulations were performed on the model system to simulate the tensile load at T = 500K. The first one started from a stress-free cube on which a uniaxial stress was applied along [100] direction. This was done by assigning Σ_{11} a nonzero positive value, all other Σ_{ij} being zero. Under the action of such a load the matrix **h** starts to change in a well-defined manner, i.e., the MD simulation cell starts to distort away from its original cubic shape. Then one can look for the phase transition by monitoring the evolution of the various components of the **h** matrix as the imposed stress is being increased.

Fig. 6.12 shows the variation of the lateral lattice parameters a_y and a_z with applied uniaxial stress. When the tensile stress is increased from low values up to $\Sigma_{11} = 0.0180 \times 10^{12}$dyn/cm^2, the normal contraction in the transverse directions is observed in accordance with Poisson's effect. Very interesting results were found when the uniaxial stress increases to the value of $\Sigma_{11} = 0.0229 \times 10^{12}$dyn/cm^2. As shown in Fig. 6.13 the evolution of system properties, two successive processes of symmetry breaking were observed [see Fig. 6.13 (d)]. First, a split of a_y and a_z from their previous values (they were the same at the beginning) occurs. The obvious increase in a_y and decrease in a_z show clearly that the bifurcation has happened. In the meanwhile there was no change being observed in other properties. This indicates that the system is in the eigenstates of Born instability as predicted by the theoretical analysis. In this stage the bifurcation is symmetric [see Fig. 6.13(d)] and the off-diagonal elements of **h** matrix $\langle h_{ij} \rangle$ are

essentially zero to within ± 0.005, showing that the system has an orthorhombic structure. About 7500 time steps after the bifurcation, the second symmetry breaking occurs. And correspondingly, an impulsive change in internal energy and stress and a step change in the x component of MSD were observed. Consequently, a further split of a_y and a_z appeared, and a sudden extension in a_x was observed. A nonzero off-diagonal element was found with the value $\langle h_{12} \rangle = -0.2954 \pm 0.0036$. Fig. 6.14 shows projections of the instantaneous atomic configuration at t = 30000 Δt (after the second symmetry breaking). As seen in the x-y projection there is a residual $[\bar{1}10]$ shear distortion in the (110) plane (the diagonal of the x-y plane). The system has transformed into a distorted b.c.t. structure with new lattice parameters $a_x' = (0.9283 \pm 0.0051)a_0$, $a_y' = (0.6655 \pm 0.0060)a_0$, and $a_z' = (0.7966 \pm 0.0013)a_0$.

Another simulation study was carried out on a pre-stressed f.c.c. crystal. In this study all the simulation procedures were the same as the first one but now with a pre-imposed hydrostatic stress $\Sigma_0 = 0.0900 \times 10^{12}$dyn/cm^2. The initial configuration was at strain $\varepsilon_0 = 0.0365$. Then a uniaxial tensile stress is applied along [100] during simulation. Again a bifurcation appears even before the small tensile stress $\Sigma_{11} = 0.0106 \times 10^{12}$dyn/cm^2 was applied. As is seen in Fig. 6.15 a further separation in the lateral lattice parameters occurs at a larger tensile stress. Fig. 6.16 shows the time evolution of system properties at $\Sigma_{11} = 0.0151 \times 10^{12}$dyn/cm^2. One sees two processes of symmetry breaking. The first has already happened since the previous run and the other occurs around 2500 time steps. The same characteristics of the impulsive change in internal energy and stress, and the step change in x component of MSD as in previous stress-free case show that, even the crystal is initially in pre-stressed states, the uniaxial stress-induced structural phase transition has the same nature and is through the same mechanism. In present case the nonzero off-diagonal element is $\langle h_{13} \rangle = 0.1605$ which shows that the shear distortion is now in (101) plane along $[\bar{1}01]$ direction (the diagonal of x-z plane). The system ends up as, again, a b.c.t. structure (see Fig. 6.17) with lattice new parameters $a_x' = (0.7162 \pm 0.0011)a_0$, $a_y' = (0.8481 \pm 0.0010)a_0$, and $a_z' = (0.9190 \pm 0.0003)a_0$.

In summary, one has seen that at small uniaxial stress the system shows a normal elastic behavior. That is, it elongates in the loading direction and contracts in the transverse directions according to Poisson's effect. When the system is further stressed to pass the point where $C_{22} = C_{13}$ (bifurcation point), Born instability takes the system to the bifurcation path along which the tetragonal symmetry is broken. A orthorhombic symmetry is established. Since along this secondary path all the components of the internal stress are stationary, the system is unstable. The orthorhombic state is just a transient state.

As the difference between the lateral lattice parameters grows a restoring force is eventually developed which tends to move the system further away from this transient state.

According to the generalized Hooke's law this distorting force can be expressed as, at the bifurcation point, $\delta\varepsilon_{xx} = 0$

$$\begin{aligned} \delta\sigma_{xx} &= C_{12}\delta\varepsilon_{yy} + C_{13}\delta\varepsilon_{zz} \\ \delta\sigma_{yy} &= C_{22}\delta\varepsilon_{yy} + C_{23}\delta\varepsilon_{zz}. \\ \delta\sigma_{zz} &= C_{23}\delta\varepsilon_{yy} + C_{33}\delta\varepsilon_{zz} \end{aligned} \tag{6.2}$$

Since along the bifurcation path we have $\delta\varepsilon_{zz} = -\delta\varepsilon_{yy}$, then the distorting force is

$$\begin{aligned} \delta\sigma_{xx} &= (C_{12} - C_{13})\delta\varepsilon_{yy} \\ \delta\sigma_{yy} &= (C_{22} - C_{23})\delta\varepsilon_{yy} \\ \delta\sigma_{zz} &= -(C_{33} - C_{23})\delta\varepsilon_{yy} \end{aligned} \tag{6.3}$$

For the orthorhombic symmetry one can expect $C_{12} - C_{13} > 0$, $C_{22} - C_{23} > 0$, and $C_{33} - C_{23} > 0$. Furthermore, since the separation between a_y and a_z is small one can also expect $C_{22} - C_{23} \sim C_{33} - C_{23}$. Thus Eq.(6.3) represents the driving force for the second symmetry breaking. This driving force eventually triggers the orthorhombic to b.c.t. transition and recovers the system back to a higher order of elastic symmetry.

In general the relative stability of the f.c.c. and b.c.c. (or b.c.t. in present case) at finite temperature is a difficult question to answer. To answer this question requires a detailed and accurate computation of the free energy difference. From our calculations we have noticed that before and after the transitions there were no changes in the internal energy and stress. This indicates that the structural phase transition is a continuous process during which there is no energy change involved. We can infer that the local free energy minima in configuration space for distorted f.c.c. and b.c.c. lattice seem to be equal, the transient state with symmetry breaking helps the system to overcome the energy barrier between these two states.

6.3.2 Stress Bifurcation and Spinodal Failure with Symmetry Constraint

In Chapter 2 we have shown that from the view of elastic wave propagation Born instability is a shear instability. It also has been shown [Grimvall 86] that based on the assumption of elastic continuum the shear modulus in the (110) plane along the $[1\bar{1}0]$ direction can be expressed as $G(110)[1\bar{1}0] = (C_{11} - C_{12})/2$. In sec. 6.2 we have

demonstrated that, in the case of pure dilatation, if the shear distortion is forbidden, Born instability can also be hidden. We will show by simulations that this is so in uniaxial loading. Then we systematically demonstrate that Born instability is actually a shear instability even at small length scale, i.e., the level of micro-crystals (containing few hundred to thousand atoms).

The simulation model and procedure in this study were the same as in the last subsection. But now the uniaxial tensile stress was loaded along the [001] direction with the constraint of equal edges in transverse directions to prevent strain bifurcation. This was achieved by the following procedures: When solving the equation of motion for **h** matrix we first solved for h_{11}, then the constraint of no strain bifurcation was forced by setting $h_{22} = h_{11}$. The system was still allowed to expand in the loading direction and contract in the lateral directions according to Poisson's effect.

The two model systems, a stress-free and a pre-stressed f.c.c. lattice, were used as the initial configurations in the present simulation study. The purpose of the first simulation is to show that the only constraint of no strain bifurcation does not prevent Born instability. In this case the Born instability manifests itself in the form of stress bifurcation instead of strain bifurcation. The second will demonstrate that once the constraint of conserving the original tetragonal symmetry is imposed, Born instability will be hidden.

The first simulation was started from a stress-free cube, the uniaxial tensile stress was imposed along [001] direction. We found that when this stress was raised to the value $\Sigma_{11} = 0.0229\times 10^{12}$dyn/cm^2 (the critical stress in previous strain bifurcation simulation) using two intermediate runs at $\Sigma_{11} = 0.0100\times 10^{12}$dyn/cm^2 and 0.0185×10^{12}dyn/cm^2, the sample system is still very stable. That is, it elongates in the direction of applied stress and contracts in the transverse directions as expected in equilibrium. When the stress was raised to even higher value of $\Sigma_{11} = 0.0276\times 10^{12}$dyn/cm^2, some obvious changes in the system properties are observed. Fig. 6.18 shows the time evolution of system properties. The internal energy increases rapidly at the beginning of simulation in response to the increase of applied uniaxial stress, and saturates to certain value after about 2500 time steps, then it fluctuates about the equilibrium value as seen in Fig. 6.18 (a). A usual elastic behavior of elongation in loading direction and contraction in the lateral directions is shown in Fig. 6.18 (d).

Remarkably different behaviors of the system are shown in the stress and the MSD changes with the passage of time. As clearly seen in Fig. 6.18 (b), instead of strain bifurcation, a stress bifurcation appears after about 2500 time steps. In fact, when the equilibrium was reached the average values of the components of the internal stress are $\langle\sigma_{11}\rangle = (0.0029 \pm 0.0003)\times 10^{12}$dyn/cm^2, $\langle\sigma_{22}\rangle = (-0.0027 \pm 0.0002)\times 10^{12}$dyn/cm^2,

$<\sigma_{33}> = (- 0.0276 \pm 0.0003) \times 10^{12} dyn/cm^2$, $<\sigma_{12}> = (0.0210 \pm 0.0001) \times 10^{12} dyn/cm^2$, and $<\sigma_{13}> = <\sigma_{23}> = 0$. A finite shear stress $<\sigma_{12}>$ was developed. The appearance of this shear stress clearly shows that the system has passed the bifurcation point. These developed internal stresses confirm our previous interpretation of the second symmetry breaking. The stepwise increases of the x and y components of the MSD, as shown in Fig. 6.18 (c), indicate that all the atoms in the lattice have an obvious movement in the transverse directions. Consequently, a shear distortion of the system about the (110) plane (diagonal of the x-y plane) occurs (see in Fig. 6.19 the x-y projection of an instantaneous atomic configuration after t = 30000 Δt). This shear distortion gives rise to an in-plane displacement of atoms and accounts for the step change in the x and y components of MSD. The projections of the atomic positions shows that the structure of the lattice has changed to a distorted b.c.t.

The second simulation was to show that the constraint of conserving original tetragonal symmetry prevents Born instability and therefore changes the course of the phase transition. In this simulation study, the same initial configuration of the pre-expanded f.c.c. crystal, as employed in the second simulation of last subsection, was used. The initial uniform strain was $\varepsilon_0 = 0.0356$ induced by a pre-imposed hydrostatic stress $\Sigma_0 = 0.0900 \times 10^{12} dyn/cm^2$. This hydrostatic stress was maintained during all following runs of uniaxial tensile stress load. In this simulation, Born instability was forbidden by the constraint of tetragonal symmetry. The system fails at the tensile stress $\Sigma_0 = 0.0160 \times 10^{12} dyn/cm^2$. Fig. 6.20 shows the time evolution of system properties at this load. The changes in internal energy, internal stress, and MSD show all features of spinodal transition. That the static structure factor S(k) drops down to zero indic that the system has lost its original f.c.c. order.

We have demonstrated in sec. 6.3.2 that in the case of pure dilatation the only instability that can show up on the primary deformation path is the spinodal instability. Here we show that, for uniaxial loading, one can also suppress Born instability by ruling out the possible shear distortion. All these facts show that Born instability is actually a shear instability. Based on these direct observations from simulations, we can go a step further and make our previous conclusion more general: As along as the shear distortion is forbidden, one can also suppress Born stability. The only instability can occur is the spinodal instability. Thus one can define the primary path more clearly as a normal distortion path.

In practice the constraint of conserving the original symmetry can be achieved by increasing the deformation rate. In simulation this can be done by either following the kinetics of deformation process or increasing the increment of the tensile stress in each

constant stress run. We performed a (TΣN) ensemble MD simulation on the pre-expanded model with large increment of tensile load. We found that even without the constraint of symmetry conserving the large normal deformation rate can also suppress the Born instability.

6.4 Temperature Effect on the Stress-Induced Structural Response

In sec. 6.2 we have already seen that for pure dilatation the observed critical strain of spinodal instability is smaller than the value predicted by elastic constants. This difference exceeds the error of our computation. Since the critical strain determined by elastic constants is based on the extrapolations of the elastic constants at small strains, while the simulated critical strain is a direct observation on a "real" dynamic system, this discrepancy between the theory and observation implies that there must be some underlying physics. On the other hand, the temperature effect on the crystalline instabilities is also a very interesting problem that needs to be studied.

In Chapter 4 one has seen that thermal softening has a larger effect on bulk modulus than on shear modulus. Consequently, one can expect that thermally induced softening will also have a larger effect on the critical strain of spinodal instability. Since we have seen that the shear modulus is only a weak function of temperature, there would be only small change in the critical strain of Born instability. In order to see this, a series of simulations of uniform volume expansion of f.c.c. crystal at different temperatures were carried out on both (ThN) and (TΣN) ensembles. The detailed procedures of the simulation were the same as in the case of T = 500K. The temperatures simulated here were T = 800K, 1000K and 1200K.

We found that at temperatures below T = 1000K, the only instability observed in our simulations was spinodal instability. The system always fell apart first in the form of planar decohesion, then broke down into pieces. Fig. 6.21 and 22 show two projections of instantaneous atomic configurations during spinodal transitions at T = 800K and 1000K. The planar decohesion is clearly seen in the projections on x-y and x-z planes. The corresponding critical strains observed were ε_c(T=800K) = 0.0369 and ε_c(T=1000K) = 0.0275. To check the possible size effect and ensure the final structure state of the transition, we performed (ThN) ensemble simulation runs of dilatation on a larger system with 1372 atoms at T = 800K. In this simulation the system failed at the same critical strain ε_c(T=800K) = 0.0369, but the final structure was somewhat different from the small system. The failure of the system was in the form of local decohesion with some disordering around the decohesion zone as shown in Fig. 6.23.

At temperature T = 1200K it was difficult to maintain the system in the crystalline order even at small tensile stress. The system failed at the critical strain ε_c(T=1200K) = 0.01156. The behavior of the system showed all the characteristics of spinodal transition. Fig. 6.24 shows the results of a (ThN) ensemble run. As has been seen before in melting transition (Chapter 4), the internal energy increases as a consequence of entropy increase [see Fig. 6.24 (a) and (b)]. Furthermore, the drop of the static structure factor to zero and the persistent increase of the MSD [Fig. 6.24 (c) and (d)] indicate that the system has lost its crystalline order, and the transition shows all the features of melting. The projections of an instantaneous atomic configuration (Fig. 6.25) confirms that the system has been completely disordered.

For the spinodal transition, so far we have seen that the (ThN) ensemble MD simulation reveals a remarkable difference in the behavior of the internal energy at high and low temperatures. At low temperature, the consequence of the spinodal instability is an internal energy drop. In this case the spinodal transition is truly a mechanical failure, i.e., either fracture or local decohesion. The creation of new surface accounts for the release of the strain energy. While at high temperature, the internal energy shows a jump when spinodal instability is reached. The spinodal transition takes the system to a homogeneously disordered structure. In this case the system lowers its free energy by gaining entropy. Thus the transition is not purely mechanical failure any more. It is the result of the combination of thermodynamic and mechanical effect. Therefore as far as the final state of the transition is concerned, one can distinguish two spinodal transitions: A high temperature spinodal transition by which the system ends up in a homogeneous disordered structure, and a low temperature spinodal transition, through which the system evolves into a lower energy state in the form of either fracture or decohesion.

Fig. 6.26 compares the observed critical strains and the theoretic predictions for both Born instability and spinodal instability. For spinodal instability finite differences in critical strains between predictions and observations are seen at low temperatures. The physical meaning of spinodal instability states that when the bulk modulus vanishes, the system has no cohesion at all and becomes completely unstable. This gives the upper bound of stability of crystal lattice. This is exactly the case of zero temperature where the only contribution to the elastic constants is the Born term. But at finite temperature, the fluctuation term may contribute to destablize the lattice even before the absolute decohesion point is achieved. At low temperature this term is usually small, but when the system is expanded close to the critical strain, the large stress gradient region (as indicated by the inhomogeneous nucleation of cavitation) may be instantaneously formed and make the stress fluctuation very significant. This is not surprising that the critical strain observed is

smaller than that obtained by extrapolation of the small strain value of elastic constants. When temperature is increased the stress fluctuation also becomes larger and larger even away from the critical strain. This thermal activation has a significant contribution to the homogeneous nucleation of the disordered phase. Another feature of this figure is that at high temperature the spinodal curve of the critical strain crosses the Born curve. This indicates that at high temperatures these two instabilities will compete with each other. This is the situation we have seen in Chapter 4 in the case of pure heating to melting.

It is of interest to consider the temperature effect on shear modulus which give rise to Born and shear instability. In Chapter 4 we have known that as the temperature increase both the $G(100)[010] = C_{44}$ and $G(110)[1\bar{1}0] = (C_{11} - C_{12})/2$ decrease. If we take the stress-free configuration at T = 500K as our reference state, measure the strain with respect to the reference state, and plot the thermal softening curves of shear moduli, G(100)[010] and $G(110)[1\bar{1}0]$, and the results at T = 500K together, a very interest result comes out. Fig. 6.27 shows that the data of the thermal softening and the expansion softening at T = 500K fall on the same curves. This strongly suggest that the shear modulus is only a weak function of temperature. Or as a good approximation one can think that the shear modulus is only a function of volume. Jaszczak and Wolf [Jaszczak 92] have showed that for a Lennard-Jones f.c.c. crystal the thermal stiffening in C_{11} and C_{44} were only about 8% and in C_{12} about 1% even at T = 1000K, while at the same temperature the expansion softening for all these three elastic constants are about 60%. These results support our observation. With this in mind it is not surprising that the critical strain of Born instability does not change much when temperature increases, but the bulk modulus is significantly affected by temperature.

Table 6.1A Elastic constants of an f.c.c. crystal in unit of 10^{12} dyn/cm^2. Values are calculated using both fluctuation formula and stress-strain curve method. For the perfect crystal, the x, y, and z axes are aligned with ⟨001⟩ symmetry axes. The data point at different temperatures are found to be well fitted by either a linear function or a second-order polynomial $C_{ij} = a + b\varepsilon + c\varepsilon^2$. Listed in the table are the fitting coefficients for different temperatures.

T (K)	Elastic Constant	a	b	c
0	C_{11}	1.8068	-32.331	210.14
	C_{12}	1.5706	-20.493	117.108
	C_{44}	0.43973	-11.258	72.957
500	C_{11}	1.5495	-30.791	147.39
	C_{12}	1.3776	-20.192	59.025
	C_{44}	0.36652	-10.207	71.022
1000	C_{11}	1.2207	-25.881	-354.04
	C_{12}	1.1234	-23.074	0
	C_{44}	-	-	-

Table 6.1B Bulk modulus B_T and shear modulus G(110)[1$\bar{1}$0] of the same system as functions of strain. Listed are the fitting parameters of the expression $a + b\varepsilon + c\varepsilon^2$ at different temperatures.

T (K)	Elastic Modulus	a	b	c
0	B_T	1.6089	-18.884	83.806
	G(110)[1$\bar{1}$0]	0.11809	-6.0590	52.667
500	B_T	1.4360	-24.149	0
	G(100)[1$\bar{1}$0]	0.08684	-4.7807	0
1000	B_T	1.2694	-35.293	0
	G(100)[1$\bar{1}$0]	0.05332 6	-4.5611	0

Table 6.2 Critical strains predicted by spinodal and Born instability criteria: $C_{11}(\varepsilon_c^S) + 2C_{12}(\varepsilon_c^S) = 0$ or $-V\left(\frac{\partial P}{\partial V}\right)_T = 0$ (spinodal), and $C_{11}(\varepsilon_c^B) - C_{12}(\varepsilon_c^B) = 0$ (Born). They are corresponding to the vanishes of bulk modulus B_T and shear modulus $G(110)[1\bar{1}0]$, respectively.

T (K)	Spinodal instability ε_c^S	Born instability ε_c^B
0	0.0244	0.0656
500	0.0182	0.0595
800	-	0.0468
1000	0.0117	0.0360
1380	0.0022	-

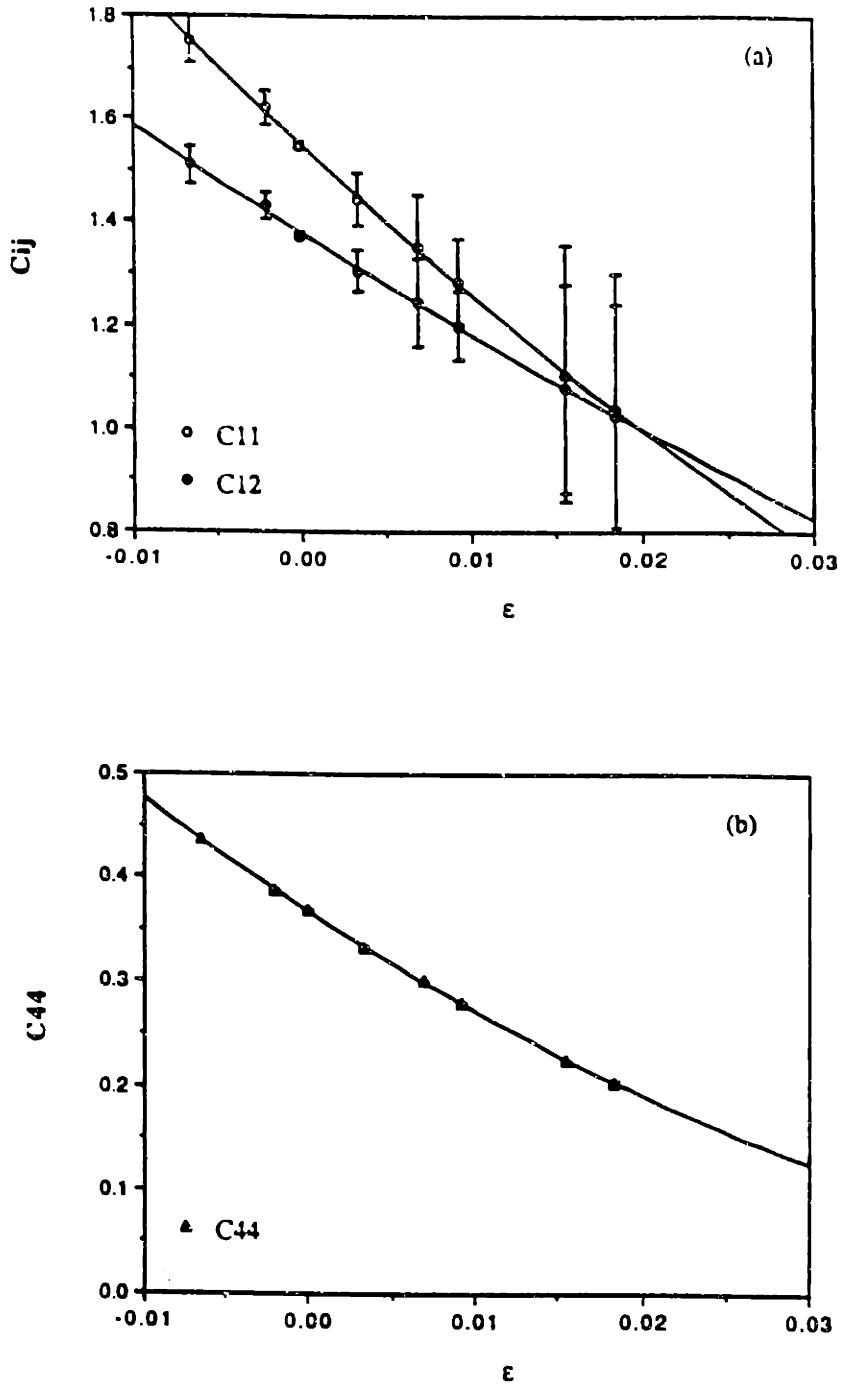

Fig. 6.1 Isothermal elastic constants as a function of strain at T = 500K. Isothermal elastic constants calculated using fluctuation formula. The normal strain is imposed uniformly in all three directions along cubic axes. Shown are data points of C11 and C12 in (a), and C44 in (b). All the elastic constants are in units of 10^{12} dyn/cm^2 The cross point of C11 and C12 gives the critical strain for Born instability.

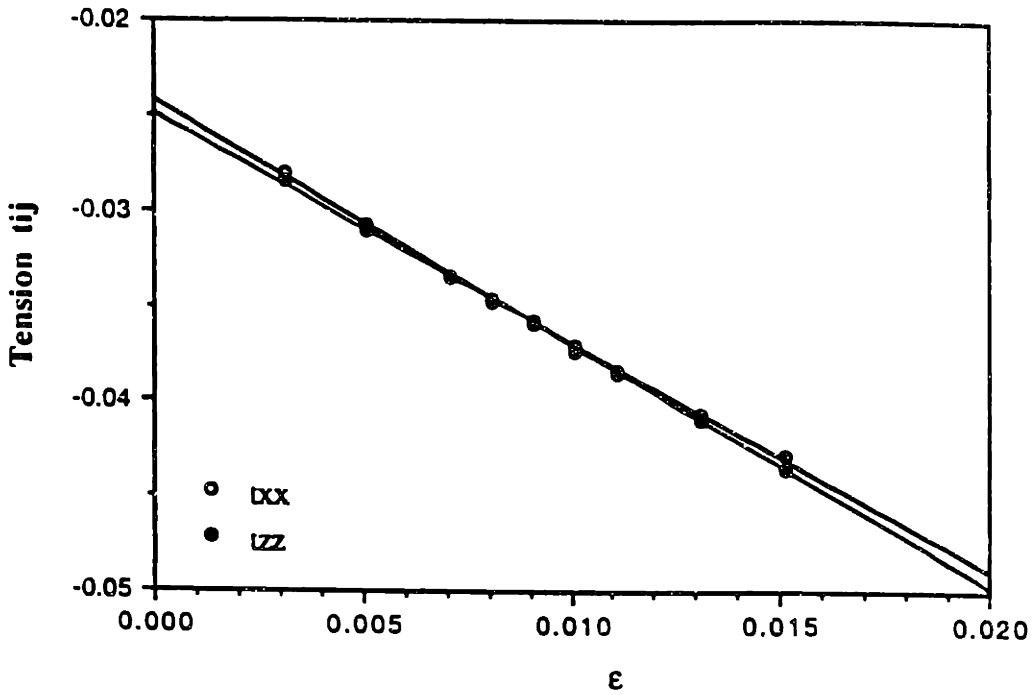

Fig. 6.2 A typical isothermal stress-strain curve at T = 500K. A uniform strain $\varepsilon_0 = 0.0091$ is pre-imposed on an f.c.c. crystal. The thermodynamic tension t_{xx} and t_{zz} are calculated as a function of strain in x direction at fixed $\varepsilon_{yy} = \varepsilon_{zz} = \varepsilon_0$. The thermodynamic tension is in unit same as elastic constant. The negative slopes of these curves represent the C11 and C12 elastic constants respectively.

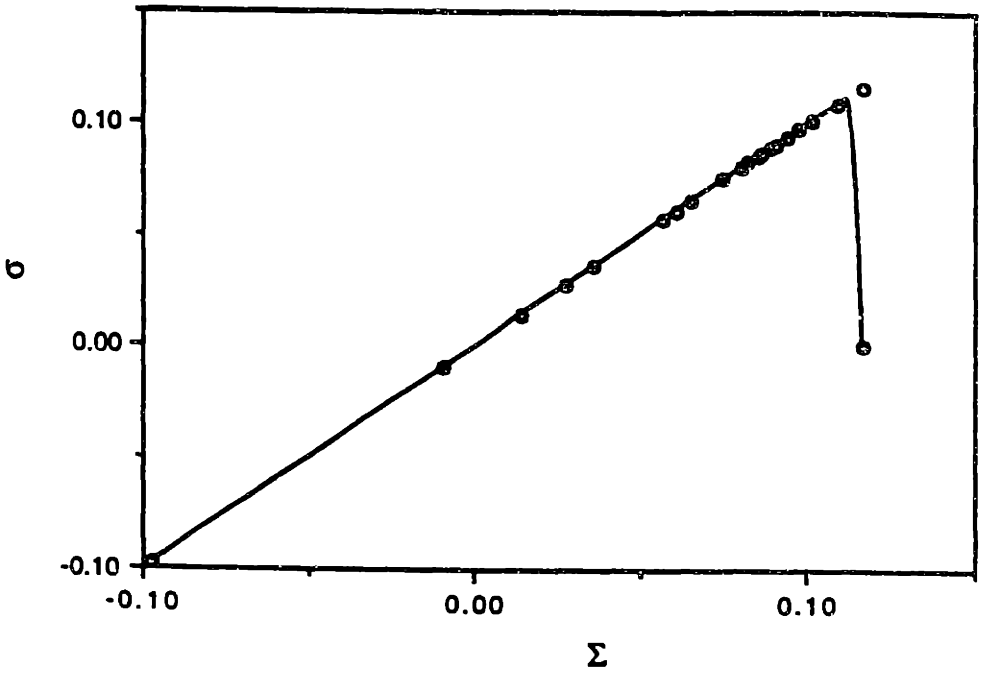

Fig. 6.3 Response of the internal stress σ to the imposed hydrostatic stress Σ.
When system is in mechanical equilibrium the internal stress is equal to the imposed stress. At a tensile load of $\Sigma_c = 0.1162 \times 10^{12}$ dyn/cm^2 the sudden drop of σ indicates that the system fails.

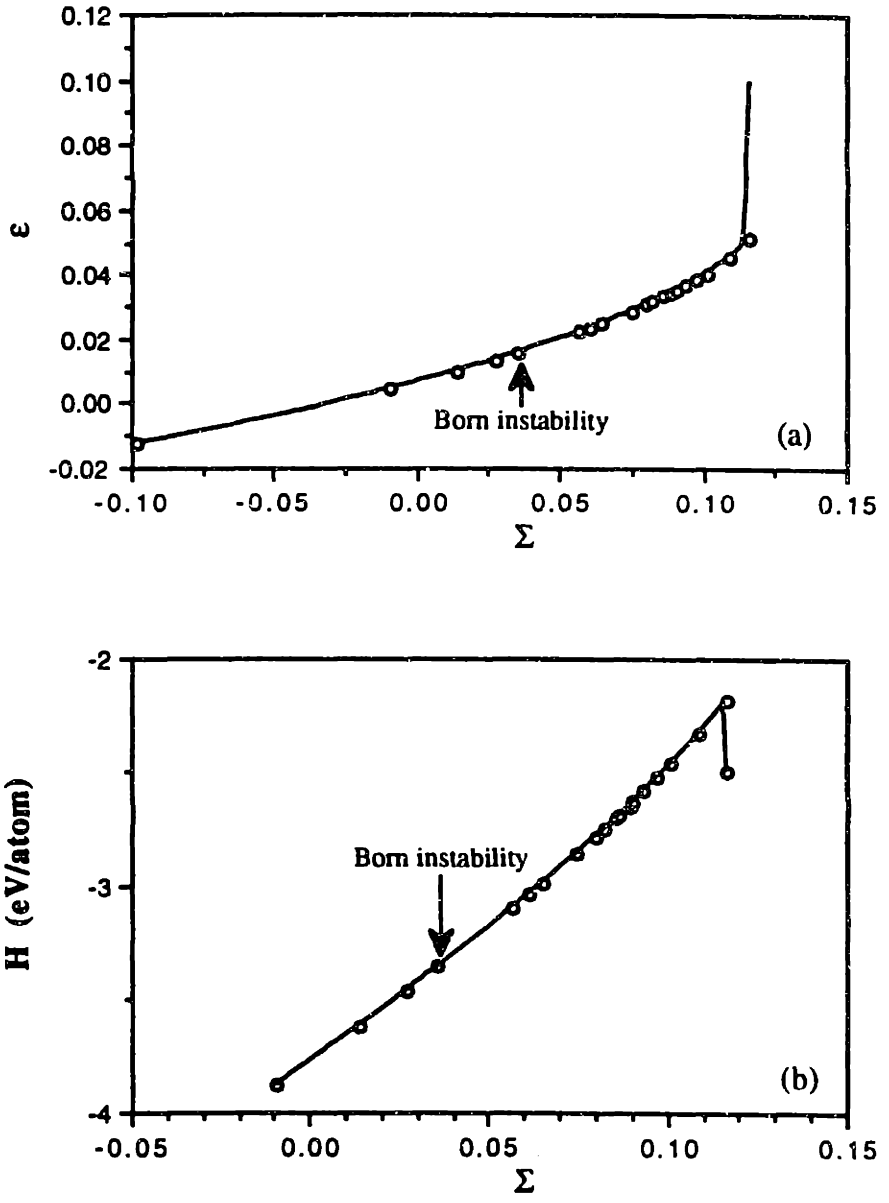

Fig. 6.4 Variations of the internal strain e and the enthalpy H/N with imposed hydrostatic stress.
The pronounced jump in enthalpy and strain show that pure dilatation along the primary path takes the system to spinodal instability. The rapid change of system properties characterize the transition associated with this instability. The observed critical strain ec is smaller than the value predicted by elastic constants. This difference is due to thermal fluctuation (see sec. 6.4 for detail).

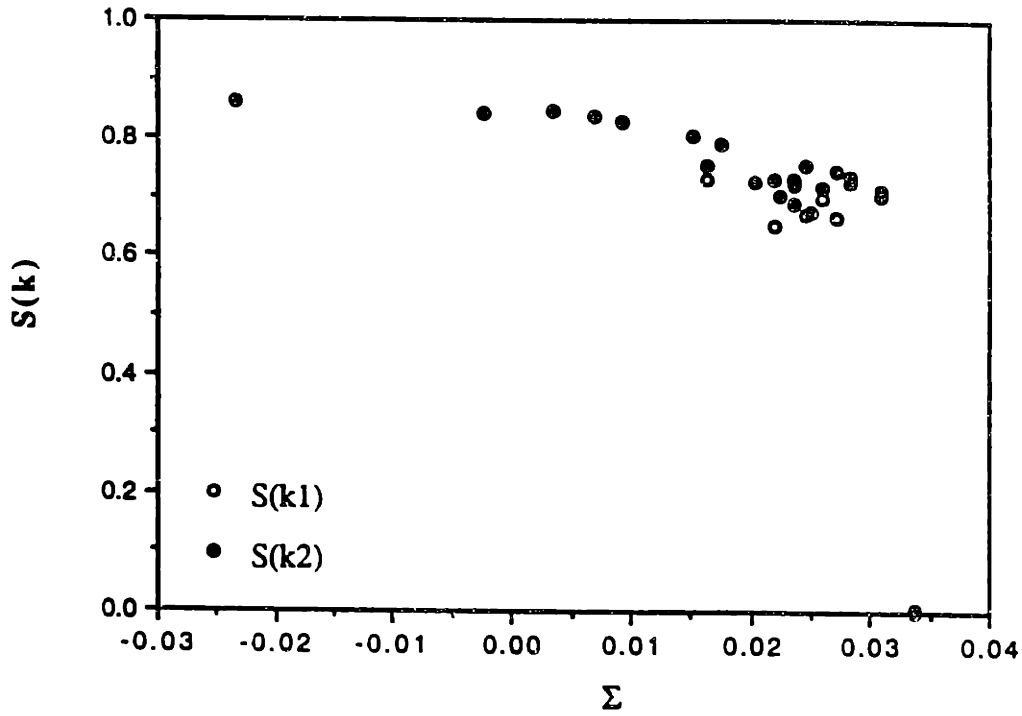

Fig. 6.5 Variation of static structure factor S(k) with the imposed stress.
In the stable region along the primary path the static structure factor steps down slightly and then shows rapid decrease to zero. The sudden drop of S(k) points to the onset of spinodal instability. The vanishing of S(k) indicates that the system has completely lost its original f.c.c. order.

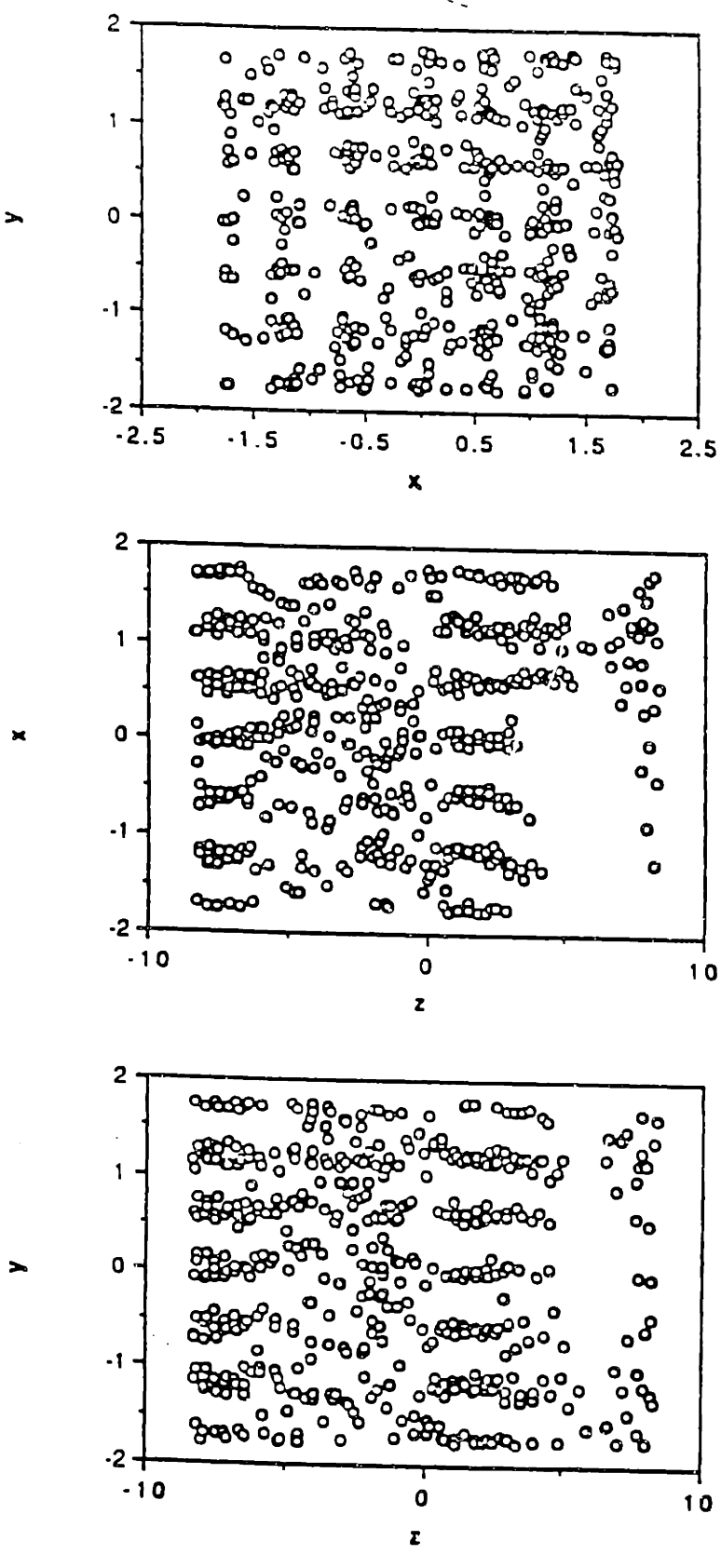

Fig. 6.6 Projections of an instantaneous atomic configuration after transition. In (TΣN) simulation once the system fails, the internal and external stresses do not balance any more (see Fig. 6.3). The volume of the system keeps increasing and, eventually, the system breaks down into pieces. Shown here are three projections of an instantaneous atom positions after about 5000 Dt.

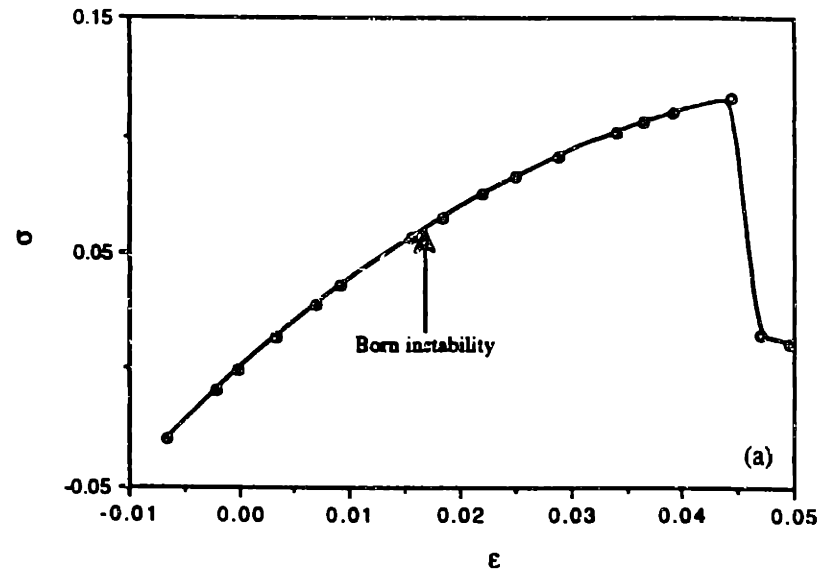

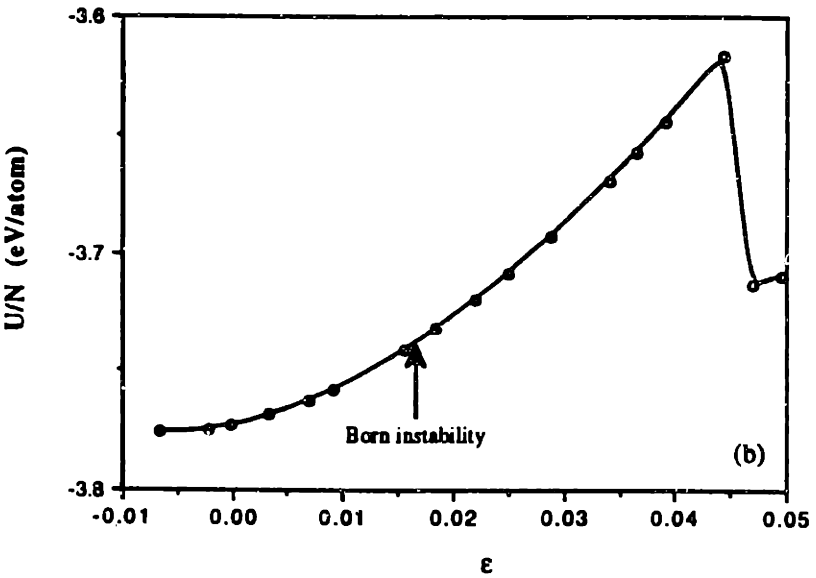

Fig. 6.7 Internal stress and internal energy in response to the imposed strain. Mechanical failure of an f.c.c. crystal under pure dilatation, simulated on a (ThN) ensemble. Instead imposed stress, a uniform strain is imposed on the system in this simulation. Sudden drops in internal stress and internal energy at ec = 0.0539 indicate the onset of spinodal instability. The decrease in internal energy shows that the system has transformed into a lower energy state.

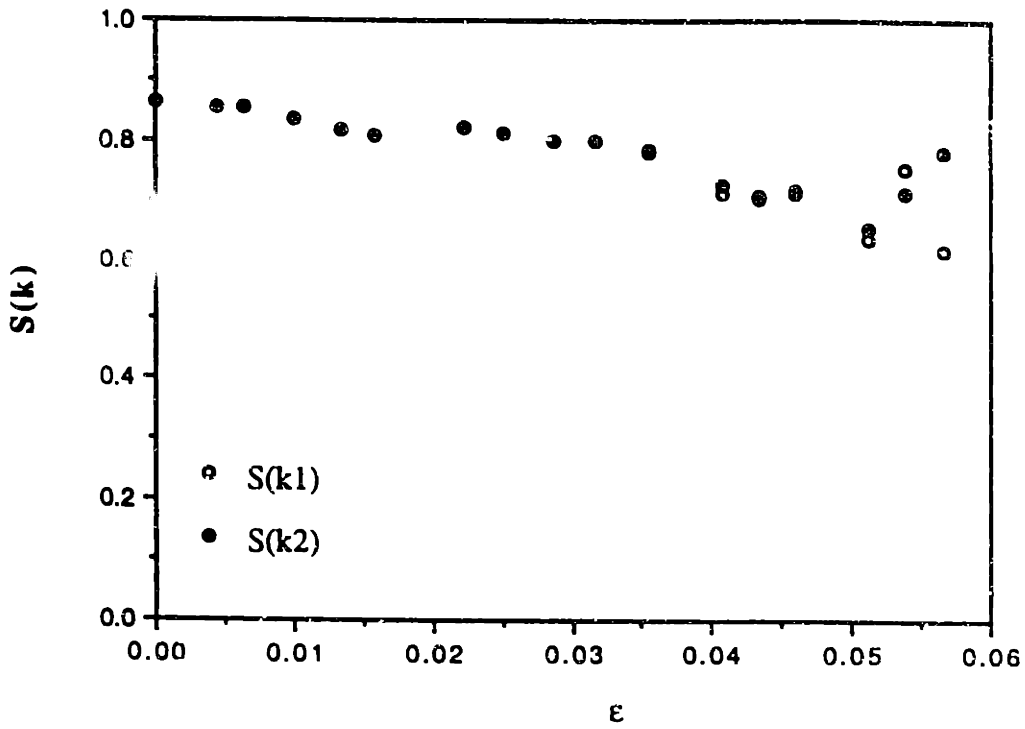

Fig. 6.8 Variation of static structure factor with imposed strain.
The static structure factor steps down slightly in a similar way as in the (TΣN) simulation (see Fig. 6.5), but it does not go to zero at the observed critical strain. This indicates that the system still stays in ordered state after the transition.

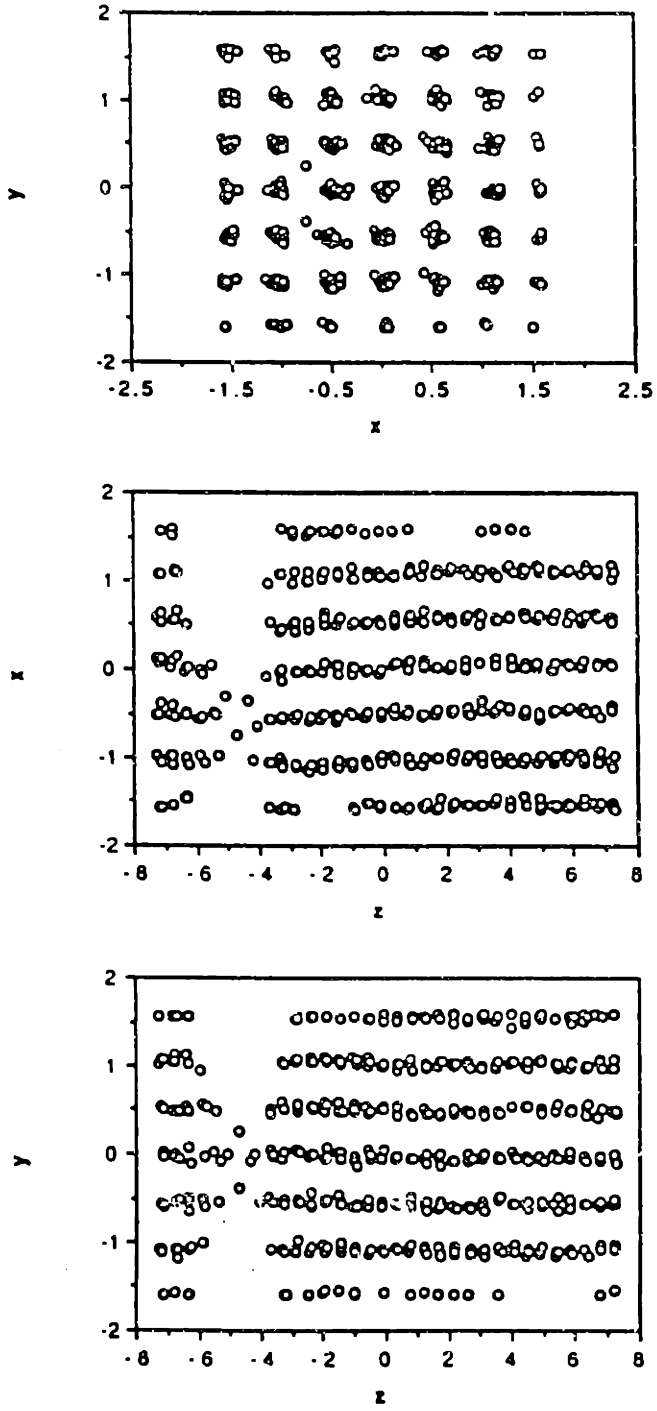

Fig. 6.9 Projections of an instantaneous atomic configuration after transition. Projections of the atomic positions on x-z and y-z planes show clearly that a planar decohesion occurred. The decohesive cleavage fracture is perpendicular to the long dimension (z) of the simulation cell. The initial geometric arrangement of the simulation cell is in such a way that it contains (3,3,14) unit cells of f.c.c. crystal in x, y, and z directions.

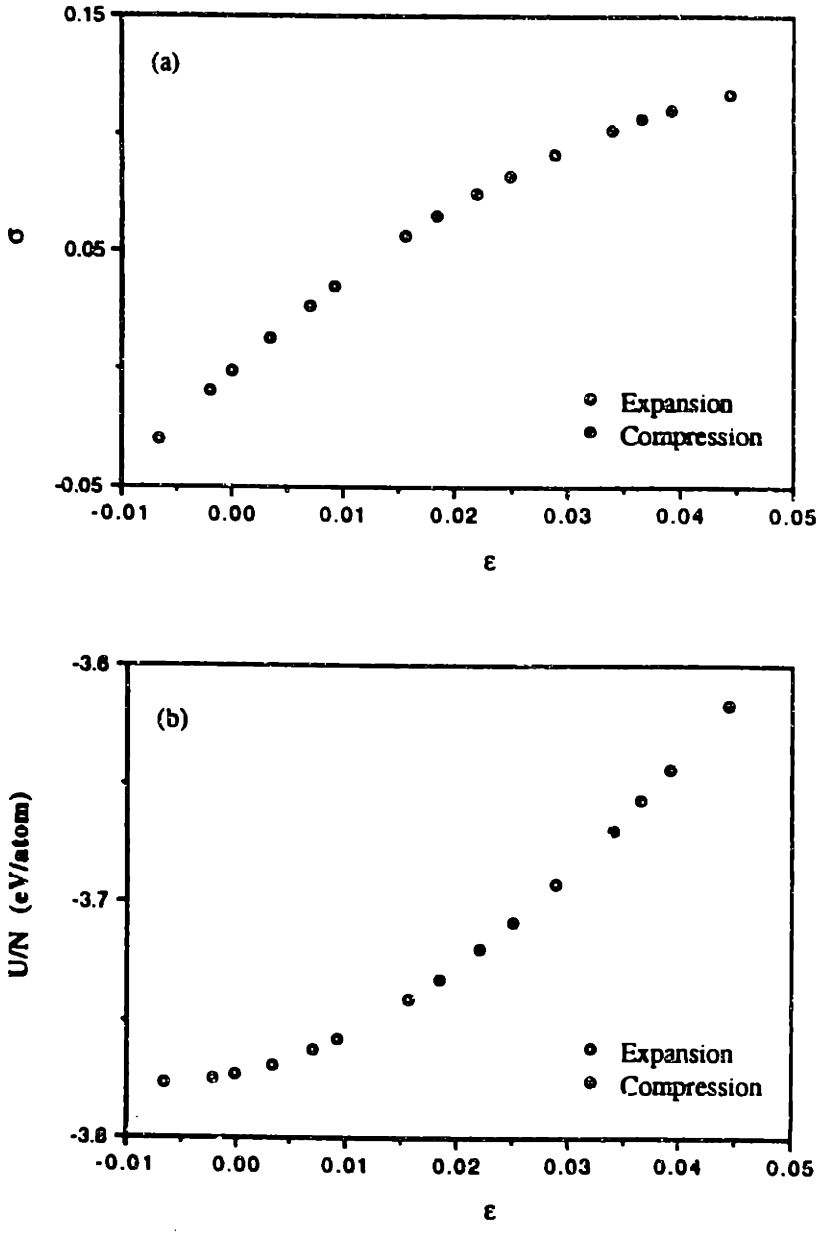

Fig. 6.10 Reversibility of an f.c.c. crystal in the "unstable region" predicted by Born instability.
Plotted here are the internal stress (a) and the internal energy (b) in response to the volumetric deformation. The open circles show the results for pure dilatation and the solid circles represent the response to the compression. The reversibility of the system along the primary path shows that the system is very stable even in the region where Born instability condition is satisfied.

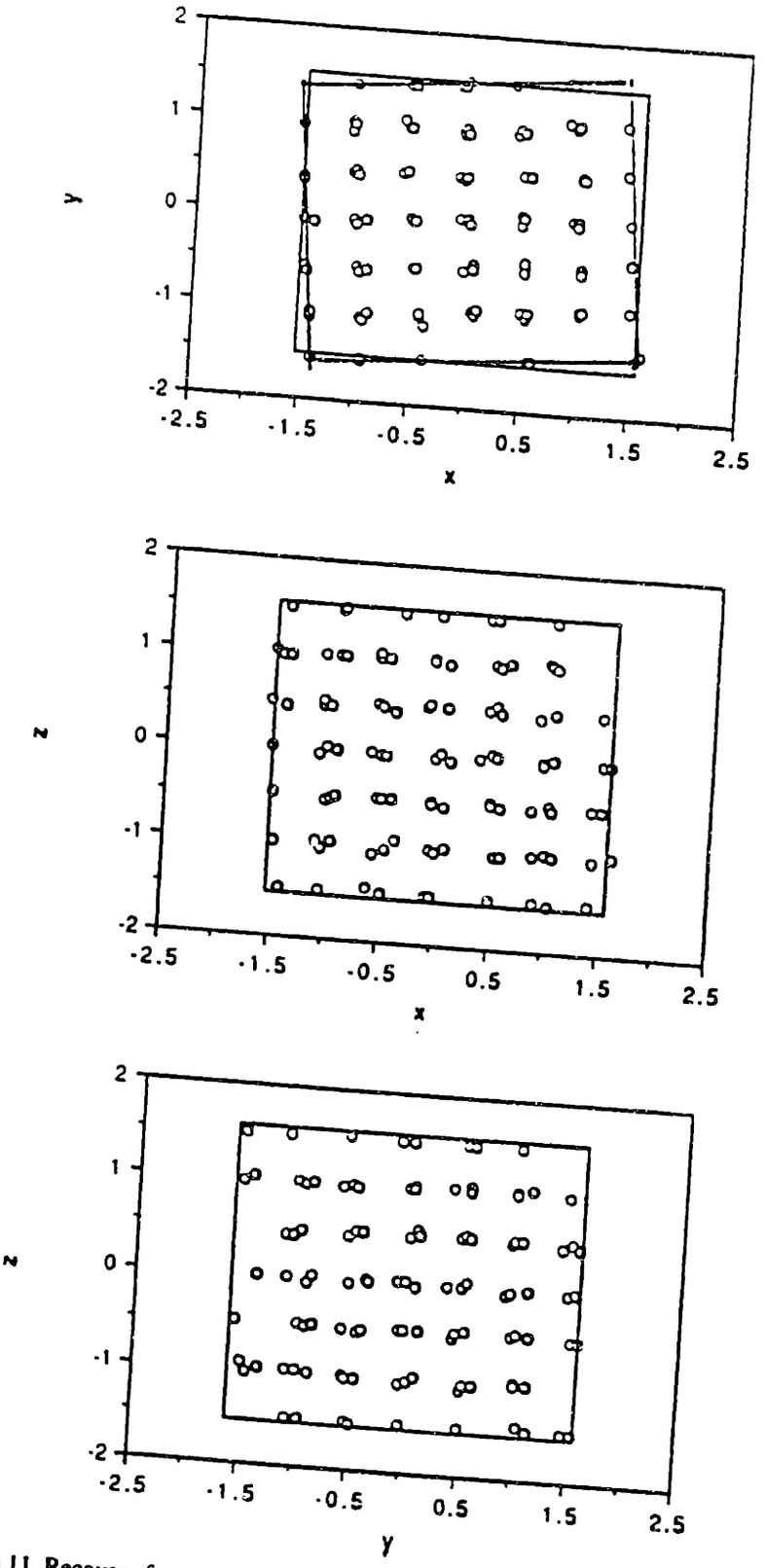

Fig. 6.11 Recovery from small shear perturbation.
Presented are three projections of time averaged atomic configuration (averaged over 200 Δt after 10000 Δt) recovered from a mall shear perturbation in (110) plane along $[\bar{1}10]$ direction. Here x-y plane is (001) plane and (110) is along the diagonal of x-y plane. The full coverage of the system from shear distortion demonstrates that keeping the system in cubic symmetry (here by imposed hydrostatic stress) prevents Born instability.

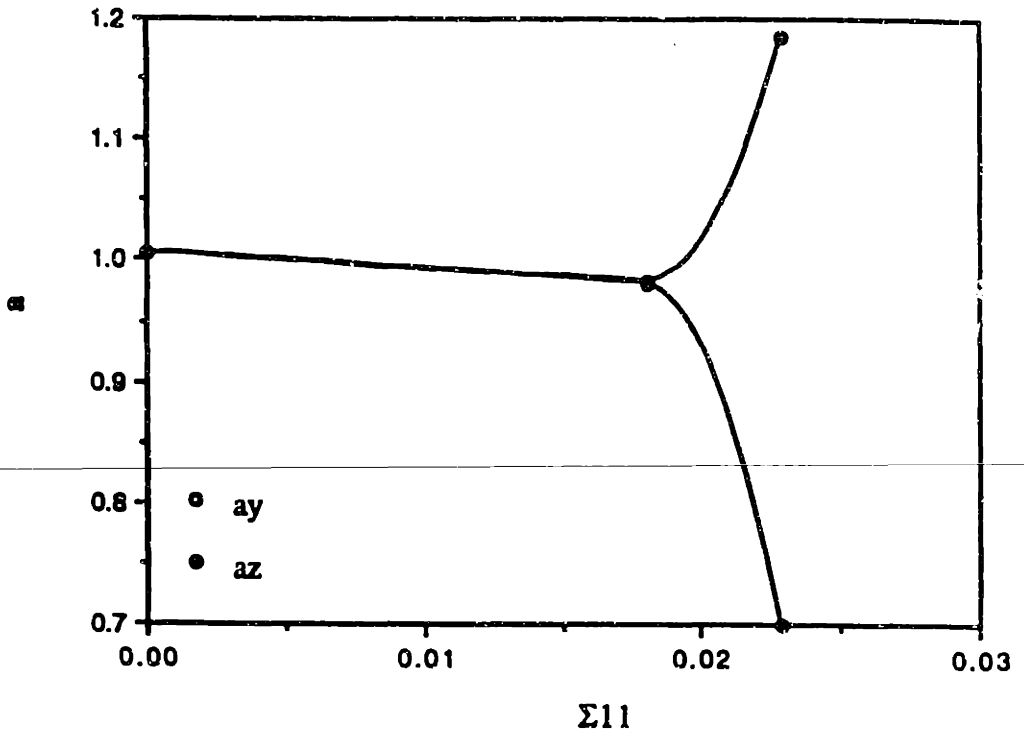

Fig. 6.12 Bifurcation of a stress-free f.c.c. crystal under uniaxial tensile stress load.
A uniaxial stress is loaded on an initially stress-free f.c.c. crystal along x direction. A clear bifurcation in stress-lattice parameter relation in lateral plane is observed after certain uniaxial tensile stress loading.

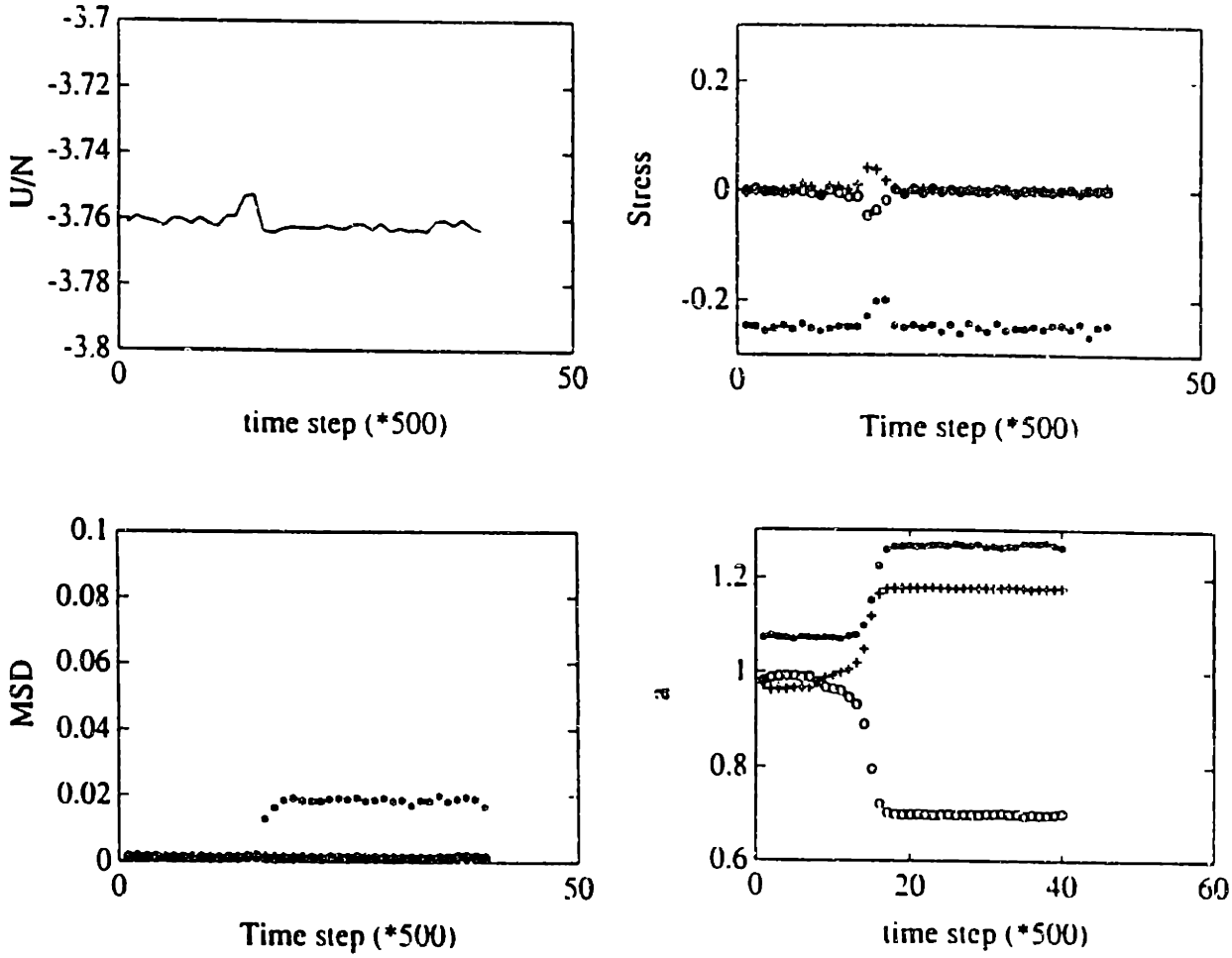

Fig. 6.13 Time evolution of system properties under uniaxial tensile stress load. Behavior of the internal energy U/N (a), internal stress (b), MSD (c), and the lattice parameters (d). Where the star, the cross and the open circle donate the x, y and z component of the property. Two successive processes of symmetry breaking are observed along the trajectory. The first one starts at the bifurcation point and takes the system into an orthorhombic structure. In this stage the bifurcation is symmetric and does not cause any change in other properties. The second one occurs around 7500 Dt after a further rapid change in ay and az. An impulsive change in internal energy and stress is observed. The step change in the x component of MSD indicates that there is an atomic shuffling [Chueng 92] in x direction.

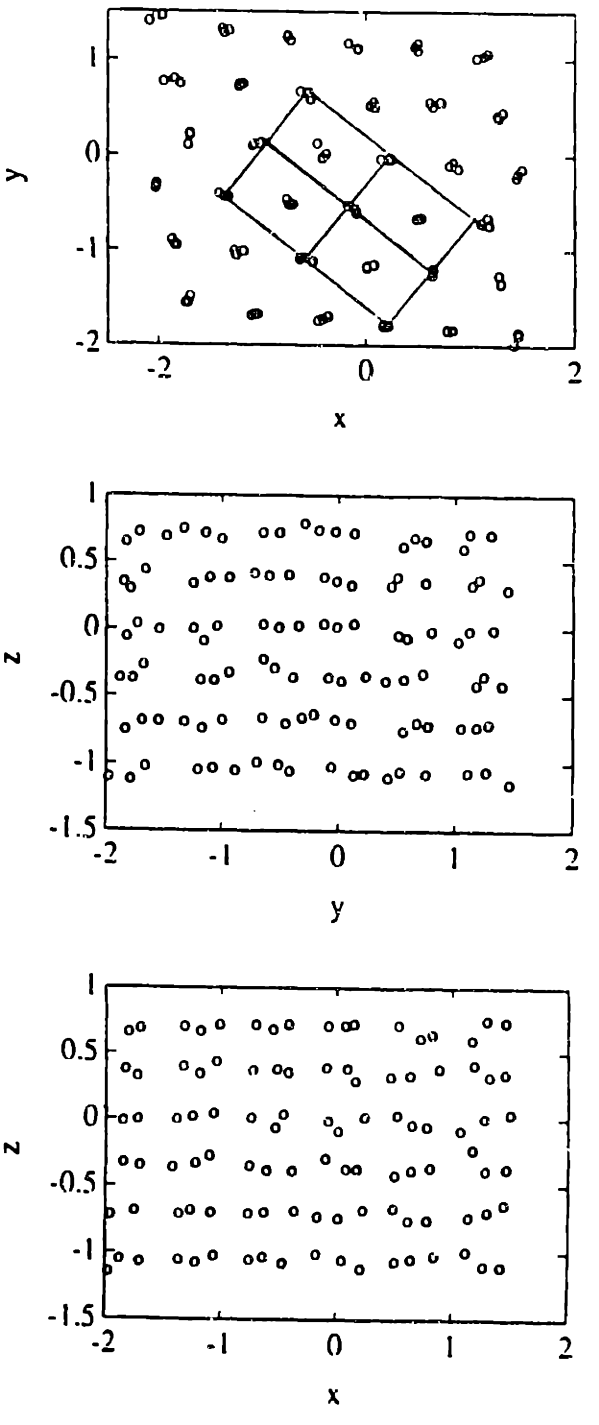

Fig. 6.14 Three projections of the instantaneous atomic configuration at t = 30000 dt (after the second symmetry breaking).
As shown clearly by the network in x-y projection the system has transformed into a distorted b.c.t. structure with ax'=(0.9283±0.0051)a0, ay'=(0.6655±0.0060)a0, and az'=(0.7966±0.0013)a0.

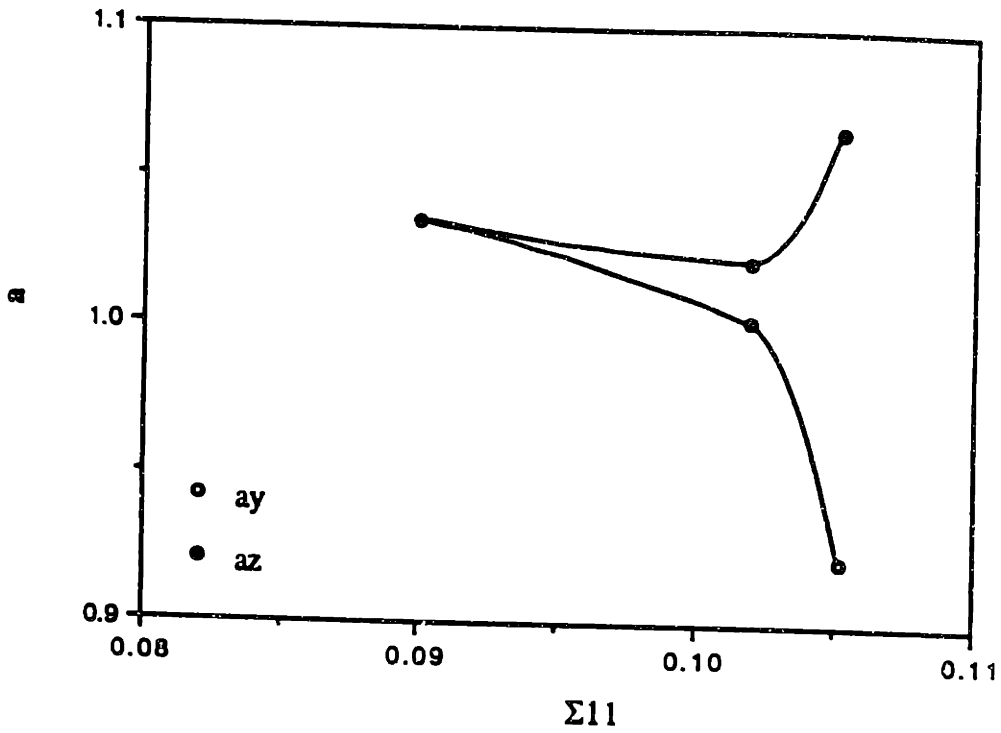

Fig. 6.15 Bifurcation of a pre-stressed f.c.c. crystal under uniaxial tensile stress load. Same as Fig. 6.12 but with pre-imposed hydrostatic stress $\Sigma_0 = 0.0900 \times 10^{12}$ dyn/cm^2, initial configuration is at uniform strain $\varepsilon_0 = 0.0356$. Giving this impose uniaxial stress along x direction during simulation. Again bifurcation occurs but at somewhat small value of uniaxial stress $\Sigma_{11} = 0.0106 \times 10^{12}$ dyn/cm^2.

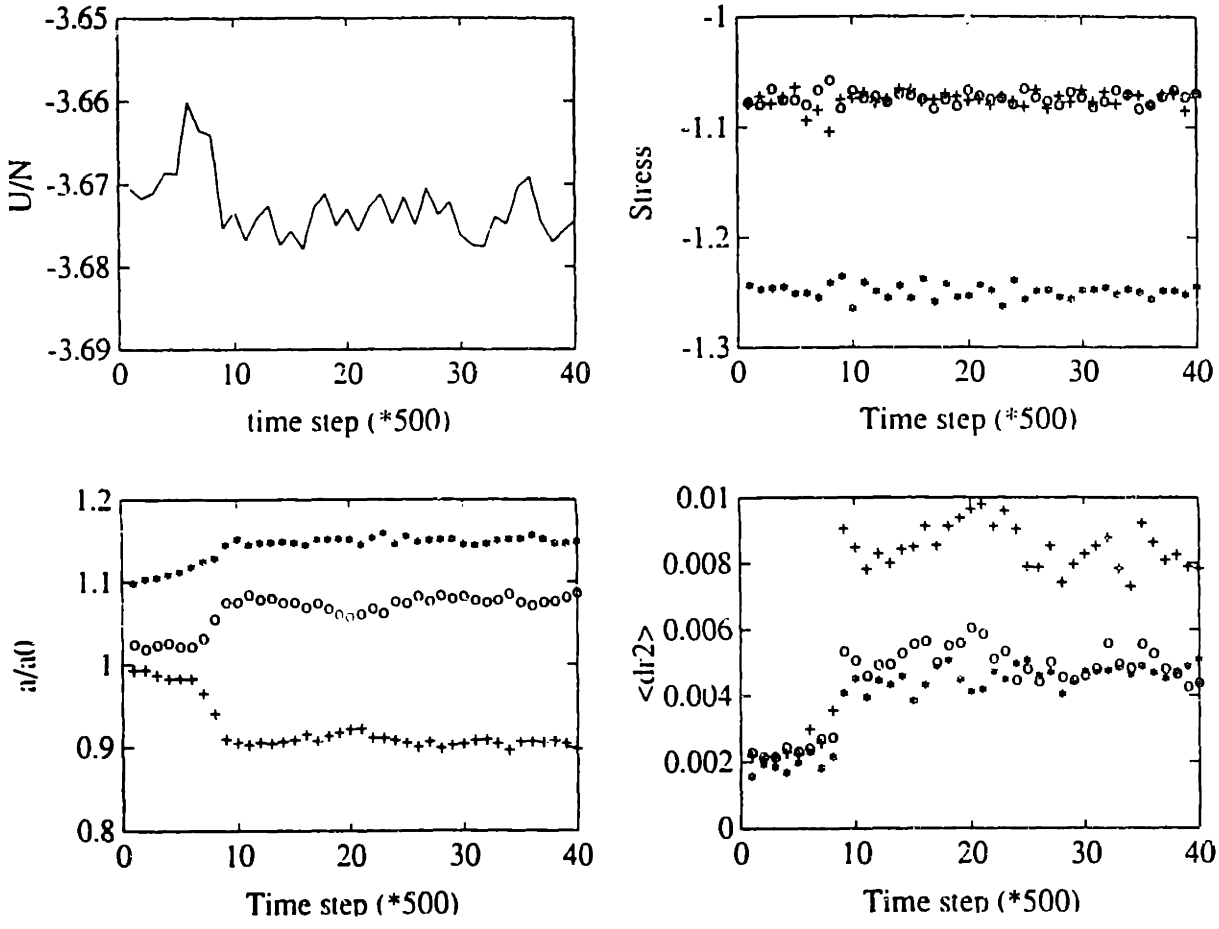

Fig. 6.16 Time evolution of system properties.
Same as Fig. 6.13. Again one sees two symmetry breaking but the impulsive changes in internal energy and internal stresses are smaller.

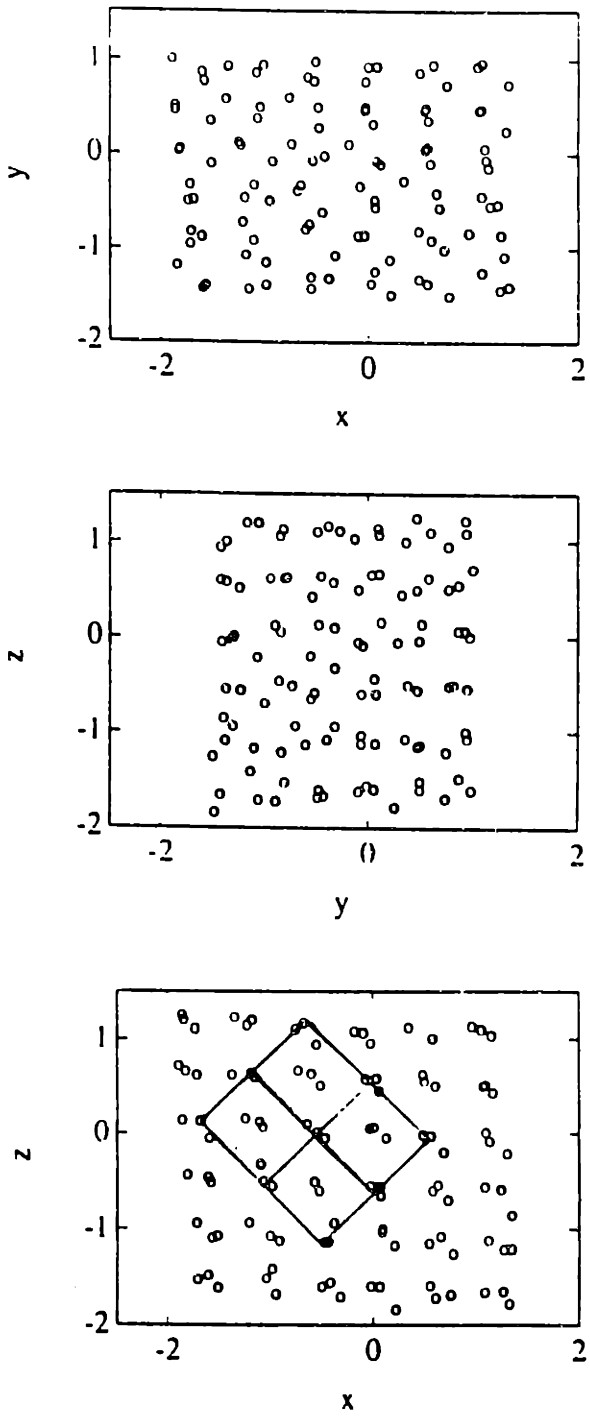

Fig. 6.17 Projections of an instantaneous atomic configuration after the second symmetry breaking.
The projection in x-z plane shows that there is a residual shear distortion in (101) along $[10\bar{1}]$ (the diagonal of x-z plane). The structure of the final state after transition is a distorted b.c.t. with some degree of disorder.

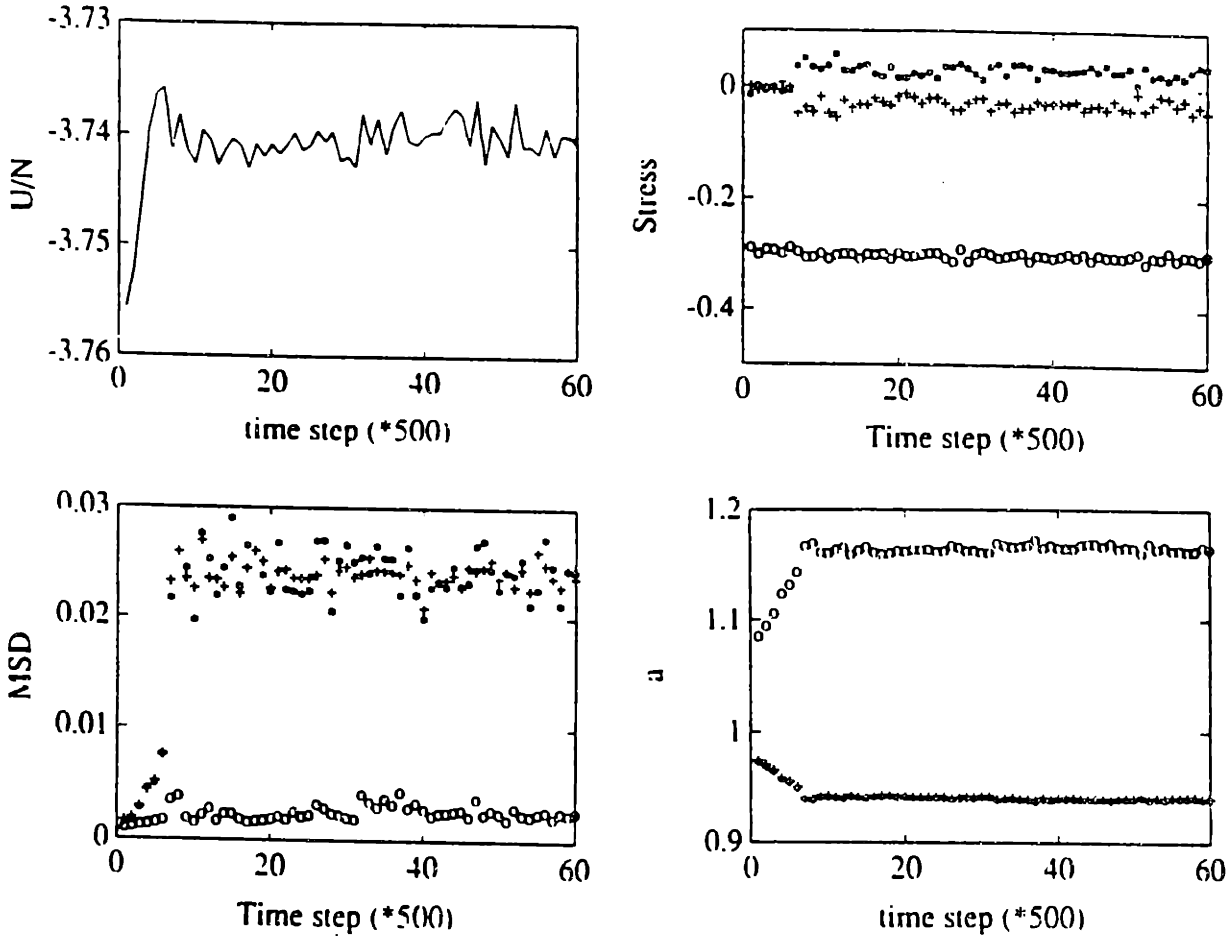

Fig. 6.18 Stress bifurcation under the symmetry constraint in transverse direction. Same as Fig. 6.13. Uniaxial stress is along z axis with the constraint of equal edge in transverse directions (by setting h11 = h22) to prevent strain bifurcation. The internal energy, x and y components of MSD show a step change [see (a) and (b)], which is due to a shear distortion. A internal stress bifurcation is observed. In the meanwhile the system expands further in loading direction (z) and contracts in the lateral directions according to Poisson's effect.

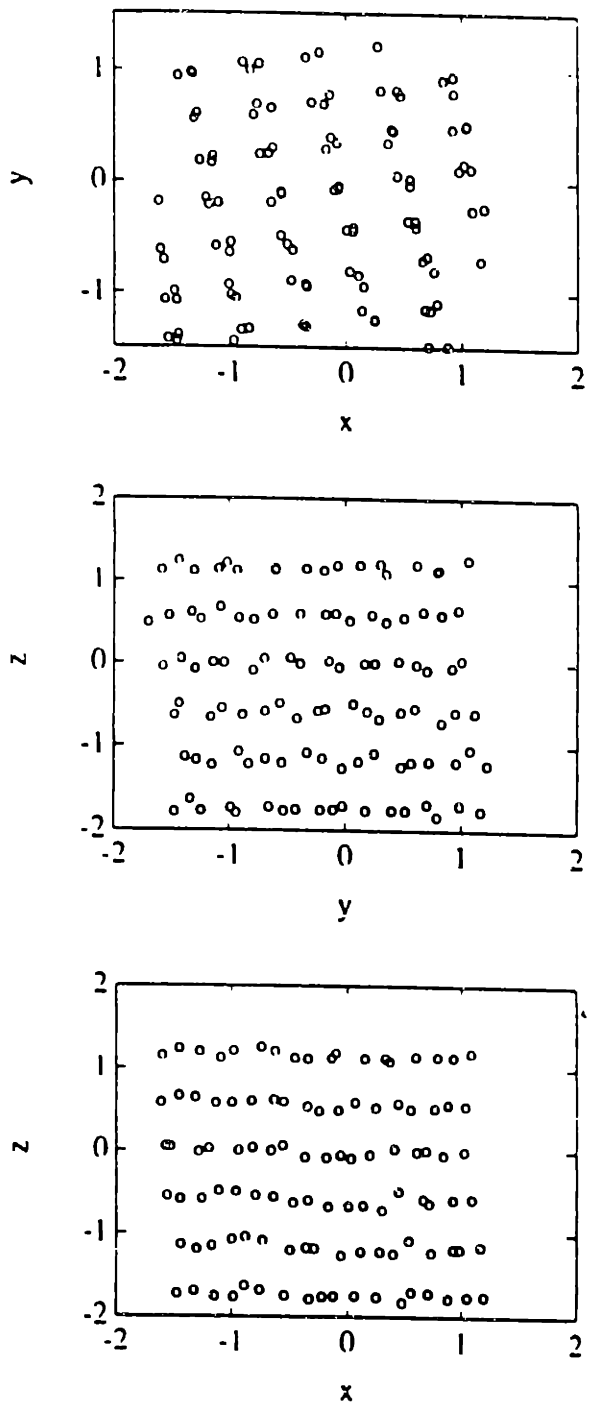

Fig. 6.19 Projections of an instantaneous atomic configuration after stress bifurcation. Similar to the case of strain bifurcation, a shear distortion about (110) plane is observed which indicates that the bifurcation point has been passed. The projections of the atomic positions show that the system has changed to a distorted b.c.t. structurte.

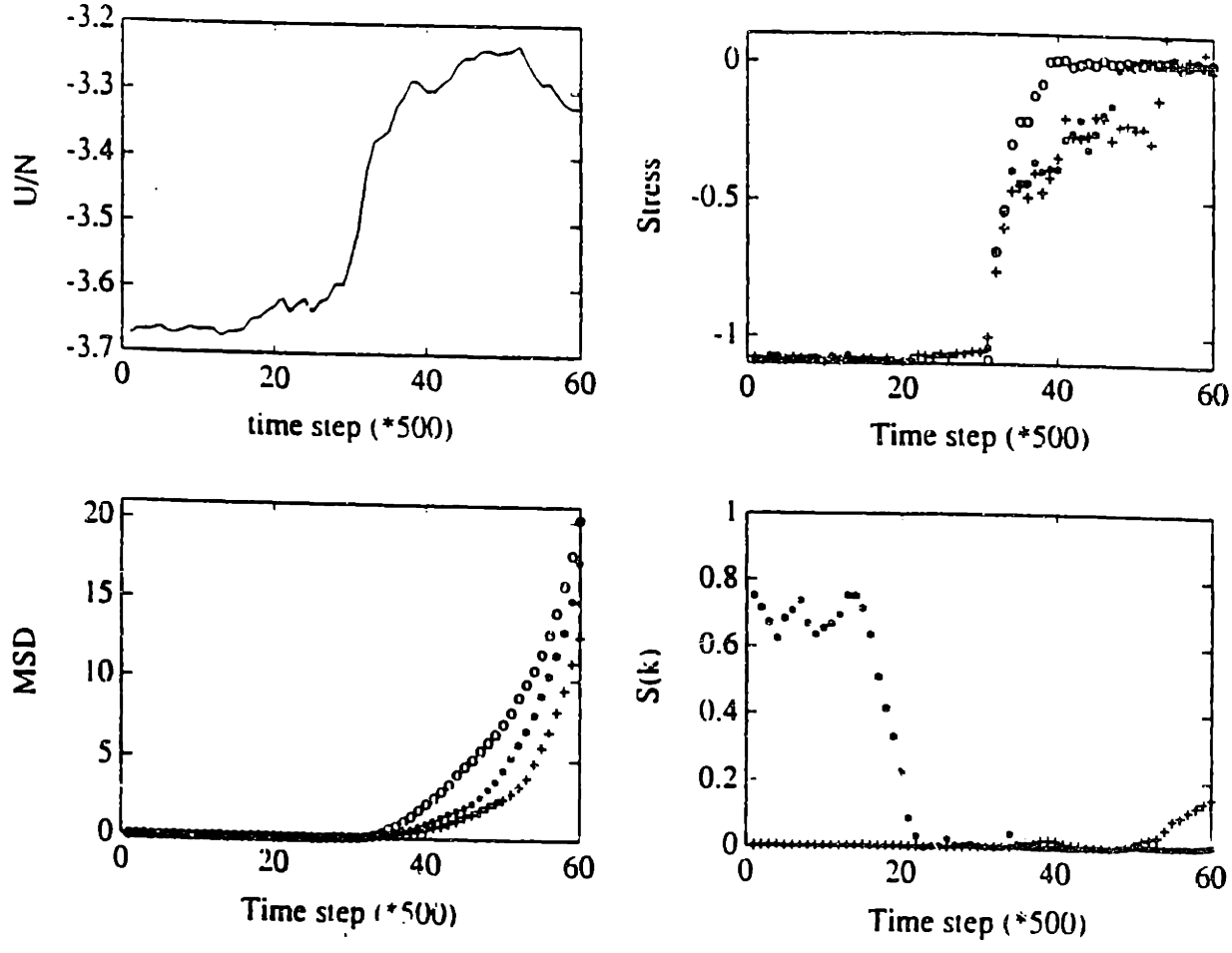

Fig. 6.20 Spinodal failure of an f.c.t. crystal under uniaxial stress.
Same as Fig. 6.18 but with a pre-imposed hydrostatic stress $\Sigma_0 = 0.0900 \times 10^{12}$ dyn/cm^2 and constraint of conserving the original tetragonal symmetry. In this simulation we do not see any more strain bifurcation. System fails at the stress $\Sigma_{11} = 0.0160 \times 10^{12}$ dyn/cm^2. The transition show all features of spinodal instability (compared to Fig. 6.4 and 6.5). Again we demonstrate that along the primary path one cannot see Born instability.

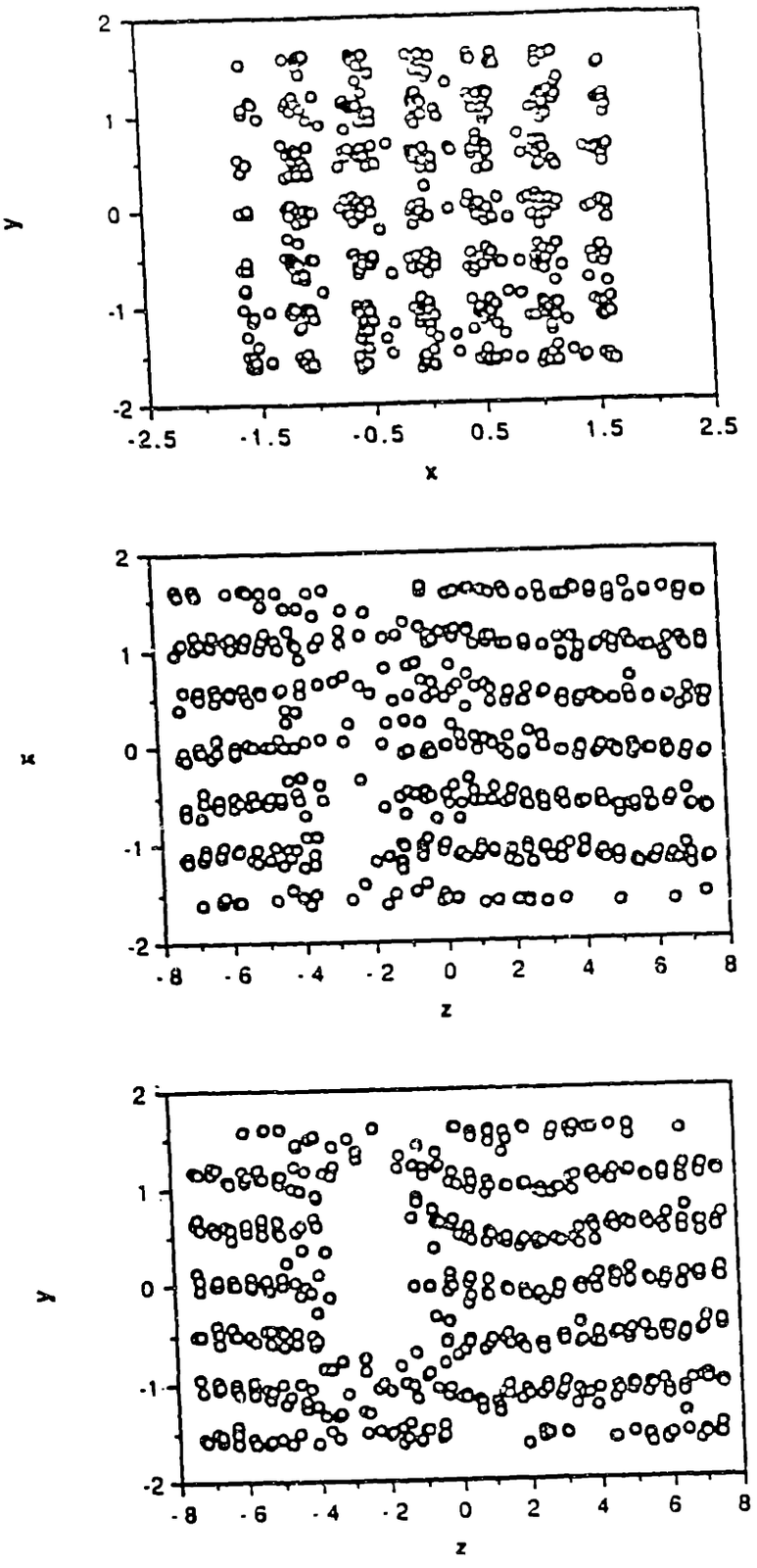

Fig. 6.21 Projections of an instantaneous atomic configuration during spinodal transition at T = 800K.
Same as Fig. 6.6. Failure of an f.c.c. crystal under uniform volume expansion is simulated through (TΣN) ensemble MD simulations at various temperatures. At T = 800K system first fails in the form of cleavage fracture parallel to the short dimensions of the simulation cell as seen in the projection on x-y and x-z planes. Then the system breaks down into pieces.

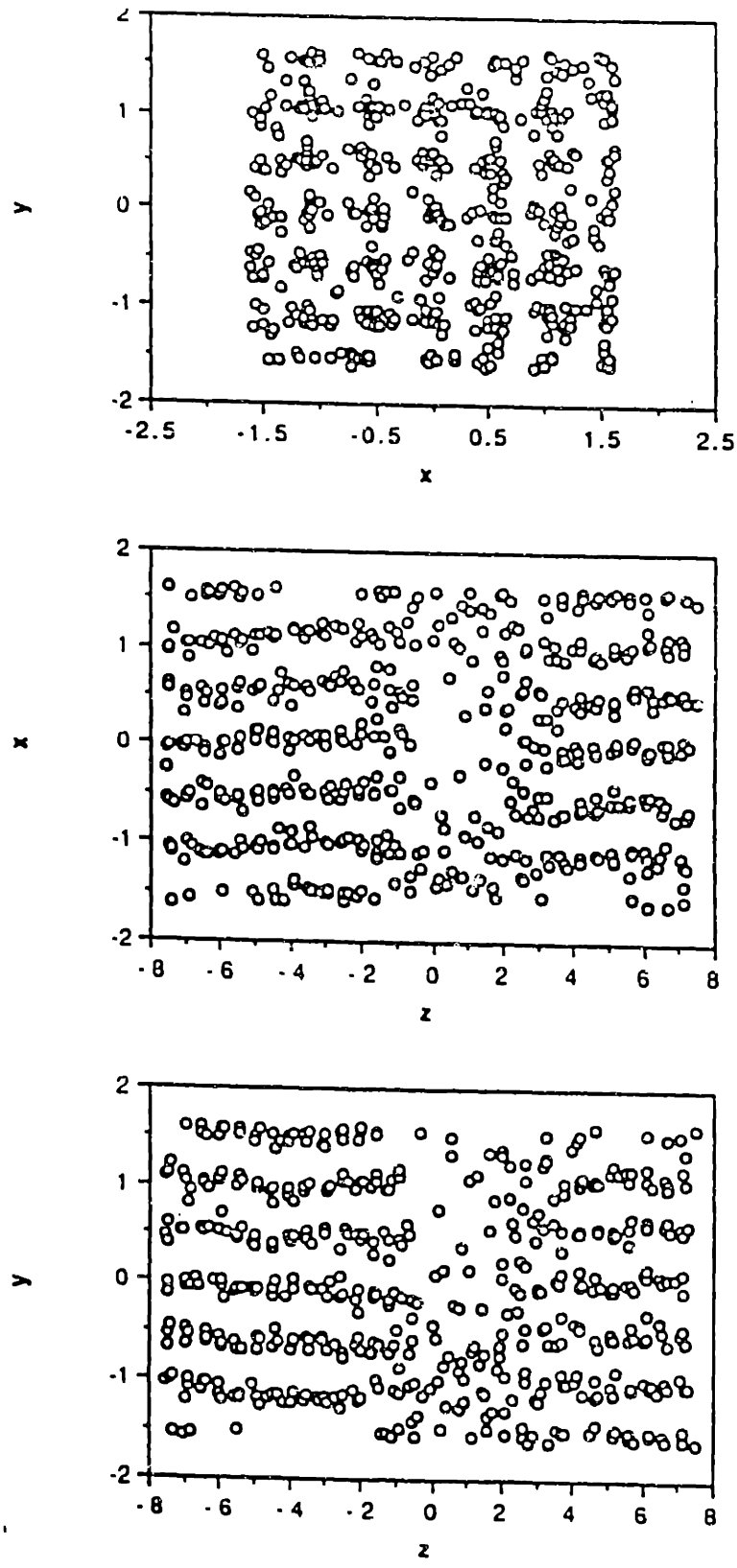

Fig. 6.22 Projections of an instantaneous atomic configuration during spinodal transition at T = 1000K.
Same behavior is seen as in Fig. 6.21.

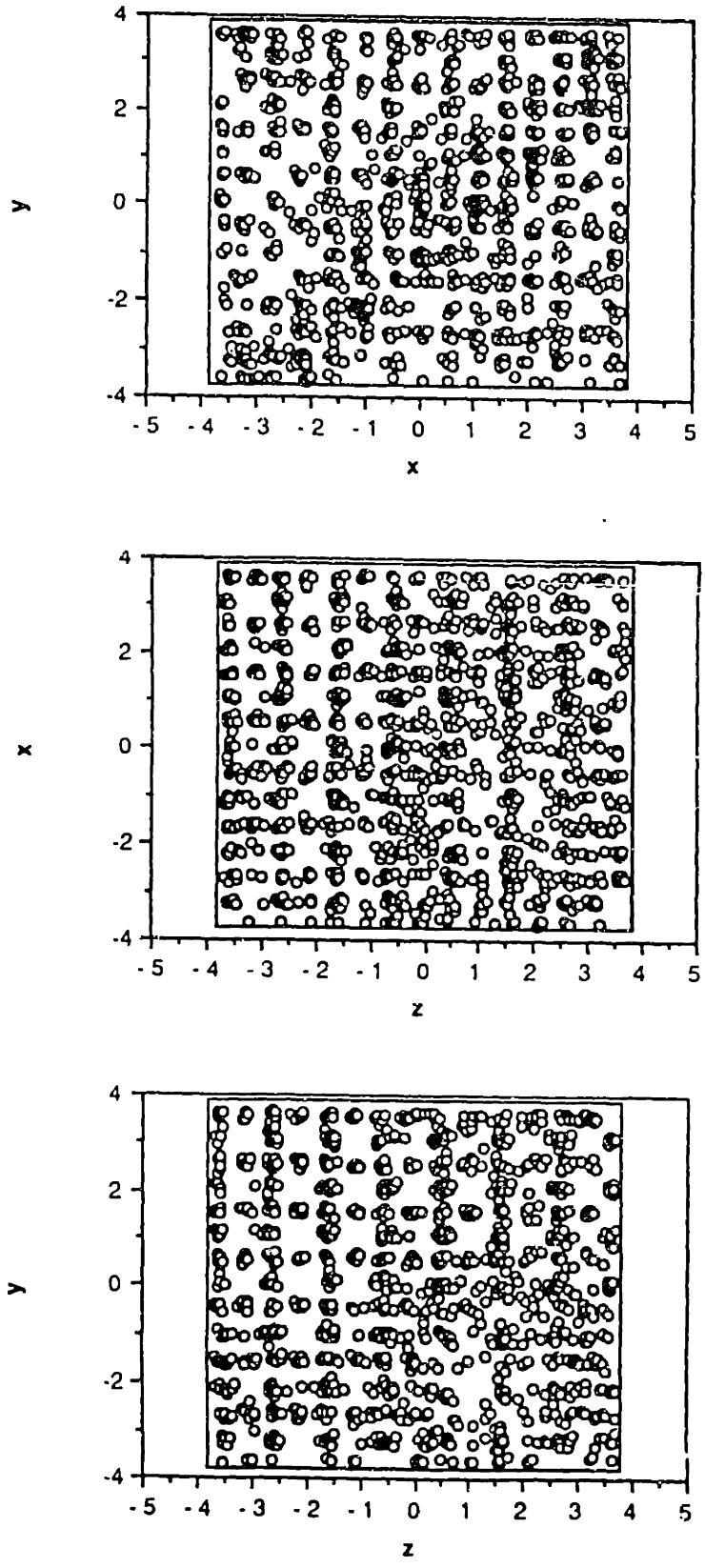

Fig. 6.23 Local decohesion of large system at spinodal instability.
Same as Fig. 6.6. Failure of an f.c.c. crystal (N = 1372) under pure dilatation at T = 800K is simulated through (ThN) ensemble MD simulation. In this case the system fails in the form of local decohesion centered at disordered zone, as shown in the projections in x-z and y-z planes.

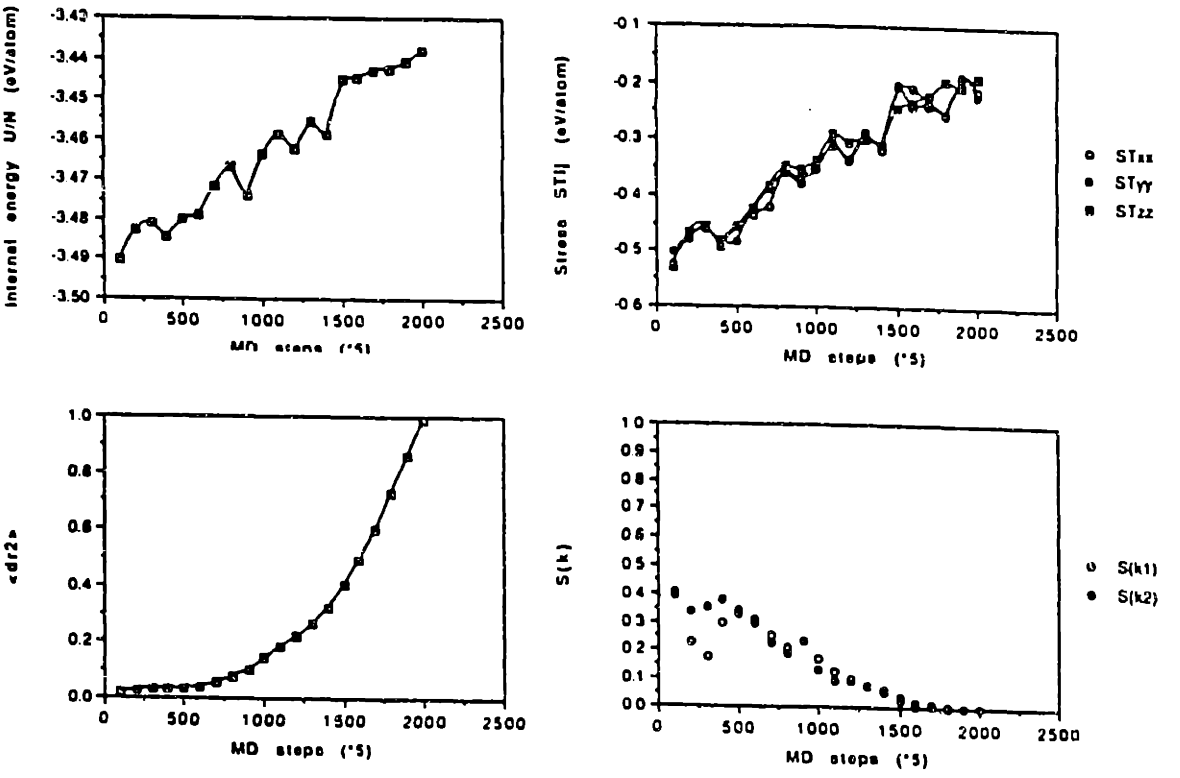

Fig. 6.24 Structural disordering after spinodal transition at T = 1200K.
Time evolution of internal energy (a), internal stresses (b), MSD (c), and static structure factor (d). This simulation is carried out on a (ThN) ensemble to maintain as higher value of imposed-strain as possible. The large increase in internal energy and release of the internal stresses point to the onset of spinodal. The rise in the internal energy is due to the entropy increase since the volume of the system is fixed during simulation. Static structure factor shows that after 7500 Dt system completely losses its crystalline order. The persistent increase in mean-squared displacement shows that system behaves very much like melting during the transition.

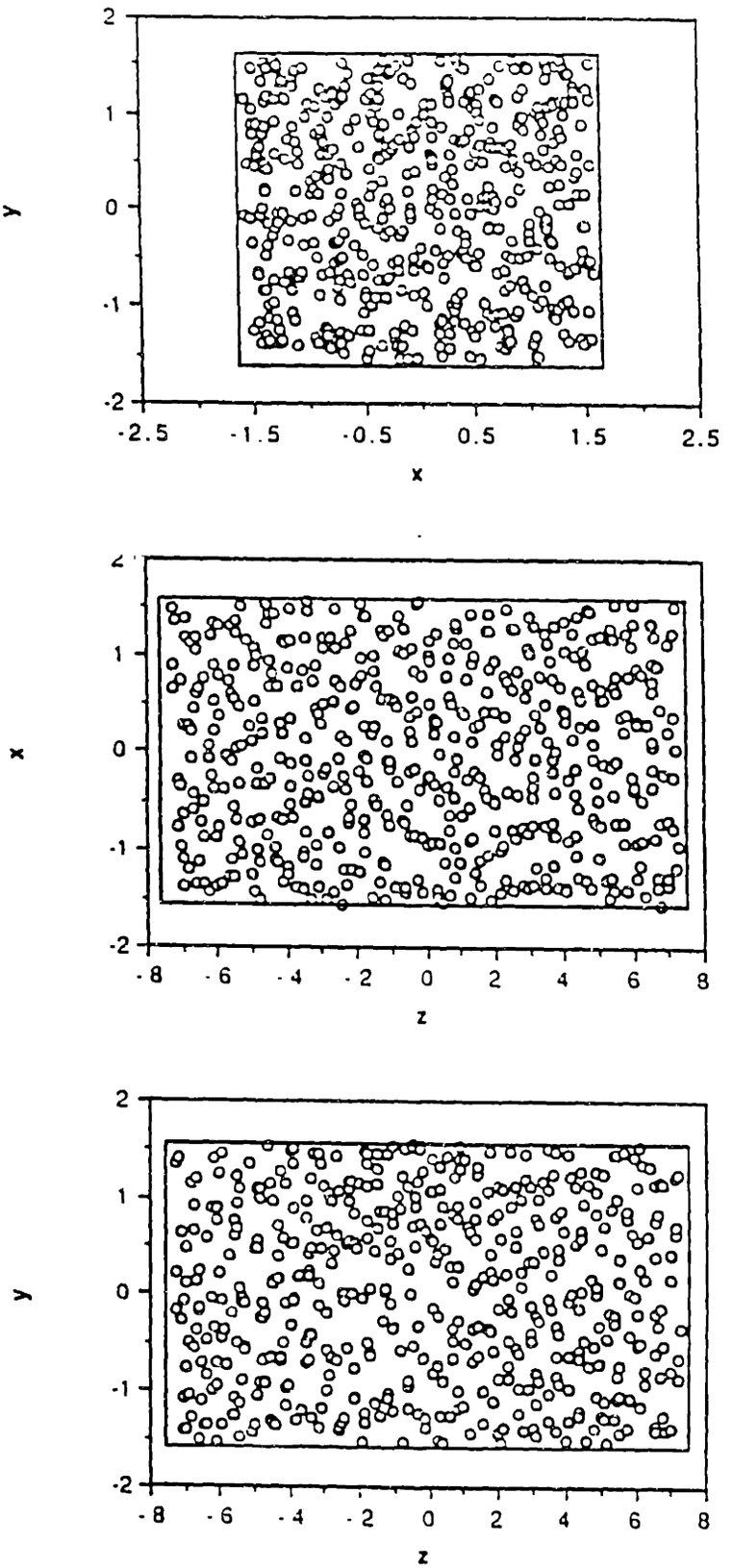

Fig. 6.25 Instantaneous atomic configuration after the spinodal transition at T = 1200K. The three projections of the instantaneous atomic configuration show that the system has been completely disordered.

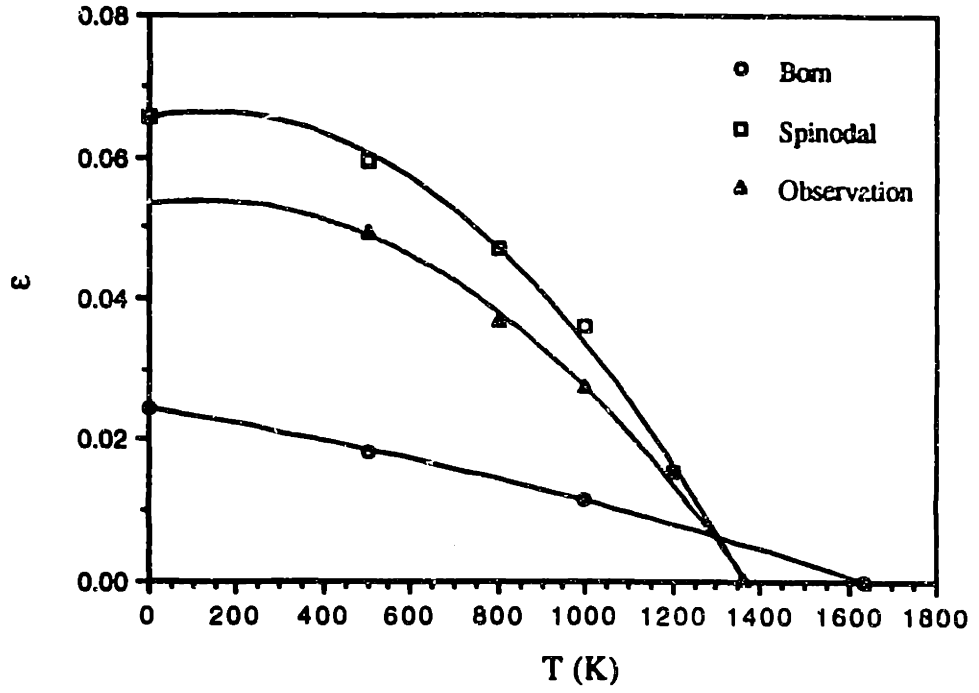

Fig. 6.26 Prediction and observation values of the critical strain for Born and spinodal instability at different temperatures.

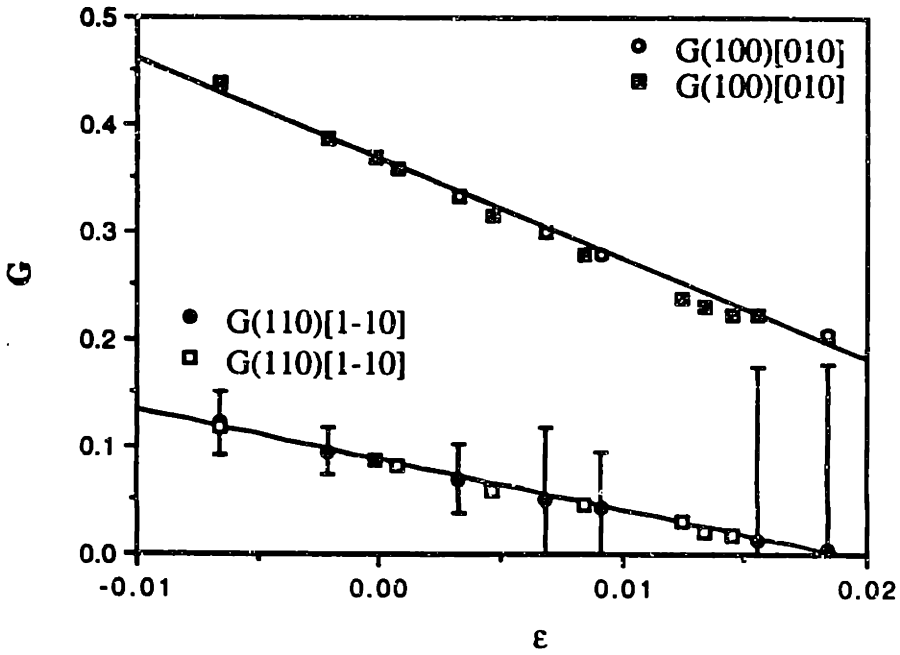

Fig. 6.27 Effect of the thermal and expansion softening on the shear moduli.

Chapter 7
Unstable Structural Responses of Brain-Boundary Superlattice with EAM Potential

7.1 Introduction

In previous chapters we have demonstrated by direct observations from MC and MD simulations that the failure behavior of a perfect crystal under applied stress or strain load can be well described by elastic instability criteria and the corresponding eigendeformation paths. These eigendeformation paths are extremely important in the sense that they uniquely define the deformations which can lead to specific failure mode of certain instability and suppress the others. The instability criteria themselves are very general and independent on the elastic symmetry and atomic interaction of the crystal, while the eigendeformation states of the instabilities are different for different symmetries. We have studied the structural responses of an f.c.c. crystal, which we treated as a homogeneous system, to various elastic deformations. However, if the crystal is inhomogeneous, such as including grain boundaries or interfaces, its elastic behavior may be dramatically affected by the presence of the planar defects [Schuller 90, Phillpot 90]. It is of interest to ask if there is any effect of the crystalline inhomogeneity on the instability of the crystal and the transition associated with the instability.

A simple and well-studied model system which enables us to deal with this issue is the so-called grain-boundary superlattice (GBSL). [Wolf 89a, 89b, 90a, 90b, Jaszczak 90, 91] In this chapter, for simplicity, we will focus on the spinodal instability of a grain-boundary superlattice model under applied hydrostatic stress and uniaxial strain, since in these cases the deformations induced by the imposed stress or stain coincided with the primary path of deformation associated with the spinodal instability. The question we will address is: Given the deformation along the primary path which leads to spinodal instability in perfect crystal, does it lead to the same instability in GBSL? We have already known from Chapters 2 and 3 that this system has tetragonal elastic symmetry, and the dilatation should be able to lead to spinodal instability. Therefore, the direct simulation of a GBSL system will be a crucial test of this theoretical prediction. Another question we are interested in is the final state that the GBSL system will evolve into after the instability has set in.

The interface systems are intrinsically inhomogeneous. This inhomogeneity may cause dramatic difference in structural and elastic properties at or near an interface and in

the nearby bulk material. Since the presence of incoherence of the two parts of crystalline lattices beside the interface (we only consider pure element system), a narrow structurally disordered region and a volume expansion appears at the interface even at zero temperature. These structural disordering and volume expansion have similar effects on the elastic properties as in the case of thermal expansion [Jaszczak 92], i.e., the structural-disordering stiffening and volume-expansion softening. However, because of their localization near the interface, these types of structure disorder and volume expansion are inhomogeneous. In our so called model of Σ29 GBSL (see Chapter 3), a overall extension of 3.5% in GB normal ([001]) and a contraction of -1.2% by Poisson's effect in the lateral directions [100] and [010] are observed at zero temperature, which give a overall volume expansion of 0.9%.

The elastic response of materials is known to be particularly strongly affected by small changes in volume, or in the interatomic distances [Phillpot 90]. For instance, the thermal expansion of most materials, typically only a few percent different from zero temperature to melting, causes an elastic softening in elastic constants typically by about 50%. By comparison, the changes in interatomic distances due to the presence of interfaces may be considerably larger, suggesting that the elastic response near an interface may differ largely from that of the nearby bulk perfect-crystal material. Calculations of local elastic constants of GBSL [Kluge 89] have shown that this is indeed the case.

It has been shown [Wolf 89a, Phillpot 90, Jaszczak 92] that the interplay of the structural disorder and the volume expansion at the interface is mainly responsible for the so-called supermodulus effect * (i.e., a strengthening of certain elastic moduli and a softening of others) of superlattice materials. Figs. 7.1 (a), (b), (c), and (d) show some properties of a Σ5 GBSL as a function of the modulation wavelength Λ at T = 0K, calculated by Wolf and Lutsko [Wolf 89a]. Since in their paper all the results of elastic moduli they presented are normalized by the average values of these quantities in the $\Lambda \rightarrow \infty$ limit, we also quote their results of $\Lambda \rightarrow \infty$ here in Table 7.1. Their calculations showed that the anomalous elastic behavior, including dramatically reduced shear modulus and significantly enhanced Young's and biaxial moduli, is primarily an interface effect whose magnitude is controlled by the result of the competition between the local structural disordering and volume expansion due to the presence of interfaces in the system. According to Fig. 7.1 (a) the increase in the young's and biaxial moduli, Y_z and Y_{bz}, is coupled with a drastic decrease in $G_{xz} \equiv C_{44}$ [see Fig. 7.1 (b)]. As can be seen from Fig. 7.1 (c) this behavior in the elastic moduli is accompanied by an expansion in the z-direction which, despite the resulting Poisson contraction in the x-y interface plane, gives rise to an

* For a recent review, see MRS Bull. XV(9) (1990); XV(10) (1990).

overall expansion of the system volume which indicates an increasing amount of structural disordering with decreasing of the modulation wavelength Λ (or the number of the atomic planes between two GB's).

It is interesting that the behavior of the elastic constants do not show anomalies except for C_{33}. As shown in Fig. 7.1 (d), all other elastic constants decrease monotomically as Λ decreases, or equivalently as the overall volume increases. Although C_{33} shows only a small overall enhancement over the related bulk value ($\Lambda \rightarrow \Lambda^{\infty}$), the Young's modulus Y_z is enhanced significantly. These two results are not in conflict given that the Young's modulus is a combination of the elastic constants: $Y_z = C_{33} - 2C_{13}^2/(C_{11} + C_{12})$. Assuming C_{33} to be independent of Λ, an increase in Y_z can be caused by a decrease in $C_{13}^2/(C_{11} + C_{12})$ as Λ decreases. A fast decrease in C_{13}^2 than in $C_{11} + C_{12}$, as is the case in Fig. 7.1 (d), gives rise to such an increase in Y_z as Λ gets smaller. The shear modulus, by contrast, is related to only a single elastic constant ($G_{xz} = G_{yz} = C_{44}$). Its decrease therefore cannot be a result of a balance among different elastic constants but the "normal" behavior of the elastic constant as system volume is increased. Thus the "supermodulus effect" may be aptly named, in that a "super elastic-constant effect" may not exist.

The GB energy, E_{GB}, represents a more quantitative measure for the effect that the GB's in the superlattice exert on each other. The GB energy, defined as the difference in energy between the GBSL and an undistorted perfect-crystal reference system with the same number of atoms but no interfaces, provides a direct measurement of the degree of structural disorder per interface in the system. According to Fig. 7.1 (a), for larger values of Λ E_{GB} is practically independent of Λ. For $\Lambda \leq 5a$, however, a sharp decrease in E_{GB} occurs. Noting that the force which the GB's exert on each other is governed by $dE_{GB}/d\Lambda$, it is obvious from the results in Fig. 7.1 (a) that for the shorter distances the GB's attract one another. As evidenced by the GB energy for $\Lambda \leq 5a$, the sharp decrease signals a decreasing amount of structural disorder per interface as the elastic strain fields of different GB's start to overlap, with the consequence of smaller elastic anomalies. [Wolf 89b, 90c, 90d].

Another interesting result they found is that the Poisson's effect tends to enhance the elastic anomaly. With the mechanism of structure-disordering stiffening and volume-expansion softening in mind, it is not surprising that the Poisson contraction tends to decrease the volume fraction, and thus to enhance the elastic anomalies.

Based on these insights gained form these studies and its 3d periodicity, one would expect that the GBSL may be a very desirable model for present study of crystal instability. Since the elastic properties of the GBSL are governed by the supermodulation wavelength

Λ, one can obtain a suitable model by purposely choosing Λ which allows one to maintain the inhomogeneity of the system but does not lose too mush crystalline order. The model we will use has the value of Λ = 8a, which contains 8 atom planes between two GB's. As discussed in Chapter 3, the simulation cell contains two GB's and 16 atom planes each with 29 atoms.

7.2 Thermal Expansion of GBSL

In order to build up the reference states for the study of the applied stress later on, we first look at the thermal expansion of the stress-free system. The system is heated up from T = 0K with a temperature increment of ΔT = 200K. For each temperature, the GBSL system was first equilibrated for 10,000 time steps under zero applied stress, and another 50,000 time steps were made to generate the atomic trajectories for property calculations. The anisotropic thermal expansion of the GBSL system is illustrated in Fig. 7.2 (a), which shows the changes in the average lattice parameters normal (a_z) and parallel ($a_{x,y}$) to the interface. As one might expect from the enhanced anharmonicity associated with the extension in z-direction and the contraction in x- and y-directions (see above), which give rise to a local volume expansion at GB's even at zero temperature, the thermal expansion of a_z is larger than that of $a_{x,y}$.

Fig. 7.2 (b) shows system internal energy as a function of temperature. It increases gradually as the system expands until temperature T = 800K, at which a decrease in internal energy is observed. At this point an anomalous expansion in x- and y-directions and a contraction in z-direction occurs. The overall result is a volume decrease indicating the disappearing of the disordered region in the GBSL. A recrystalization occurs. The system recovers from the twisted state and goes back to an f.c.c. lattice with the lattice parameters $(a/a_0)_{x,y}$ = 1.0124 and $(a/a_0)_z$ = 1.0101, respectively. These values are very close to a/a_0 = 1.0113 of the perfect f.c.c. crystal at this temperature. The static structure factor shows clear evidence of the recrystalization process. As can seen in Fig. 7.2 (c), as temperature increases the structure factors $S(\mathbf{k}_1)$ and $S(\mathbf{k}_2)$ both decrease gradually. At T = 800K, $S(\mathbf{k}_1)$ drops all the way down to zero while the $S(\mathbf{k}_2)$ still stays at a finite value. Since our $\mathbf{k}_1$ and $\mathbf{k}_2$ are chosen such that for a perfect GBSL they give the values $S(\mathbf{k}_1)$ = 1 and $S(\mathbf{k}_2)$ = 1 for region A and B, respectively. At T = 800K the vanishing of $S(\mathbf{k}_1)$ indicates the disappearance of region A and points to the recrystalization.

7.3 Elastic Properties and Instabilities of GBSL under Applied Hydrostatic Stress

In principle the fluctuation formula is not strictly applicable to inhomogeneous system [Wallace 84]. Jaszczak and Wolf [Jaszczak 92] have showed, by comparison of the elastic constants computed using this formula and by stress-strain computer experiment, that the elastic constants C_{ij}, for $i, j \leq 3$, can be reliably calculated by the fluctuation formula to 1% or better. Other elastic constants, in particular the shear elastic constants, could not be reliably calculated for the superlattice via fluctuation formula. The reasons for this are yet unknown. It may presumably be related to inhomogeneous strain. Fortunately, we can still calculate the elastic constants C_{ij} of GBSL , at least for $i, j \leq 3$. This is enough for us to estimate the critical strain for the instabilities we will study. In the following, the spinodal instability criterion is calculated from $(C_{11} + C_{12})C_{33} - 2C_{13}^2$, and the Born instability criterion is given by $C_{11} - C_{12}$. The Young's moduli are calculated using Eqs. (2.18a) and (2.18b).

We calculated the elastic-constant tensors of the (001) GBSL's for two temperatures, T = 0K and 300K. At zero temperature, the average elastic-constant tensor were computed through a lattice-dynamics method that included the "relaxation term" arising from the intrinsic inhomogeneities of the superlattice*. [Lutsko 89, Wolf 89a] Fig. 7.3 (a) shows the results of elastic constants as a function of lattice parameter $(a/a_0)_{x,y}$. They show the quantitatively similar behavior as compared to that shown in Fig. 7.1 (b). The spinodal criterion and Born criterion were calculated and plotted in Fig. 7.3 (b). Where $(C_{11} + C_{12})C_{33} - 2C_{13}^2 = 0$ and $C_{11} - C_{12} = 0$ give the critical lattice parameters of the spinodal and Born instabilities, with values of $(a/a_0)^S_{x,y} = 1.0369$ and $(a/a_0)^B_{x,y} = 1.0550$. It is interesting to note that, in contrast to the case in perfect f.c.c. crystal, the elastic constants predict a smaller critical strain for spinodal instability in GBSL.

According to our theoretical analysis (see Chapter 2), at spinodal instability all Young's moduli should vanish. As shown in Fig. 7.3 (c) the actually computed Young's moduli predict very similar critical lattice parameters as the criterion does, which give values of $(a/a_0)^S_{x,y} = 1.0373$ for $Y_{x,y} = 0$, and $(a/a_0)^S_{x,y} = 1.0369$ for $Y_z = 0$, respectively. We have noted that the Young's modulus Y_z is smaller than Y_x (= Y_y). This can be understood based on the elastic constants shown in Fig. 7.3 (a). The ratio of Y_x and Y_z is given by $Y_x/Y_z = (C_{11}^2 - 2C_{13}^2)/(C_{11}C_{33} - C_{13}^2)$, from Fig. 7.3 (a) one can see that C_{11} is very close to C_{33} but obviously C_{13} is greater than C_{12}. This gives $(C_{11}^2 - 2C_{13}^2)/(C_{11}C_{33} - C_{13}^2) > 0$, therefore, Y_x is greater than Y_z. Physically this can be

* These dat are got from Dr. S. R. Phillpot at Argonne National Laboratory.

understood in the following way: Although the structural disordering at the GB tends to stiffen the GBSL, since in a full relaxed state the GBSL shows a large extension in GB normal direction and a Poisson contraction parallel to GB, the larger volume fraction in GB normal will decrease the Young's modulus in this direction.

In order to get the instability picture of GBSL at finite temperature, we also calculated the elastic properties of the same system at T = 300K. As one might expect, the system behavior at this low temperature should not deviate much from the zero temperature. Fig. 7.4 (a) shows the elastic constants of the GBSL varying with lattice parameter. At small stress the system behaves very similarly to the case of T = 0K. Until large applied stress all the elastic constants decrease more rapidly indicating larger softening of the system. Fig. 7.4 (b) shows the instability criteria at this temperature, which give the critical lattice parameter $(a/a_0)^S_{x,y} = 1.0339$ for spinodal instability and $(a/a_0)^B_{x,y} = 1.0426$ for Born instability, respectively. Correspondingly, the Young's moduli Y_x and Y_z give the critical lattice parameter of spinodal instability as $(a/a_0)^S_{x,y}(Y_x=0) = 1.0374$ and $(a/a_0)^S_{x,y}(Y_z=0) = 1.0354$ as shown in Fig. 7.4 (c). Again we note that the Young's modulus Y_z is smaller than Y_x, which indicates that under hydrostatic stress system may fail first in z-direction.

7.4 Grain-Boundary Fracture at T = 300K

As mentioned at the beginning of this Chapter, the question we will address in the present study of GBSL is that given that the pure dilatation of an f.c.c. crystal leads to spinodal instability, does it also lead to the same instability in GBSL? In previous sections we have built up the pictures of the elastic behavior of the GBSL under hydrostatic stress. Based on these results the GBSL, indeed, will fail at the critical lattice parameters (or strains) predicted by spinodal instability.

The simulations of the GBSL under hydrostatic stress were carried out by means of a modified Parrinello-Rahman MD method [Ray 84] on a (TΣN) ensemble. At every applied stress the system was first equilibrated for 5,000 to 10,000 time steps. Then another 10,000 to 20,000 time steps were performed to calculate the system properties. Comparing the simulations of the perfect crystal and GBSL, the latter is more complicated. We found that although according to an applied stress the system has an certain average volume in response to this stress, since now the two lattice parameters $a_{x,y}$ and a_z can vary independently, there can be large instantaneous fluctuations and correlative vibrations in these lattice parameters around the average volume. This large fluctuation can give rise to one to several order of magnitude increase in the mean-squared displacement compared to

that of a perfect crystal at same temperature. These fluctuation may be important in triggering the failure of the system in the region near the critical strain. So for the large strain deformations runs of 50,000 time steps were made to get reliable average properties of the GBSL.

Fig. 7.5 (a) shows the average internal stress in response to the applied hydrostatic stress. At small applied stress the internal stresses respond isotropically. The three components of the normal stress are essentially the same and very close to the value of the applied stress. This force balance continues until the internal stress suddenly drops down at a maximum value of applied stress $\Sigma_c = 0.0951 \times 10^{12}$ dyn/cm^2. This rapid drop behavior, as we have seen in the case of perfect crystal (see Chapter 6), points to the onset of spinodal transition. At this critical applied stress an anisotropy in the internal stress tensor appears, which indicates the inhomogeneous nature of the transition. This sudden drop behavior is also seen in the system enthalpy [see Fig. 7.5 (b)]. As before, the decrease in system enthalpy suggests that the transition corresponds to a mechanical failure of the system, and thus is a low temperature spinodal transition.

Although a homogeneous stress was imposed on the system, the structural responses of the GBSL in lattice parameters are anisotropic. As can be seen in Fig. 7.6 (a), there appears a smaller expansion of a_z in the GB normal direction than $a_{x,y}$ in x- and y-directions. At first glance, one may think that this is contradictory to the fact that the Young's modulus Y_z is smaller than Y_x (= Y_y). This can be understood once one notices the following factors: First of all, the system is subjected to a hydrostatic stress, the overall response of the system to this stress is the consequence of the complex interplay between various elastic moduli. Second, although a small Young's modulus Y_z suggests a large expansion in z-direction, the large Poisson's ratio ν_{zx} (see Table 7.1) indicates a large contraction also in this direction in response to the extensions in x- and y-directions. The overall effect of the combination of these factors may lead to a small expansion in z-direction.

Fig. 7.6 (b) shows the variation of the static structure factors $S(\mathbf{k}_1)$ and $S(\mathbf{k}_2)$ of the GBSL with the applied hydrostatic stress. The slight change and sudden drop to zero in $S(\mathbf{k})$'s as the applied stress increases show that the system stays in ordered structure until the transition occurs. After the transition the system may have lost its structural order or have transformed into another ordered state.

In order to address the question about the final state that the system ends up and the details of the transition, we have carried out more careful analysis of the results of the simulation runs at the critical applied stress. Fig. 7.7 (a), (b), (c) and (d) show the time evolution of system properties during the transition. As clearly shown in Fig. 7.7 (a), after

7,500 time steps the internal energy of the system undergoes a large and swift change which indicates the onset of the transition, then it starts to saturate to a certain value. This is obviously a manifestation of an abrupt release of elastic energy in the relatively short time interval of about a few hundred time steps (or around 0.9 psec). After this change another rapid increase in internal energy is seen starting around t = 15,000 time steps. This divides the transition into two stages.

Corresponding to the first change in internal energy, the internal stresses also drop down very rapidly while show some anisotropic behavior [see Fig. 7.7 (b)] in response to the change in system structure. That the z-component of the normal stress is completely relaxed within a hundred time steps indicates a fully planar decohesion occurs perpendicular to the z-direction. The partial relaxation of the internal stresses in x- and y-component shows that the system has not completely broken down in these directions. Since the sudden release of the internal stresses, the force balance between the internal and external stresses were destroyed. The large stress gradient at the border of the simulation cell induces a shock perturbation and causes a large expansion rate. The system eventually fails also in other directions.

The structural responses of the system also show the brittle nature of this transition. In response to the sudden loss of the balance between the internal and external stress, a large acceleration of expansion appears [see Fig. 7.7 (c)]. The rapid increase in lattice parameters can no longer be interpreted as elastic deformations. Consequently, the static structure factor S(k)'s rapidly drop down to zero, indicating the destruction of the system structure order. Visual examination of atomic positions projected on the three coordinate planes in Fig. 7.8 (an instantaneous atomic configuration at t = 20,000 time steps) shows that the system fractures along the grain boundary, and finally becomes disordered. Carefully examining several intermediate configurations during the transition clearly showed that the transition begins with a nucleation of cavitation (or may be a creation of small crack) at the GB and immediately starts to propagate along the GB. In the second stage of the transition, the system further fails in other two directions and breaks down into pieces.

It should be pointed out that the disorder seen in Fig. 7.8 may not be truly an evidence of the structural disordering transition. Since when the GB fracture occurs the sudden release of the internal stress leads to a rapid change in the expansion rate of the lattice parameters from zero to a large value within a very short period of time. This is equivalent to putting the system under an extreme condition of shock. Thus the configuration shown in Fig. 7.8 is obviously not a true equilibrium state.

Since we are more interested in the first stage of the transition, we carried out a recovery study of the system from the first stage of failure in an attempt to capture the equilibrium state of the system after the first stage. This structural recovery was simulated, with the configuration of Fig. 7.8 as the initial input atomic positions, by compressing the system gradually back to its original lattice parameters $(a/a_0)_{x,y} = 1.0387$ and $(a/a_0)_z = 1.0270$ at the beginning of the transition. After about 3,500 time steps of constant volume run at these lattice parameters it was found that the crystal order was reestablished; the structure had fallen back to the undistorted f.c.c. state with a planar defect. Fig. 7.9 shows the projections of an instantaneous atomic configuration after 10,000 time steps. The crystalline region and the trace of the GB fraction region are clearly seen in this figure.

It was found [Wolf 89b] that the Poisson's effect plays an important role in enhancement of the elastic anomalies in a GBSL, particularly of the Young's moduli. Based on this observation one may ask if this has any effect on the instability or affect the transition. To check this a series of (ThN) ensemble MD simulations of elongation deformation was performed, which allows us to express the in-plane Poisson contraction of the GBSL completely. The simulation started from a stress-free configuration of the same GBSL model as used before. The elongation was simulated by a uniaxial tensile loading along the z-direction (GB normal) while fixing the lateral lattice parameter $(a/a_0)_{x,y}$ at the stress-free value in all runs. Figs. 7.10 show the system properties in responses to the elongation. Similar to the case of hydrostatic stress loading the internal energy and stresses show a sudden drop when the GB fracture occurs [see Fig. 7.10 (a) and (b)]. The static structure factors in Fig. 7.10 (c) clearly show that the transition does not change the structure order of the GBSL. As obviously seen in Fig. 11, the projections of an instantaneous atomic configuration at $(a/a_0)_z = 1.0900$ (the point in Fig. 7.10 (a) at which the stresses drop down), a cavitation is nucleated at one GB, and with further stretch it starts to grow along the GB. The system eventually fails in the form of GB fracture too.

In summary of our simulation results, we conclude that, at low temperature, along the primary path the GBSL is unstable when the hydrostatic loading takes it close to the critical region predicted by the spinodal instability criterion. The system fails in the form of GB fracture and shows all the features of spinodal transition.

7.5 Grain-Boundary migration and Fracture at T = 500K

As mentioned earlier that a fundamental characteristic of all interface systems is their intrinsic inhomogeneities. The presence of an interface signifies that the immediate region surrounding the interface can have properties which could be quite different from those of

the bulk region away from the interface. It has been known [Yip 89] that the basic understanding of the properties of interface materials largely relies on the detailed knowledge of local properties, such as local volume expansion, elastic constants and so on, in the interface region. It is a little surprising that the instability criterion based on the global elastic constants of the GBSL still well predicts the mechanical failure behavior of the interface system. Maybe this gives an example that once the model system with interfaces is properly prepared its mechanical behavior still can be reasonably described by the global properties which are easily calculated using the known formulae.

Stimulated by the success in predicting the elastic behavior of a GBSL system at low temperature we attempted to study the instability of the same at high temperature. Based on the thermal expansion study of this system we have known that this system starts to recrystalize at 800K. Unfortunately this gives a upper limit of temperature which we cannot go beyond.

We chose the temperature T = 500K and followed the same simulation procedures described in last section to simulate the GBSL under hydrostatic stress. Figs. 12 (a) and (b) show the internal stress and enthalpy in responses to the applied stress. At small applied stress the system responds normally as we have seen in Fig. 7.5 for the low temperature. When the applied stress increases to the values of $\Sigma_m = 0.0743 \times 10^{12}$dyn/cm^2, the system enthalpy and the internal stress appear to level off from the original curves. With further increase in the applied stress the enthalpy and internal stress first increase somewhat then rapidly drop down, indicating a transition.

The consequent responses in structure are shown in Figs. 13. At the applied stress Σ_m there is not much changes in lattice parameters being observed [see Fig. 13 (a)], but large changes in the static structure factor occur. As seen in Fig. 7.13 (b) one of the static structure factor $S(\mathbf{k}_1)$ decreases a lot, from 0.6 in last applied stress to 0.3, and the other recovers a little. These changes in $S(\mathbf{k})$'s indicate disappearance of region A of the GBSL and the migration of the GB's.

In order to examine GB migration, we calculated the planar static structure factor $S_p(\mathbf{k})$. Figs. 7.14 show the results for $\Sigma_m = 0.0743 \times 10^{12}$dyn/cm^2 at t = 4,500 time steps [Fig. 7.14 (a)] and 50,000 time steps [Fig. 7.14 (b)]. The cross of $S(\mathbf{k}_1)$ and $S(\mathbf{k}_2)$ localizes the GB region. At end of this run one GB had moved towards the left-hand side. Fig. 7.15 shows the projections of the atomic configuration after t = 50,000 time steps. As can be seen clearly in this figure, there are only two well-ordered atomic planes of the region left as the result of the GB migration. Careful analysis showed that the migration mechanism of the GB is through the planar twist of the GB layer. Since the structure disordering at the interface largely enhances the anhoarmonicity at the GB, which

consequently leads to a high atomic mobility of the atoms in this region. This planar twisting decreases one region of the GBSL and leads to the growth of the other. As we have seen, when the GB's get close to each other, they start to attract one another. This will decrease the GB energy and is responsible for the enthalpy decrease observed in Fig. 7.12.

At still larger applied stress, the system fails in the same way as in GB fracture as we have seen at T = 300K. As clearly evidenced from Fig. 7.16, the rapid increase in internal energy and sudden release of the internal stress give rise to a lower enthalpy state. The complete release of the z-component of the stress indicates the very brittle fracture along the GB. Consequently the system starts anomalous expansion.

Table 7.1 Average elastic moduli and constants in the $\Lambda \rightarrow \infty$ limit for the (001) 36.87° ($\Sigma 5$) twist boundary (in unit of 10^{12} dyn/cm^2). Y, G, Y_b, and ν are, respectively, Young's modulus, the shear and biaxial modulus, and Poisson's ratio; B is the bulk modulus. For example, ν_{zx} is the value of ν for stress in the x- and contraction in the z-direction. The GB energy (in mJ/m2) has also been included. [Wolf 89a]

Quantities	EAM (Au)
$C_{11} = C_{12}, C_{33}$	1.955, 1.807
$C_{12}, C_{13} = C_{23}$	1.422, 1.571
$Y_x = Y_y, Y_z$	0.567, 0.346
$G_{xz} = G_{yz}, G_{xy}$	0.440, 0.284
B	1.600
Y_{bz}	0.647
$\nu_{yx} = \nu_{xy}$	0.109
$\nu_{zx} = \nu_{zy}$	0.775
$\nu_{xz} = \nu_{yz}$	0.465
E_{GB}	524

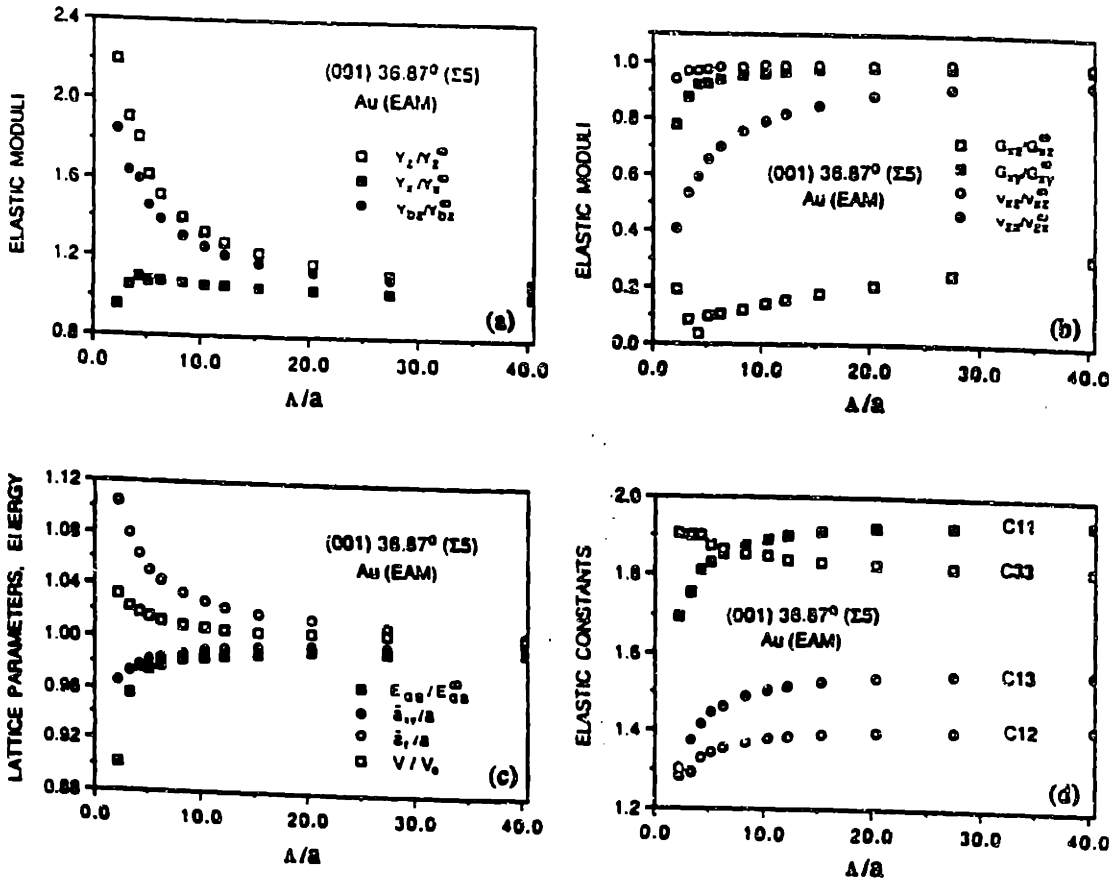

Fig. 7.1 Variations of elastic properties, lattice parameter and grain-boundary energy of GBSL with modulation length. (a) Young's and biaxial modulus, (b) Shear moudulus and Poisson's ratio, (c) Lattice parameters and GB energy, and (d) Elastic constants at T = 0K.

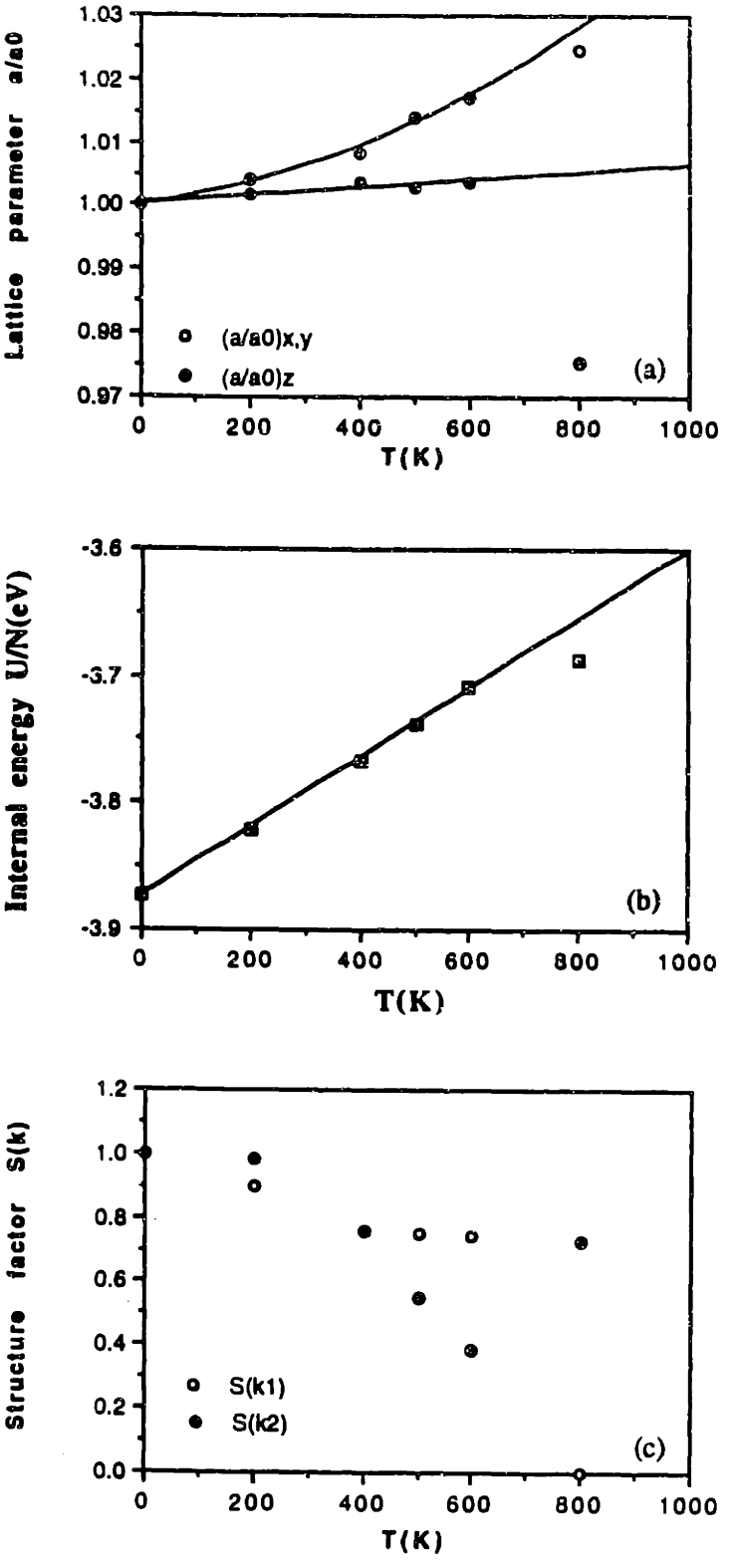

Fig. 7.2 Thermal expansion of GBSL.
(a) Normalized lattice parameters, (b) Internal energy, (c) Static structure factors S(k1) and S(k2), as a function of temperature.

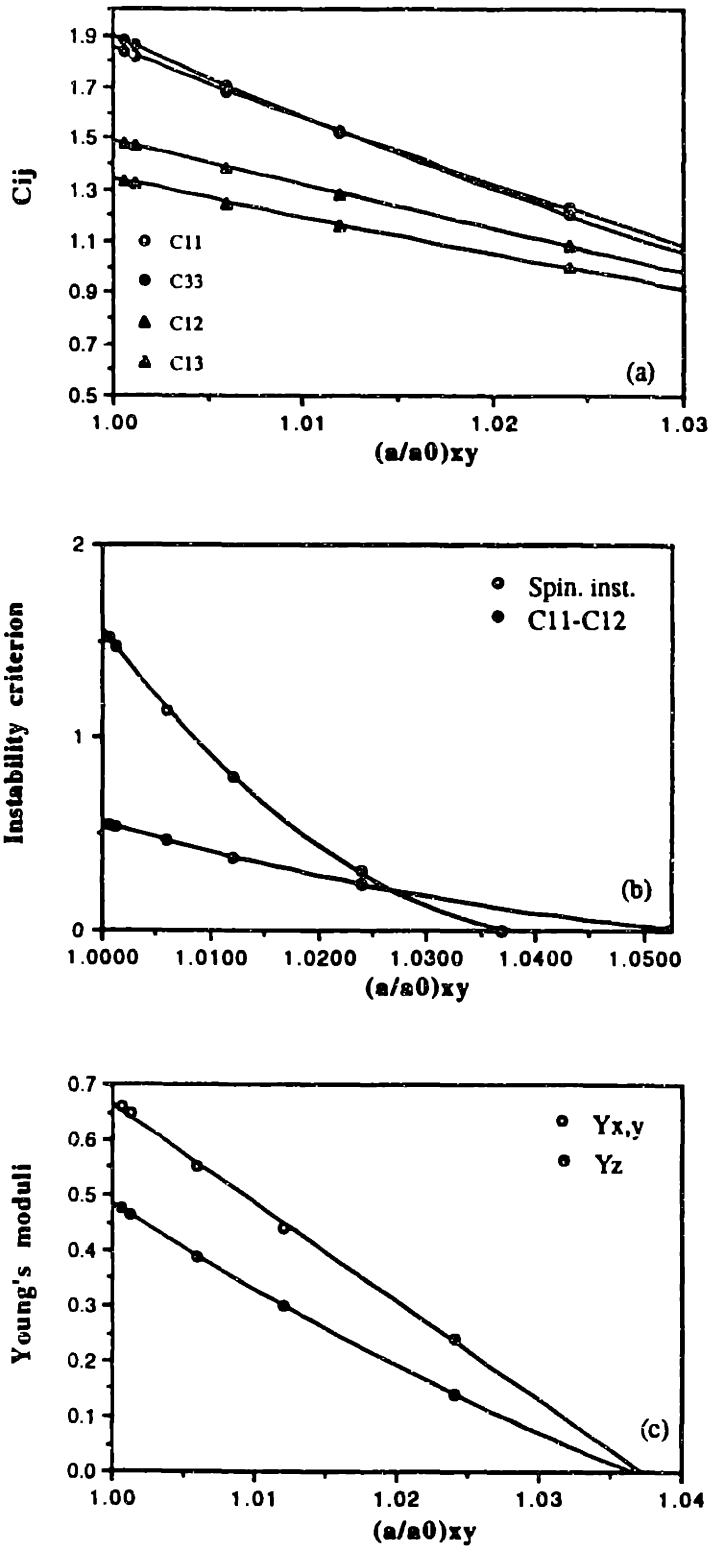

Fig. 7.3 Elastic properties of GBSL as a function of lattice parameter at T = 0K. (a) Elastic constants, (b) The spinodal and Born instabilities, (c) Young's moduli.

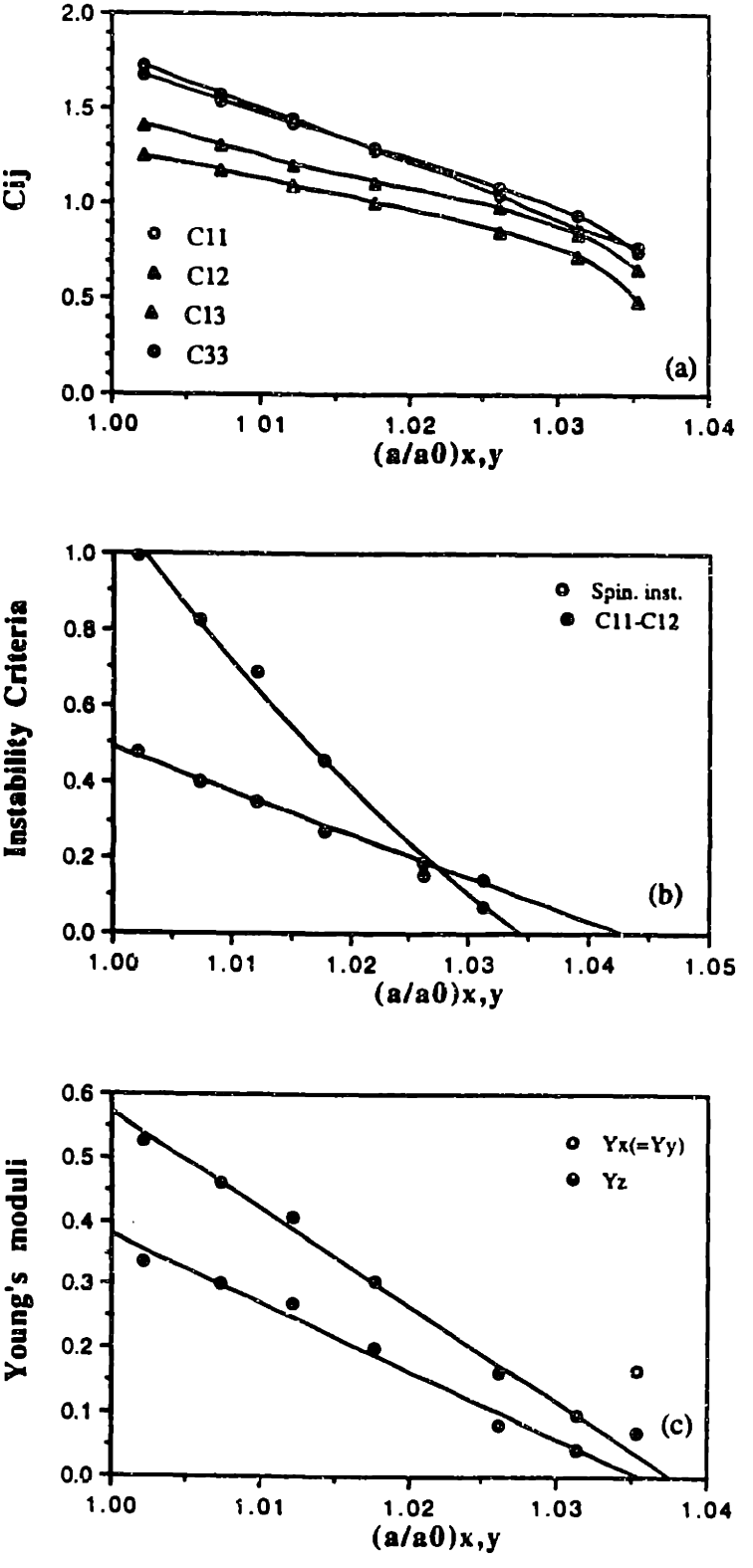

Fig. 7.4 Elastic properites of GBSL as a function of lattice parameter at T = 300K. The same as in Fig. 7.3 except for T = 300K.

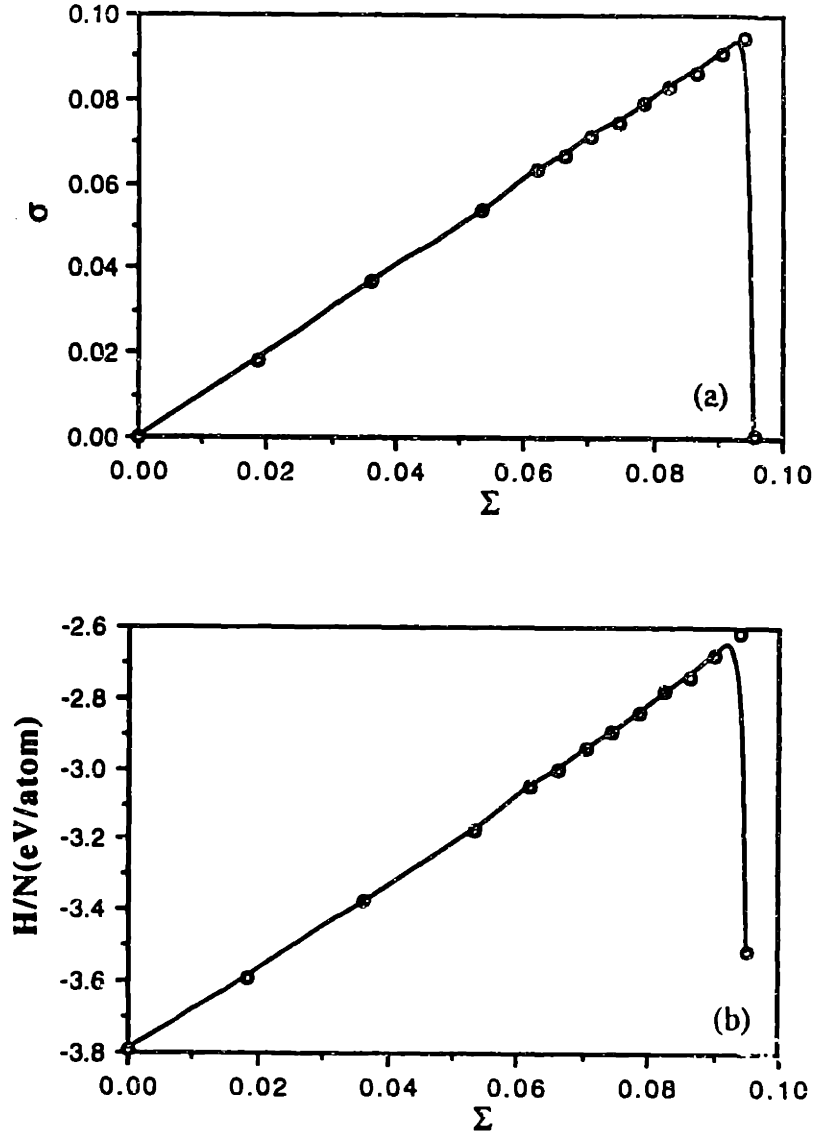

Fig. 7.5 Internal stress and energy in response to applied hydrostatic stress. Mechanical failure of the GBSL indicated by the sudden drops in both internal stress (a) and enthalpy (b).

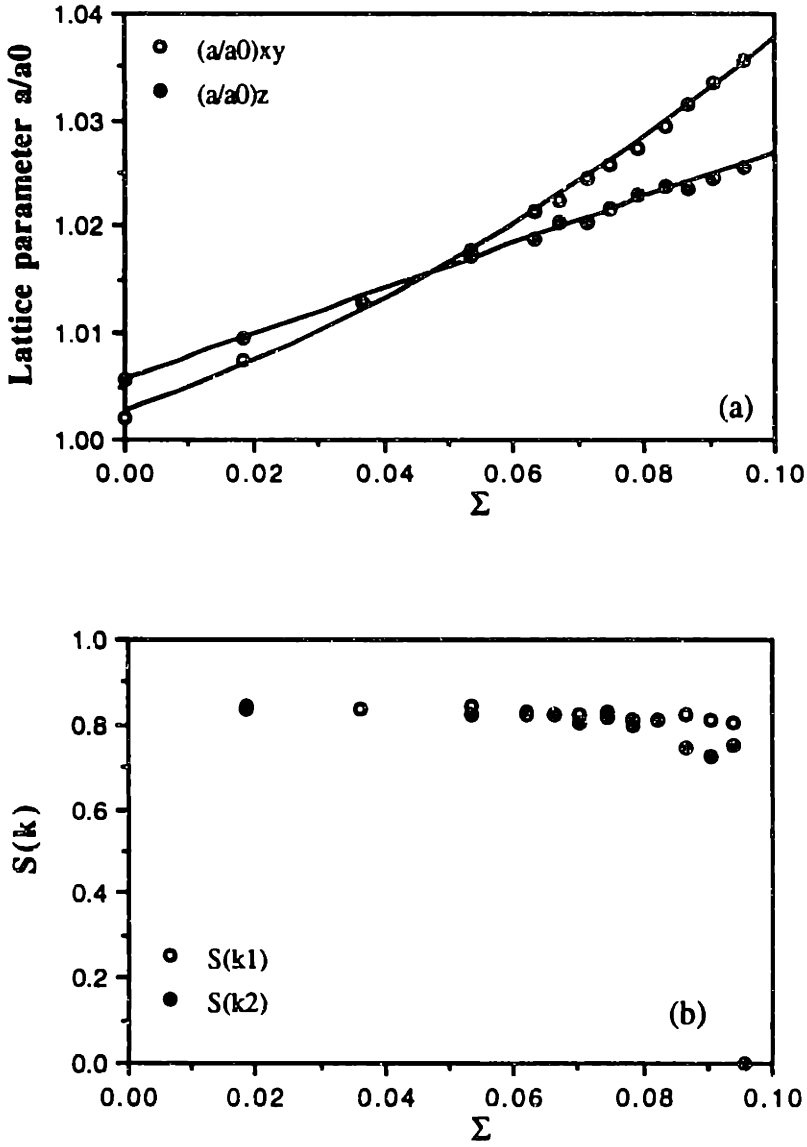

Fig. 7. 6 Lattice parameter and structure factor in response to the applied hydrostatic stress.
(a) Lattice parameter-stress relation, (b) Static strucutre factor.

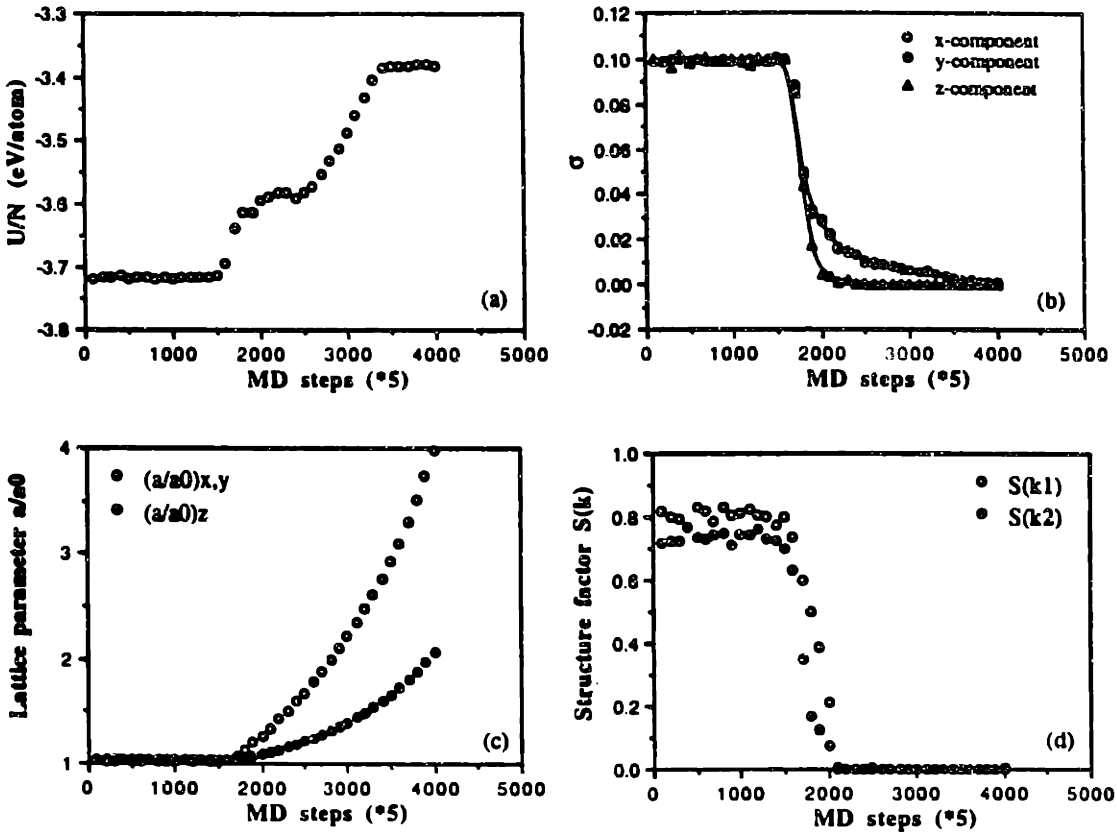

Fig. 7.7 Time evolutions of system properties under applied hydrostatic stress. Behaviors of the internal energy (a), internal stresses (b), lattice parameters (c), and static structure factors (d) during the transition. The sudden jumps in the internal energy and the internal stresses show that the transition has all the features of spinodal transition like the fcc crystal in Chapter 6. The changes in internal energy and stresses indicate clearly that there two stages of the transition. In the first stage, as indicated by the internal stresses, the stress in z-direction is completely relaxed while that in x- and y-directions still staying in finite, the system fractures along the grain boundary. Since after the first stage of transition the system losses the stress balance it keep expanding and eventually fails in the form of fregmentation. In this stage the crystalline order of the system is completely lost as seen in S(k)'s.

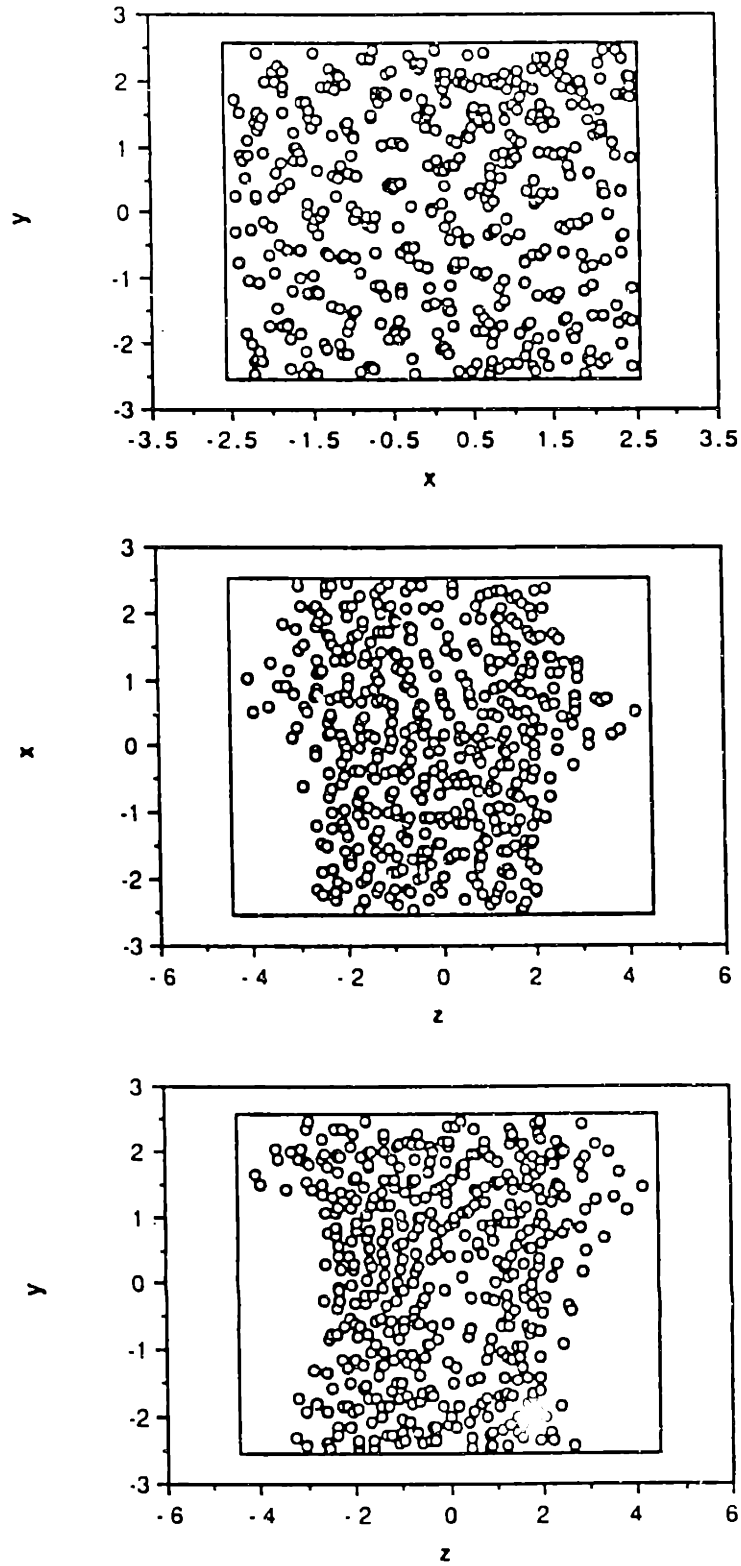

Fig. 7.8 Projections of an instantaneous atomic configuration at the end of the first stage of the ransition.
As shown in the prjections on x-z and y-z planes the system fractures along the grain boundary and becomes structurally disordered.

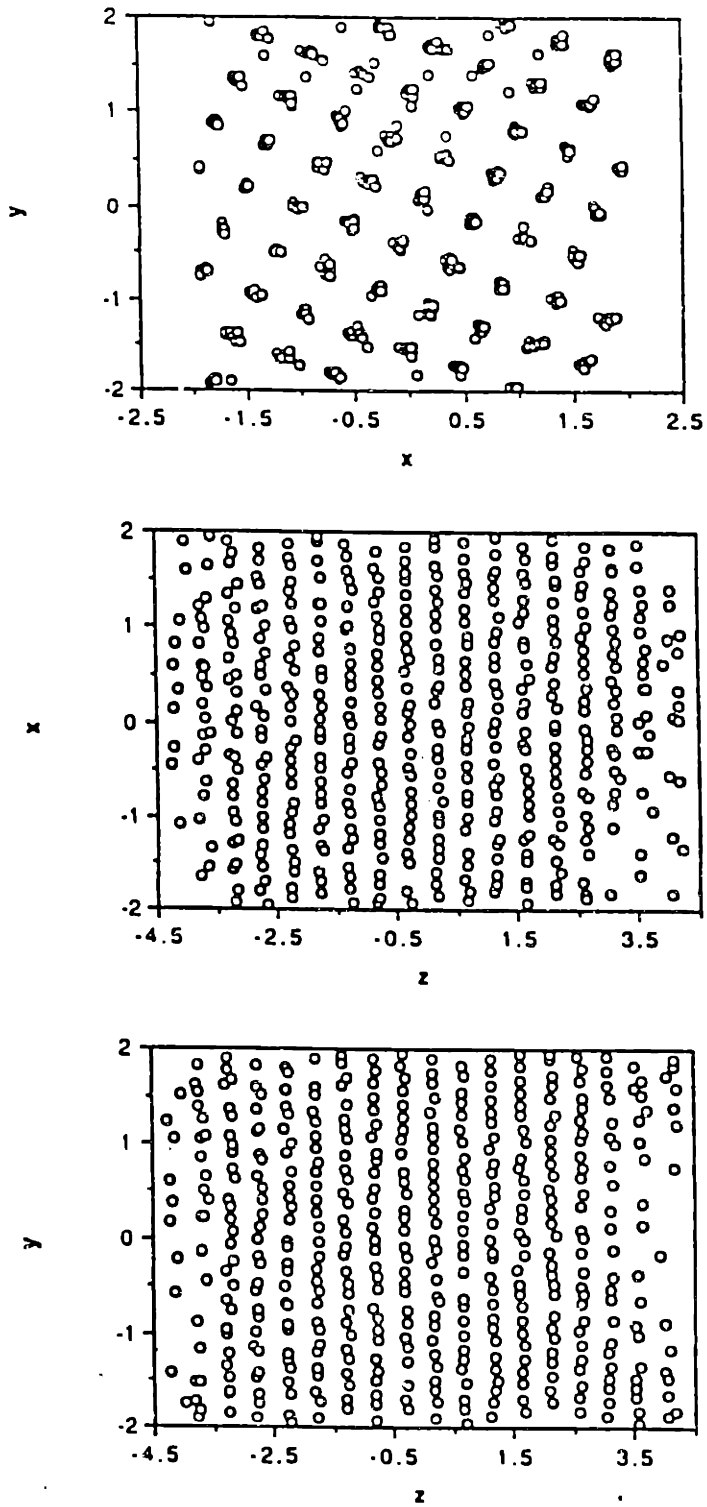

Fig. 7.9 Structural recovery after the first stage of the grain-boundary fracture. Structural recovery from the GB fracture, simulated using the configuration shown in Fig. 7.6 as initial configuration and compressing the system graduately back to its original lattice parameters at begining of the transition. A recrystalization of the fractured system is observed. The system ends up as an fcc crystal with lattice parameters 1.0140, 1.0269, and one disordered boundary.

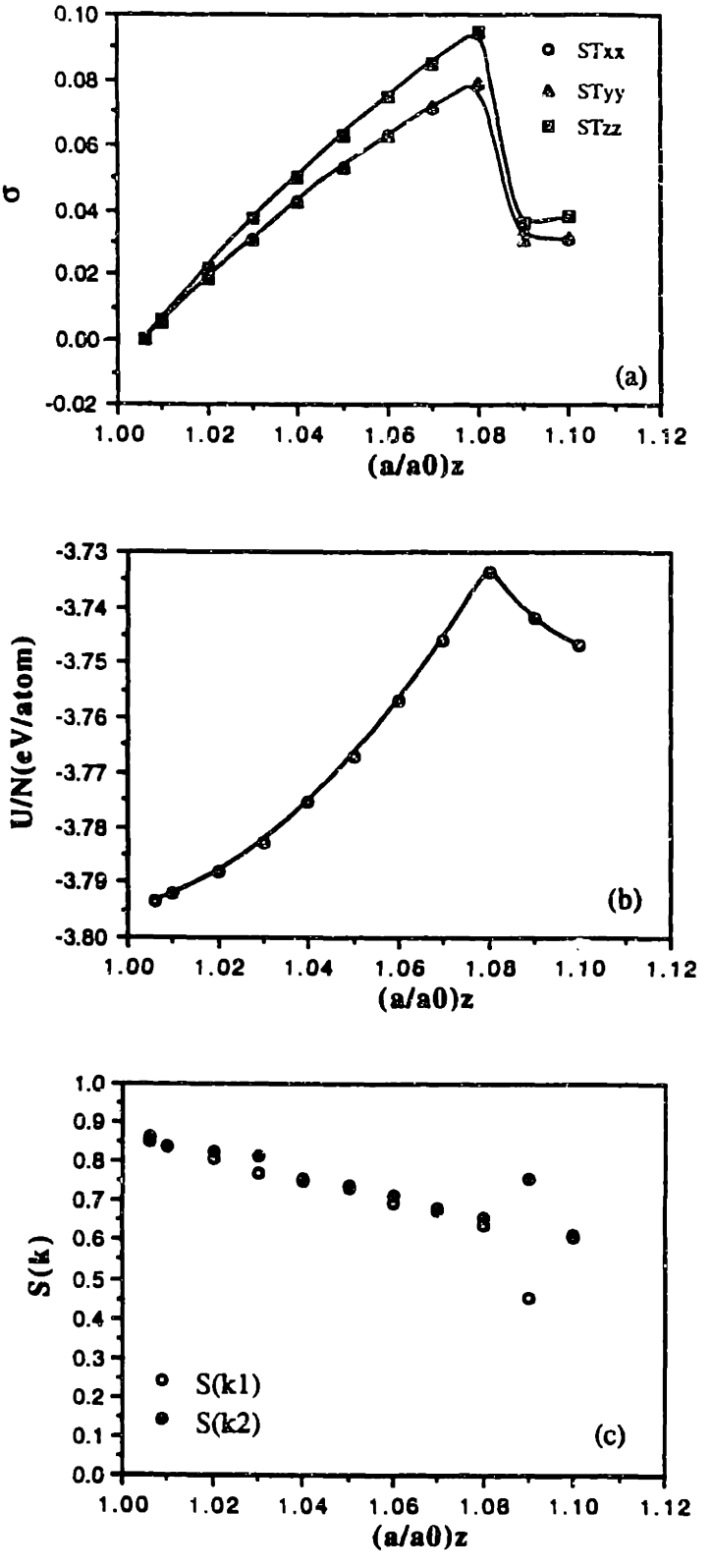

Fig. 7.10 Internal energy and stresses in responses to uniaxial strain load at T = 300K. Grain boudary fracture under enlogation is simulated by uniaxial stretch loadin along the GB normal without allowing Poisson's contraction in lateral directions. The drops in the internal energy and stresses show the characteristics of the spinodal transtion.

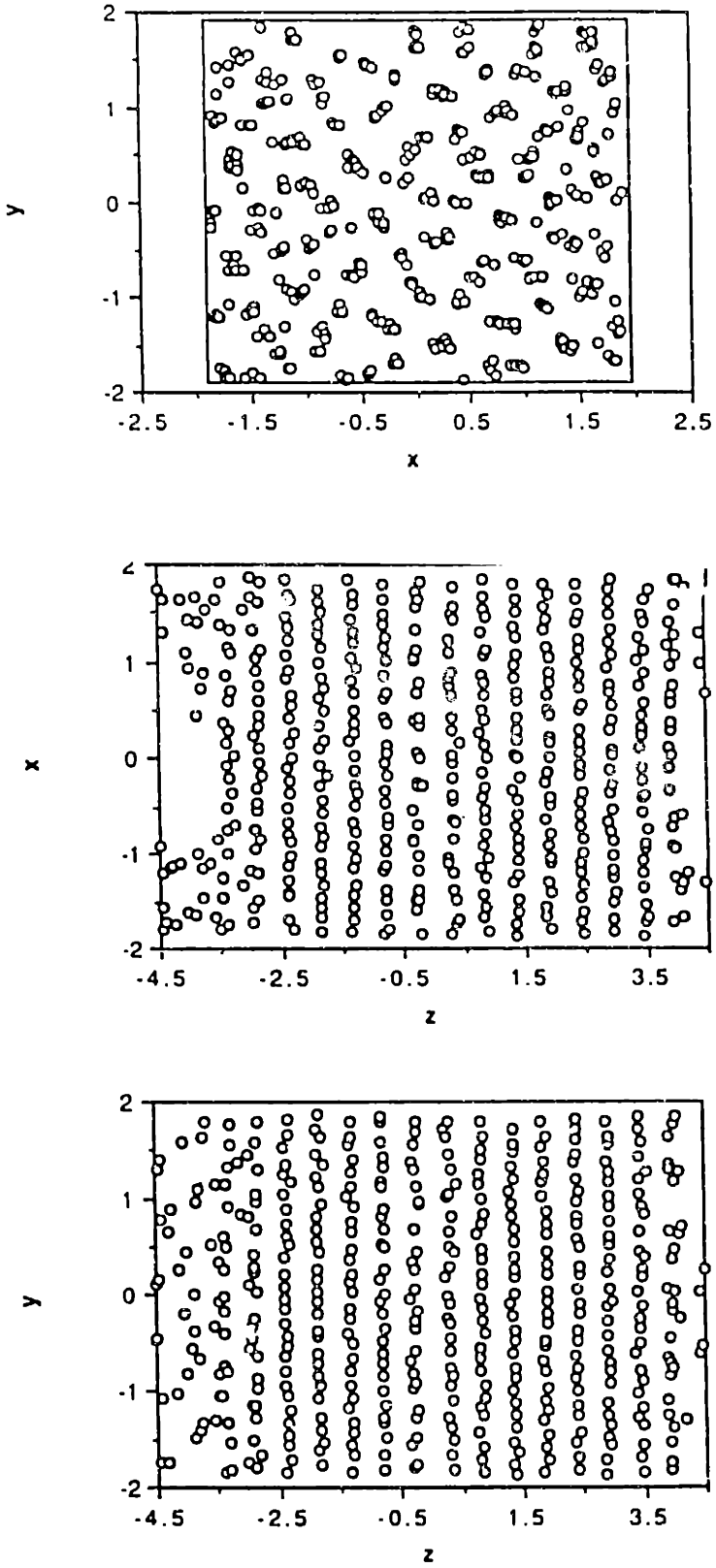

Fig. 7.11 Projections of an instantaneous atomic configuration after the internal energy drop. As clearly seen in the x-z and y-z projections a caviation is nucleated at one grain boundary, and with the further stretching it starts to grows along the GB, the system eventually fails in the form of GB fracture.

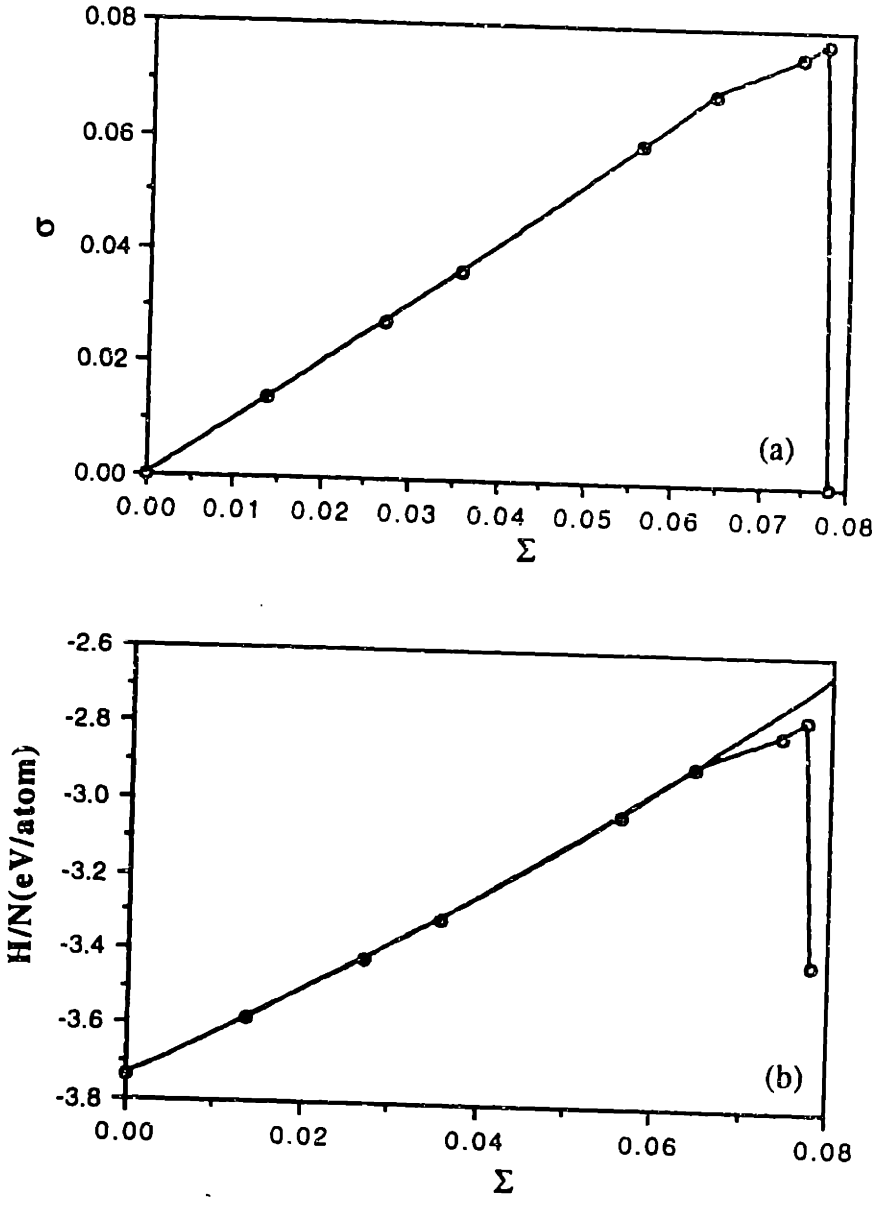

Fig. 7.12 System enthalpy and internal stresses in responses to the applied hydrostatic stress at T = 500K.
At small applied stress the and internal stress enthalpy respond normally as in Fig. 7.4. When the applied stress increases to the value of S = 0.7412 (eV/atom) a GB migration is observed, but no any anormalous changes in other properties are observed. At still higher applied stress, system fails in the same way, as seen at T = 300K, of GB fracture.

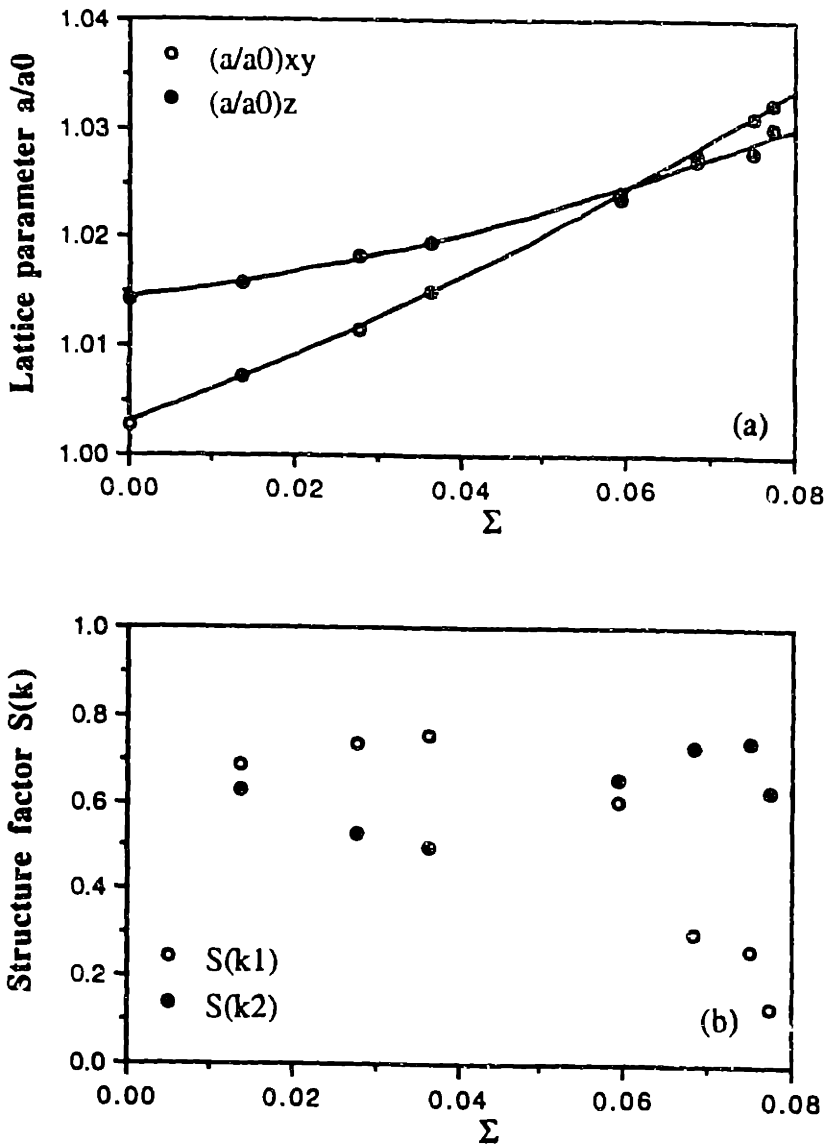

Fig. 7.13 Lattice parameter and structure factor in response to applied hydrostatic stress at T = 500K.
Shown here are the lattice parameter-stress relation (a), and static structure factor. At imposed stress S = 0.7412, the GB starts to migrate. Consequently there is a larger expansion seen in z-direction, and correspondingly a decrease in one of the static structure factor S(k1). The overall effect of this GB migration is enhanced degree of disorder in the system since the GB's move close together.

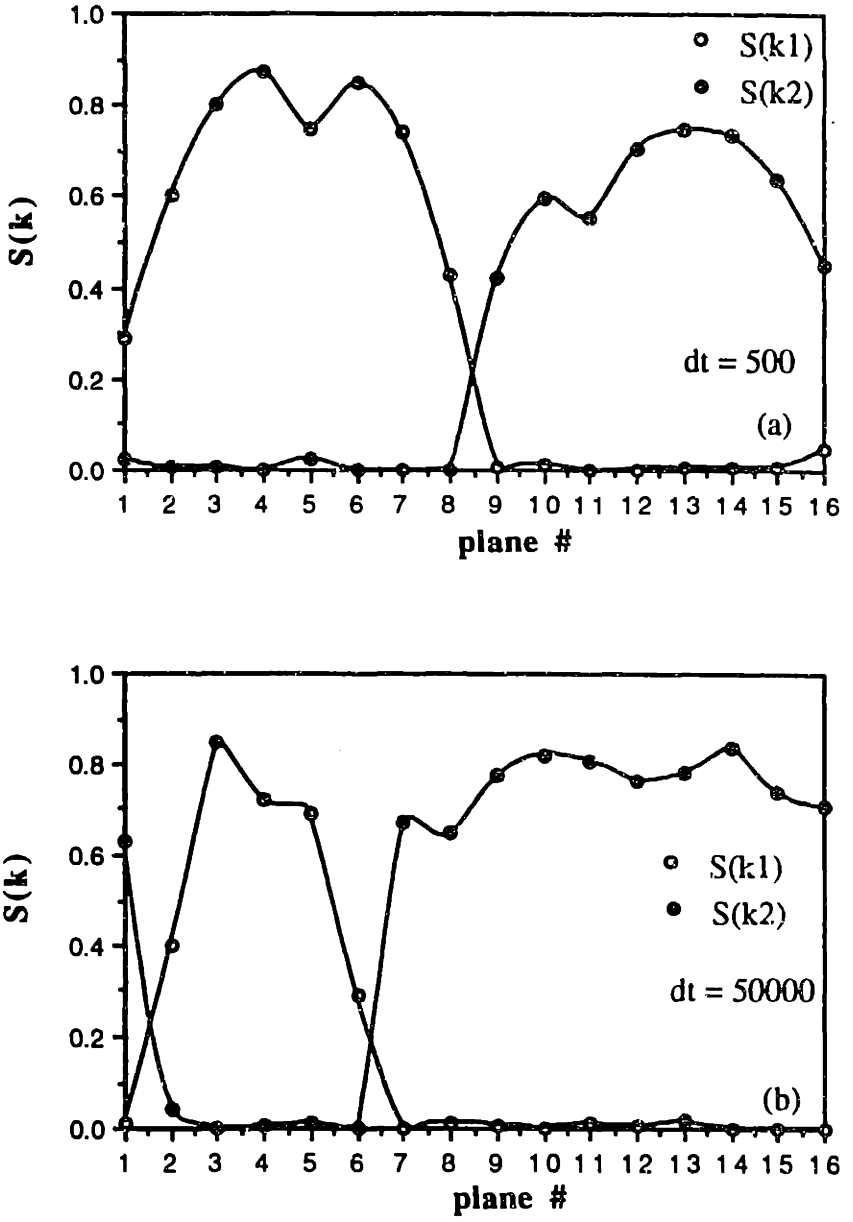

Fig. 7.14 Grain-boundary migration.
Instantaneous values of Sp(k1) and Sp(k2) show the GB migration. (a) When t = 500 time steps, and (b) t = 50,000 time steps.

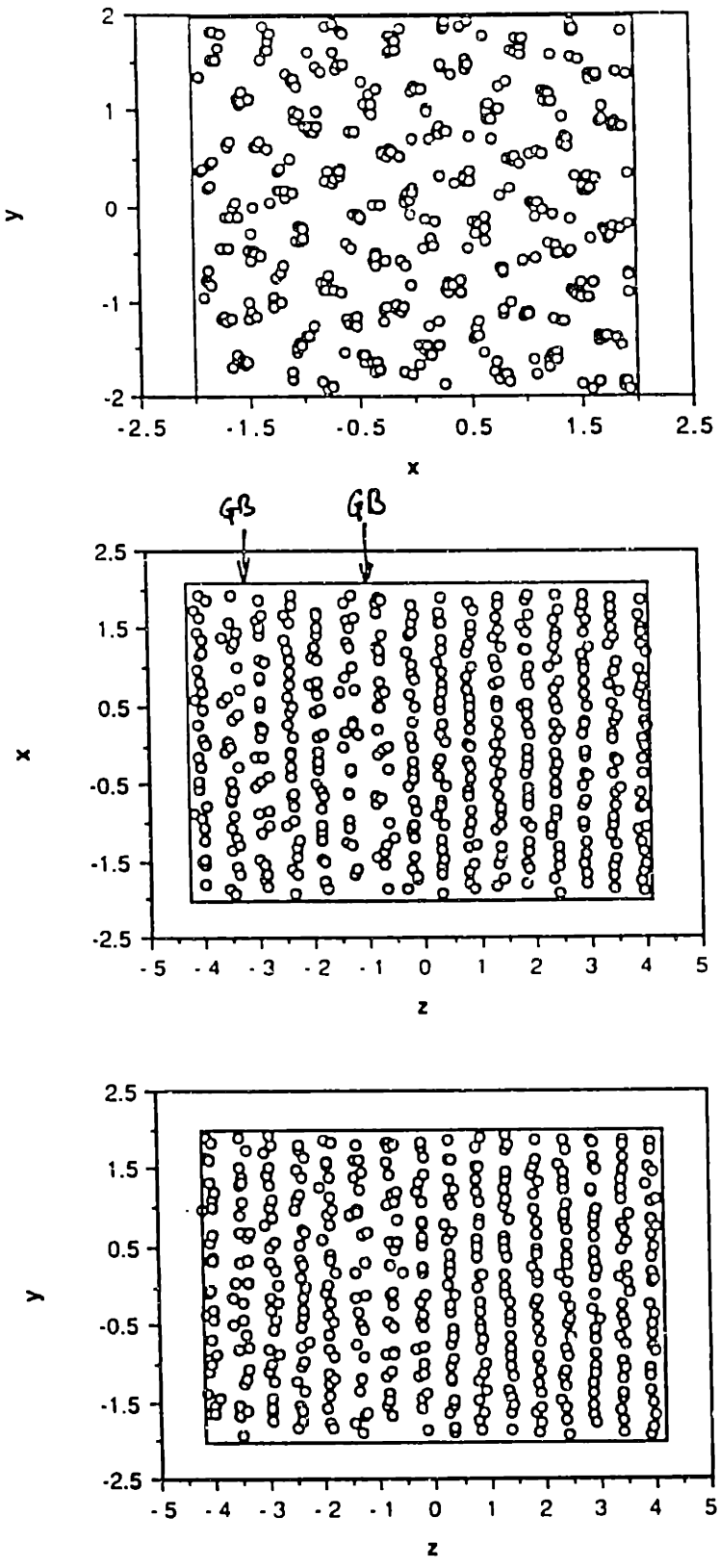

Fig. 7.15 Instantaneous atomic configuration showing the GB migration.

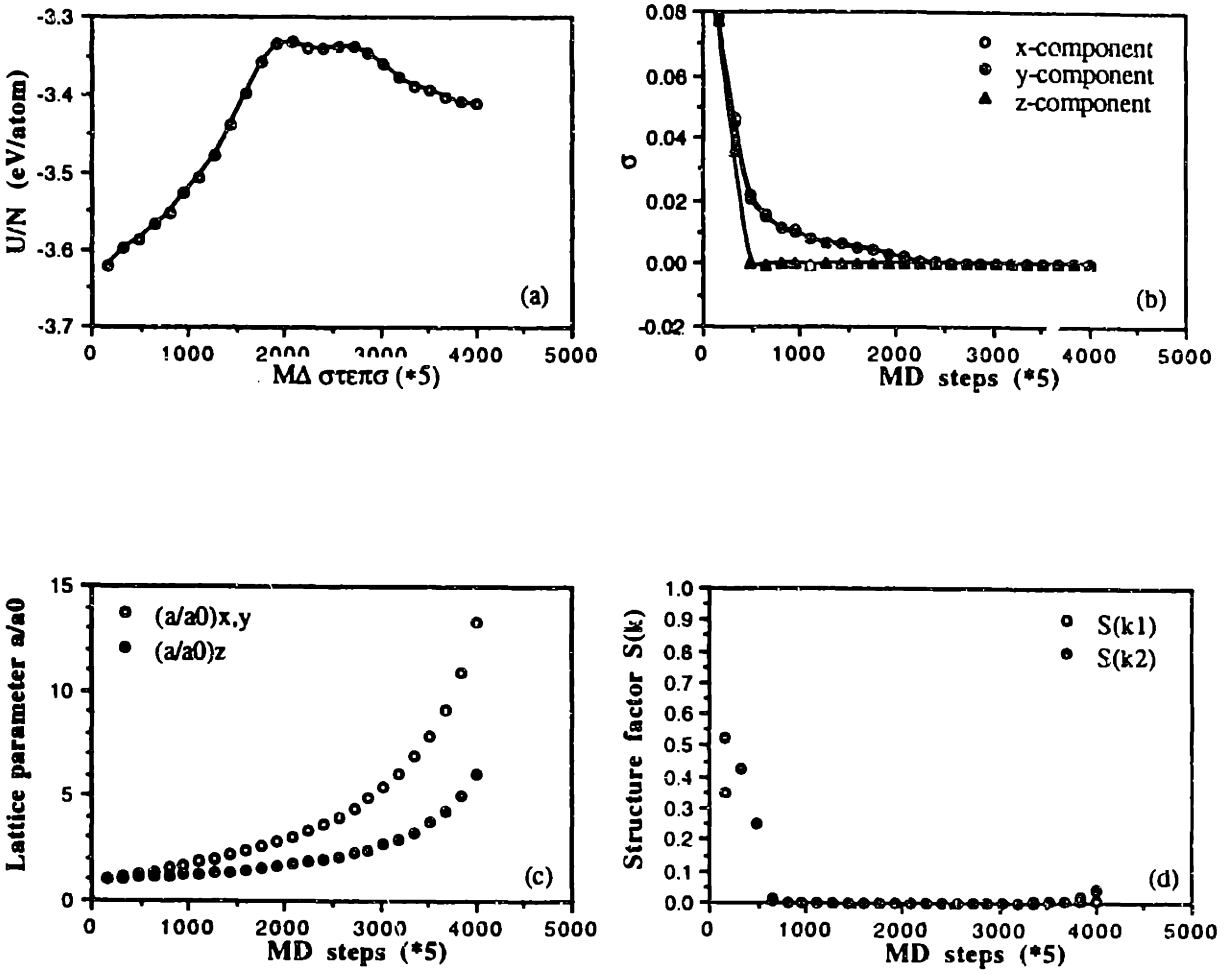

Fig. 7.16 GB fracture and fragmentation of GBSL at large applied stress at T = 500K.
Changes of the internal energy (a), internal stresses (b), lattice parameters (c), and S(k)'s (d) show the similar behavior of the system as in Fig. 7.7. The two stages of the spinodal transition are clearly seen in the internal stresses.

Chapter 8
Conclusions and Recommendations for Future Work

8.1 Conclusions

The different conditions of elastic instability of an infinite crystal under stress or strain boundary conditions, the corresponding mechanisms of unstable structural responses, and the final states of the transformed lattice have been studied through examination of finite-strain elastic constants and moduli of an f.c.c. crystal under dilatation, uniaxial stress, and uniaxial strain. This investigation has been carried out using an integrated approach combining continuum elasticity through the principle of virtual work and the solutions of eigenvalue of elastic constant matrices with the direct Monte Carlo and molecular dynamics simulations of the unstable structural responses of the crystals. This integrated approach has led to the following conclusions:

(1). There exist three kinds of instabilities in crystalline solids. They are: Spinodal (dilatational) instability which is determined by the vanishing of the bulk modulus; Born (normal distortional) instability which is given by $C_{11} = C_{12}$, or the vanishing of the shear modulus $G(110)[1\bar{1}0] = 0$; and shear distortional instability which corresponds to the complete loss of the shear resistance of the (100) planes along the [010] direction of the crystal.

(2). Each instability is associated with a certain set of eigenstates of strain which defines a particular deformation path (failure mode). For spinodal instability the mode is pure dilatation and simply a continuation of volumetric deformation of the primary path. Born instability is a symmetry breaking instability, its failure mode consists of normal distortions (secondary path of deformation) and yields a volume conservation along the secondary path of deformation.

(3). As a consequence of conclusion 2, the crystal instabilities manifest themselves only when the crystal is in the eigenstates. Which instability can be seen depends on how the crystal is deformed. Under the stress boundary condition (imposing stress with no constraint on the strain response) the Born instability is always dominant, while under the strain deformation or the compliant boundary condition (imposing stress with some

constraints on the strain response) one can maintain the crystal in stable condition until a critical strain.

(4). Compared to thermodynamic criterion of first order phase transformation which determine the transition through the equality of the free energies of two phases, elastic instability criteria, on the other hand, predict the instability by the elastic constants or moduli of the initial phase and do not provide direct information about the final state of the transformed lattice.

(5). From the direct observations through atomistic simulations, all the unstable structural responses associated with spinodal instability have the feature of catastrophic failure, and are discontinuous, first-order processes. The final states of the transitions are temperature dependent. At low temperatures the transitions take the form of decohesive cleavage fracture. At high temperatures the unstable structural response of the f.c.c lattice at the instability is homogeneous disordering with all features of mechanical melting. The mechanism of the spinodal transition is an inhomogeneous nucleation of cavitation at low temperatures, while at high temperatures, a homogeneous nucleation of disordered phase with the assistance of enhanced thermal fluctuation. Although these transitions can take different forms depending on temperature, their underlying cause, i.e., large stress fluctuations at the critical strain, is essentially the same.

(6). Under applied stress, the structural phase transitions triggered by Born instability show the features of martensitic transition but are continuous, second-order processes. When the system is uniaxially stressed close to the limit of Born instability, it can undergo shear strain with practically no cost in energy, the system transforms from f.c.c. lattice to distorted b.c.c.. In the case of pure heating (P = 0), Born instability initiates a homogeneous, first-order melting transition. Compared to the spinodal transitions, these transitions take place through a completely different mechanism of symmetry breaking or bifurcation. This bifurcation, in the case of finite applied stress, provides a link in configuration space between f.c.c. and b.c.c. lattice, while in the case of pure heating to melting, triggers a homogeneous disordering. The orthorhombic distortion predicted by analytical analysis plays only an intermediate role in triggering a further shear distortion observed in simulation.

(7). Spinodal instability also shows itself in inhomogeneous crystalline system, for instance the interface material we have studied. The transition show the same mechanism

as we have seen in the f.c.c lattice but, in the present case, it takes the form of grain-boundary fracture.

The results summarized above will now be discussed in more detail. By applying the principle of virtual work to a stressed crystal, we showed that the three elastic instability criteria of the crystal under stress boundary condition naturally appear as a consequence of the requirement which determines the inflection point of the strain energy. This procedure attributes the instability of crystals to an eigenvalue problem of the matrix of current (deformed) elastic constants. By solving the conditions which give the zero eigenvalue of the elastic constant matrix, one can not only show that these conditions are just the three instability criteria, but also by taking one step further, one can solve for the eigenvectors which basically define the eigen-deformation paths or the failure modes. There exist eigen-deformation paths which point out clearly that the instability of the crystal cannot show up anyway. Whether one sees the instability depends on how one deforms the system. With this treatment we recover all the results about crystal instabilities obtained by Milstein and Hill [Hill 77, Milstein 79a] using a different approach.

Guided by theoretical analyses, the series of simulations presented in this thesis constitute the first attempt to study systematically crystal instability and the unstable responses of the lattice at finite temperature. By purposely controlling the loading environments we have studied the instability of two potential models of f.c.c. crystals of Cu and Au, and the behavior of these two systems under different loading conditions.

We have determined by Monte Carlo simulation and elastic constant calculations the spinodal instability of an f.c.c. Lennard-Jones Cu lattice under symmetric isothermal extension along the three directions of initial cubic symmetry. We have shown that at several temperatures the critical strains determined for the spinodal instability criterion are in agreement with the direct observations of the instability from the MC simulations. At low temperatures the observed critical strains are quite close to those predicted by bulk modulus. At high temperatures the observed critical strains are smaller than the theoretical values. The reason for this behavior can be traced to the presence of the large thermal fluctuations at high temperatures. A significant contrast brought out by our simulation results is that although melting at high temperature and fracture at low temperature have very different final structural states of transitions, the underlying cause is essentially the same, namely, large stress fluctuations at the critical strain.

The behavior of the crystal in the region of critical strain is well predicted by spinodal instability. The values of these critical strains define an instability curve in the temperature-density phase diagram as shown in Fig. 5.22. It has been suggested that the

freezing curve which, like the melting curve, is defined only for temperatures above the triple point T_t, is effectively also the mechanical instability curve in the sense of heating a crystal rapidly up to the limit of superheating. [Wolf 90b] It can be seen in Fig. 5.22 that the critical strains observed in the present work delineate the extension of the mechanical instability curve to temperatures below T_t. It has been conjectured that in crossing this instability curve the lattice will become disordered, thus providing a simple thermodynamic connection between melting and solid-state amorphization. [Wolf 90b] What we have found is that in crossing such a curve the lattice does become mechanically unstable as manifested by sudden jumps in the hydrostatic pressure and the potential energy; however, the atomic configuration into which it evolves depends on the temperature. At low temperatures, the spinodal instability is accompanied by symmetry breaking as shown clearly by the density profiles along the three cubic directions. At the same time, the system becomes nonuniform by the formation of a local region of relatively low density. We interpret this crystal response as cavitation which at T = 242.3K (about 0.20 T_t) leads to cleavage fracture upon further lattice dilatation. At T = 581.4K (about 0.48 T_t), in addition to cavitation-like behavior, significant local disordering occurs as the system is strained beyond the point of instability. At high temperature T = 969.1K (0.81 T_t) the system response at the onset of instability is homogeneous and complete disordering as in a melting transition. At still higher temperature T =1550.5K (1.29 T_t) the system melts even in compression.

Along with the critical strain curves of spinodal instability in Fig. 5.21 we also plot the critical strains of Born instability predicted by the vanishing of the shear modulus $G(110)[1\bar{1}0]$. It can be seen that at low temperatures the Born instability curve lies below the spinodal curve; as the temperature is increased they cross each other, and at high temperatures the critical strains of Born instability are larger than that of spinodal instability. According to continuum elasticity analysis, pure dilatation will suppress the Born instability. This seems to be true in our observation from simulations. But since the values of the critical strains of both the Born and spinodal instabilities are close to each other there is some ambiguity in drawing definite conclusions about this issue. Part of the ambiguity stems from the relatively shallow well-depth of the potential as compared to an EAM-type potential [Daw 84, Wolf 89a] for metals. Thus the Lennard-Jones potential gives considerably lower values for the elastic constants which make it difficult to distinguish between critical strains of the spinodal and Born instabilities.

To distinguish these two instabilities we have also performed MD simulations using an EAM potential for f.c.c. Au metal. In this case the spinodal and Born instabilities predicted by elastic moduli are clearly separated. For spinodal instability the pure

dilatation-induced transitions show all the features of spinodal transitions we have seen in L-J potential model. That is, cleavage fracture is observed up to T = 1000K, and homogeneous disordering occurs at higher temperature T = 1200K (still below the mechanical melting temperature T = 1380K). In these simulations the Born instability is successfully suppressed with the constraint of pure dilatation even though it predicts smaller critical volume expansion. On the other hand, several series of MD simulations have been performed to simulate the uniaxial tensile stress loading (the load is in x-direction in both simulations). In this way we leave the system free in the lateral directions y and z. The system thus can to fail either at the Born instability or at the spinodal instability. Since Born instability has a smaller critical extension, the system does fail at the bifurcation point predicted by Born instability up to the highest temperature T = 1200K simulated. The transition conserves the volume and thus shows the continuous feature of martensitic transition. This behavior is well in agreement with that predicted by our theoretical analysis.

In general, a crystal structure can be described by two sets of parameters, one defines the lattice and the other defines the structure within the primitive lattice cell. Our simulations show that when the deformed system is stable, both of these parameters are static (have certain average value). When the spinodal phase transitions take place, both the lattice parameters and structure parameters change from static to dynamic variables, whereas the transitions associated with Born instability involve a similar change in lattice parameters but not in the structure variables. In the case of spinodal transition, the driving force is the large stress fluctuations which result from the loss of the correlation of the near neighbor atoms, while in the case of martensitic transition, although the lattice parameters change with time, the neighbor atoms do not lose their spatial correlation and move in a collective manner, the lattice can spontaneously undergoes a shear.

Considering the mechanical melting transition, there are still some ambiguities in determining the underlying cause [Phillpot 90]. We have shown explicitly that both spinodal and Born instability can initiate this transition, but with completely different mechanisms. In the former case, pure dilatation leads to the sudden jump in the internal energies and lattice parameters as shown in Figs. 4.6 (a), (b), and 4.7 (a) and (c). The mechanical melting requires a latent heat and volume, therefore, is a discontinuous, first-order phase transformation. The mechanical melting temperatures are well predicted by the critical strain curves. As can be seen in Figs. 5.21 and 6.26, the extrapolation of critical-strain curves of the spinodal instability, which is an extrapolation from the finite applied stress load to zero load, gives the melting temperature $T_s^{s'}$ = 1357.2K for L-J model of Cu and $T_s^{s'}$ = 1368K for the EAM model of Au. These temperatures are very close to the

observed mechanical melting points for these two models, i.e., T_s = 1365K for L-J model of Cu and T_s = 1360K for EAM potential model of gold.

In the literature, the Born criterion is usually used as the criterion for mechanical melting [Tallon 79a, Boyer 85, Wolf 90b, Okamoto 90], but no direct observation reported shows clearly the connection of the Born instability and mechanical melting. When extrapolating our critical strain data for the Born instability to zero load [cf. Figs. 5.21 and 6.26], one gets the mechanical melting temperature for L-J model of Cu is T_s^B = 1444.3K, and T_s^B = 1454.8K for EAM potential model of Au. In simulation when the system is heated up under zero applied stress, since there is no constraint on the strain response the system is free to follow any one of the three instability conditions which gives the smallest critical expansion. The bifurcation occurs at T = 1350K which is 30K lower than observed in the case of spinodal instability.

8.2 Recommendations for Future Work

In this thesis we have studied the elastic instabilities of a crystal lattice with cubic and tetragonal symmetry through a combined approach of continuum elasticity analysis and atomistic simulations. For the theoretical part of analysis, it could be useful to extend the present work to other elastic symmetries. This should be quite straightforward by using the equation of instability developed in Chapter 2. The current linearized elasticity analysis is applicable not only to a homogeneous system but also it may provide information on the possible local fail modes in an infinite system with imperfections. For the simulation part, the present work can be readily extended to other systems of different structures, for example, the molecular systems of ice, benzene, the covalent bonding system like Si, and binary alloy systems where elastic instability may be achieved by local distortion. The work that has not been done in this thesis is a systematic investigation of the system size effect on elastic instability and the final state of the unstable system. Based on the results of the largest system of N=1372 we have studied, we believe that for very large systems the instability criterion may be satisfied locally by thermal activation so that the failure of the system may take the form of creation of defects.

Both melting and solid-state amorphization (SSA) are the processes during which the system undergo structural disordering. It has recently been proposed that considerations of thermodynamic parallels between conventional melting by heating and solid-state amorphization suggest a unified picture of how crystals undergo structural disordering. [Johnson 86, Cahn 86, Richet 88, Wolf 90a, Green 90,] Following the observations that structural disordering is always accompanied by a volume expansion, it

has been suggested that volume expansion should play a central role in SSA in an analogous manner to the melting transition. The implication is that at temperatures below the triple point, essentially the melting point at zero pressure T_m, a sudden volume expansion may bring about structural disordering.

Regarding this volume-expansion induced crystal-to-amorphous transition, it appears that the present results do not generally support this hypothesis. In both potential models we studied, structural disordering only occurs at the high temperatures just below the melting point under volumetric deformation. In the case of superheating a crystal to melting, the Born instability triggers the structural disordering only at the mechanical melting temperature. It is interesting to note that the destruction of long-range order occurs only in the high temperature region where thermal disordering is large. We feel that in view of the SSA as a mechanical catastrophe alias elastic instability like mechanical melting, the local structural distortion is important in triggering SSA. Several recent works have given evidence of this effect [Hsieh 89, Sabochick 91]. Li et al. [Li 92] reported that in a simple L-J model of two species, a shear distortion of the simulation cell is found at the onset of amorphization. At the same time, sharp decreases in the bulk and shear moduli are also observed. A study of the propagation of a crack tip [Becquart 92] has shown that under shock stress large local distortions, either local expansion or contraction, are induced in a pure Al metal system, and the system is amorphized at 300K. It seems clear that a combined approach of elastic instability analysis with either experiment or computer simulation can bring insight into the mechanism of SSA.

Another closely related area that the elastic instability analysis may be applied is the study of fracture. Much work in this area is concerned with the propagation of the crack tip assuming that the crack tips already exist in the system. Some recent results have appeared in attempts to correlate the elastic instability with direct simulation to understand the nucleation of microcracks [Blumberg Selinger 90] and the microscopic origin of hydrogen embrittlement in Pd-H system [Zhong 92]. Several studies of two-dimensional systems which fails mechanically under different deformations have shown insightful results [Ashurts 76, Dodson 84, Sahimi 86]. Further study should emphasize on the direct correlation between the elastic instability and the failure behavior.

References

Allen M. P. and Tildesley D. J., in *Computer Simulation of Liquids* (Clarendon Press, Oxford, 1987).

Anderson H. C., J. Chem. Phys. **72**, 2384 (1980).

Ashurt W. T. and Hoover W. G., Phys. Rev. B**14**, 1465 (1976).

Blumberg Selinger R. L. B.Wang Z. G., Gelbart W. M., and Ben-Shaul A., Phys. Rev. A**43**, 4396 (1990).

Blumberg Selinger R. L. B.,Wang Z. G., and Gelbart W. M., J. Chem. Phys. **95**, 9128 (1991).

Binder K., J. Comput. Phys. **59**, 1 (1985).

Bolling G. F. and Richman R. H., Phil. Mag. **19**, 247 (1969).

Bolling G. F. and Richman R. H., Scr, Metall., **4**, 539 (1970a).

Bolling G. F. and Richman R. H., Acta. Metall., **18**, 673 (1970b).

Bolling G. F. and Richman R. H., Met. Trans., **2**, 2451 (1971).

Born M., J. Chem. Phys. **7**, 591 (1939).

Born M. and Huang K., in *Dynamical Theory of Crystal Lattice* (Clarendon Press., Oxford, Landon, 1956).

Boyer L.L., Phase Transitions **5**, 1 (1985).

Cahn R. W., and Johnson W. L., J. Mater. Res. **1**, 724 (1986a).

Cahn R. W., Nature **323**, 668 (1986b).

Chueng K. S., Harrison R. J. and Yip S., J. Appl. Phys., **71**, 4009 (1992).

Collard S. M., and Mclellan R. B., Acta Metall. Mater. **39**, 3143 (1991).

Daw M. S. and Baskes M. I., Phys. Rev. Lett., **50**, 1285 (1983).

Daw M. S. and Baskes M. I., Phys. Rev. B**29**, 6443 (1984).

Delaey, G. J. and Drishnan R. V., J. Phys. Chem. Solids, **48**, 1015 (1987).

Dodson B. W. and Taylor P. A., Phys. Rev. B**30**, 1679 (1984).

Fecht H. J. and Johnson W. L., Nature **334**, 50 (1986).

Finnis M. W. and Baskes M. I., Phil. Mag. A**50**, 45 (1984).

Gaeges J., Gleiter H., and Perepezko J. H., Phys. Lett. A **119**, 79 (1986).

Green J. L., Durben D. J., Wolf G. H., and Angell C. A., Science **249**, 649 (1990).

Girifalco L. A., and Weizer V. G., Phys. Rev. **114**, 687 (1959).

Grimvall G., in *Thermophyscal Properties of Materials* (North-Holland, New York, 1986).

Grover R., Getting I. C., and Kennedy G. C., Phys. Rev. B**7**, 567 (1973).

Guy A., in *Elements of Physical Metallurgy* (Addison-Wesley, New York, 1960).

Haile J. M, in *Molecular Dynamics Simulation* (Wiley-Sons, New York, 1992).

Hill R. and Milstein F., Phys. Rev. B**15**, 3087 (1977).

Holian B. L. and Grady D. E., Phys. Rev. Lett., **60**, 1355 (1988).

Hsieh H., and Yip S., Phys. Rev. B**39**, 7476 (1989).

Jaszczak J. A., Phillpot S. R., and Wolf D., J. Appl. Phys. **68**, 4573 (1990).

Jaszczak J. A. and Wolf D., J. Mater. Res. **6**, 1207 (1991).

Jaszczak J. A. and Wolf D., Phys. Rev. B**46**, 2473 (1992).

Johnson W. L., Prog. Mater. Sci. **30**, 81 (1986).

Johnson W. L., in *Materials Interface - Atomic-Level Structure and Properties*, edited by D. Wolf and S. Yip (Chapman and Hall, London, 1992).

Kieffer J., and Angell C. A., J. Non-cryst. Solids **106**, 336 (1988).

Kirby R. K., in *American Institute of Physics Handbook*, edited by Gray D. E. (McGraw-Hill Book Co., Inc., New York, 1963), Second Ed., p. 4-64.

Kittel C., in *Introduction to Solid State Physics* (wiley-Sons, New York, 1956)

Landau L. and Lifshitz E., in *Theory of Elasticity* (Pergmon Press, New York, 1970).

Li M., and Johnson W. L., (to be published on Phys. Rev. Lett.)

Lutsko J. F., Wolf D., Yip S., Phillpot S. R. and Nguyen T., Phys. Rev. B**38**, 11572 (1988).

Lutsko J. F., J. Appl. Phys., **65**, 2991 (1989a).

Lutsko J. F., Wolf D., Phillpot S. R., and Yip S., Phys. Rev. B**40**, 2481 (1989b).

Lutsko J. F., in *Computer Simulation in Materials Science*, edited by Meyer M. and Pontikis V (Kluwer Academic, Netherlands, 1991).

Luzzi D. E. and Meshii M., Res. Mechanica **21**, 207 (1987), and papers in J. Less-Comm. Met. **140** (1988).

Malvern L., in *Introduction to the Mechanics of A Continuous Medium* (Prentice-Hall, New Jersey, 1969).

Metropolis N., Rosenbluth A. W., Rosenbluth M. N., Tellar A. H. and Tellar E., J. Chem. Phys. **21**, 1087 (1953).

Milstein F, J. Appl. Phys. **44**, 3825 (1973).

Milstein F. and Hill R., J. Mech. Phys. Solids, **25**, 457 (1977).

Milstein F. and Hill R., J. Mech. Phys. Solids, **26**, 213 (1978).

Milstein F. and Hill R., J. Mech. Phys. Solids, **27**, 255 (1979a).

Milstein F. and Hill R., Phys. Rev. Lett., **43**, 1411 (1979b).

Milstein F. and Farber B, Phys. Rev. Lett., **44**, 277 (1980).

Murnaghan F. D., in *Finite Deformation of an Elastic Solid* (Wiley, New York, 1951).

Murnaghan F. D., Proc. Nat. Acad. Sci. **30**, 244 (1944).

Najafabadi R. and Yip S., Scr. Metall., **17**, 1199 (1983).

Neighbours J. R., and Alers G. A., Phys. Rev. **111**, 707 (1958).

Okamoto P. R., Rehn L. E., Pearson J., Bhadra R., and Grimsditch M., J. Less-Common Met. **140**, 231 (1988).

Okamoto P. R. and Meshii M., in *Science of Advanced Materials*, edited by Wiedersich H. and Meshii M. (AMS International, Materials Park, OH, 1990), p 33.

Overton W. C., Jr., J. Chem. Phys. **37**, 2975 (1962).

Parrinello M. and Rahman A., J. Appl. Phys. **52**, 7182 (1981).

Phillpot S. R., Wolf D., and Yip S., MRS Bulletin XV, 38 (1990).

Ray J. R. and Rahman A., J. Chem. Phys. **80**, 4423 (1984).

Ray J. R., Moody M. C. and Rahman A., Phys. Rev. B**32**, 733 (1985a).

Ray J. R., Moody M. C. and Rahman A., Phys. Rev. B**33**, 895 (1985b).

Reismann H. and Pawlik P., in *Elasticit Theory and Applications* (Wiley-Sons, New York, 1980).

Richet P., Nature **331**, 56 (1988).

Saada A. in *Elasticity Theory and Application,s* (Pergamon Press, New York, 1974).

Sabochick M. and Lam N. Q., Phys. Rev. B**43**, 5243 (1991).

Sahimi M. and Goddard J. D., Phys. Rev. B**33**, 7848 (1986).

Schuller I. K., Fartash A., and Grimsditch M., MRS Bulletin XV, 33 (1990).

Sciortino F., Stanley H. E., Shao J., Wolf G. H. and Angell C. A., Phys. Rev. Lett. (to be published).

Soules T. F., and Busbey R. F., J. Chem. Phys. **78**, 6307 (1983).

Speedy R. J., J. Phys. Chem. **86**, 3002 (1982).

Swenson C. A., J. Phys. Chem. Sol. **49**, 1339 (1968).

Tallon J. L., and Robinson W. H., Phil. Mag. **36**, 741 (1977).

Tallon J. L., Phil. Mag. **39**, 151 (1979a).

Tallon J. L., J. Phys. Chem. Sol. **40**, 831 (1979b).

Tallon J. L., J. Phys. Chem. Sol. **41**, 837 (1980).

Thurston R. N., in *Physical Acoustics*, edited by Mason W. P (Academic, New York, 1964), Vol. 1, Part A.

Ubbelohde A. R., in *The Molten State of Mater: Melting and Crystal Structure* (Wiley, Chichester, 1978).

Venkataraman G., Feldkamp L. A., and Sahni V. C. in *Dynamics of Perfect Crsytals* (The MIT Press, Cambridge, 1975).

Wallace D., in *Thermodynamics of Crystal* (Wiley-Sons, New York,1972).

Wallace D., in *Solid State Physics*, edited by Ehrenreich H., Seitz F., and Turnball D. (Academic, New York, 1970), Vol. 25.

Wallace D., Shiferl S. K., and Straub G. K., Phys. Rev. A**30**, 616 (1984).

Wang J. H., Yip S., Phillpot S. R., and Wolf D., J. Alloys and Compounds. (to be published).

Wang Z. G., Landman U., Selinger R. L. B., and Gelbart W. M., Phys. Rev. B**44**, 378 (1991).

Wolf D. and Lutsko, J. F., Phys. Rev. Lett. **60**, 1170 (1988).

Wolf D. and Lutsko, J. F., J. Mater. Res., **4**, 1427 (1989a).

Wolf D. and Lutsko, J. F., J. Apll. Phys. **66** 1961 (1989b).

Wolf D., Mater. Sci. Eng. A**126**, 1 (1990a).

Wolf D., Okamoto P. R., S. Yip, Lutsko J. F. and Kluge M., J. Mater. Res. **5**, 286 (1990b).

Wolf D., Acta-Scr. Met. Proc. Series **4**, 52 (1990c).

Wolf D., Surf. Sci. **225**, 117 (1990d).

Wolf D. and Jazzack J., in *Materials Interface*, Chapter 2, edited by D. Wolf and S. Yip, (Champman-Hall, New York, 1992).

Wood W. W., in Physics of Simple Liquids, edited by Temperley H. N. V., Rowlinson J. S., and Rushbrooke G. S. (North Holland, Amsterdam, 1968a).

Wood W. W., J. Chem. Phys. **48**, 415 (1968b).

Wood W. W., J. Chem. Phys. **52**, 729 (1970).

Yip S. and Wolf D., Materials Science Forum, **46**, 77 (1989).

Zhang Q., Durben D. J., Wolf G. H., and Angell C. A., Science **254**, 829 (1991).

Zhong W., Cai Y., and Tomanek D., Phys. Rev. B**46**, 8099 (1992).